



**HAL**  
open science

# Composants micro-optiques pour systèmes miniatures d'imagerie à base de technologie MEMS

Jose Vicente Carrion Perez

► **To cite this version:**

Jose Vicente Carrion Perez. Composants micro-optiques pour systèmes miniatures d'imagerie à base de technologie MEMS. Micro and nanotechnologies/Microelectronics. Université de Franche-Comté, 2016. English. NNT: 2016BESA2034 . tel-01672056

**HAL Id: tel-01672056**

**<https://theses.hal.science/tel-01672056>**

Submitted on 23 Dec 2017

**HAL** is a multi-disciplinary open access archive for the deposit and dissemination of scientific research documents, whether they are published or not. The documents may come from teaching and research institutions in France or abroad, or from public or private research centers.

L'archive ouverte pluridisciplinaire **HAL**, est destinée au dépôt et à la diffusion de documents scientifiques de niveau recherche, publiés ou non, émanant des établissements d'enseignement et de recherche français ou étrangers, des laboratoires publics ou privés.

# SPIM

## Thèse de Doctorat

UFC

école doctorale **sciences pour l'ingénieur et microtechniques**  
UNIVERSITÉ DE FRANCHE-COMTÉ

N° X | X | X |

THÈSE présentée par

**JOSÉ VICENTE CARRIÓN PÉREZ**

pour obtenir le

Grade de Docteur de  
l'Université de Franche-Comté

Spécialité : **Sciences pour l'Ingénieur**

**Design and fabrication of micro optical components  
for miniaturized optical imagers**

Unité de Recherche :  
Institut FEMTO-ST

Soutenue publiquement le 22 décembre 2016 devant le Jury composé de :

HEIDI OTTEVAERE	Rapporteur	Professeur, Vrije University of Brussels, Belgique
IGNACIO MORENO SORIANO	Rapporteur	Professeur, Université Miguel Hernández de Elche, Espagne
YVES JOURLIN	Examineur	Professeur, Université Jean Monnet, Saint-Etienne
FRANCK CHOLLET	Examineur	Professeur, Université de Franche-Comté, Besançon
CHRISTOPHE GORECKI	Directeur de thèse	Directeur de recherche CNRS à FEMTO-ST, Besançon
NICOLAS PASSILLY	Encadrant de thèse	Chargé de recherche CNRS à FEMTO-ST, Besançon

A la mémoire de mon grand-père,  
la meilleure personne que j'ai jamais connu.





# ACKNOWLEDGMENTS

Je voudrais d'abord remercier mon encadrant Christophe Gorecki de m'avoir donné l'opportunité de réaliser mes travaux de thèse au sein du groupe MOEMS à l'Institut FEMTO-ST pendant ces trois années. Son aide et ses conseils ont été d'une grande utilité pour finir ce travail en temps voulu. Je voudrais aussi souligner le rôle de mon co-encadrant Nicolas Passilly, d'avoir toujours eu la porte de son bureau ouverte pour moi et pour tous ses conseils et idées sans lesquels je ne serais jamais arrivé au bout. Je ne remercierai jamais assez Jorge « el joven » Alberio de m'avoir aidé les premiers mois à m'adapter à la ville et m'avoir donné les premières formations en salle blanche, Sophie Marguier pour sa bonne humeur 7 jours sur 7 et le reste de l'équipe MOEMS avec qui j'ai eu la chance de travailler.

Une thèse sur la fabrication de composants optiques comme celle-là contient une partie technologique très importante, c'est pourquoi je voudrais particulièrement remercier tout le personnel de salle blanche MIMENTO, et spécialement, David Raddenzati, Laurent Robert, Djaffar Belharet et Cyril Million pour toutes les heures passées avec moi et sans lesquelles je n'aurais jamais réussi à accomplir mes objectifs.

J'aimerais aussi relever les bons moments partagés avec mes collègues de bureau (Stéphane « Lebron » Perrin, Justine Lullin, Vincent Maurice, Alpha Diallo et Quentin Tanguy) et les remercier pour l'atmosphère de travail et le bonheur partagé pendant ces 3 ans, 2 mois et 25 jours. Je vous considère plus comme des copains que des collègues. Et même si elle n'est pas une collègue de bureau, mention spéciale à Sandrine « Bordel » Quarroz pour tous les rires apportés pendant, et pas seulement, les moments plus compliqués.

Durante este tiempo he tenido la suerte de conocer a gente excepcional y hacer amistades que guardaré toda la vida. Nunca olvidaré la acogida que un grupo de franceses (y no franceses) han dado a este español y con los que he podido compartir una cerveza en el Brasseliande, un kilómetro corriendo, un partido de fútbol, un festival de música (o vino amarillo), una barbacoa, una soirée, un rato de consola, un paseo y sobretodo muchas muchas risas. Si algo me ha enseñado esta experiencia (aparte de cómo fabricar micro-axicones utilizando un láser de potencia variable o hinchando vidrio) es, entre otras cosas, a derribar clichés estúpidos sobre otras nacionalidades, razas o religiones. De entre todas las personas que he conocido en Besançon me gustaría destacar a Yannick, Gloria y Amelia (ma gueule, mi amiga y mi ahijada), Antonio (generoso como pocos), Abel (la classe espagnole), John Dudley y Venancio (que me llevaron a conocer a Coralie), Julien (La roulade), Ludo (Casillaaas), Mathieu y Zou (La banda de conardinhos).

Dejando lo mejor para el final quiero mencionar a mis padres por el esfuerzo enorme

---

que han hecho toda su vida para que yo llegue hasta aquí, a mi hermano por haberme apoyado siempre, a Coralie (mi guapa) por haberme ayudado (y sufrido) tanto todo este tiempo y seguir a mi lado, a mi “bella” familia por hacer mi vida en el extranjero un poco más fácil y a mis amigos “Golfos” de Albacete a los que tanto he echado de menos.

# CONTENTS

0.1	Opening words . . . . .	1
0.2	Objectives of thesis . . . . .	1
0.3	Thesis structure . . . . .	3
<b>1</b>	<b>Context of work</b>	<b>5</b>
1.1	Basic properties of refractive and diffractive microlenses . . . . .	7
1.1.1	Aberrations . . . . .	8
1.1.1.1	Spherical Aberrations . . . . .	10
1.1.1.2	Coma . . . . .	11
1.1.1.3	Astigmatism . . . . .	12
1.2	Technological context . . . . .	13
1.3	Material context . . . . .	15
<b>2</b>	<b>Fabrication techniques for optical components based on continuous profiles</b>	<b>17</b>
2.1	Diamond turning . . . . .	17
2.2	E-beam lithography . . . . .	20
2.3	Laser beam lithography . . . . .	22
2.4	Photoresist processing in optical lithography fabrication . . . . .	25
2.4.1	Optical absorption and contrast. Suited exposure wavelengths . . . . .	28
2.4.2	Exposure dose and development rate . . . . .	30
2.4.3	Etching . . . . .	31
2.4.4	Issues related when working with thick photoresist . . . . .	35
2.5	Other direct fabrication techniques . . . . .	35
2.5.1	Half-tone mask lithography . . . . .	36
2.5.2	Focused Ion Beam (FIB) . . . . .	37
2.5.3	Femto-second laser micromachining . . . . .	37
2.6	Comparison between optical lithography fabrication techniques . . . . .	38
2.7	Conclusions of chapter 2 . . . . .	40
<b>3</b>	<b>Laser beam lithography. Characterizations and realizations</b>	<b>43</b>
3.1	Characterization of laser lithography system . . . . .	44

3.1.1	Designing the pattern. Factors to take into account . . . . .	47
3.1.1.1	Sub-pattern division. Writing field . . . . .	48
3.1.1.2	Correct focusing of the exposure . . . . .	52
3.2	Characterization of Photoresist AZ-4562 . . . . .	54
3.2.1	Spin coating . . . . .	56
3.2.2	Solvent elimination and hydration of coated photoresist . . . . .	60
3.2.3	Patterned components after development of photoresist . . . . .	63
3.2.3.1	Single exposure . . . . .	63
3.2.3.2	Double exposure . . . . .	65
3.2.4	Baking of developed photoresist . . . . .	66
3.2.5	Pattern transfer into the substrate . . . . .	68
3.3	Recipe for fabrication of glass-based microoptical components through gray-scale lithography process . . . . .	72
3.4	Realizations . . . . .	74
3.4.1	Fabrication of glass-based micro axicons . . . . .	75
3.4.1.1	Fabrication process . . . . .	76
3.4.2	Optical performance of glass-based microaxicons . . . . .	79
3.4.3	Optical performance of photoresist axicons . . . . .	86
3.5	Conclusions and perspectives of chapter 3 . . . . .	87
<b>4</b>	<b>Fundamentals of glass-reflow processes</b>	<b>89</b>
4.1	Fundamentals of glass processing and induced surface deformations in glass Borofloat 33 . . . . .	90
4.1.1	Chemical composition of glasses . . . . .	91
4.1.2	Physical properties of glass . . . . .	92
4.1.2.1	Thermal properties . . . . .	92
4.1.2.2	Optical properties . . . . .	94
4.1.2.3	Mechanical properties . . . . .	94
4.1.3	Annealing of glass substrate . . . . .	95
4.2	State of the art of glass reflow processes . . . . .	96
4.2.1	Conclusions of chapter 4 . . . . .	101
<b>5</b>	<b>Glass reflow processes. Characterizations and realizations</b>	<b>103</b>
5.1	Principle and technologies involved in the fabrication . . . . .	104
5.2	Glass blowing as a fabrication process . . . . .	105
5.2.1	Cavities sealed under vacuum pressure . . . . .	107

---

5.2.2	Cavities sealed under atmospheric pressure . . . . .	108
5.3	Characterization of the process . . . . .	109
5.3.1	Volume evolution in rectangular cavities . . . . .	109
5.3.2	Ring-shaped concentric cavities . . . . .	114
5.3.3	Conical lens generation . . . . .	118
5.4	Recipe for parallel fabrication of glass-based axicons through glass reflow process . . . . .	122
5.5	Optical performance of microaxicons fabricated by glass blowing process .	124
5.5.1	Optical performance of two rings based microaxicon . . . . .	125
5.5.2	Optical performance of fours rings based axicon . . . . .	127
5.6	Roughness and repeatability of blowing process . . . . .	132
5.7	Conclusions of chapter 5 . . . . .	132
<b>6</b>	<b>General conclusions and perspectives of work</b>	<b>135</b>



# LIST OF FIGURES

1.1	Quantization, or blazing, of a prisms. . . . .	6
1.2	Different quantization schemes for diffractive lenses: (a) conventional quantization based on Fresnel zones; (b) superzone concept to increase the aperture of lenses. Source:[Sinzinger et al., 2006]. . . . .	6
1.3	Focusing of a collimated beam. . . . .	8
1.4	Point spread function of ideal lens. Source: [Olympus, 2012] . . . . .	9
1.5	1D point spread function (PSF) of an ideal lens. . . . .	9
1.6	Spherical aberration. Variation of focus with aperture. . . . .	10
1.7	Comparison of a spherical (a) and aspherical (b) surface. Source: [Fischer et al., 2000] . . . . .	11
1.8	Coma. Variation of magnification with aperture. . . . .	11
1.9	Schema illustration of astigmatism. . . . .	12
1.10	Comparison between expansion coefficient ( $\alpha$ ), transition temperature ( $T_g$ ) and passing band for some common plastic and glass materials. . . . .	15
2.1	Machining of microstructures in a turning process. Source: [Brinksmeier et al., 2012] . . . . .	18
2.2	Main processing steps for microoptical components replication. Source: [Sinzinger et al., 2006] . . . . .	18
2.3	General classification of lithography technologies. . . . .	20
2.4	Schema of electron penetration into a substrate (left) and energy expansion inside the electron-sensitive resist (right). Source: [Kley, 1997]. . . . .	21
2.5	Schema of Heidelberg DWL200 Direct Writing Laser System. Red line corresponds to the writing system composed by the HeCd laser, AOM and AOD. Yellow line corresponds to the imaging system composed by two cameras and the illumination system. . . . .	24
2.6	Pattern generation in positive and negative photoresist. . . . .	25
2.7	Development rate and exposure dose for a ideal (red), real (blue) and low (green) contrast photoresist. . . . .	26
2.8	(a) Organic Molecule of Novolac. (b) Changes in development rate of Novolac and PAC. . . . .	27
2.9	PAC reaction when exposed to UV radiation. . . . .	27

2.10	Absorption coefficient as a function of the wavelength for some positive photoresists. Source:[MicroChemicals, 2013c]. . . . .	28
2.11	Contrast curves for high and low contrast positive photoresists. Source: [MicroChemicals, 2007a]. . . . .	30
2.12	Development rate and dark erosion as a function of the developer concentration for the photoresist AZ-9260 of Microchemicals. Source:[MicroChemicals, 2013a]. . . . .	31
2.13	Schema of a reactive ion etching chamber. . . . .	33
2.14	Principle of <i>Bosch</i> etching pump process. Source: [Queste, 2008]. . . . .	34
2.15	Edge bead produced during slow spin coating process. . . . .	35
2.16	(a) The three primary steps in gray-scale technology. Source: [Waits et al., 2005] (b) Filling factor and transmitted energy level in half-tone masks. . . . .	36
3.1	Relation between layers in designed structure and power percentage associated to each one. . . . .	45
3.2	Schema of the sub-pattern division carried by the writing system before exposure. . . . .	47
3.3	Focal distance of writing lens and coated substrate placed at correct distance for best resolution. . . . .	48
3.4	(a) Image of component designed. (b) Image created by the <i>Conversion Job Manager</i> software. . . . .	49
3.5	(a) Image created by the conversion software with the component divided into two <i>lic</i> files. (b) Zoomed images of the <i>lic</i> files. . . . .	49
3.6	Figure of exposed component into photoresist after development with overlapped working fields. . . . .	50
3.7	Profile of a 32-level stairs structure divided into four <i>lic</i> files. . . . .	50
3.8	(a) Image created by the conversion software with the component divided into five <i>lic</i> files. (b) Developed pattern with vertical lines passing over the structure and modifying its profile. . . . .	51
3.9	Modified pattern to avoid vertical lines created during the conversion process. (a) Image created by the conversion software. (b) Developed pattern. . . . .	51
3.10	Diffractive lens of 500 $\mu\text{m}$ diameter and 7 levels. (a) Image created by the conversion software with the component divided into two <i>lic</i> files. (b) Microscopy image of the developed component with the vertical line passing over the structure. . . . .	52
3.11	Developed component with different values of focus and power exposure. . . . .	53
3.12	(a) Typical coating cycle for spin coating photoresist deposition. (b) Coating cycle for double spin coating of photoresist deposition. . . . .	57
3.13	Schema of centrifugal and frictional forces during spin coating. . . . .	57



3.14 Thickness obtained for the photoresist AZ-4562 as a function of the speed spin for two durations. Blue line corresponds to a single spin during 30 seconds, red line corresponds to a single spin during 7 seconds and the green line correspond to thickness obtained through double spins (30 + 10 sec). . . . .	58
3.15 Position of measured points to evaluate thickness variations in the coated substrate. . . . .	59
3.16 Coated substrate with withdraw from edges. . . . .	60
3.17 Development time (after exposure) as a function of rehydration time (before exposure) for positive photoresist AZ-9260 (similar characteristics to AZ-4562). Source: [MicroChemicals, 2013f] . . . . .	61
3.18 Photoresist collapse on substrate because of thermal shock during solvent evaporation. . . . .	62
3.19 Temperature evolution during photoresist solvent evaporation to avoid thermal stress. . . . .	62
3.20 Depth achieved in photoresist after single exposure as a function of power exposure and layer in the design. . . . .	64
3.21 Photoresist lifts off the substrate because of a too long development process. . . . .	64
3.22 Depth achieved in photoresist after double exposure as a function of layer in design. . . . .	65
3.23 Contrast curve of exposed photoresist. . . . .	66
3.24 Changes in developed structure after baking step. . . . .	67
3.25 Profile evolution of two stair-like structures of 4 and 8 levels during 1, 2 and 5 minutes reflow at 120° C. . . . .	68
3.26 (a) Microscope image of a diffractive lens after development process. (b) Microscope image of same lens after 1 minute reflow at 120°C. . . . .	68
3.27 Schema of the process followed to measure selectivity. . . . .	70
3.28 (a) Schema of the pyramid structure used in the fabrication process. (b) Profile of developed (blue) and etched (red) pyramid structure of 1 mm side, 1.3 μm thickness and 8 levels. . . . .	72
3.29 Schema of resist stepped structure, refractive profile in photoresist and etched glass micro axicon. . . . .	76
3.30 Schema of diffractive structure patterned in photoresist with vertical dimensions of design and protection layer. . . . .	76
3.31 (a) Profile of component after development. (b) 3D image of developed component. . . . .	77
3.32 (a) Profile of component after baking at 120° C during 5 seconds. (b) 3D image of baked component. . . . .	78
3.33 (a) Profile of component after etching process. (b) 3D image of etched component. . . . .	78
3.34 Schema of Bessel beam formation behind an axicon. . . . .	79

3.35	Schema of a Bessel beam formation behind an axicon. . . . .	80
3.36	(a) Normalized Gaussian beam distribution of 20 mm focal length lens. (b) On-axis intensity. . . . .	81
3.37	(a) Normalized Gaussian beam distribution of same lens with and a perfect axicon of $\alpha = 0.5^\circ$ . (b) Corresponding on-axis intensity. . . . .	81
3.38	Shape of axicons with radius of curvature 0 and 1.5 mm. . . . .	82
3.39	(a) Normalized beam distribution with non-perfect axicon ( $\alpha=0.5^\circ$ , $R_c=20\text{mm}$ ). (b) On-axis intensity. . . . .	82
3.40	Schema of the characterization system. Source: [Baranski et al., 2014] . . . . .	83
3.41	Schema of characterization system. . . . .	83
3.42	(a) Experimental normalized Gaussian beam distribution with a 25.4 mm focal length lens (33.8 mm BFP). (b) On-axis intensity. . . . .	84
3.43	(a) Normalized beam distribution with axicon. $R_c=10.87$ mm, $e_0=3.77$ $\mu\text{m}$ , $\alpha=0.47^\circ$ . (b) On-axis intensity. . . . .	84
3.44	Transverse intensity distributions at (a) $z= 19$ mm., (b) $z= 22$ mm., (c) $z= 23.6$ mm. (maximum on-axis intensity) and (d) $z= 26$ mm. . . . .	85
3.45	(a) Radial intensity distribution of dark hollow beam. $z=38.2$ mm (b) Transverse intensity distribution. . . . .	86
3.46	(a) Normalized beam distribution with axicon. $R_c=1.5$ mm, $e_0=14.04$ $\mu\text{m}$ , $\alpha=1.79^\circ$ . (b) On-axis intensity. . . . .	87
3.47	Radial intensity distribution of dark hollow beam. $z=28.4$ mm . . . . .	87
4.1	Specific volume vs temperature during the sate transformation of glass. Source: [Wlodarczyk, 2011] . . . . .	90
4.2	Thermal properties of glass Borofloat33 as a function of the temperature. (a) Thermal conductivity, $\lambda$ . (b) Thermal expansion, $CTE$ . (c) Specific heat capacity, $C_p$ . Source: [Schott, 2016a] . . . . .	93
4.3	(a) Optical transmittance and (b) refractive index, $n$ of Borofloat33 as a function of the temperature. Source: [Schott, 2016a] . . . . .	94
4.4	Viscosity-temperature relation in Borofloat33 glass. . . . .	95
4.5	Temperature evolution during annealing process. . . . .	96
4.6	(a) MEMS based process sequence of GFP technology. (b) Contactless formation of GFP lens by viscous flow: schematic (left) and SEM cross section of 50 $\mu\text{m}$ lens (right) before and after thermal anneal at 720°C. Source: [Merz et al., 2003]. . . . .	97
4.7	(a) Fabrication process for glass blowing on wafer level. (b) Cross section of fabricated hollow glass semisphere. Source: [Eklund et al., 2007]. . . . .	97
4.8	(a) Schema of the effect produced by the process of double-step anisotropic etching. (b) Fabrication process of microlenses. (c) Glass microlenses matrix with 100% fulfill factor on a Si frame. Source: [Albero et al., 2008]. . . . .	98

4.9	(a) Conceptual schematics of a 3D spherical shell resonator fabrication using wafer-scale metal-on-glass stack glassblowing. (b) Photographs of a continuous metal trace fabricated on a glass-blown spherical shell structure. Source: [Prikhodko et al., 2011]. . . . .	98
4.10	(a) Schematic of the process flow for the glass wafer. (b) A detail view of a wafer level vacuum packaged mirror with an inclined window (window size: 3mm x 4mm). Source: [Stenchly et al., 2012]. . . . .	99
4.11	(a) Schematic of the process flow for the glass wafer. (b) Optical photograph of glassblown TSG inverted-wineglass structure. Outer diameter is 4200 m. Glassblown at 1650 °C. Source: [Senkal et al., 2013]. . . . .	99
4.12	(a) Measured 2D Modulated Transfer Function (MTF) of glass millimeter-sized lenses in different situations, <i>a</i> single item, <i>b</i> square array with applied compensation strategies and <i>c</i> square array without compensation. (b) Microfabricated glass lenses. Silicon is selectively eliminated by grinding and polishing for vertical integration purposes. Source: [Albero et al., 2015]. . . . .	100
4.13	(a) Fabrication process. <i>a</i> Silicon wafer. <i>b</i> Thermal oxidation. <i>c</i> Immersion photolithography, RIE and deep RIE. <i>d</i> Anodic bonding. <i>e</i> Glass reflow process. <i>f</i> Lapping and polishing process. <i>g</i> Backside photolithography and deep RIE. (b) Cross section view of silicon pillars. Source: [Van Toan et al., 2015]. . . . .	100
5.1	Schema of an axicon fabricated by the proposed technique. . . . .	104
5.2	Simplified schema of glass blowing fabrication process. . . . .	105
5.3	First part of the fabrication process until anodic bonding between the wafers.	106
5.4	Fabrication process for cavities enclosed under vacuum pressure. . . . .	107
5.5	Fabrication process for cavities enclosed under atmospheric pressure. . . . .	108
5.6	Schema of AET oxidation furnace employed in the fabrication process. . . . .	109
5.7	Test 1. (a) Schema of rectangular cavities etched in silicon and sealed with glass substrate. (b) 3D image of same schema. . . . .	109
5.8	Temperature evolution during the reflow process at softening point glass. . . . .	110
5.9	SEM image of a group of blown cavities of different sizes after reflow process.	110
5.10	Cross section SEM image of two cavities and parameters measured in characterization process. . . . .	110
5.11	Cross section SEM image of a silicon cavity bonded with glass substrate of (a) 20, (b) 130 and (c) 200 $\mu\text{m}$ width. . . . .	111
5.12	Evolution of cavities and glass surface after reflow at 820°C. (a) Height (blue) and width (red) measured in blown cavities and deformed surface on glass (green). (b) Thickness pushed (blue) and slope (red) measured in glass surface. . . . .	112
5.13	(a) Height and (b) width evolution of blown volume in cavities as a function of etched width. . . . .	113

5.14 Influence of separation between cavities onto pushed glass thickness. . . . 113

5.15 (a) Schema of ring-shaped concentric cavities etched in silicon and sealed with glass substrate. (b) 3D image of same schema. . . . . 114

5.16 Microscope image and profile measured of cavities etched in silicon. . . . 115

5.17 Temperature evolution during the reflow process at (a) 800°C and (b) 850°C. 116

5.18 (a) Conic surface generated depending on magnitude and sign of the conic constant,  $K$ . (b) Graphic representation of shapes generated for different  $K$  values at constant radius of curvature  $R_c$ . Source: [Wikipedia, 2015]. . . . 116

5.19 Measured and fitted profile for component of 2 mm diameter heated at 850°C. Separation between cavities is (a) 108  $\mu\text{m}$ , (b) 133  $\mu\text{m}$ , (c) 158  $\mu\text{m}$ . . . . 118

5.20 Photography of silicon wafer with cavities etched with (a) two and (b) four rings before anodic bonding onto a glass wafer. . . . . 119

5.21 Schema of ring-shaped concentric cavities etched in silicon and sealed with glass substrate. (a) 0.9 mm and (b) 1.95 mm diameter lens. . . . . 119

5.22 Temperature evolution during the reflow process at 850°C and annealing process at 560°C during 3h30m. . . . . 120

5.23 Temperature evolution during the reflow process at 700°C during 4h. . . . 120

5.24 Cross section SEM image of etched silicon bonded with glass substrate after reflow process at 700°C. . . . . 121

5.25 Measured and fitted profile of fabricated components after glass liberation. Components fabricated with (a) two and (b) four rings. Position of cavities is represented in grey color at the bottom of each profile . . . . . 121

5.26 3D optical surface topography of components fabricated with (a) two and (b) four rings. . . . . 122

5.27 Schema of bonded wafers after reflow glued to glass substrate with UV adhesive ready for backside polishing. . . . . 124

5.28 Set-up image to observe transmissive components when illuminated by a Gaussian beam. . . . . 125

5.29 (a) Longitudinal normalized intensity distribution of two rings fabricated axicon. (b) On-axis intensity. . . . . 126

5.30 Intensity distribution with analyzed axicon at (a)  $z = 22$  mm., (b)  $z = 24$  mm. and (c)  $z = 26.4$  mm. (maximum on-axis intensity). . . . . 126

5.31 (a) Radial intensity distribution of dark hollow beam.  $z = 54.6$  mm (b) On-axis intensity. . . . . 127

5.32 (a) Longitudinal normalized intensity distribution of two rings fabricated axicon. (b) On-axis intensity. . . . . 127

5.33	Calculated intensity distributions (Normalized by the maximum value in each longitudinal plane) along the propagation axis for 4 rings-based axicons ( $\alpha=2.46^\circ$ , incident collimated Gaussian beam, $W_o=5$ mm). Axicon parameters and experimental conditions are changed to see the influence onto Bessel beam generation. (a) Ideal axicon (no bluntness, $R_c = 0$ ) – Aperture radius $\phi= 0.96$ mm. (b) Ideal axicon (no bluntness, $R_c = 0$ ) – Aperture radius $\phi= 1.96$ mm. (c) Fabricated axicon ( $R_c = 4.44$ mm) – Aperture radius $\phi= 0.96$ mm. (d) Fabricated axicon ( $R_c = 4.44$ mm) – Aperture radius $\phi= 1.96$ mm. . . . .	128
5.34	Calculated intensity distributions (with exponent 0.3 for better visualization) along the propagation axis for 4 rings-based axicons ( $\alpha=2.46^\circ$ , incident collimated Gaussian beam, $W_o=5$ mm). Axicon parameters and experimental conditions are changed to see the influence onto Bessel beam generation. (a) Ideal axicon (no bluntness, $R_c = 0$ ), aperture radius $\phi= 0.96$ mm. (b) Ideal axicon (no bluntness, $R_c = 0$ ), aperture radius $\phi= 1.96$ mm. (c) Fabricated axicon ( $R_c = 4.44$ mm), aperture radius $\phi= 0.96$ mm. (d) Fabricated axicon ( $R_c = 4.44$ mm), aperture radius $\phi= 1.96$ mm. . . . .	129
5.35	Intensity distribution with analyzed axicon at (a) $z= 15.6$ mm., (b) $z= 16.8$ mm. and (c) $z= 17.6$ mm. (maximum on-axis intensity). . . . .	130
5.36	Calculated transverse intensity profile of the beam generated by the 4 rings-based axicons ( $\alpha=2.46^\circ$ , $R_c = 4.44$ mm, incident collimated Gaussian beam $W_o=5$ mm, aperture radius $\phi= 0.96$ mm) for 3 distinct longitudinal positions (non-diffracting zone). . . . .	130
5.37	(a) Radial intensity distribution of dark hollow beam. $z=34.4$ mm (b) On-axis intensity. . . . .	131
5.38	Calculated transverse intensity profile of the beam generated by the 4 rings-based axicons ( $\alpha=2.46^\circ$ , $R_c = 4.44$ mm, incident collimated Gaussian beam $W_o=5$ mm, aperture radius $\phi= 0.96$ mm) for 2 distinct longitudinal positions in the hollow zone. . . . .	131
5.39	Evolution of blown area inside etched cavities as a function of the etched area. . . . .	134
6.1	3D schema of two silicon wafers bonded to a glass wafer to avoid wafer bowing during reflow. . . . .	138
6.2	Cross section schema of two silicon wafers bonded to a glass wafer to avoid wafer bowing during reflow at temperatures over $800^\circ\text{C}$ . (a) Before reflow. (b) After reflow . . . . .	139
6.3	SEM image of cross section of reflowed cavity and measured parameters to obtain the propagation angle of deformations. . . . .	140
6.4	SEM image of cross section of reflowed cavity and measured parameters to obtain the propagation angle of deformations. . . . .	141



# LIST OF TABLES

2.1	Comparison of reviewed direct-writing techniques. . . . .	39
3.1	Characteristics of Heidelberg DWL200 direct writing system. Sources: [FEMTO-ST, 2015b, LAAS/CNRS, 2016a] . . . . .	46
3.2	Comparison of some employed photoresist in laser lithography. . . . .	54
3.3	Physical and chemical properties of positive photoresist AZ-4562. Source: [GmbH, 2016]. . . . .	55
3.4	Specifications of RC8 Spin Coater of MicroTec used in this thesis work. Source: [poliFAB, 2016]. . . . .	55
3.5	Thickness values and variations obtained for each spin speed. . . . .	60
3.6	Thickness values and variations obtained for double spins. . . . .	60
3.7	Composition of Borofloat33 optical glass from Schott. . . . .	69
3.8	Tests of photoresist etching in glass. . . . .	71
3.9	Layers assigned during linearization process. . . . .	77
4.1	Mechanical and thermal properties of glass Borofloat33 of Schott. . . . .	96
4.2	Summary of some important parameters of glass reflow fabrication. . . . .	101
5.1	Geometrical values of etched cavities. . . . .	115
5.2	Fitted values for cavities etched with different sizes and separations. . . . .	117
5.3	Geometrical values of etched cavities of components fabricated with two and four rings. . . . .	119
5.4	Fitting results for fabricated lenses. . . . .	122
5.5	Fitting results for fabricated lenses. . . . .	132





# LIST OF ACRONYMS

## **INTRODUCTION:**

MOEMS: Micro-Opto-Electro-Mechanical Systems

OCT: Optical Coherence Tomography

## **CHAPTER 1:**

COC: Cycloolefin copolymer

DOEs: Diffractive optical elements

DRIE: Deep reactive ion etching

GFP: Glass flow process

GRIN: Gradient-index

GTM: Gray-tone mask

IC: Integrated circuit

IR: Infra-red

MIR: Mid-Infrared

PCB: Printed circuit board

PSF: Point spread function

RIE: Reactive ion etching

ROEs: Refractive optical elements

## **CHAPTER 2:**

AOD: Acousto optical deflector

AOM: Acousto optic modulator

BFP: Back focal plane

CD: Critical dimensions

DMD: Digital micro-mirror

DXF: Drawing eXchange Format

FIB: Focus ion beam

F/C: Fluorine to carbon ratio

HEBS: High energy beam sensitive

lic: License

MFLs: Micro-Fresnel lenses

MIMENTO: Microfabrication pour la MEcanique, les Nanosciences, la Thermique et l'Optique

OPC: Optical proximity correction

PAB: Post-apply bake

PAC: Photoactive compound

PV: Peak-to-valley

RF: Radio frequency

SOI: Silicon-on-insulator

SPDT: Single point diamond turning

**CHAPTER 3:**

CA: Chemically amplified

DHB: Dark hollow beams

IPFS: Intensity point spread function

PEB: Post-exposure bake

TTV: Total thickness variation

**CHAPTER 4:**

CTE: Linear coefficient of thermal expansion

NA: Numerical aperture

MTF: Modulated transfer function

VTF: Vogel-Fulcher-Tamman

**CHAPTER 5:**

CMP: Chemical-mechanical planarization

CNC: Computer numerical control

SEM: Scanning electronic microscope

TIS: Total integrated scatter

SLM: Spatial light modulator

# LIST OF SYMBOLS

## CHAPTER 1:

$\phi$ : Phase shift  
 $\lambda$ : Wavelength of the wave  
 $\lambda_o$ : Design wavelength of a lens  
 $\eta$ : Diffraction efficiency  
 $\theta_o$ : First order diffraction angle  
 $v_i$ : Abbe number

## CHAPTER 2:

$L$ : Wavelength of an electron  
 $v_b$ : Acceleration voltage  
 $\delta_{xy}$ : Lateral resolution of positioning system  
 $\gamma$ : Contrast of a photoresist

## CHAPTER 3:

$\alpha$ : Opening angle of axicon  
 $\beta$ : Deviation angle  
 $\delta$ : Thickness of ring  
 $\tau_L$ : Transmittance of the lens  
 $J_o$ : Bessel function of the first kind

## CHAPTER 4:

$\lambda$ : Thermal conductivity  
 $dQ$ : Heat flux  
 $\beta$ : Thermal expansion coefficient  
 $C_p$ : Specific heat capacity  
 $\sigma$ : Internal stress  
 $E$ : Young modulus  
 $\nu$ : Poisson's ratio  
 $\alpha$ : Absorption coefficient  
 $\eta$ : Viscosity of glass



# INTRODUCTION

## 0.1/ OPENING WORDS

Microoptics is an enabling technology that involve the reduction in size of optical systems where components range in size from several millimeters to hundreds of microns. Microoptical components include elements of miniaturized optics destined to focus, collect, distribute or modify optical radiation to obtain a desired response. Miniaturization of imaging systems shows nowadays a strong potential for many applications, particularly interesting, e.g., for novel biomedical devices generation [Zhu et al., 2013]. Reduction in size allows these devices become more affordable because of their reduced cost and easiness of use thanks to their compactness, without denying of their performances. For this purpose, the imaging specifications require a substantial effort onto the development of high quality microoptical components. In particular, for considering optical aberrations that might avoid reaching high resolutions for beam-shaping to increase systems performances or for improving efficiencies.

Depending on wavelength or environment where the component will be used, the selection of materials (e.g. plastic or glass) is important. In the environment of this work, we aim at developing complicated, wafer-level fabricated, imaging systems, so robust components should be preferred, orientating our choice towards glass. This selection also affects the fabrication technique. When small devices are considered, not many solutions exist to generate high quality components able to equip imaging systems. As new applications require smaller systems, the development of high quality microoptical components become mandatory, always considering geometrical and chromatic aberrations for good performance.

In order to search higher diffraction efficiencies or reduce aberrations, more complex profiles (diffractive, conical with  $k \neq 0$ , aspheric, non-axial components, freeforms) and technologies are necessary. Continuous surfaces or multi-order diffractive surfaces lead to more achromatic behavior which is appealing for systems using e.g. different wavelengths for illumination and detection or based on spectral variations like confocal microscopy or optical coherence tomography (OCT).

## 0.2/ OBJECTIVES OF THESIS

The main goal of the thesis is focused on the parallel generation of continuous profile glass-based micro-optical components with controlled phase profiles. They are intended to be integrated onto microsystems devices and actuators. The result to be expected is

miniaturization and integration of optical elements into functional systems and platforms applicable in various branches of the technology.

Two technologies are studied and adapted for the parallel fabrication of considered components. First one is widely known and employed by numerous groups and companies for the last decades. Laser beam gray-scale lithography fabrication [Kaste et al., 2014] has become a powerful technique for making microoptical components with arbitrary surface relief profiles. Accurate control of process parameters along with the generation of continuous-relief microoptical components in a single exposure step and development materials are just some of the advantages of this maskless lithography fabrication method. Response of fabricated components depends directly on fabrication parameters like laser intensity, laser intensity variation step and spacing of adjacent scans. To optimize the optical performance of components, a correct preparation of the photoresist, reduction of dead blaze by adaptation of the dose distribution and optimization of grating periods are essential. Thus, precise control of these parameters is necessary to obtain good quality optical components. Several approaches are considered for transferring the generated components in photoresist into more robust materials through chemical or physical (or both) etching. Recipes are adapted to adjust etching ratios and modify the profile of final components.

This fabrication process, nevertheless, has some limitations. Glass components have different etching rates and redeposition of non-volatile by-products leads to low selectivity [Thiénot et al., 2006] making the process very long with the subsequent augmentation of substrate surface roughness. In aims of searching higher surface quality keeping the parallel fabrication of components at wafer-level, one second approach is considered. The technique is of recent study for the last 15 years under the name of Glass Flow Process (GFP) [Merz et al., 2003]. The annealing of glass at high temperature leads to changes in viscosity and provokes its deformation. If glass is bonded to a silicon substrate with etched cavities at a defined pressure, deformations can be controlled to generate the refractive surface of the component. As no process is performed directly to the component surface, continuous profiles with low roughness values can be achieved. This experimental approach can be considered for the fabrication of more versatile profiles directly on glass substrate. As it is based in standard Micro-Opto-Electro-Mechanical Systems (MOEMS) fabrication process, no special equipment is needed.

As an example to test the potential of considered techniques for the parallel generation of non-spherical components, the fabrication of glass-based microaxicons has been considered. First time proposed by McLeod in 1954 [McLeod, 1954], refractive axicons are continuous profile components that produce Bessel beams from an incident collimated beam, which exhibits a long and narrow focal line along the optical axis. Such non-diffracting unique property makes them useful in applications like alignment and metrology or coherence tomography. Axicons are usually fabricated by diamond turning or grinding and polishing. Parallel generation of this component is not easily achieved and, in most cases, the scanning approach of the fabrication technique leads to low mass-production efficiency. By considering maximum phase variations and resolutions achievable in this component, the fabrication of this type of lens will set the potential of the considered technique for the fabrication of more complex profiles.

## 0.3/ THESIS STRUCTURE

This thesis work is organized into 5 chapters followed by a chapter for conclusions and future work related to the subjects covered. This chapter is a general introduction and describes the motivation and main objectives of this thesis.

**Chapter 1** concerns the state of the art of this thesis work. It includes a technological review in the fabrication of variable profile microoptical components and the material context where the work developed in this thesis is focused. Selection of material for considered components along with the technologies employed in the fabrication process are justified in this chapter.

Main objective is focused in the parallel fabrication of glass-based microoptical components with a continuous controlled profile. As two technologies are involved in generation of such components, thesis structure has two well differenced parts. **Chapter 2** is devoted to the analysis of fabrication techniques for optical components based on continuous profiles. Several techniques exist for the direct generation of components with continuous profiles. Here, most important ones are described and special attention is given to laser beam lithography, one of the technologies employed in this thesis work. In this context, some important parameters are analyzed regarding the fabrication process. Substrate coating, exposure, development of generated pattern and components transfer in substrates through etching are described. Photoresist considerations are also described concerning parameters like optical absorption, sensitivity or contrast in order to justify the type of photoresist employed in subsequent experiments. **Chapter 3** concerns practical realizations regarding laser beam lithography lens fabrication. To probe the efficiency of the exposure system as a flexible method for glass-based lens fabrication at wafer-level, complete characterization of both system and positive photoresist employed is mandatory. Fabrication steps must be adapted for both patterning possibilities of exposure system and optical response of photoresist to achieve good repeatability and optical performance of generated components. Transmission of fabricated lens is also analyzed and conclusions are obtained. This technique is first time employed for the fabrication of continuous profile components in FEMTO-ST Institute. This work will serve as a starting point for future work in the generation of diffractive and refractive microoptical components in photoresist or glass.

Chapters 4 and 5 concern the second technology studied. After limitations of the first fabrication method are considered, second approach is employed for the parallel generation of same optical component. As the technique is first time considered for the fabrication of glass-based refractive microaxicons, a complete characterization of the process is mandatory. First part of **chapter 4** is focused in the fundamentals of glass processing and induced deformations in glass Borofloat33. Most important thermal, optical and mechanical parameters involved in the fabrication process are described and numerical parameters of employed glass are given. In second part, the state of the art of glass blowing processes is analyzed. **Chapter 5** concerns the characterization and realizations by glass blowing process. First part of the chapter is dedicated to the description of the fabrication process. In this thesis work cavities sealed at atmospheric pressure are considered to induce deformations in the upper surface of glass substrate

and generate the continuous refractive profile of the considered component. The characterization process considers, first, rectangular cavities of different sizes etched at variable separation and second, ring-shaped concentric cavities to generate the conical surface of the lens. Final subsection contains the analysis of the optical performance of fabricated components. Transmission is analyzed and conclusions are obtained.

**Chapter 6** concludes the work covered in this thesis and discusses the capabilities of considered fabrication methods for the generation of other complex optical components.



## CONTEXT OF WORK

The function of an optical system is often to generate a desired phase profile on an incident optical field. Passive optical components are used in optical systems to collect, modify or distribute optical radiation. For example, lenses are the most widely employed optical elements. They can be refractive, diffractive or a combination of both (hybrid components). Refractive Optical Elements (ROEs) are designed using the laws of geometrical optics, consisting in macroscopic surfaces that treat light by the refraction and reflection of geometrical rays at optical interfaces. Variations of the optical path length determine the generated phase distribution. Lenses, prisms and mirrors are some examples of refractive or reflective components. On the other hand, diffractive optical elements (DOEs) are planar components consisting of zones, which retard the incident wave by a modulation of the refractive index or the surface profile. Interference of light emitted from different zones forms the desired wavefront. In refractive components light is refracted at continuous surfaces profiles, whereas in DOE it is diffracted by the periodic structure of the components. Optical performance of DOEs is determined by the periodicity and spatial structure of its surface. It is measured in terms of diffraction efficiency, which is the amount of light that goes into a particular diffraction order.

Relation between refractive and diffractive components can be found in the quantization of a refractive profile thanks to the periodic nature of a light wave. In fact, if a light wave is delayed by one wavelength (phase lag of  $\phi = 2\pi$ ), no difference to the original wave can be found (Eq. 1.1).

$$U(x, \phi) = A_0(x)e^{i\phi} = A_0(x)e^{i\phi+2\pi} = U(x, \phi + 2\pi) \quad (1.1)$$

A retardation  $\phi$  occurs when the wave of wavelength  $\lambda$  passes through a dielectric material of thickness  $t$  with refractive index  $n$  like a glass or a photoresist.

$$\phi = \frac{2\pi}{\lambda}(n - 1)t \quad (1.2)$$

In refractive components, light is manipulated by analog phase elements of considerable thickness (compared to wavelength). In the case of complex profiles, the fabrication is almost impossible with mechanical profiling techniques because of small lateral

extension required (few microns in the outer zone of a Fresnel Lens for example) and very difficult by microlithography because of the large phase depth of components, up to millimeters in some cases. Thus, the insensitivity of the light wave to phase jumps of  $N \cdot 2\pi$  allows the thickness reduction of an optical element without changing its effects on a monochromatic wave. This is very convenient from the point of view of components fabrication. In diffractive components conceived by refractive profile quantization (Fig. 1.1), maximum thickness can be reduced to  $t_{max} = \lambda/(n - 1)$ , corresponding to  $\phi = 2\pi$ . This means that diffractive surface thickness is reduced to the order of some micrometers, which is easily achievable by existing lithographic techniques. This reduction of thickness at multiples of  $2\pi$  is called blazing and results in laterally periodic elements. In transmission, each of these periods generates a beam which interfere with beams emitted through the rest of the profile to form the output light distribution.

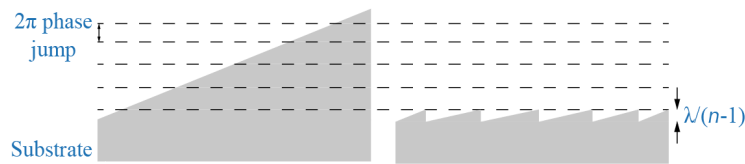


Figure 1.1: Quantization, or blazing, of a prism.

If this quantization is applied to a circularly symmetrical phase profile as the one of a microlens, the result is a series of concentric rings called Fresnel zones (Fig. 1.2 (a)). The phase slope of the microlens becomes increasingly steep towards the edges so that Fresnel zones become smaller. This aspect usually limits the achievable numerical aperture of diffractive lens. If the period of the outermost zones is too small to be fabricated with the available technology, quantization can be made by multiples of  $2\pi$  since, as it can be seen, no changes are induced on the monochromatic wave (Fig. 1.2 (b)). This is beneficial for techniques which allow the fabrication of deep continuous relief profiles. However, fabrication techniques with high lateral resolution are needed as generation of phase jumps with sharp edges is necessary for good performance of blazed elements.

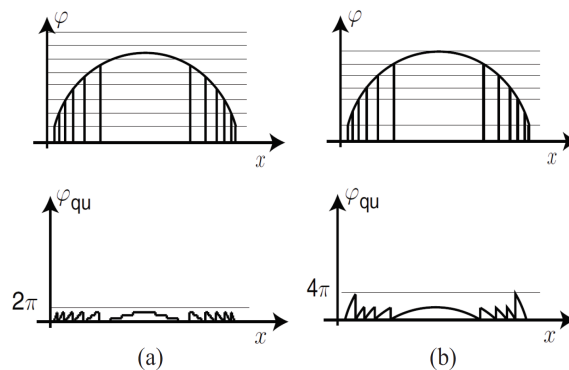


Figure 1.2: Different quantization schemes for diffractive lenses: (a) conventional quantization based on Fresnel zones; (b) superzone concept to increase the aperture of lenses. Source:[Sinzing et al., 2006].

Almost any phase profile, including aspheric or asymmetric, can be fabricated as a diffractive optical element, which provides a great degree of freedom for the design. It can be noticed that a diffraction efficiency of 100% is predicted by the scalar theory for DOEs with continuous surface profile. If, however, quantization of the phase surface leads to stair-shape profiles, efficiency is reduced. The diffraction efficiency of this type of profile depends on the number of phase levels  $M$ . For linear gratings the first-order diffraction efficiency  $\eta$  is given by [Swanson et al., 1989]:

$$\eta = \left( \frac{\sin(\pi/M)}{\pi/M} \right)^2 \quad (1.3)$$

For eight levels, diffraction efficiency reduces already to 95% whereas in binary grating (two phase levels) it drops to only 40.5%. Consequently, although many fabrication techniques using the quantization of the phase surface and based on star-shape profiles have been developed, it remains of high interest to fabricate continuous surface profiles.

## 1.1/ BASIC PROPERTIES OF REFRACTIVE AND DIFFRACTIVE MICROLENSSES

In this section, a comparison between some basic properties of refractive and diffractive microlenses, i.e. focal length, dispersion and aberrations are studied.

A refractive optical component is usually described by the refraction index, which is dependent of the wavelength ( $n(\lambda)$ ) and two curvatures  $c_1$  and  $c_2$  which are inversely proportional to the radius of curvature ( $R_c$ ). A phase function describes a diffractive planar lens which, in the case of a rotationally-symmetric lens with arbitrary profile can be:

$$\phi(r) = 2\pi(a_2r^2 + a_4r^4 + \dots) \quad (1.4)$$

where  $r$  is the radial coordinate. The focal length of a refractive ( $f_r$ ) and diffractive ( $f_d$ ) lenses can be calculated with the next expressions:

$$f_r(\lambda) = \frac{1}{n(\lambda) - 1} \frac{1}{c_1 - c_2} \quad (1.5)$$

$$f_d(\lambda) = f_o \frac{\lambda_o}{\lambda} \quad (1.6)$$

where  $f_o$  and  $\lambda_o$  are the design focal length and wavelength. It can be appreciated that in the case of refractive lenses, variations of focal length as a function of the wavelength are small and depend only on the factor  $(n(\lambda) - 1)$ . For diffractive lenses, these variations are linearly proportional to changes in illumination wavelength  $\lambda$ . Diffractive lenses are, then, highly dispersive so its performance varies strongly with the wavelength. High dispersion in diffractive microlenses is typical and their operation is restricted to monochromatic applications. Dispersion of such lenses can be described with the Abbe number, which for refractive ( $v_r$ ) and diffractive ( $v_d$ ) lenses are:

$$v_r = \frac{n(\lambda_1) - 1}{n(\lambda_2) - n(\lambda_3)} \quad (1.7)$$

$$v_d = \frac{\lambda_1}{\lambda_2 - \lambda_3} \quad (1.8)$$

Dispersion can be calculated for any wavelength range but in these expressions are normally standard being  $\lambda_1 = 587.6nm$ ,  $\lambda_2 = 486.1nm$  and  $\lambda_3 = 656.3nm$ . In contrast to the refractive lens, Abbe numbers in diffractive microlenses are always negative. This fact makes these last useful in hybrid (refractive/diffractive) components to compensate for the chromatic aberration of the refractive element and obtain optical systems relatively thin and lightweight made of only one material. From equations 1.7 and 1.8 it can be appreciated that in contrast to refractive components, Abbe numbers for diffractive lenses are independent of employed material. A strong dispersion corresponds to a low Abbe number, which can be employed to reduce chromatic aberration of refractive components.

### 1.1.1/ ABERRATIONS

Aberrations can be defined as deviations of the image point from an object that do not converge in the ideal position predicted by paraxial optics. Factors like shape of the component, refractive index of material, or wavelength range of source can provoke its presence. In this subsection, a definition of different types of aberrations and possible solutions to correct or reduce them are analyzed.

Before talking about aberrations we have to define the diffraction limit of an optical system, as it constitutes a limiting factor for microlenses performance. In the ideal case, an optical elements would create a point infinitely small from an object. However, diffraction occurs and light is diffracted at the apertures of optical elements. The ideal point becomes then a blur of finite extension and the lens performance is affected. Light distribution in the image plane is determined by the Fourier transformation of the pupil function of the lens, i.e. the image of a point source generated by the lens or point spread function (PSF):

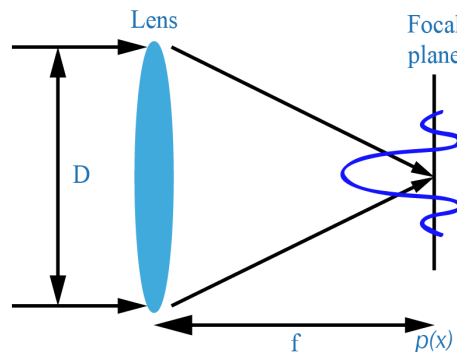


Figure 1.3: Focusing of a collimated beam.

In the case of lenses with circular apertures, the PSF is calculated as the Fourier transform of the function  $\text{circ}(r/D)$ , being  $D$  the lens aperture and  $r$  the radial coordinate. This transformation generates the so-called Airy disc pattern (Fig. 1.4) of which radius in refractive and diffractive lenses can be expressed as:

$$r(\lambda) = 1.22 \frac{\lambda f}{D} \quad (1.9)$$

$$r(\lambda) = 1.22 \frac{\lambda_o f_o}{D} \approx \text{cte} \quad (1.10)$$

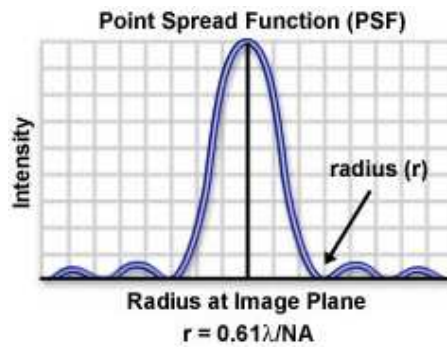


Figure 1.4: Point spread function of ideal lens. Source: [Olympus, 2012]

Figure 1.5 shows the 1D form of the psf of an ideal lens. Lens with no optical aberrations are called diffraction-limited. From the image, we can see that the extension of the PSF increases when the aperture  $D$  decreases. From this, it can be extended that with a reduction of the lens diameter (scaling) the diffraction-limited performance can be easier achieved. When a lens is not diffraction limited, it means that aberrations are responsible for light distribution whose extension is larger than the Airy disc.

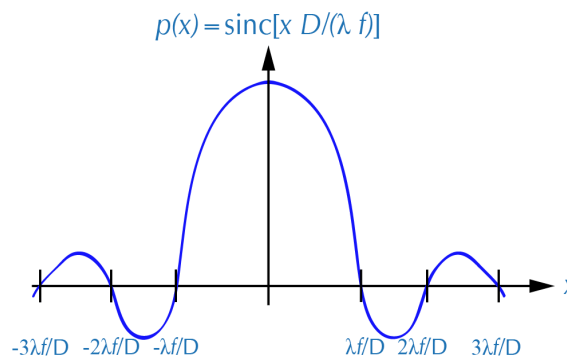


Figure 1.5: 1D point spread function (PSF) of an ideal lens.

Aberrations can be classified attending to different parameters. If spectral bandwidth is considered, aberrations can be separated in two groups. First type (Spherical aberration, Coma, Astigmatism, Field of curvature and Distortion) are related to monochromatic radiation while Axial and Lateral chromatic aberrations are related to polychromatic effects. Last two types of aberrations were already defined in terms of dispersion in

previous section. This classification can also be made between on-axis and off-axis aberrations. In this case only Spherical and Axial chromatic aberrations are of the first type. In next subsections, definition and possible solutions to correct most common aberrations are discussed.

### 1.1.1.1/ SPHERICAL ABERRATIONS

This monochromatic aberration is related to variations in focus distance with the radius of the lens. On the edge of the lens, rays (also called marginal) are bent more strongly than rays closer to the optical axis (also called paraxial rays) and, then, they are focused at different distance from the lens. This effect is represented in figure 1.6. The distance between two different focus points is called longitudinal spherical aberration (double arrowed red line in figure).

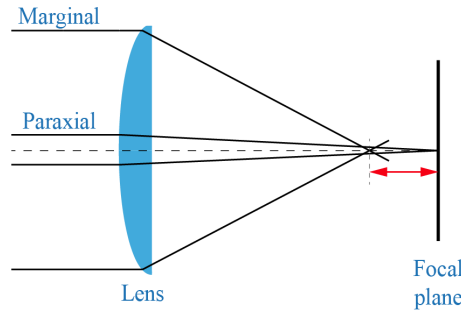


Figure 1.6: Spherical aberration. Variation of focus with aperture.

From equation 1.4, we can see that spherical aberration in diffractive microlenses, for a single wavelength ( $\lambda_0$ ), can be corrected by a correct choice of coefficients  $a_2, a_4$  of the phase function. In refractive lenses, spherical aberration can be minimized by varying the shape of the component. The exact shape depends on the refractive index of the material employed in the fabrication. One solution consist in modifying the shape of the lens to a so-called aspherical profile [Kweon et al., 2007]. This type of shape differs from the classical spherical profile in that where a spherical lens is defined by only the radius of curvature, aspheric surfaces cannot be. In the geometry of an aspherical lens, the localized curvature changes across the surface and is, then, defined by an analytical formula, usually given as a function of sag variation across the surface. The most common form of an aspheric profile is a rotationally symmetric surface with the parameter sag  $z$  defined as [Czajkowski, ]:

$$z = \frac{cr^2}{1 + \sqrt{1 - (1+k)c^2r^2}} + \sum_{i=1}^N a_i r^{2i} \quad (1.11)$$

Where  $c$  is the curvature at the vertex,  $k$  is a conic constant,  $r$  is the radial coordinate and  $a_i$  are the higher-order aspheric terms. Figure 1.7 is a comparison between a spherical and an aspherical surface light distribution. Variations in curvature of the component with the radial coordinate can be appreciated the along with absence of spherical aberration

in the image plane of the lens.

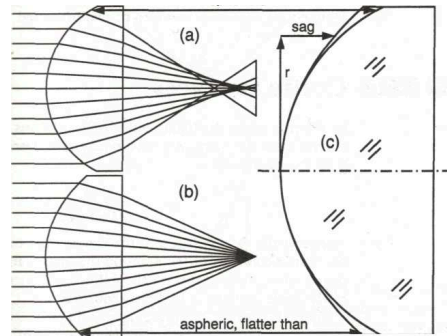


Figure 1.7: Comparison of a spherical (a) and aspherical (b) surface. Source: [Fischer et al., 2000]

### 1.1.1.2/ COMA

This kind of aberrations occurs when oblique rays enter the edge of the lens and the image plane created crosses the image plane at different height than the principal ray (Fig. 1.8). The difference between height of marginal and principal rays in the image plane is a measure of coma (double arrowed red in fig. 1.8). In this case, the image plane blur resembles the shape of a comet.

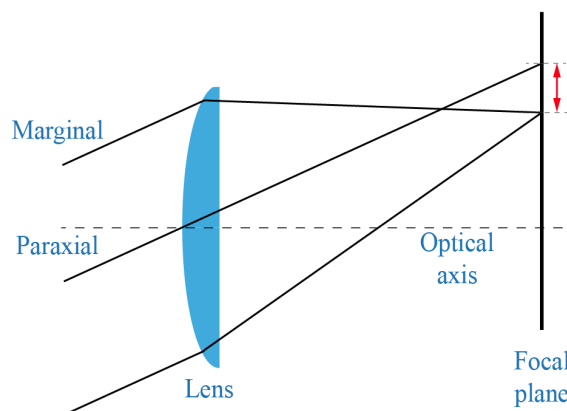


Figure 1.8: Coma. Variation of magnification with aperture.

In the case of equal conjugates and planar substrate, diffractive lenses show no coma aberration. If not, proper bend of substrate can correct them. For refractive lenses, the shape corresponding to minimum spherical aberration can also be employed to correct coma [Herzig, 1997].

1.1.1.3/ ASTIGMATISM

This kind of aberration is observed when rays that propagate in two perpendicular planes have different focus (Fig. 1.9). On the image plane there is a longitudinal separation in the optical axis between the tangential  $T_1$  and sagittal  $S_1$  images so the images of an object point are formed in two different planes. This type of monochromatic aberration occurs when the optical system is not perfectly symmetrical due to design (cylindrical lenses) or fabrication or misalignment errors in the surfaces of the component. This aberration can be eliminated by shifting the aperture stop [Herzig, 1997] or by introducing a lens displaying the opposite effect to reduce the astigmatic difference or the distance between the tangential and sagittal images [Luxorion, 2016].

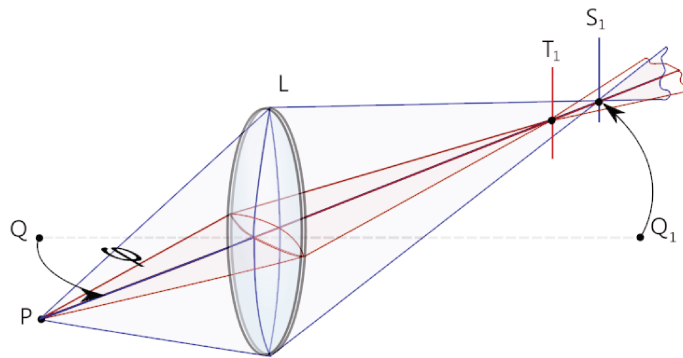


Figure 1.9: Schema illustration of astigmatism.

So far, we have described some of the most important characteristics of refractive and diffractive optical components and the aberrations they have to deal with. Employing one or another type of component depends on parameters like spectrum of light source, optical task or efficiency required. Considering fabrication techniques, an advantage of diffractive optical components is the high degree of freedom in the design and generation of arbitrary wavefronts. Main drawback is the strong wavelength dependence so they are mostly used in monochromatic applications of laser light, such as beam shaping. Diffractive lenses are combined with refractive components for dispersion correction in broadband applications leading to more achromatic components which also make optical systems lighter. Shape of refractive lenses can be optimized to correct aberrations but their fabrication becomes more challenging. Refractive components with precise focal length or aspheric shapes are more difficult to make. In most cases, the selection of one or another type of profile is determined by technological limitations to generate the desired shape.

As it has been analyzed, optical performance of refractive and diffractive components is related to reduction of aberrations, overall in refractive components, or improvement of efficiency in the case of diffractive elements. Considering the existing microoptical components fabrication techniques, spherical surfaces are much easier to manufacture and measure so they are the most standard surface to be found on optical systems. However, high resolutions are not easily achieved because of aberrations like spherical aberration, coma or astigmatism [Fischer et al., 2000]. Strong wavelength dependence of single-order (modulo  $2\pi$ ) diffractive components leads to dispersion effects which



reduce the image contrast for wavelengths different than the design one. In purpose of searching higher diffraction efficiencies and reducing aberrations, more complex shapes become necessary. For instance, positive and negative dispersion profiles can be combined in a single component (hybrid achromat) to correct chromatic aberration [Rossi et al., 1995] or multi-order diffractive lenses that are easier to fabricate thanks to the reduction of number of zones. Blazing the surface for higher diffraction orders enables the design of achromatic singlets [Faklis et al., 1995]. Finally, aspheric profiles can reduce spherical aberrations.

This thesis work is focused in the generation of optical components with determined shape profiles to achieve good optical performance. They are intended to work at broad-band wavelengths so diffractive components are avoided to focus on the generation of refractive lenses with continuous profiles. Spherical aberration should be corrected by the use of a more complex variable profile avoiding spherical surfaces. Illumination is considered to be on-axis so coma or astigmatism aberration presence can be corrected by generating perfectly symmetrical components. Next section concerns the technological context of this work for the fabrication of considered components.

## 1.2/ TECHNOLOGICAL CONTEXT

A variety of techniques is available for the fabrication of microoptical components. Some of them have evolved for decades and are now employed to make commercial microcomponents of good optical quality. Others have been demonstrated to be capable of producing useful components but still require considerable effort before they can be regularly used in parallel fabrication.

History of optics started with glass fabrication. Traditional methods for glass processing are grinding and polishing. The first one is a mechanical process employed to remove material. It provides a surface profile as close as possible to the desired shape. The second one is based on mechanical and chemical processes. Final surface may be obtained with tolerances well below the illumination wavelength. The term microoptics is in close relation with microelectronics. This relationship exist as far as their fabrication techniques are connected. Microoptics uses, as well as microelectronics, planar, lithographic fabrication techniques. The process of structuring planar substrates [Hoerni, 1959] came with, originally, the fabrication of printed circuits boards (PCB) in the 1920s [Voelkel, 2012] and is still nowadays the most important technological approach for microoptics fabrication [Sinzinger et al., 2006]. In the 1950s, fabrication techniques applied for integrated circuit (IC) generation where used in the conception of first multi-level optical elements through mask aligning of  $N$  steps for components with  $2^N$  levels. A skilled operator could align manually the mask over the previous exposed substrate but misalignments were unavoidable, thus, decreasing the optical performance of components. In the 1970s diamond turning appeared as a fabrication tool in an effort to generate arbitrary surface shapes. Dimensions of first components were far from actual microoptical elements sizes as they ranged from millimeters up to meters (overall employed in astronomical telescopes). Miniaturization of optical elements arrived with the appearance of fiber optics for communications, illumination and image transmission systems. In the 1980s, laser pattern generation was possible thanks to the apparition of,

first, electron (1982) [Fujita et al., 1982] and, later, laser beam (1983) [Gale et al., 1983] lithography. Depending on resist sensitivity and sizes of components (micrometers in the case of laser and nanometers in the case of electron beam lithography) one technology is selected.

From 1980s some other techniques have appeared and are still employed nowadays. Selective ion exchange [Oikawa et al., 1981] between a metal and glass substrate leads to variations in refractive index of gradient-index (GRIN) lens. The substrate is immersed in a molten salt bath and metal ions diffuse into the bulk, replacing (depending on the type of glass used) some of the silicon, sodium or potassium. After a certain time, there is a gradation index from the surface into the bulk of the substrate [Herzig, 1997]. Other fabrication technique consists in the ultraviolet exposure through a mask of a photosensitive glass to record a latent image of a lens array [Borrelli et al., 1985]. When heated over the glass softening point, expansion of patterned glass generates the refractive surface of the component (photothermal expansion). High fill factors are difficult to be attached due to interstitial regions. This process can be applied to both glass or plastics [Kufner et al., 1993]. Annealing at high temperature is also involved in the widely used thermal reflow technique [Popovic et al., 1988] to generate, in most cases, spherical microlenses employed as optical imagers [Badar, 2012] or optical coupling elements in communication systems [Shyu et al., 2007]. In this fabrication method, a substrate coated with photoresist is exposed to a pattern with circular apertures. After development of unexposed parts of the resist, the substrate is heated in a furnace over the melting point of the photoresist. Surface tension relaxation during heating creates the lens profile [Daly et al., 1990] and subsequent etching transfers the pattern into the substrate [Nussbaum et al., 1997].

Some of these techniques are driven by isotropic changes in materials which lead to spherical or nearly spherical profiles. These optical profiles are extensively used because of their ease of manufacture and measure. However, as we have seen, aberrations associated to this type of profile make difficult to achieving good optical performance. As more complex profiles have to be proposed to be integrated in optical systems, the use of classical binary photolithography (UV exposition through mask and etching) limits our freedom in the design of optical structures. For lens generation, non-linear transfer from reflowed resist to more robust substrate by changing etching recipes has led to aspherical profiles. However, more versatile techniques exist that are also able to provide a well-controlled shape. At this point, we need to use technology systems that allow us to give a variable profile to our components. Apart from binary mask technology for multilevel pattern generation [Swanson, 1989], one of the most interesting fields is the direct fabrication of continuous surface profiles which offers great flexibility in design and good optical quality of fabricated components [Kley, 1997]. In scanning lithography, local variation of photoresist exposure leads to variable optical surfaces in order to achieve higher efficiencies and reduction of aberrations. Different sub-technologies exist depending on precision, materials and application requirements. E-beam [Pease, 1981] and laser lithography [Haruna et al., 1990] are the most representative ones. Generated components in resist are then transferred to more robust materials through chemical or physical etching. Two main drawbacks for this approach are the low selectivity of some glasses which increases etching time and, then, surface roughness of fabricated components. Other disadvantage is attached to the scanning nature of the process. If parallel

fabrication of components is needed, laser pattern generation time is directly scaled to the number of components to be generated so mass-production efficiency is reduced. As this thesis work is more interested in the parallel fabrication of versatile shape optical components, the second approach (GFP) is studied for the parallel generation of optical components with complex profile directly on glass substrate. Main fabrication steps are the pattern generation through UV lithography and annealing at high temperature. Both steps are performed at wafer-level so parallel fabrication is achieved. Other advantage of this technique is that refractive profile of components is generated directly in the substrate with no fabrication steps performed on its surface so low roughness values are obtained.

### 1.3/ MATERIAL CONTEXT

During the design of a system, optical material selection must be done carefully in order to achieve the desired optical performance under defined conditions.

Considering low-cost materials, low-cost fabrication and replication techniques, plastic optics are the primarily choice. Polymer lenses can be easily replicated by injection or compression molding or fabricated from cast plastic molds. Optical plastics have lighter weight, higher impact resistance and more configuration possibilities than glass materials. Configuration flexibility is one of greatest advantages of plastics. Elaborate profiles like aspherical or freeform can be easily molded to improve optical quality of systems. However there are other disadvantages that must be considered. One principal issue is its relatively low heat tolerance as plastics melt at much lower temperature than glass, which also deteriorates adhesion quality and robustness of possible coatings. These effects reduce greatly freedom in the optical design process. Surface abrasion and chemical resistance are also lower. One important limitation is the high thermal expansion coefficient (10 times higher than glasses) or low transition temperature (5 times lower) as it can be appreciated in the next figure:

	Type	$\alpha$ ( $10^{-5} \text{ }^\circ\text{C}$ )	$T_g$ ( $^\circ\text{C}$ )	Passing Band (nm)
Glass	BF33	0.32	525	470 - 2000
	BK7	0.71	559	350 - 1750
Plastic	PMMA	6.74	105	390 - 1600
	PC	6.60	130	360 - 1600

Figure 1.10: Comparison between expansion coefficient ( $\alpha$ ), transition temperature ( $T_g$ ) and passing band for some common plastic and glass materials.

Vertical integration of lens with other optical or mechanical structures through MOEMS fabrication processes involves steps at high temperature, e.g. anodic bonding ( $200^\circ$  to  $400^\circ$ ), that can determine the use of one or other material. Robustness required for a

certain application due to hardness of working environment can also be a determining factor.

A design with glass and plastic lenses can lead to a high quality optical system. In combination with glass lenses, plastic components can however reduce tremendously price and complexity of the optical system. As optical power is mainly distributed in glass lenses of the system, optical aberrations, especially distortion in wide field-of-view systems can be efficiently removed with one or two weak-powered plastic aspheric correctors. Effect of temperature on focus can also be minimized with plastic elements. Acrylic (poly-methyl methacrylate), polystyrene, polycarbonate and COC (cycloolefin copolymer) are few of the most used plastics materials.

Although their fabrication might be more challenging, glass microlenses offer some clear advantages in comparison with the ones fabricated in plastic, like better aging and suitability for harsh environments. Concerning MOEMS (Micro-Opto-Electro-Mechanical Systems), the most interesting fabrication techniques are the ones allowing the parallel fabrication of microoptical components directly into the substrate with vertical integration possibilities. These techniques help avoiding refraction index matching issues and mechanical stress at the surface between different materials. In this framework, borosilicate glass is an excellent candidate for microlenses fabrication, thanks to the compatibility of his thermal expansion coefficient with the one of silicon. High temperature assembling processes like anodic bonding can be then considered. Thus, techniques that allow the fabrication of glass based microoptical component at wafer-level can be used for vertical integration on silicon.

In the work developed in this thesis, the fabrication of glass-based optical components has been considered. Because of their advantages compared to plastic lenses considering temperature tolerance, resistance in harsh working environments and vertical integration possibilities at high temperature, this appears to be the proper choice. Thermal expansion compatibility of employed materials, glass Borofloat33 and silicon, is very convenient since refractive surface of considered components is generated after heating at temperatures over the annealing point of the glass substrate.

## FABRICATION TECHNIQUES FOR OPTICAL COMPONENTS BASED ON CONTINUOUS PROFILES

In this chapter we focus in the analysis of different technologies for the direct fabrication of microoptical components with a controlled surface profile. Several approaches are studied and advantages and disadvantages of each technique are discussed. The selection of one technology is determined by parameters like application, material or size of components desired. Time efficiency in the fabrication process or mass-production possibilities are other factors to take into account. Considering materials, special attention is paid in the properties and considerations of thick film positive photoresist processing in lithography fabrication of optical components. All technologies described in this chapter involve a direct writing step by which more complex shape structures rather than classical spherical shape can be generated.

### 2.1/ DIAMOND TURNING

Diamond turning is a well established method for the fabrication of microoptical components being the first one historically considered for the fabrication of arbitrary surface profiles [Sinzinger et al., 2006]. The technique is based in a programmable machining lathe that uses a machine and a cutting tool adapted for the generation of optical surfaces. When rotating, the tool is approached to the surface to be cut (Fig. 2.1). Is a direct fabrication method where the requested surface is generated in the workpiece. Machining metals like copper or aluminum produce the best optical surfaces [McClure, 1991] for which surface roughness can be down under 1 nm. Roughness surface of machined materials has been studied [He et al., 2015] in terms of tool feed rate, depth of cut or rotating speed to avoid strong light-scattering in optical components [Teague et al., 1981].

This technique is not usually employed to directly machine glass. Cutting speed can be reduce to modify the characteristics of material removal from brittle to plastic deformation [Nakasuji et al., 1990] but the extremely small material removal is too time consuming. Optical components machined directly in plastic materials like acrylic have been fabricated [Hatakoshi et al., 1990]. Even if this technology has been longly considered

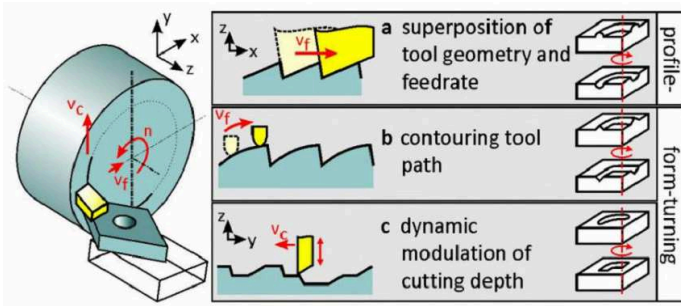


Figure 2.1: Machining of microstructures in a turning process. Source: [Brinksmeier et al., 2012]

restricted to symmetrical components [Herzig, 1997, Sweatt et al., 2008], it has been recently adapted for the generation of no rotational profiles like 3D forms in aluminum alloy material with  $0.5 \mu\text{m}$  variations peak-to-valley (PV) [Fang et al., 2013]. Diamond turning is, however, mostly used in molds generation for lens replication. Phosphor-bronze [Hocheng et al., 2004] or high strength ceramic materials like silicon carbide (SiC) and tungsten carbide (WC) [Yan et al., 2010] are employed as masters to create the mold where complex surface optical components can be replicated. Hybrid components fabricated by sol-gel glass casting in diamond turned molds [Bernacki et al., 1995] or cylindrical aspheric PMMA microlenses [Biesenbach et al., 1994] have been demonstrated.

Once the master has been fabricated, its replication can be performed in several ways, [Gale, 1997b]. The choice depends on replication materials, changes in physical dimensions or feature size [Harvey, 1997]. As their softening temperature is relatively low and optical transmission is good in the visible region, polymers materials are usually employed [Heckele et al., 2003]. Here, the most important replication technologies are exposed.

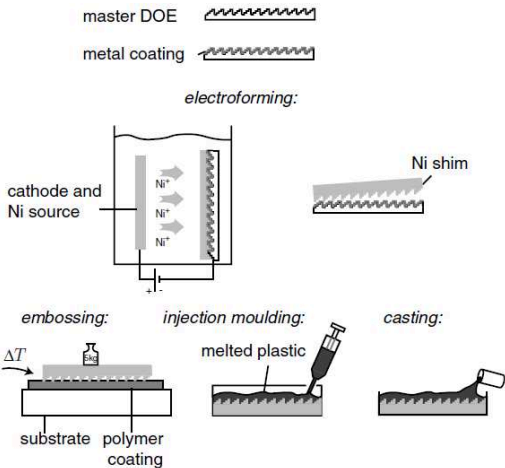


Figure 2.2: Main processing steps for microoptical components replication. Source: [Sinzinger et al., 2006]

- **Embossing**: the master form is pressed onto a polymer, heated over its softening point. To avoid surface roughness, the polymer is placed onto a flat surface [Jahns et al., 1992]. Because of the high temperature, the master enters into the polymer and molds it. Once the process is finish, the replicated polymer is cooled down and separated. Replication of structures from 25 nm to high aspect ratios have been achieved using this technique [Chou et al., 1995].

- **Injection molding**. A melted plastic is introduced into a mold containing the master to be replicated [Rubin, 1972]. After cooled down, plastic hardens and can be removed. In other approach of the technique, plastic is introduce in a solid state (powder), heated and melted while being inside the mold. This technology is of special interest for polymer optics industry [Beich, 2005].

- A similar approach by curing the polymer material with UV radiation is performed during replication process by **casting**. After exposed, the master is released and the deformed polymer is ready. From a single master, several wafer-sized replicas can be fabricated and diced to obtain the final component. Single and double sided replicas can be made. Quality of replicated structures is comparable to the original ones [Rudmann et al., 2004].

As this thesis work is focused in the parallel generation of glass-based microoptical components, diamond turning is not the proper technology for our purpose. One reason is that the technique is not well adapted for direct fabrication on glass substrate. As components are generated one at a time, fabrication at wafer-level is very time consuming and parallel generation is directly not achieved. Even if recent studies show the potential of this technique for the conception of complex surface profiles directly in substrate, we focus in the generation of variable profile components with other techniques. In this context, **lithography** is a more versatile and widespread fabrication approach for the generation of considered components. Next part concerns the description and analysis of this technology in order to introduce the experimental results obtained in next chapters.

Lithography can be defined as the process of generating a pattern from a mask onto a layer of sensitive material called resist. This pattern can be then transferred into more robust substrates trough etching or lift-off or be directly employed for optical purposes. Several sub-techniques exist depending on the type of mask and radiation employed in the exposure. If the pattern is generated through exposition of a physical mask (containing the pattern), we talk about mask lithography. In the case of employing an electronic mask, lithography can be divided into laser beam lithography or electron beam lithography depending on the type of radiation used (photons or electrons respectively). In figure 2.3 this, very, general classification is shown.

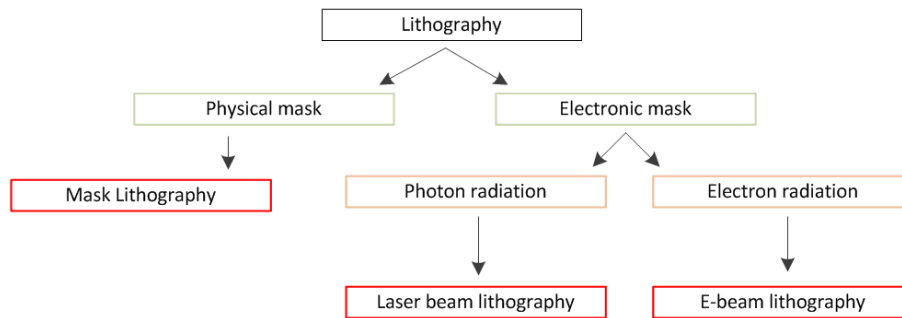


Figure 2.3: General classification of lithography technologies.

Because of the nature of this work, the most interesting technologies to fabricate variable profile refractive components are the ones that allow the direct generation of the pattern into the bulk sensitive resist. Direct writing techniques like Laser beam or e-beam lithography allow the controlled exposure of a photoresist that must be processed such that local thickness of the developed resist film is a continuous, if possible, linear function of exposure energy. During exposure, substrates are scanned and energy dose is adapted to the position of the writing tool according to the optical design. They allow the fabrication of complex elements randomly shaped like variable continuous relief or hybrid microlenses which are difficult, or impossible, to fabricate with other technologies, e.g. by thermal reflow. These techniques also avoid the mandatory submicron alignment needed in multiple exposure steps. In following subsection we focus in these two technologies, the most representative ones in direct pattern generation, paying special attention to laser beam lithography, as this technique is the first approach employed for the fabrication of the considered optical components. Other direct writing technologies are briefly analyzed like Focus Ion Beam (FIB), laser ablation or half-tone mask lithography even if, this last one, is not properly considered a direct writing technology. In optical lithography, resolution of a writing system is related to source wavelength ( $\lambda$ ) and numerical aperture ( $NA$ ) of projection system (Eq. 2.1). Values are different as we will see in next subsections.

$$Resolution = \frac{\lambda}{NA} \quad (2.1)$$

## 2.2/ E-BEAM LITHOGRAPHY

In this field, historically, electron-beam lithography is the first to be considered [Ehbets et al., 1992]. Interaction of electrons with an electron-sensitive resist provokes changes in its solubility proportionally to energy dose and post-development leads to variations in resist profile [Bogdanov, ]. The electron beam is deflected to define the working field. For very small beam deflections, a special type of lenses (electrostatic) are used. Electromagnetic scanning is required for larger beam deflections. Because of the inaccuracy and finite number of steps in the pattern to be generated, working fields range from 100  $\mu\text{m}$  to 1 mm. If larger pattern have to be exposed, x-y stage (controlled by interferometry) moves. Accuracy of stage is critical for stitching (individual working fields placed exactly next to each other) and avoiding overlay between subsequent scans. Exposition of pattern is carried in a vacuum chamber and specialized equipments can reach prices over one million dollars. Scan width in these systems is on the order of 10



nm. In research applications, it is common to adapt an electronic microscope by using relatively low-cost accessories (<100K US Dollars). In these cases the scanning width increases to 20 nm [Wikipedia, 2016].

One of the main advantages of e-beam systems is that resolution is not limited by source wavelength like in optical lithography so smaller features can be fabricated [Kemme, 2009]. Wavelength of an electron ( $L$ ) is given by the *deBroglie* expression (Eq. 2.2), where  $v_b$  is the acceleration voltage. Most of systems operate at 1kV or more so electron wavelength has no influence on limiting resolution.

$$L = \frac{1.2}{\sqrt{v_b}} \text{ nm} \quad (2.2)$$

In e-beam lithographic systems, resolution is limited by other factors. Interactions between electrons and resist can lead to scattering effects, overexposing certain zones of the resist and modifying the desired pattern [Kyser et al., 1974]. Also, photoresist have a resolution limit set by molecule size of its components. Back scattering of electrons in patterning process, known as Proximity Effects (Fig. 2.4), limits the resolution so for certain applications very thin resist layers are required. This effect can, nevertheless, be minimized by controlling electron voltage and writing strategy [Kley, 1997].

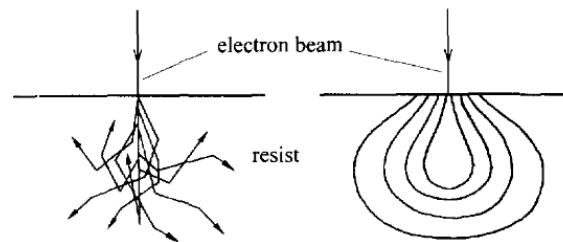


Figure 2.4: Schema of electron penetration into a substrate (left) and energy expansion inside the electron-sensitive resist (right). Source: [Kley, 1997].

In organic resists like polymethyl methacrylate (PMMA) or metal halides resolution can be down to 2 - 5 nm although main drawback is time consuming (typically few hundreds pixels $\cdot s^{-1}$  so even days can be taken to generate a pattern) and that it is too expensive for volume manufacturing [Grigorescu et al., 2009]. This technology plays, nevertheless, a major role in nanopatterning and mask making for other advanced lithographic processes [Tseng et al., 2003, Nock et al., 2008].

Size of components considered in this work will range from few hundreds of micrometers to millimeters in width and few micrometers in height. E-beam lithography is then not well suited for the generation of such elements. At these sizes, scattering effects will be huge and time necessary extremely long. Mass-production cannot be considered with this technology so other approach must be considered. Through the controlled exposure of a photoresist by direct laser beam writing a wide variety of micro-optical components can be generated. Next subsection is dedicated to the analysis of the named technology, one of the approaches employed for the fabrication of complex shape considered optical components.

### 2.3/ LASER BEAM LITHOGRAPHY

In most laser lithography systems, writing spot formed by laser visible or UV radiation which is focused and modulated onto photosensitive resist [Schnabel, 2004], creating different energy (or gray) levels in correlation with beam actual position. The focused laser beam scans line by line the substrate surface which is displaced by a movable x-y table, controlled interferometrically. Using data from an electronic design (CAD, DXF), the laser lithography system will expose the resist with a variable dose energy. Intensity of the laser beam is regulated by an acousto optic modulator (AOM) according with to user's design. Subsequent wet-chemical development removes areas with higher dissolution rates (exposed or unexposed zones depending in the type of photoresist, positive or negative) and 3 dimensional structures will remain in the resist.

Direct laser beam writing system being a form of maskless lithography was first reported and optimized in 1983 by Gale and Knop [Gale et al., 1983] and has several advantages, like accurate control of process parameters, flexibility in fabricating continuous-relief micro-optical elements via single exposure scan and development, and no need for submicron alignment of multiple exposure steps [Gale, 1997a]. Contrary to E-beam lithography, photon radiation is absorbed and no scattering effects are observed in the bulk of the photoresist and minimum spot size is fixed by writing lens and wavelength of exposition. Freedom in the design of optimized structures that are found by computer design techniques is one the major advantage [Gale et al., 1992]. Limitations in the fabrication process are due to positioning errors in scans with is traduced as unwanted structures on the microlens surface, mainly in the direction normal to the scan lines. This results in reduced optical performance of the microlens and stray light outside the focused spot [Gale et al., 1994b]. Straightness of scan lines is then the major limitation. Other disadvantage is that, as other scanning technologies, exposition time is proportional to the size of the pattern to be generated so this method is not well suited for collective fabrication or mass-production.

This technology was originally employed in IC generation and still nowadays is widely employed to generate a pattern onto a chrome-on glass mask for binary mask lithography. The pattern is later transferred into a photoresist layer by exposure through a mask aligner. Considering (as this thesis work does) the direct fabrication of structures in photoresist, several optical components have been demonstrated. Micro-Fresnel lenses (MFLs) of 9.6 mm and 1  $\mu\text{m}$  thickness were fabricated with better resolution than same components generated by E-beam lithography [Haruna et al., 1990]. Microlens arrays, kinoforms and other diffractive structures with periods between 10 - 100  $\mu\text{m}$  and relief amplitude of 5  $\mu\text{m}$  are demonstrated [Gale et al., 1991, Gale et al., 1994a]. Modifications in laser systems with rotational approach has been employed in which the linear displacement allows the generation of large elements up to 250 mm diameter [Bowen et al., 1994]. Recently, continuous optical components have been demonstrated like the fabrication of a continuous f/15 Fresnel microlens array was fabricated on a photoresist coated silicon wafer as a mold for components replication in polydimethylsiloxane (PDMS) 2.4 x 2.4 mm size and 1.2  $\mu\text{m}$  thickness [Aristizabal et al., 2013].

Optical components for communications like a beam coupler from a diode-laser into a multimode fiber based in the assembly of two DOEs generated by laser beam lithography has demonstrated an average efficiency of 74% in [Herzig et al., 2001]. Structures generated in thicker film substrates give more freedom in the design of the components. Photoresist films with thickness of 30  $\mu\text{m}$  have been exposed with a 50 mW He-Cd laser with lateral resolution of writing spot of 3.5  $\mu\text{m}$  to obtain straight sidewall structures [Cheng et al., 2002]. In other investigation, positive photoresist Shipley 1813 was employed in the fabrication of structure with aspect ratios of 130:1 through laser lithography and DRIE in 100 silicon substrates [Aebersold et al., 2010]. Other type of laser beam direct-writing lithography is based in the use of a digital micro-mirror (DMD) electronic masking device, comprising an array of micro-mirrors that can be rapidly ( $\sim 24 \mu\text{s}$ ) re-configured by software. Even if, at the beginning, this technology was more focused in imaging display applications [Sampsel, 1994], it has been demonstrated to act as a grayscale lithographic tool as well [Dudley et al., 2003]. The energy level one generates the gray scale is by controlling the amount of time the photoresist is exposed by the UV light that a micro-mirror reflects. The exposure efficiency and width of the pattern depend on the spot overlapping parameter, getting resolutions from 4 to 18  $\mu\text{m}$  at efficiencies from 20 to 100 % [Ryoo et al., 2011]. In [Lu et al., 2006], Lu et al. created polymer scaffolds to study encapsulated cell behavior and in [Rammohan et al., 2011], Rammohan et al. fabricated 3D structures including cantilevers, microneedles and covered microchannels in a single step using this methodology. This work, however, is more interested in the generation of versatile structures by the direct exposition of the laser beam into the photoresist and subsequent transfer into more robust glass substrate. Generation of complex 3D structures directly in photoresist is of recent study and increasing interest. Potential of gray-scale lithography for the fabrication of components for MEMS applications is studied in [McKenna et al., 2010] by the generation of structures with 128 different levels of energy. The potential of this technology for free-form optical components generation is analyzed in [Dunkel et al., 2012] where the writing system fabricates an array of 25x25 spherical microlenses with 60  $\mu\text{m}$  sag with a shape deviation of less than 1.3  $\mu\text{m}$  (rms). Mechanical applications can also be found in [Kaste et al., 2014]. Here, an 8  $\mu\text{m}$  thickness cone-shaped actuator is generated with different slopes by photoresist exposures from 22 to 65 different energy levels.

The MIMENTO platform (Microfabrication pour la MEcanique, les Nanosciences, la Thermique et l'Optique) in FEMTO-ST Institute is equipped with a laser system Heidelberg model DWL200 from Heidelberg Instruments Microtechnik GmbH. So far, this equipment has been employed for the generation of patterns in chrome-on-glass masks for other lithography fabrication processes. This is the first time this laboratory considers this technique for the direct generation of 3D microstructures in photoresist. Work developed in this thesis will serve as a start point for future research investigations developed in this field.

Fig. 2.5 represents the writing system set-up. The emission of the HeCd laser at  $\lambda=442$  nm is modulated by two AOM and focused onto the substrate coated with photoresist. The combination of the substrate motion system along with the direct deflection of the beam by an acousto optical deflector (AOD, employed like a shutter and when deflected, beam misses a pinhole and is blocked) give the process reasonable scanning speed (depending on pattern complexity, between 20 minutes and 1 hour).

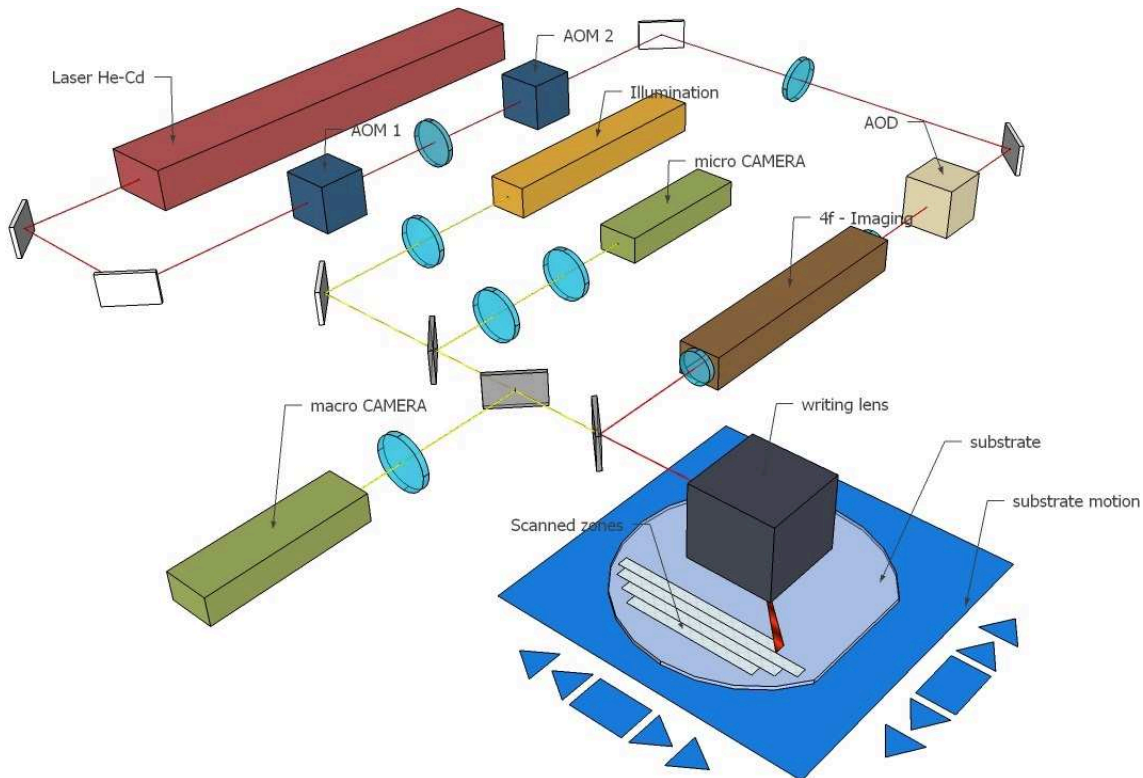


Figure 2.5: Schema of Heidelberg DWL200 Direct Writing Laser System. Red line corresponds to the writing system composed by the HeCd laser, AOM and AOD. Yellow line corresponds to the imaging system composed by two cameras and the illumination system.

Quality of fabricated optical components are affected by equipment mechanical parameters like synchronization between AOD, AOM and stage position (precision value is typically  $\delta_{xy} = 0.5 \mu\text{m}$ ), laser beam stability and precise focus value. Resolution limit minimum feature size the system can fabricate and depends on the laser beam focus plane (typical value:  $0.8 \mu\text{m}$  at  $\lambda = 442 \text{ nm}$ ). To achieve this value, control of focus distance between writing lens and photoresist is important.

After exposure, development of photoresist reveals the generated pattern. Then, it can be transferred into more robust substrates like silicon or glass through chemical or physical (or both) etching. Before continue with the analysis of other fabrication techniques of optical components based on continuous profiles, some important properties considering photoresist lithography processing must be analyzed. Its composition and preparation previous exposure affect all steps involved in the fabrication process. Then, next section is devoted to most important concepts and characteristics involved in photoresist processing for lithography fabrication.

## 2.4/ PHOTORESIST PROCESSING IN OPTICAL LITHOGRAPHY FABRICATION

Photoresist are light-sensitive polymers employed to create a pattern coating on a surface. This pattern is revealed thanks to a change of solubility in the resist during its exposition to radiation. Considering this change, we can talk of positive photoresist when exposed zones become more soluble than unexposed zones. In the opposite case, we say that a resist is negative. After exposition, exposed parts of positive photoresist are diluted in developer and abandon the substrate. In the case of negative photoresist, chemical properties are different so that the zones exposed to ultraviolet light harden through a process known as crosslinking or polymerization. Unexposed zones remain more soluble than exposed ones to developer [Bogdanov, 2000], then, these last remain on the substrate. Figure 2.6 shows both types of photoresist after development of exposed pattern:

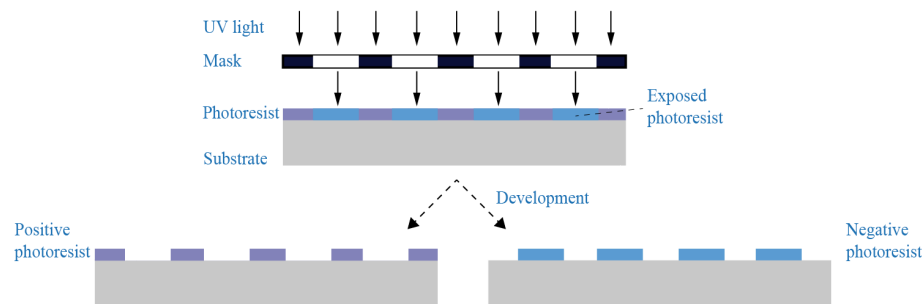


Figure 2.6: Pattern generation in positive and negative photoresist.

Other classification can be made considering the thickness of the film between so-called thin and thick photoresist. Here, the difference is not so obvious. Photoresist film thickness for semiconductor industry applications has been typically less than  $2 \mu\text{m}$  to get good resolution and critical dimensions (CD) for etch and implant operation [Gary E. Flores, 2016]. However, there is an increasing number of applications demanding thicker photoresist layers with high aspect ratios [Brunet et al., 2002] in MEMS areas like electroplating [Lorenz et al., 1998], microfluidics [Guerin et al., 1997] or microgears [Bertsch et al., 1999]. In these applications thickness of photoresist films range from 5 to several tens of  $\mu\text{m}$  and are referred as thick. In this work we employed the terminology thick photoresist, as components fabricated range between 3 and  $15 \mu\text{m}$  thickness and literature always refers in same terms when talking about components thickness around these values.

Fabrication of structures in photoresist is one of the first steps in the photolithography fabrication process. Depending on desired components, photoresist parameters can be completely different and play a key role in final results [Dill et al., 1975]. When binary structures are considered, characteristics like high contrast (defined as the exposure level threshold to provoke changes in the solubility of the resist) is strongly recommended, as we need a sharp relationship between radiation dose applied and depth achieved in photoresist. In this frame, researchers usually work with photoresists that allow this "1" or "0" activation states, clearing completely exposed zones during development

whereas non-exposed photoresist remains with step sidewalls. This is quite the opposite characteristics we wish for the development of a continuous profile. Here, developed depth should have a certain linear relationship with exposure dose [Kley, 1997]. In this case, resist film is thicker than penetration depth of exposure light so that the gradient effect is reached by controlling parameters like time or energy level.

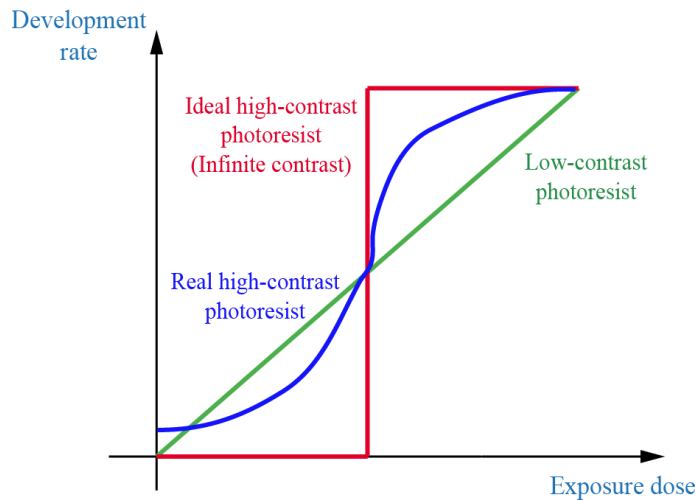


Figure 2.7: Development rate and exposure dose for a ideal (red), real (blue) and low (green) contrast photoresist.

In general, photoresists are a mixture of photosensitive polymers made of three organic chemical components:

**The resin:** is the matrix material. It establishes important resist properties. Major component is a low molecular novolac resin (also known as novolak [Roy et al., 2003]), a cresol resin synthesized from phenol and formaldehyde (Fig. 2.8 (a)). Properties depend on length of the molecular chain which can change thermal stability, dark erosion (lost of shape in component during development of exposed photoresist), development rate and adhesion [MicroChemicals, 2007b]. In the case of a positive photoresist, resin becomes more soluble at near ultraviolet wavelengths [Whelan, 2012] which enables the development of exposed areas.

**Photo Initiator** (also known as Photo Active Compound or PAC): added to the novolac matrix, it modifies solubility of the solution, reducing or promoting it. Before light exposure, PAC inhibits the development rate by more than one order of magnitude (Fig. 2.8 (b)). During the exposure, PAC transforms into a carboxylic acid, and solubility increases by more than three orders of magnitude, being even higher than the one of pure novolac [MicroChemicals, 2007a]. In the case of resist used in this thesis work (positive photoresist AZ-4562 of MicroChemicals [Clariant, 2013]), PAC belongs to the group of diazonaphtho-guinones (DQN).

**Solvent:** allows photoresist to be applied in liquid state. After coating, photoresists usually contain between 20 and 40 % of solvent by weight and it can further be removed

with a softbake. By removing solvent of photoresist, film thickness is reduced, adhesion is improved, resist is less susceptible to particulate contamination and development properties changes [Mack, 2008]. In AZ-4562 photoresist, solvent is PGMEA (Propylene-glycol-mono-methyl-ether-acetate) and in presence of developer, it converts to acetic acid, increasing dark erosion effects. A high presence of solvent remaining after softbake decreases thermal stability and can round resist structures.

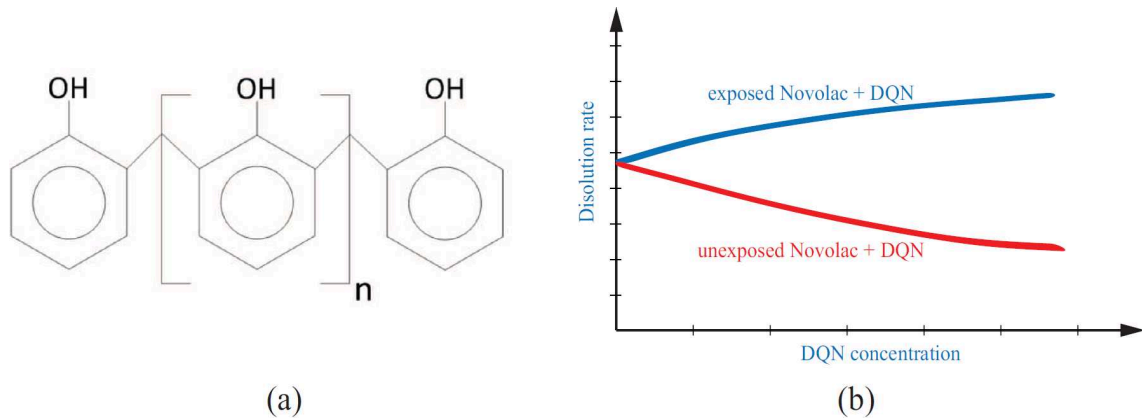


Figure 2.8: (a) Organic Molecule of Novolac. (b) Changes in development rate of Novolac and PAC.

In case of positive photoresist, UV irradiation of laser makes the exposed photoresist more soluble than unexposed zones. This is accomplished by the photo initiator PAC, a photosensitive component present in the resist. When exposed by ultraviolet or near ultraviolet light, the PAC gets excited and undergo a chemical reaction to transform into carboxylic acid accompanied by the release of nitrogen gas and absorption of water (fig. 2.9). This acid causes the exposed photoresist bleaching, becoming more transparent to UV radiation. As acids react with bases, the carboxylic acid is very soluble in a solution of aqueous base. So by using an aqueous base as developer, exposed photoresist is soluble, but unexposed photoresist is not [Mack, 1994]. Carboxylic acid makes alkaline solubility of exposed resist increase more than three orders of magnitude, being more than one order of magnitude higher than solubility of unexposed parts of photoresist [MicroChemicals, 2007a].

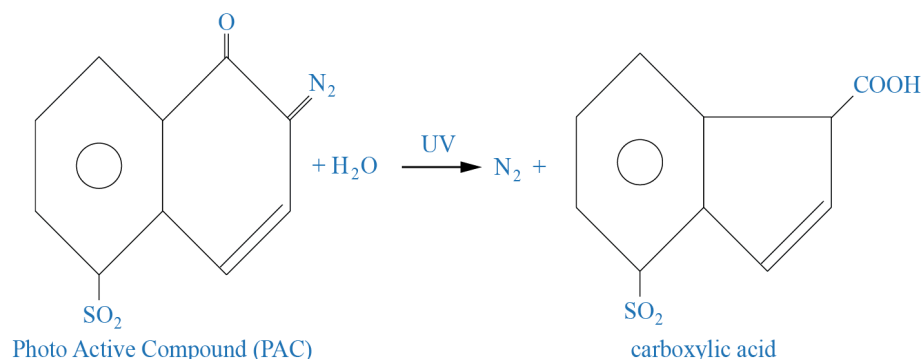


Figure 2.9: PAC reaction when exposed to UV radiation.



## 2.4. PHOTORESIST PROCESSING IN OPTICAL LITHOGRAPHY FABRICATION

Steps to achieve a continuous profile in photosensitive resist can seem quite simple: first, a sensitive photoresist is deposited onto a substrate whose parameters are adjusted to get the desired thickness, usually through spin-coating. Then, during the exposition step, a beam (of electrons or photons) expose locally the photoresist until it achieves the activation threshold and becomes soluble to the following development step. However, some obstacles transform this process into something more complicated. Interaction between irradiation source, resist and substrate, resist materials, design of exposure system, writing strategy or environmental conditions are just some of the parameters that one should take into account when working with photoresist.

In what follows, some of the parameters that should be considered when selecting a photoresist for lithography fabrication will be discussed. For the purpose of this thesis work, these parameters will be focused on the processing of thick resist films to fabricate microoptical components using the grayscale lithography fabrication technique.

### 2.4.1/ OPTICAL ABSORPTION AND CONTRAST. SUITED EXPOSURE WAVELENGTHS

**Optical absorption** bands of unexposed photoresist usually ranges from wavelengths approximately between 320 to 470 nm, so their spectral sensitivity matches the optical emission of Hg lamps in most mask aligners: i-line = 365 nm, h-line = 405 nm and g-line = 435 nm (Fig. 2.10).

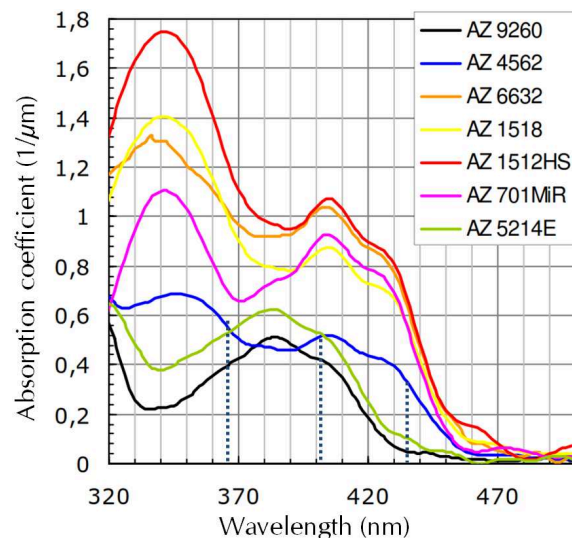


Figure 2.10: Absorption coefficient as a function of the wavelength for some positive photoresists. Source:[MicroChemicals, 2013c].

The intensity of light transmitted through a resist is:

$$I = I_o \exp(-ad) (1 - R)^2 \quad (2.3)$$



where the optical absorption coefficient  $a$  is:

$$a = \left( \frac{4\pi k}{\lambda} \right) \quad (2.4)$$

where  $I$  is the light intensity,  $I_0$  is the light intensity in  $d=0$ ,  $d$  is the depth below the resist surface,  $\lambda$  is the wavelength and  $R$  is the surface reflectance.

Photoresist extinction coefficient  $k$  can be calculated using the Dill parameter:

$$k = \lambda \frac{A(\lambda)PAC + B(\lambda)}{4\pi} \quad (2.5)$$

where  $A$  and  $B$  are photoresist coefficients. The refraction index of solvent-free photoresist can be calculated with a Cauchy approximation with the next expression:

$$n = N_1 + \frac{N_2}{\lambda^2} + \frac{N_3}{\lambda^4} \quad (2.6)$$

where  $N_1$ ,  $N_2$  and  $N_3$  are the Cauchy coefficients. In this thesis work, Cauchy coefficients of the positive photoresist employed (AZ-4562 of MicroChemicals) are provided by the manufacturer ( $N_1 = 1.5761$ ,  $N_2 = -0.00470265 \mu\text{m}^2$  and  $N_3 = 0.003569 \mu\text{m}^4$ ). Refractive index of the photoresist at 632.8 nm is then 1.5866.

From eq. 2.4 and 2.5, we can see that the absorption coefficient depends on the amount of solvent remaining in photoresist. After coating, a certain amount of solvent (between 20 % in thin films and 40 % in thick films) remains in the photoresist depending on resist type, solvent, film thickness and coating technique. A too high amount of solvent during exposure can promote mask contamination, reduce adhesion to substrate, increase dark erosion during development [Kim et al., 2013] or provoke bubbling problems during subsequent thermal processes [MicroChemicals, 2013c]. To improve exposure results, the remaining solvent concentration can be reduced by applying a softbake after coating of resist onto the substrate. Placing the substrate on a hot plate or in an oven (duration depending on the resist and the thickness) provokes diffusion and evaporation of solvent and reduce its concentration to 5 - 10 % [Mack, 1988, Shaw et al., 1977].

We have previously defined **contrast**. This parameter can be represented by the Hurter-Driffied curve [Ekhorutomwen et al., 1996] or also called contrast curve. The curve shows the remaining thickness at minimum ( $D_0$ ) and maximum ( $D_{100}$ ) exposure energies as a function of the exposure dose. Below the dose threshold  $D_0$ , the resist solubility is not changed, being the minimum exposure value required. This threshold value is used to predict the exposed photoresist profile [Paulus et al., 1999, Amarie et al., 2005, Wang et al., 2006, Jiao et al., 2006]. The contrast along with post-exposure development process determines the exposed profile [Lee et al., 2008]. The contrast is measured by the parameter gamma  $\gamma$ :

$$\gamma = \frac{1}{\log_{10} \frac{D_{100}}{D_0}} \quad (2.7)$$

In binary photolithography resists with high contrast are desired, as they show better resolution than low contrast ones. Nevertheless, in gray-scale lithography, low contrast values are preferred (Fig. 2.11) in order to have a more linear response of photoresist with increasing values of exposure. Nonlinearities are an obstacle as intermediate exposure levels are essential [LeCompte et al., 2001]. A resist with infinite contrast (step curve) will show perfect vertical profiles once the threshold value is exceeded [of Technology, 2008].

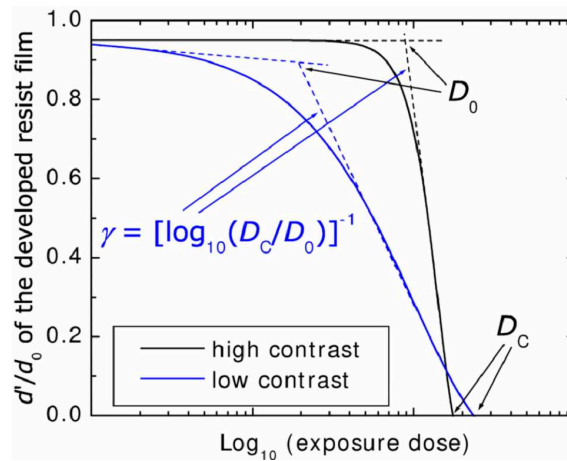


Figure 2.11: Contrast curves for high and low contrast positive photoresists. Source: [MicroChemicals, 2007a].

Contrast of photoresist depends on several factors like molecular weight of resist, secondary reactions initiated by radiation in the resist mass or solvent used during development [Ivanov, 1992]. The lithographic process is affected by the relation between contrast of a photoresist and density changes during baking [Paniez et al., 1992], its correlation with sensitivity [Genkin et al., 1994] and solvent selected for development process [Cowie, 1994]. Methods to optimize the contrast of a photoresist [Waldo III, 1990] or predict the development model for Optical Proximity Correction (OPC) [Wu et al., 2015] have been proposed. In [El-Kareh, ], other resist properties like photospeed, etch resistant, contamination or charging are summarized.

#### 2.4.2/ EXPOSURE DOSE AND DEVELOPMENT RATE

From the point of view of optical resist, the principle of photolithography is a change in resist solubility in certain developer areas exposed to UV light [Mack, 2008]. In diazonaphtho-guinoes photoresists group, like AZ-4562 photoresist, PAC changes, in the wavelength range of 350 - 450 nm, into carboxylic acid, which is very soluble in basic developer.

The exposure wavelength is strongly related to the theoretical resolution limit achievable (eq. 2.1). In addition, an optimized dose is necessary. If it is too low, development time to eliminate exposed zones of photoresist will increase and dark erosion effects will appear. If, on the contrary, dose is too high, scattering of light, diffraction and even reflection

from the substrate can over expose the resist, damaging the structure. Substrate surface quality is also important. If it is too rough or textured, beam can be scattered or reflected and if it is transparent, light can be laterally guided. Both cases provoke unwanted zones of substrate to be exposed.

Before transferring of fabricated profile into the substrate, development of exposed resist is necessary. Here, recipes are different depending on photoresist used during the exposition step. The development process is critical in photoresist processing and depends on its development properties. Development rate can be defined as the change of resist/developer interface position with time. Dissolution rate in basic solution (homogeneous mixture of two or more compounds with a pH over 7) depends on the variations of energy the resist has received during the exposing step. For positive photoresist, zones with a higher degree of exposure will develop faster than zones less exposed. Chemicals changes in negative photoresist are different and exposed zones becomes more resistant to developer. This rate of solubility differential determines the structure final profile.

In positive photoresists, dark erosion effects increase faster than development rate with developer concentration (Fig. 2.12) [MicroChemicals, 2013a]. Developer solutions should be chosen to offer the best selectivity (relation between development rate and dark erosion ratio, i.e. eq. 2.8). In chapter 3, some development tests are presented and the effects of different developer dilutions are taken into consideration to obtain the best surface quality on components.

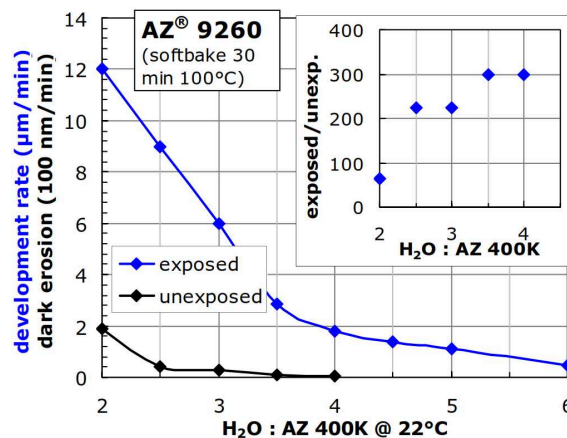


Figure 2.12: Development rate and dark erosion as a function of the developer concentration for the photoresist AZ-9260 of Microchemicals. Source:[MicroChemicals, 2013a].

$$Selectivity = \frac{Development\ rate}{Dark\ erosion\ ratio} \quad (2.8)$$

### 2.4.3/ ETCHING

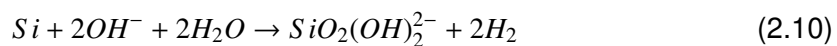
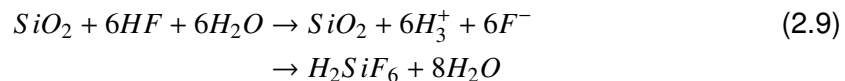
Next step in the lithography process corresponds to the transferring of patterned structure in photoresist into the substrate. The etching process removes resist and substrate atoms at different rate. Areas covered with photoresist are protected until resist layer is

completely removed. Between different etching techniques, first classification usually done is between isotropic or anisotropic processes. For the first, substrate material is removed at the same rate in all directions. In the second case, etch rates are not equal in different directions. Etch rates are function of the etching process and material.

Isotropy of the process is also affected by substrate material. In crystalline substrates like silicon, crystal planes disposition inside the substrate may favor one direction or another. Orientation of crystal planes affects directly to the etch rate. On the other side, glass, as an amorphous isotropic material, does not introduce any anisotropy other than the one introduced by the etching technique. Anisotropy of a process is determined by the ratio between etch rates in different directions. In microoptical components fabrication both processes are important.

The most important parameter is the selectivity of the process. It is defined as the ratio of etch rates between masking material and substrate material and limits the achievable depth etched in substrate. Selectivity should be repeatable from one wafer to another. If, during the process, by-products of the etching reaction are not correctly evacuated they can be re-deposited on the substrate, creating a micromask that decreases the etching rate and selectivity. In other cases, cleaning conditions of equipments can also affect repeatability of results. Considering photoresists, selectivity depends on resist material, properties and previous preparation as well as in nature of the etching process.

Considering the medium in which the etching process is performed, a distinction can be made between wet and dry etching. First one is a purely chemical process performed in a liquid solvent. This is an isotropic process (only affected by material planes disposition). Substrate coated with patterned photoresist is introduced into a liquid containing the active compound. Areas that are not protected by the mask are exposed to the etching liquid and a chemical reaction takes place provoking substrate dissolution [Anner, 1990]. Diffusion processes remove dissolved material. Proper solvent should be selected in function of substrate material. In case of glass etching, hydrofluoric acid (HF) is the typical selection [Sinzinger et al., 2006] (Reaction 2.9), while in silicon etching, potassium hydroxide (KOH) in a KOH/H<sub>2</sub>O dissolution is employed [Seidel et al., 1990] (Reaction 2.10).



This technique is suited for isotropic etching of thin layers or the fabrication of microlenses through spherical etch grooves [Eisner et al., 1996, Albero et al., 2009, Chen et al., 2010]. Nevertheless, when considering deep structures or high aspect ratios this technique is not recommended, since lateral resolution is not small enough.

Dry etching is performed in plasma generated in a vacuum chamber (Fig. 2.13) and directed onto the substrate [Anner, 1990]. Positive ions hit the surface and destroy

substrate material bonds. This is a physical process highly anisotropic in the direction of the accelerated plasma ions, which allows the fabrication of high aspect ratio structures.

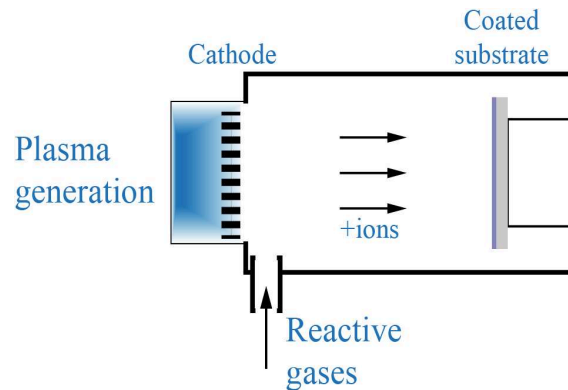


Figure 2.13: Schema of a reactive ion etching chamber.

To improve etching selectivity, a mixture of reactive gases and ions take part in the ion etching process. In this case, etching effects are a combination of physical and chemical reactions. In function of selected gases, etch rates can be different [Stern et al., 1994]. Selectivity and anisotropy of the process are determined by the ratio between reactive and inert gas, which is very interesting for the fabrication of continuous profile structures in glass.

Transferring of resist pattern into glass by dry etching was first proposed in 1971 [Hanak et al., 1973]. Typical dry etch rates from 0,01 to 1  $\mu\text{m}/\text{min}$ . These variations are caused by ions energy and reactive etch gases in the chamber. On the one hand, for diffractive optical components fabrication, slow etch rates are preferred because of their reasonable depths (often  $< \lambda/(n - 1)$ ) and the required accuracy. On the other hand, for the transferring of refractive resist components, a faster etching (to reduce time) is desirable ([Voelkel et al., 2011]).

In the generation of considered components (refractive surfaces with continuous profiles), the desired anisotropy of the etching process (to achieve the final variable surface profile) and size of components considered (between 10 and 20  $\mu\text{m}$  thickness) leads us to the selection between the two most representative dry etching technologies in the generation of microstructures: Reactive and Deep Reactive ion etching (RIE and DRIE).

In RIE, chemical and physical attack are performed to remove simultaneously substrate and photoresist atoms until the microstructure shape is completely transferred to the substrate [Oikawa et al., 1981]. Plasma is generated by applying a strong radio frequency (RF) electromagnetic field at 13.56 MHz in a vacuum chamber where etching gases are introduced. Reactive components created are directed by the electromagnetic field to the coated substrate. High-energy ions from the plasma attack photoresist and substrate and react with them. It is a single step process where amount of gas (or gases) and time are controlled to define the process. DRIE, also known as *Bosch* process [Laermer et al., 1996] is based in the cyclic repetition of etching and passivation steps. The first is a chemical and ionic assisted etching of the substrate with  $\text{SF}_6$  gas, and the

second is a passivation step of the side-walls of the pattern using a polymer gas assisted ( $C_4F_8$ ). After silicon etching during some seconds,  $SF_6$  gas is immediately pumped out of the chamber and  $C_4F_8$  gas is injected. A thin layer of Teflon is deposited over the already etched pattern (side-walls and bottom) during the passivation step. Right after,  $SF_6$  gas is again introduced in the chamber and the cycle starts again [Queste, 2008]. In this case, the process is controlled by the number of etching-passivation steps inside the chamber.

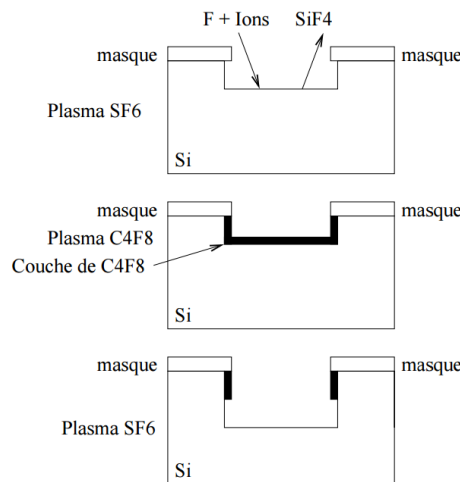


Figure 2.14: Principle of *Bosch* etching pump process. Source: [Queste, 2008].

In this work, we have employed the RIE approach to generate the microlenses in glass substrate. As the components are just few micrometers depth, this approach is more convenient to control the etching rate of photoresist and substrate and depth of etched components.

Etching optical glasses is more challenging because some elements do not react in the etch chamber to form volatile compounds. Because of this, high voltages are also required so the process tends to cause deterioration of the photoresist which leads to low selectivities. Major challenges to control etched components dimensions are low etch rate, low etch selectivity of glass to the resist mask and achieving high aspect ratios. Good results can be obtained using  $SF_6$  or  $C_2F_6$  [Park et al., 2005], although some optical glasses contain atoms that do not react to form volatile compounds. In this case, photoresist mask is deteriorated, resulting in a lower process selectivity [Kempe, 2009]. Oxygen plasma is an effective method for photoresist removal. Once the etching has led to the transfer of the full structure in the substrate, by-products originated in reactions ( $CO$ ,  $CO_2$  and  $H_2O$ ) are easily removed from surface.

We can conclude that required photoresist film layer is a function of selectivity and thickness of the structure to be etched in substrate. Mechanical properties of photoresist like adhesion to substrate, thermal stability or resistance to mechanical deformation have to be considered. Shape of the structure etched in photoresist is also important. If a certain angle exist in the resist structure, selectivity of the process will most probably change it. A correct preparation of the resist coated substrate, previously to the etching step should be done carefully if good results and reproducibility are desired.

#### 2.4.4/ ISSUES RELATED WHEN WORKING WITH THICK PHOTORESIST

Working with thick resists leads to several challenges: high resist thickness require low spin coating speeds during deposition of resist onto the substrate. This is inclined to affect the resist homogeneity and subsequent size of fabricated structures. Edges of substrate are more likely to bead (Fig. 2.15) and a proximity gap can be created during the exposure process (with a reduction of lateral resolution as a consequence [Puthankovilakam et al., 2014]). Thick photoresist films contains high amounts of solvent so do not allow multiple coating (to still achieve higher thickness). In DQN based photoresist (like the one used in this thesis work) exposition converts the PAC into carboxylic acid, which provokes the changes in photoresist solubility, accompanied by the liberation of nitrogen ( $N_2$ ) as reaction by-product. In thick photoresist, high exposures energies required to process the photoresist film increases  $N_2$  formation in its bulk, which may cause bubbling or even crack the resist film.

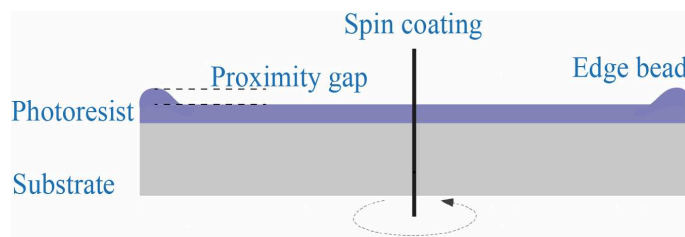


Figure 2.15: Edge bead produced during slow spin coating process.

Softbake step to eliminate part of solvent concentration in photoresist may also be more complicated than for shallow thin resist. If temperature is too low or time too short, remaining solvent may generate  $N_2$  during exposure. If it cannot dissipate properly through all thickness, strong mechanical stress can be induced and resist layer can be seriously damaged. If, on the opposite, temperature is too hot or process is made during long time, decomposition of the photo active compound (PAC) can decrease optical absorption of photoresist (Eq. 2.4) and development rate [MicroChemicals, 2013g].

In this section, we have defined the most important parameters of the lithographic processing of thick film positive photoresists. We also have taken into account some important aspect regarding the fabrication steps. In next section, we give a short review of other direct fabrication technologies that are employed in the direct generation of continuous surface microoptical structure.

#### 2.5/ OTHER DIRECT FABRICATION TECHNIQUES

In this section we review some other techniques employed in the fabrication of optical components with continuous profiles. These are Half-tone Mask Lithography, Focused

Ion Beam (FIB) and Laser Ablation.

### 2.5.1/ HALF-TONE MASK LITHOGRAPHY

Although this technology is not strictly a direct-writing technique, generation of continuous profiles microstructures using half-tone masks is shortly described here. In this approach, a grey-tone mask (GTM) is imaged using a projection mask aligner to expose a photoresist (Fig. 2.16 (a)). The mask is patterned (usually laser or e-beam lithography) with binary structures [Waits et al., 2002]. The basic principle of gray-tone mask to generate the continuous relief microstructure is to modulate the incident radiation intensity by modulating the transmission of the mask. This is achieved by creating a repetition of transparent apertures (pixels) in the mask. Varying density and diameter of pixels encode the gray level. When pixels and spacing between them are smaller than the illumination wavelength (Fig. 2.16 (b)), only the zeroth order is transmitted through the mask into the photoresist so that the fill factor allows modulating the transmitted light.

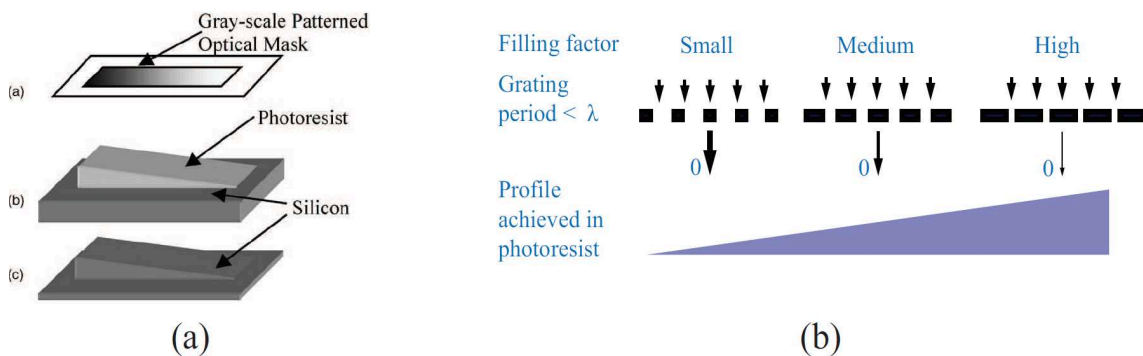


Figure 2.16: (a) The three primary steps in gray-scale technology. Source: [Waits et al., 2005] (b) Filling factor and transmitted energy level in half-tone masks.

One of main advantages is that no laser or electron beam scanning is necessary to expose the photoresist and components are generated simultaneously (parallel fabrication). Only binary structures are written, so easy control of the writing and processing is other advantage. The use of several binary structures to encode each gray level limits resolution [Reimer et al., 1997, Kalus et al., 1998]. Main disadvantages of gray-scale mask patterning are mask cost and dependence of photoresist optical density with the illumination tool. The last requires a complete resist characterization in order to design a proper optical density mask. If pattern is generated by electron beam lithography, time to generate the pattern in the mask can be very long (several days), and total time of fabrication process is then enlarged.

Several examples of fabricated structures using gray-tone masks can be found in the literature. Eight-levels Fresnel lenses generated in polyimide were fabricated with a high efficiency of 75 % [Oppliger et al., 1994]. Diffractive optic blazed gratings and lens arrays in photoresist and quartz with first-order efficiencies as high as 70 % are demonstrated



in [O'shea et al., 1995]. A 5x5 refractive microlenses array was generated in negative photoresist with components of 38  $\mu\text{m}$  diameter and 4  $\mu\text{m}$  height [Yao et al., 2000]. Minimum lateral size of fabricated structure in photoresist is found in [Waits et al., 2005] were a 69  $\mu\text{m}$  length and 5  $\mu\text{m}$  height stair-shaped structure was generated with 45 different levels (1.53  $\mu\text{m}$  steps).

### 2.5.2/ FOCUSED ION BEAM (FIB)

This technology can be employed for directly milling microrelief structures with submicron dimensions in various materials. The system is similar to an e-beam writing equipment except that is equipped with an ion source of, typically gallium ( $\text{Ga}^+$ ). The ion beam has sufficient energy to mill materials like glass, quartz, silicon or gallium arsenide ( $\text{GaAs}$ ). Ion dose, exposure time or number of expositions determine the depth achievable. Control of these parameters can lead to continuous profile microstructures. As components are directly created in the substrate, no further processing of surface is required. The removal rate depends on beam energy and materials. In a substrate of semiconductor indium phosphide ( $\text{InP}$ ) about  $0.06 \mu\text{m}^3 \cdot \text{sec}^{-1}$  were removed with the source operating at 20 keV and 160 pA focused into a spot size of 200 nm [Harriott et al., 1986]. This milling rates would correspond to a processing time of about 20 minutes for a lens fabrication of 10  $\mu\text{m}$  diameter and 1  $\mu\text{m}$  depth. In recent systems, higher energy sources allow milling of materials with sub micrometer or nano scale precision [Orloff et al., 1996].

In a different approach, this technology can also be employed for material deposition by chemical vapor deposition (CVD). Metals platinum (Pt) and tungsten (W) can be deposited on commercially available equipments. The process is based on a precursor gas sprayed on the surface through a nozzle where it reacts with the  $\text{Ga}^+$  ions. Volatile reaction products are removed through the vacuum system and desired reaction products (W or  $\text{SiO}_2$ ) remain fixed on the substrate as a thin film of 1  $\mu\text{m}$  [Reyntjens et al., 2001].

In the literature we can find some structures, overall focused in mechanical applications, fabricated with this technology. In [Daniel et al., 1999] FIB was employed for the fabrication of a microaccelerometer structure starting with bonded silicon-on-insulator (SOI) substrates. The process time was less than 2 minutes and analyze the viability for the manufacture of high value sensors. Other mechanical structures with several shapes at micro and nanometer scale like cantilevers with length ranging from 0.5 to 2  $\mu\text{m}$  by FIB milling and KOH etching of silicon were fabricated in [Brugger et al., 1997]. Recently, polymer waveguides with low sidewall roughness on gold substrate have been fabricated for symmetric planar coupling between silicon waveguide and single-mode fibers [Kruse et al., 2016].

### 2.5.3/ FEMTO-SECOND LASER MICROMACHINING

Laser micromachining with femto-second (fs,  $10^{-15}$  seconds) laser pulses has emerged as an efficient technique for the fabrication of 3D structures in transparent materials

## 2.6. COMPARISON BETWEEN OPTICAL LITHOGRAPHY FABRICATION TECHNIQUES

---

[Juodkazis et al., 2009, Zhang et al., 2010]. Permanent structural modifications can be achieved in the surface of a dielectric material by focusing femtosecond laser pulses onto its surface. In substrate surface, energy is absorbed in a non-linear process inducing very short time ionization and avoiding heat transfer processes [Gattass et al., 2008]. The two-photon absorption produces very localized modifications at submicron scale in the substrate, creating permanent changes in material.

Depending on pulse energy level, different modifications can be achieved. At low pulses energies, changes in refractive index of some glasses allow the fabrication of photonic devices [Ferrer et al., 2007]. Higher energy levels can induce periodic nanoplanes in the material aligned to laser polarization that can give rise to millimeter-sized microchannels for microfluidic applications [Samad et al., 2014]. Even higher pulse energies allow the fabrication of empty voids that can be used for three dimensional photonic bandgap devices and memories [Osellame et al., 2012]. Also with high energy pulses, transparent dielectrics materials can be ablated and optical photonic structures like optical waveguides [Nejadmalayeri et al., 2005] or diffractive gratings [Ams et al., 2009] can be produced.

Some of the advantages of laser micromachining are the compatibility with lithographic process, the few processing steps, high flexible programming of shapes and structures and the low investment necessity comparing to large clean room facilities or expensive process tools [Gower, 2000]. As disadvantages we can include the scanning approach of the technique that leads to time-consuming fabrication and not adapted for parallel fabrication.

## 2.6/ COMPARISON BETWEEN OPTICAL LITHOGRAPHY FABRICATION TECHNIQUES

Several fabrication techniques of 3D microoptical components have been presented namely diamond turning, laser, electron beam lithography and half-tone mask lithography, focused ion beam and femto-second laser micromachining. Special attention has been deposited in the lithographic approaches (laser, electron-beam and half-ton mask), as the most common methods employed for the direct fabrication of continuous surface components with variable profiles. These methods have different technological approaches and achievable structures are different depending on the method employed. Advantages and disadvantages regarding type of component desired, compatibility between writing strategies and materials or requested thickness in designed structures have to be considered.

Regarding **structure size** or achievable profile depth, e-beam lithography presents a different behavior comparing to mask lithography or laser beam isolation of photoresist. As wavelength of electron is much smaller than majority of laser beam exposing sources (350 - 450 nm), the designer can achieve smaller resolutions within the resist. Nevertheless, when exposing layers thicker than some microns, total beam waist gets bigger due to proximity effects. A focused light beam behaves different and no noticeable

scattering effects are appreciated. In this case, beam waist corresponds to the light cone defined by the focusing lens. If small resolutions are desired in a region near the resist surface, e-beam lithography is the best solution. If, on the contrary, components have to achieve a certain thickness of several or tens of microns, maybe the designer should use laser-beam or mask lithography procedures, as at deeper zones, light beam waist is narrower than electron beam. Regarding half-tone mask lithography, the projection mode also affects the desired depth results of the component. When using the contact method (mask and substrate coated in hard contact), depth achievable is comparable to the laser-beam lithography one, but mask is damaged and after several expositions should be re-fabricated (augmenting costs of the process if mass-production is desired). When using projection techniques, mask does not suffer like in other cases, but resolution achievable increases because of the distance between mask and substrate. In this case, minimum feature is larger because of scattering and diffraction of light behind the mask.

When considering **accuracy or fidelity** of patterned structure with the designed one, we should think about lateral and vertical resolution. Here, election of photoresist and correct characterization of selected one is essential. As it will be shown in next chapter, the designer needs to calibrate the exposure energy with the depth response of the photoresist. Photoresist absorption is not linear and, along with selectivity of development process, correct values of exposure have to be characterized if reproducibility is desired. In case of scanning lithography methods (e-beam and laser beam writing) accuracy of stage position is also important as, when coordinated with the exposure tool, minimum errors during exposition lead to overexposed zones that change component profile and optical performance. Nowadays stage motion systems are controlled by interferometry and micrometer accuracies are assured.

**Writing time** of each method is very different. Here, e-beam technique is the slowest one. When large fields need to be exposed (e.g. at wafer scale), whole process can take between from several hours to days depending on the writing strategy [Chopra, 2015]. This is the reason why this fabrication technique is widely used in mask making and not considered for mass production. On the other side, half-tone mask approach is perfect, as exposition of photoresist can take between several second or minutes, depending on the coating material used and all components are generated at the same time.

In next table, a comparison between reviewed direct writing technologies regarding fabrication properties and optical parameters is summarized (in order of appearance on this chapter; n.s. not specified):

Technique	Approach	Material	Lateral resolution	Depth achievable	Parallel fabrication	Fab. time (wafer-level)	Main fabrication Field
Diamond turning	Machining lathe	Metal, plastic	several $\mu\text{m}$	several mm	No	Some minutes	Molds
E-beam lithography	Scanning e-beam	Electron-resist	$< \mu\text{m}$	2-5 $\mu\text{m}$	No	Hours, days	Masks
Laser lithography	Scanning laser beam	Photoresist	1 $\mu\text{m}$	16 $\mu\text{m}$	No	Minutes, hours	Masks and optical components
Half-tone lithography	Imaging onto photoresist	Photoresist	1.5 $\mu\text{m}$	5 $\mu\text{m}$	Yes	Seconds	Optical components
FIB	Scanning ion beam	Glass, plastic	$< \mu\text{m}$	1 $\mu\text{m}$	No	Hours, days	Mechanical components
Laser micromach.	Scanning fs laser	Glass, plastic	$< \mu\text{m}$	mm	No	n.s.	Mechanical, waveguides

Table 2.1: Comparison of reviewed direct-writing techniques.

In function of these parameters, selection of the correct fabrication technology is crucial. This thesis work focuses on laser beam lithography and the use of Heidelberg DWL200

Laser Lithography System employed for 3D structures generation of thick photoresist AZ-4562 with subsequent DRIE transfer in glass. Fabrication of diffractive and refractive microoptical components with variable profiles and thicknesses between 2 and 20  $\mu\text{m}$  suits well with the equipment capabilities. To the author's knowledge, this is the first time this fabrication technique is developed in FEMTO-ST Institute and results obtained will open new fabrication possibilities for this research laboratory.

### 2.7/ CONCLUSIONS OF CHAPTER 2

In this chapter we have presented an analysis of different existing technologies for the fabrication of optical components based on continuous profiles. First technique analyzed is diamond turning, as, historically, is the first to be reported for the fabrication of variable surface components. Fabrication of high quality plastic optical components has been demonstrated with this technology but is not usually employed directly to machine glass. Diamond turning it is mostly employed in mold fabrication for replication and mass-production of other optical components in plastic and certain glasses. In other approach, lithography (and sub-technologies) is a more versatile technology for the direct generation of variable profile optical components. Between the two most representative lithography fabrication approaches (laser and e-beam), laser beam lithography is a more suitable technology for the fabrication of the components considered in this work as their size can get some millimeters in diameter and few micrometers in thickness. Fabrication of such a components by e-beam lithography will be very time consuming and scattering effects in the bulk of the electron-resist at these sizes will modify the final shape of the structure. Origins and state of the art of laser beam lithography has been analyzed and we have seen that this technique is employed in a large variety of fabrication fields like generation of optical refractive and diffractive microoptical components, pattern generation in mask for other optical lithography processes or mechanical applications.

As a fundamental part of the fabrication process, the photoresist employed has also been analyzed. Most important properties have been defined considering the processing of the photoresist in lithography fabrication like optical absorption or contrast necessities for the generation of components with versatile profiles. Fabrication steps like photoresist exposure and development or pattern transferring into robust substrates have been examined as the direct generation of components in thick photoresist films imposes some considerations that must be taken into account.

Other direct fabrication techniques like half-tone mask, focused ion beam and laser micromachining have been briefly reviewed to cover other approaches, materials and applications with the aim of a more complete analysis. A comparison between these direct fabrication techniques is shown in last part of the chapter considering advantages and disadvantages of each approach. Special focus is done in lithographic techniques as these the most ones employed in the direct fabrication of microoptical components. Among these techniques we have seen that laser beam lithography is a well suited technology for the fabrication of components considered in this work. This technology has several advantages like flexibility, accurate control parameter or no need for submicron alignment that allows the direct fabrication of variable profile components in reasonable

time.



# 3

## LASER BEAM LITHOGRAPHY. CHARACTERIZATIONS AND REALIZATIONS

In this chapter, fabrication of microoptical components by gray-scale lithography is addressed. The chapter is divided in four sections.

**The first two** are devoted to the characterization tasks developed during these three years to characterize equipment and photoresist properly. Understanding how the lithography system works and its capabilities is essential to know where the limits of the system are and what kind of structures can or cannot be fabricated. Along with equipment, characterization of photoresist is equally important. In this thesis work, thick photoresist AZ-4562 from MicroChemicals [MicroChemicals, 2016] has been employed for the fabrication of several diffractive and refractive structures, most of them during the characterization steps to know how photoresist behaves under different exposing and development conditions.

In **section three**, a fabrication recipe is summarized. Here, a series of steps for the fabrication of glass refractive components is shown in detail. Limits on thickness achievable by spin coating of photoresist through different approaches, how softbake and hydration after resist coating affect its exposure or photoresist development for different developer concentrations and exposure intensities are considered. As refractive structures are also considered, a reflow of the stepped structure at a temperature higher than the photoresist melting point is necessary to eliminate profile discontinuities. Depending on structure profile and thickness, durations are different and determine the final photoresist profile. Last step concerns structure transmission in glass through reactive ion etching. Two recipes are used and results are discussed.

In **last section**, structures fabricated in photoresist and glass are shown. First, some simple structures stair-shaped were transfer in glass under different conditions to calibrate the process. When whole process is correctly characterized, the fabrication of microoptical components can be realized, for instance of glass-based microaxicons.

## 3.1/ CHARACTERIZATION OF LASER LITHOGRAPHY SYSTEM

In this thesis work, the direct writing system DWL200 of Heidelberg has been employed for the generation of variable profile structures in positive photoresist AZ-4562 of Micro-Chemicals. The system is equipped with a laser source He-Cd operating at wavelength 442 nm. The writing spot (between 2.5 and 0.9  $\mu\text{m}$ ) is modulated at more than 55 kHz, creating the different energy levels, and focused onto a photosensitive resist. This fabrication principle is also known as gray-scale lithography by the association of each energy level to a gray value. The system patterns the coated substrate with the structure designed in the form of an electronic mask. During exposition, the focused beam scans line by line the substrate to be patterned with an energy level correlated with the actual position of the beam.

Clean room facilities at FEMTO-ST Institute (MIMENTO) have this system since 2008. Until this thesis work, the system has been employed for the fabrication of optical masks with a production of, nowadays, more than 300 masks per year. These masks are then employed in the fabrication of, for example, microfluidic tools [Singh et al., 2009], photovoltaic devices [Bodas et al., 2007], molds for optics replication [Albero et al., 2009], arrays of microlenses through different approaches [Albero et al., 2014, Albero et al., 2015, Albero et al., 2016], packaging components [Wang et al., 2015] or micromirrors for scanner devices [Lullin et al., 2015]. In this work we have considered, for the first time, the direct fabrication of refractive optical component with a continuous profile generated with the DWL200 lithography system directly in photoresist and subsequent transfer by dry etching in glass substrate.

This lithography system is widespread and similar models (DWL66, DWL400, DWL2000) are installed in research institutes in France (LAAS Laboratory in Toulouse, IEF Institute in Paris), Netherlands (MESA+ Institute in Enschede), Switzerland (EPFL Institute in Lausanne), Germany (Carl Zeiss Jena GmbH in Jena) or United States (MIT Institute in Massachusetts, Universities of UCLA in Los Angeles, Cornell in Ithaca, Berkeley and Caltech Institute in California or Princeton in New Jersey). These institutions employ the writing system mostly in the generation of binary or half-tone masks so the work developed in this thesis might serve them in their research activities too.

In section 2.3, a complete diagram of the laser lithography system model DWL200 of Heidelberg is shown along with a general description of the equipment. The DWL200 writing system is mostly used at the MIMENTO platform for the exposure of binary patterns on quartz or soda-lime masks for photolithography fabrication processes. The system writes the designed pattern in square masks that are later used to expose other substrates by photolithography. In this thesis work, we have considered the variable exposure capabilities to pattern 3D structures with variable thickness along the component profile. The system can support substrates from 3 to 8 inches. In our case, we work with 4 inches glass wafers, although we could employ larger substrates, coated with a film of photoresist. During expositions, the writing lens does not move being the stage, composed by a heavy granite piece, displaced by the motion system controlled interferometrically. This material is selected because of its weight, stability and low thermal coefficient which provides the required vibration isolation.



Optics of the DWL200 writing system consist in seven major parts, six of them dedicated to the exposure process and one more corresponding to the interferometric system for position control of the substrate holder:

- Laser unit: the solid-state wavelength stabilized HeCd laser operates at  $\lambda = 442$  nm and it can directly write on wafers with g, h-line ( $\lambda_g = 435$  nm and  $\lambda_h = 405$  nm) photoactive resists. Its power supply is placed away from the system, as it generates heat.
- Intensity modulator: the intensity exposure range is regulated by two low frequency acousto optic modulators (AOM), which are used for intensity correction to adjust the energy dose. Maximum intensity the AOM lets pass is regulated by filters from 5 to 100 % (percentage of maximum power).
- Beam shaping modulator: it defines the percentage of total power associated to each level. 63 different energy levels can be generated according to the pattern design so each layer corresponds to one energy level. One energy level (grey value) is assigned to each layer of the structure designed, regulated by the system from 0 to 100 % (table 3.1). In this table we can see that when system reaches the maximum layer/power relation (layer 63 - 100 % power) it starts from zero for subsequent layers (64/0, 65/2, ...).

Layer	Power [%]	Layer	Power [%]	Layer	Power [%]
0	0	22	36	44	70
1	2	23	38	45	72
2	4	24	39	46	73
3	6	25	40	47	75
4	7	26	42	48	77
5	9	27	44	49	78
6	10	28	45	50	80
7	11	29	47	51	81
8	13	30	48	52	83
9	15	31	50	53	84
10	17	32	52	54	86
11	19	33	53	55	88
12	20	34	55	56	90
13	22	35	56	57	91
14	23	36	58	58	92
15	25	37	60	59	94
16	27	38	61	60	95
17	28	39	63	61	97
18	30	40	64	62	98
19	31	41	66	63	100
20	33	42	67	64	0
21	34	43	69	65	2




Figure 3.1: Relation between layers in designed structure and power percentage associated to each one.

- Fast scan deflector: the acousto optic deflector generates a swift laser scan with a rate of 55 kHz. The scan angle is imaged into the back focal plane of the writing lens, so the laser beam is always perpendicular to the exposed photoresist.

- Writing lens system: The system is equipped with 4 and 10 mm focal lengths writing lens. Resolution of the system is fixed by wavelength of radiation and writing lens employed. When working in high resolution mode, minimum feature size achievable is, in theory (waist of focused beam into exposed zone),  $0.8 \mu\text{m}$  although in practice it is difficult to down it more than  $1 \mu\text{m}$  in the bulk of the photoresist. Exposure times are also different in function of the employed writing head, size and pattern complexity. The 4 mm focal lengths writing lens is used when high quality structures and resolution are needed, although is more time consuming. The 10 mm one gives lower resolution and is more suitable to be used with medium size structures. Resolution needed in this thesis work let us use in every case the 10 mm focal length writing head, which saves time during exposures.
- Camera unit: is composed by a micro camera, a macro camera and a white light source illumination and it serves to inspect and measure patterned structures and films. In case of chrome masks or direct write applications cameras are employed for overlay alignment. These two cameras control metrology capabilities of the system allowing measurement of distances between  $1 \mu\text{m}$  and 200 mm with an accuracy ranging between 0.2 and  $1 \mu\text{m}$  [LAAS/CNRS, 2016b].
- Interferometer: the global alignment  $(x, y, \theta)$  system is equipped with an XY motion stage controlled by a Mach-Zender interferometer that allows position error correction and positioning alignment of 20 nm accuracy and  $\pm 10^\circ$  inclination for exposure of non planar substrates [Radtke et al., 2007a, Radtke et al., 2007b].

Some technical characteristics of the writing system are:

Exposing laser	Helium-Cadmium	
Exposing wavelength	442 nm	
Power	125 mW	
Substrates support	20 - 200 mm <sup>2</sup>	
Writing head (focal length)	10 mm	4 mm
Resolution	2.5 $\mu\text{m}$	0.9 $\mu\text{m}$
Writing time (complete 4 inches wafer)	30-45 min.	3 hours
Alignment and metrology accuracy	20 nm	
Optical zoom cameras	x500 - x2000	

Table 3.1: Characteristics of Heidelberg DWL200 direct writing system. Sources: [FEMTO-ST, 2015b, LAAS/CNRS, 2016a]

So it can be concluded that in DWL200 equipment surface relief profile on the component is produced by the modulation of the energy levels deposited in each layer of the designed structure. These levels are regulated by the layer used during the design stage (0 to 63 associated to a grey level), laser power (0 to 100% equivalent to 125 mW) regulated by the acousto-optic modulator. If good quality surfaces are desired in components, strict control of laser dose is essential.

### 3.1.1/ DESIGNING THE PATTERN. FACTORS TO TAKE INTO ACCOUNT

First step in the lithography concerns the design of the structure or optical component. The DWL200 writing system supports most of electronic design formats: GDSII, CIF, GERBER or in the case of this thesis work with structures with several levels for gray lithography, DXF (Drawing eXchange Format, obtained with most of design softwares like AutoCAD or KLayout). In our design we can use a total of 63 different levels that are later associated to each energy dose. According to the energy association in table 3.1, higher energy levels are deposited in layers designed with higher numbers and, then, will be deeper in the photoresist after exposure. Because of the scanning nature of the technology, the designed structure is divided before the exposure into sub-patterns which correspond to the working field of the system (Fig. 3.2). For the 10 mm focal length writing head, working field has a default value of  $400\ \mu\text{m}$  (for the 4 mm focal length writing lens this value is  $160\ \mu\text{m}$ ). This division must be taken into account because it can modify the final shape of the designed structure.

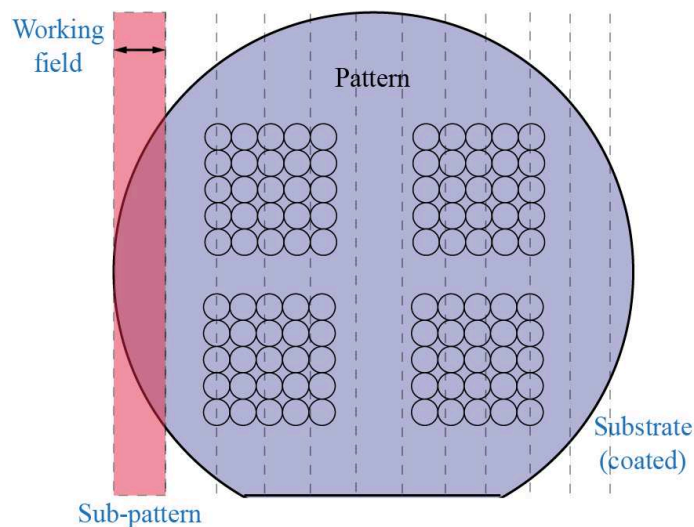


Figure 3.2: Schema of the sub-pattern division carried by the writing system before exposure.

Along with the energy level and writing field, distance between writing lens and photoresist (from now on named as "focus") is also important (Fig. 3.3). The DWL200 writing system allows variations of focus values between +127 and -127 (10 units are approximately  $1\ \mu\text{m}$ ). As substrates are coated with photoresist films of different thickness, this distance must be calibrated carefully to place the plane of the photoresist film in the image plane of the writing lens to obtain the best resolution (minimum writing spot).

These last two parameters must be controlled in order to obtain structures of good quality that do not differ from the designed ones. Next subsections analyze deeper both writing field and focus values.

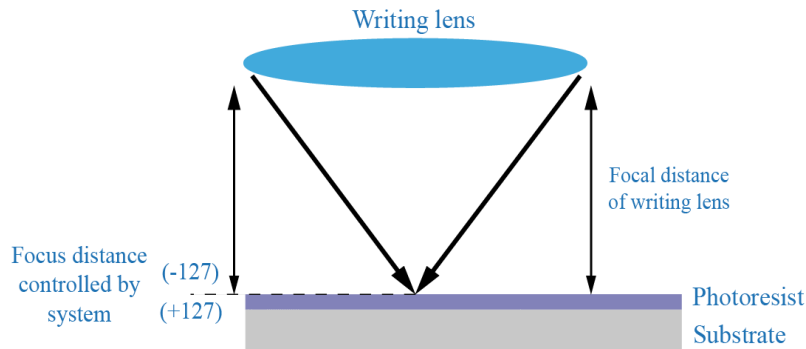


Figure 3.3: Focal distance of writing lens and coated substrate placed at correct distance for best resolution.

#### 3.1.1.1/ SUB-PATTERN DIVISION. WRITING FIELD

The system has a conversion workstation with the software in charge of the conversion process and creation of the writing field of the exposures, the *Conversion Job Manager* in Linux environment. This software converts the file into a format the writing system can use, known as *lic* files (license file). Each *lic* file corresponds to a sub-pattern unit of the complete structure and are adapted to the deflection capacity of the acousto optic deflector swift laser scan. It represents the amount of information the AOD can handle in one scan (one working field) to expose correctly all the layers in a component. Complexity of the structure also affect this division. Simple structures with two or three layers can be easily exposed in one or two writing fields depending on its size. If the same structure is designed with ten, thirty or even sixty-three (maximum) layers, the system will divide it in more smaller writing fields. This is an important factor to take into account because, along with the focus distance of the writing lens, these divisions can affect the optical performance of the component.

The conversion process starts with the structure design (Fig. 3.4(a)). Here and as example, a lens of  $300\ \mu\text{m}$  diameter consisting in 28 concentric layers was considered. Once it is loaded in the system, the conversion software creates an image of the component (Fig. 3.4(b)). After image is created, grey (energy) levels are assigned to each layer following the relationship explained in table 3.1.

When grey levels are assigned, division of the original file into the divided *lic* files is done and conversion is finished (Fig. 3.5(a)). In this case, the component has been divided into two *lic* files. These files will be patterned into the photoresist in two followed scans. If the image is zoomed (Fig. 3.5(b)), power percentage the photoresist will be exposed with in each layer can be seen.

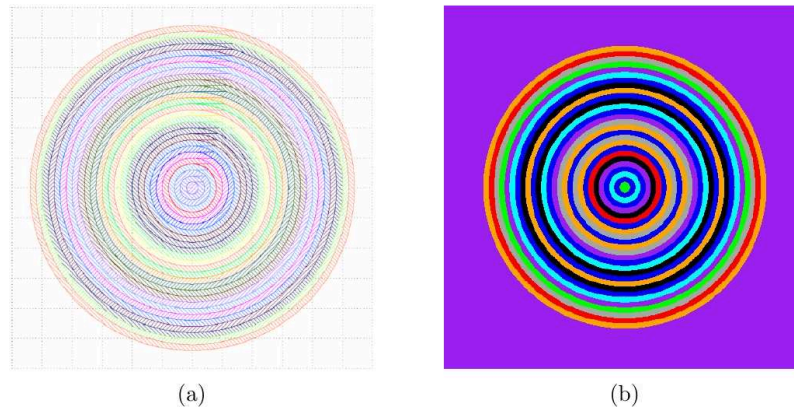


Figure 3.4: (a) Image of component designed. (b) Image created by the *Conversion Job Manager* software.

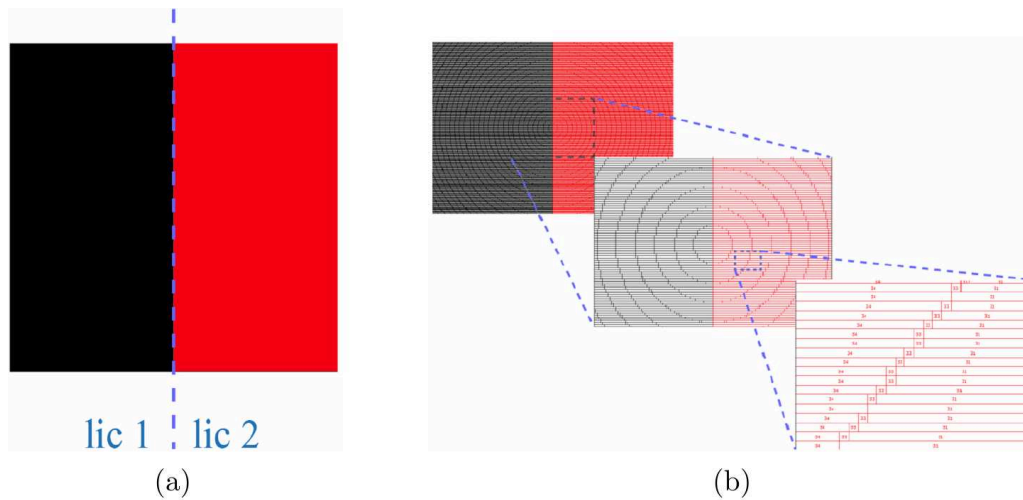


Figure 3.5: (a) Image created by the conversion software with the component divided into two *lic* files. (b) Zoomed images of the *lic* files.

The structure is then patterned into the photoresist. Exposure time depends on size of structure and complexity (number scans as a function of the writing field). Typical times are between 30 and 45 minutes for a 4 inches wafers. Figure 3.6 shows the component after development of photoresist in which the writing fields are overlapped. It can be easily seen the difference between the two patterned *lic* files that divide the optical component with a vertical line. This is traduced into a local variation of component profile than can compromise the component optical performance. In figure 3.7 this effect can also be identified. The structure consists in a 32-levels stairs. The conversion process divides the structure in five scans and alterations in the profile are clearly visible (black dashed line). These vertical lines patterned in the photoresist structure add sharp profiles of, in some cases,  $0.25 \mu\text{m}$  height.

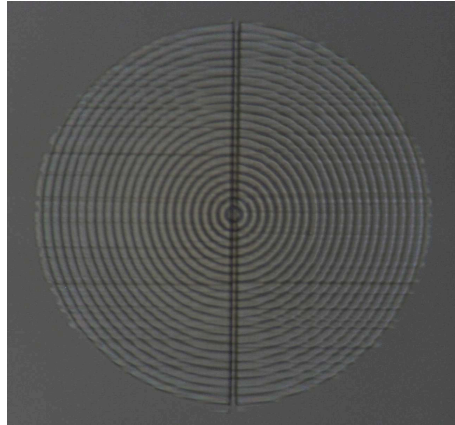


Figure 3.6: Figure of exposed component into photoresist after development with overlapped working fields.

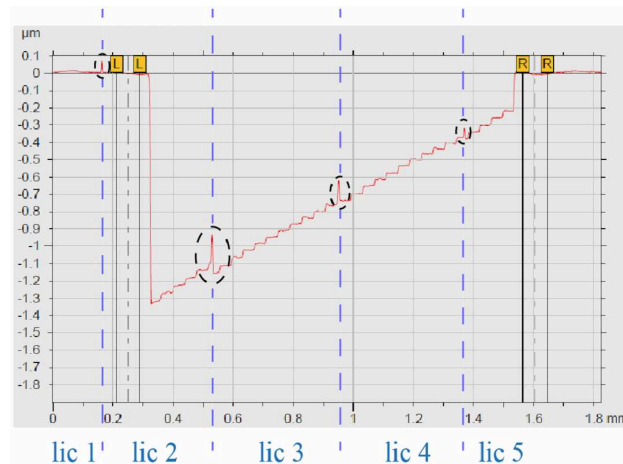


Figure 3.7: Profile of a 32-level stairs structure divided into four *lic* files.

This effect has to be taken into account when designing the structure to be exposed. The system is very flexible and large and complex patterns can be converted. The working field distance can be modified and minimum and maximum values that the AOD can handle depend on the structure to be patterned. The user can decide if convert a pattern to exposed a whole wafer at once or keep it more simple and modify structures and working field distance to avoid the sub-pattern division passes over the structure. The system allows the exposure of single components loaded (and converted) in the system individually and place them along the substrate so reducing the complexity of the conversion process.

In figure 3.8 (a), sub-pattern division is also shown. The pattern to be exposed is a series of squared structures of  $100 \mu\text{m}$  width used to know the achievable depth in photoresist through different power exposure (each square corresponds to a different energy level). Total width of the structure is  $1.7 \text{ mm}$  and  $2.25 \text{ mm}$  length. As the pattern is too big to be done in just one scan, the system divides the structure into five scans (five *lic* files) with a working field distance of  $400 \mu\text{m}$ . In figure 3.8 (a) the designer has not taken this effect into account and the pattern is divided by these vertical lines which represents the sub-pattern division carried by the system. When



exposed and developed, the structure shows the same vertical lines that modify the designed profile (Fig. 3.8 (b)). First solution to this problem can be the modification of the distance between the writing lens and the photoresist to find the focus value that minimize the writing spot (focal plane of the writing lens) in the photoresist plane. Second solution is shown in figure 3.9 (a) where the designer has moved some of the components to avoid division lines pass over the structure. In this way, vertical lines created to separate scans do not pass over the pattern structure. When developed, the structure does not show these lines and the profile is not modified (Fig. 3.9 (b)).

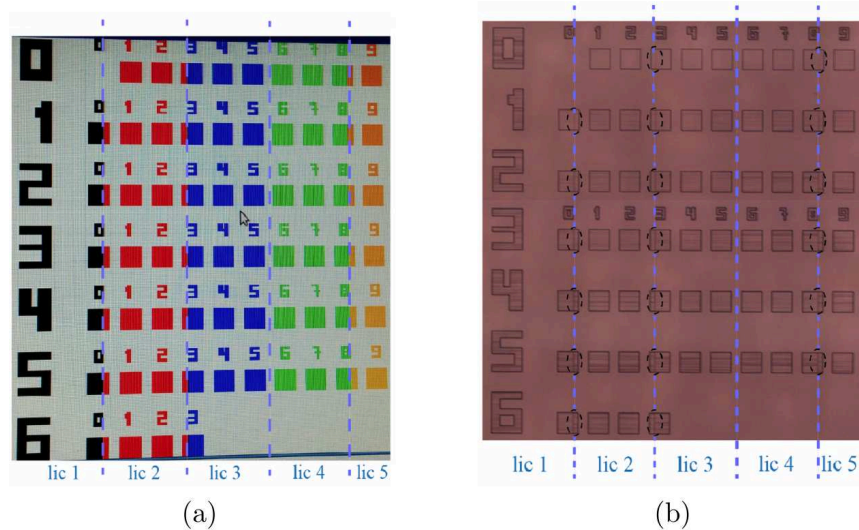


Figure 3.8: (a) Image created by the conversion software with the component divided into five *lic* files. (b) Developed pattern with vertical lines passing over the structure and modifying its profile.

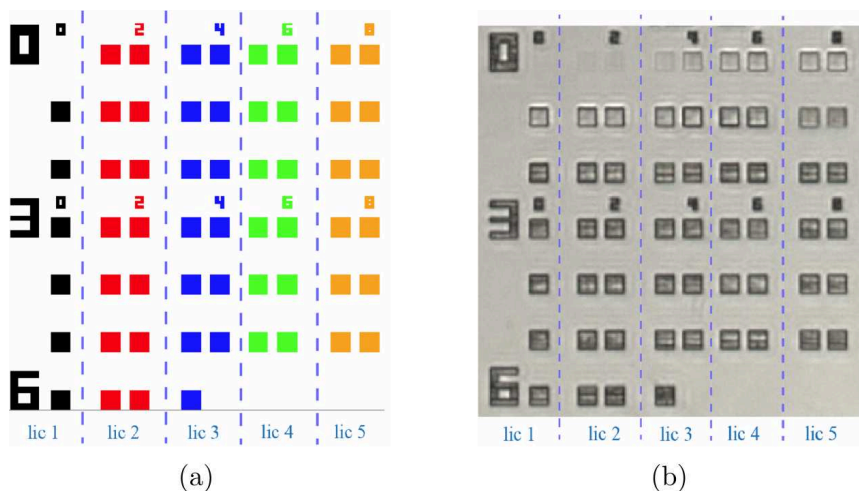


Figure 3.9: Modified pattern to avoid vertical lines created during the conversion process. (a) Image created by the conversion software. (b) Developed pattern.

Sometimes the pattern can not be modified because a whole component might be bigger than the division zones (Fig. 3.10). One solution can be simplifying the structure by

reducing the number of layers in the component. If this is not possible, the user has to minimize the "damage" by adjusting the correct exposure focus value (Sec. 3.1.1.2). With this strategy and subsequent reflow of the structure after development, the effect of the sub-pattern division onto the component can be corrected. This strategy has been followed in the fabrication of single components and results are exposed in section 3.4.1.

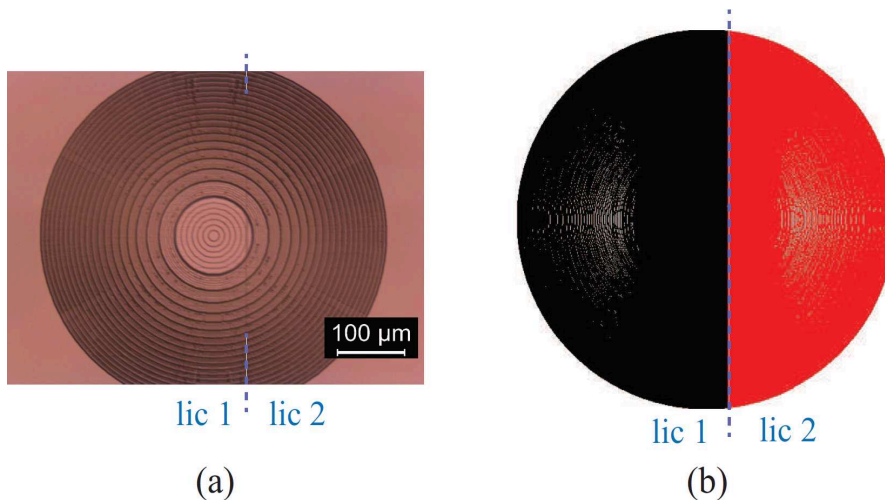


Figure 3.10: Diffraction lens of 500  $\mu\text{m}$  diameter and 7 levels. (a) Image created by the conversion software with the component divided into two *lic* files. (b) Microscopy image of the developed component with the vertical line passing over the structure.

#### 3.1.1.2/ CORRECT FOCUSING OF THE EXPOSURE

The effect of sub-pattern division in a component is also in relation with the distance between writing lens and photoresist. The focus value ( $\pm 127$ ) is introduced as an offset to correct the position of the photoresist plane. An exposure test of same structure with different focus and energy levels should be made to find the correct value. If an incorrect value of focus is used during exposure the profile and, then, component properties change.

In figure 3.11 an exposure test of the same pattern and different focus and energy values is carried out to find the correct focus distance before final exposure of the design. The figure shows a reduced zone of the substrate but effects are equally observed in the whole wafer. The pattern consists in a diffraction lens of 500  $\mu\text{m}$  diameter and four levels in a 6.5  $\mu\text{m}$  thickness photoresist layer. The border between two adjacent scans passes in the middle of the diffraction lens. This test is carried along with different power values so influence of sub-pattern division can be noticed too. Considering energy level, it was observed that difference between scans is more pronounced as energy increases until maximum power (100 %: 125 mW). Between all focus values examined, components with a more accurate profile are observed for exposures with value -40. This means that we should reduce the distance between writing lens and photoresist over 4  $\mu\text{m}$  to have the best possible resolution.



Changes in focal distance of writing lens or thickness of substrate or photoresist film make this distance different so a test like this should always be done before final exposure of designed structure to find the correct offset to achieve the best resolution.

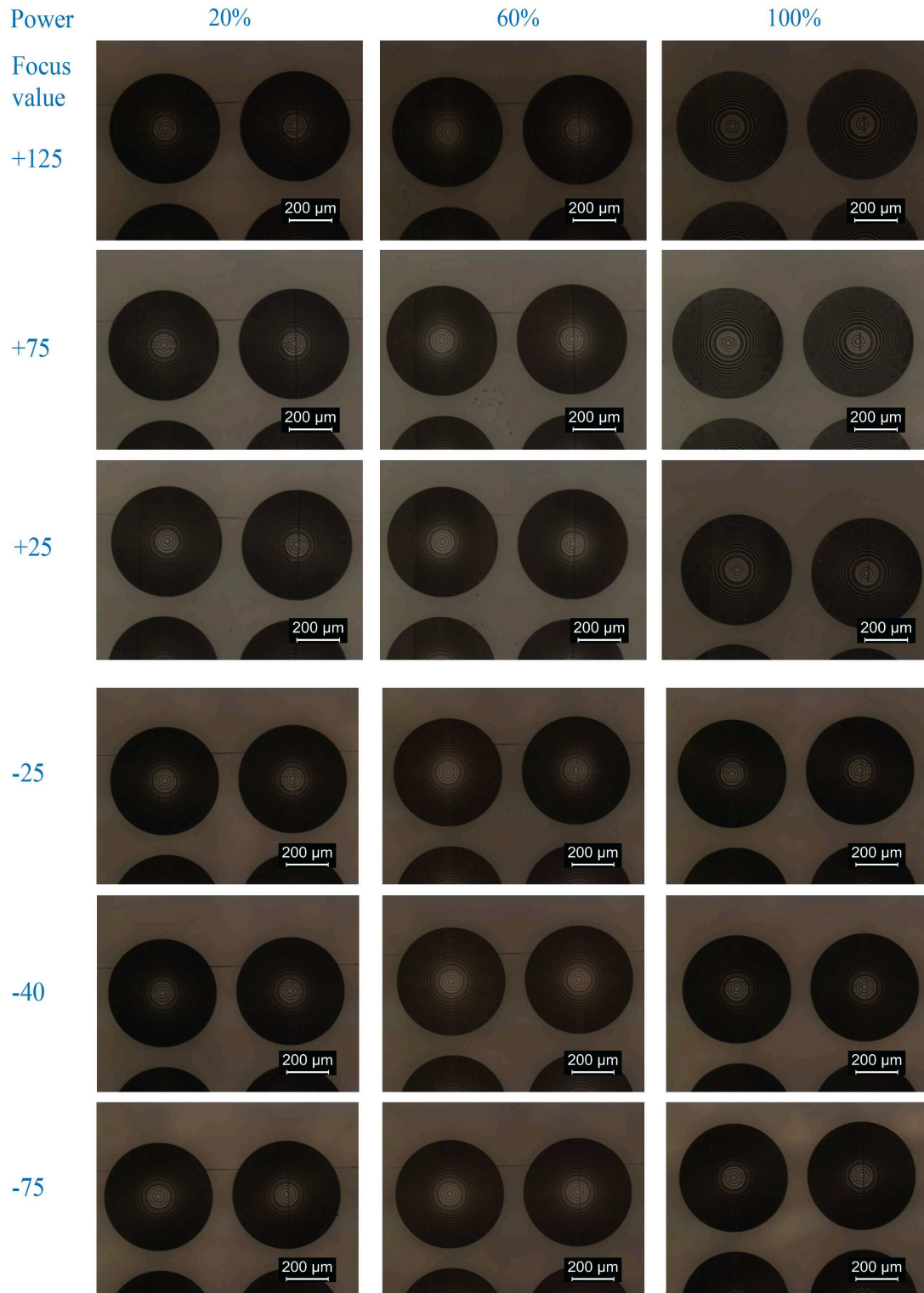


Figure 3.11: Developed component with different values of focus and power exposure.

### 3.2/ CHARACTERIZATION OF PHOTORESIST AZ-4562

Along with the calibration of the writing equipment, characterization of the photoresist employed during the exposures is also essential. In this thesis work we use the positive photoresist AZ-4562 of Microchemicals. In table 3.2, a comparison between most employed photoresist in laser lithography is shown. The photoresist employed in this work is justified because of several factors like compatibility with the partial development of exposed zones, optical absorption at exposure wavelength or thickness required. Since the resist structures are intended to be transferred by etching into glass and selectivity of photoresist vs glass is very low, high thickness values are required which is easier with more viscous photoresists.

Photoresist	Manufacturer	Positive/ Negative	Spectral absorption [ $\mu\text{m}$ ] (at 442 nm)	Viscosity [cSt]	Thickness (Single spin) [ $\mu\text{m}$ ]
AZ-1518	Clariant	+	320 - 470 (0.5)	34.2	1.5-2.5
<b>AZ-4562</b>	<b>MicroChemicals GmbH</b>	<b>+</b>	<b>320 - 470 (0.21)</b>	<b>440</b>	<b>3-50</b>
AZ-9260	MicroChemicals GmbH	+	320 - 470 (0.1)	n.s.	6.5-15
SU-8	MicroChem USA	-	350 - 400 (n.s.)	1250	0.5-200
HD-8820	HD MicroSystems	+	320 - 470 (n.s.)	180	4-10
S-1813	Shipley	+	300 - 500 (n.s.)	low	1.8-3.3

Table 3.2: Comparison of some employed photoresist in laser lithography.

This photoresist is convenient when coating thicknesses above 3  $\mu\text{m}$  are required [GmbH, 2016]. In these cases, the amount of energy necessary to expose the resist increases drastically because of the photoactive compound (PAC) absorption at the exposing spectrum wavelength. With the increasing thickness, exposure dose has to be adjusted to provide enough energy to expose until the bottom of the structure, otherwise the design cannot be completely developed. This is a non-linear relationship because of the intensity of radiation transmitted through the photoresist bulk (Eq. 2.3). Nevertheless, if the energy level is too high side effects can appear, like crosslinking (chemical bonding between polymers) of photoresist molecules [Dill et al., 1975, Tam et al., 2014], making almost impossible its development after exposure [Bogdanov et al., 2000]. If nitrogen generated during exposure does not diffuse fast enough because of the thickness, surface will show lifting effects (adhesion lost between photoresist molecules and substrate).

Here are some properties of positive photoresist AZ-4562 provided by the data sheets of Microchemicals:

Solids content [%]	39.5
Viscosity [cSt at 25 °C]	440
Absorptivity [l/g*cm] at 398nm	1.01
Solvent	methoxy-propyl acetate (PGMEA)
Max. water content [%]	0.50
Spectral sensitivity	310 - 440 nm
Coating characteristic	striation free
Filtration [ $\mu$ m absolute]	0.2

Table 3.3: Physical and chemical properties of positive photoresist AZ-4562. Source: [GmbH, 2016].

Calibration of photoresist in this lithography fabrication process follows five axes.

- First, the **achievable thickness** in photoresist. Here, the spin coating technique has been used to achieve thick photoresist films through several approaches, changing coating speeds, durations and number of spin steps. Thanks to viscosity of the AZ-4562 photoresist, high thicknesses are achievable through a single spin step. Spin coater employed was a model RC8 of SUSS MicroTec [MicroTec, 2016]. Main specifications are shown in table 3.4.

Wafer size	up to 6 inches
Maximum rotation speed	7000 rpm
Minimum step	10 rpm
Maximum acceleration	5000 rpm/s
Time range	0 to 999 s

Table 3.4: Specifications of RC8 Spin Coater of MicroTec used in this thesis work. Source: [poliFAB, 2016].

Thickness has to be in correlation with pattern depth achievable during exposures. A too thick resist layer (with several micrometers thickness under the exposed pattern) is not convenient, as it only makes the etching process longer and increases resist surface damage because of the etching chemicals. Very thick resist layers also means an increment of the distance between the writing lens and the deepest layers to be exposed with the subsequent loss of resolution. Opposite case is neither desired, as it will lead to unexposed levels of the structure, losing part of the designed structured. The necessity of homogeneous films along 4 inches glass wafer is mandatory to have components of same height along the whole substrate and reproducibility of results from one wafer to another.

- Once resist thickness on substrate is well controlled, the **exposure of the photoresist** can be performed. The writing system allows a great number of exposure combinations by association of gray levels to design layers (0 - 63) and exposure powers (0 - 100% of 125 mW). The correct preparation of the photoresist (coating, softbake and hydration time) affects directly to its response during exposure. As time of expositions is defined by the writing lens scan speed, depth of structures patterned in photoresist can be only increased by exposing the photoresist two times in a row. This strategy has been followed

to increase exposed patterns thickness into the photoresist and etched substrates for the fabrication of microoptical components.

- Photoresist response during **development** is also important. Development rates are different in function of developer used and its concentration. Different concentrations and development durations will determine the component final profile. Higher development concentration might reveal the pattern in less time but process become more aggressive and less controllable. Several tests have been done regarding developer concentration, time and exposure power, taking always care of avoiding dark erosion effects affecting unexposed parts of photoresist. These tests are crucial to have a fabrication recipe that assures good exposure results. The selection of the developer depends on the chemical reactions during exposition. In case of positive photoresists like ours, UV radiation transforms PAC molecules into carboxylic acid, which is very reactive with basic developers in an aqueous solution like AZ-400K of MicroChemicals (the one employed in this work, recommended by the manufacturer) or MF-26A of Shipley. Negative photoresist developers are solvents which dilate non-polymerized (unexposed) molecules of the resist, allowing them to leave the polymer chain and dilute in the developer. Common negative developers are PGMEA (1-methoxy-2-propanol acetate) or, in case of negative photoresist SU-8, SU-8 developer of MicroChem.

- When the fabrication of refractive structures is considered, a **short bake of photoresist** after development might be done on a hot plate at a temperature over the melting point of the photoresist (110°C in our case) during some seconds. Time of this step depends on size of levels in the structure. In this thesis work, steps of 0.5 μm height and 16.5 μm width were smoothed after 5 seconds at 120°C. This step transforms the stepped profile of the component into a smooth surface ( $R_q \approx 7.5$  nm), giving then its refractive behavior. In function of dimension and number of layers in the structure, baking times are different. In order to keep at maximum the initial developed profile, time control is mandatory, as a too long bake will lead to big changes in component profile. Several tests have been carried to achieve the best baking time.

- Last step concerns developed structures **transferring into the substrate**. In this thesis work, exposed patterns have been transferred into glass through reactive ion etching. Best etching gases have been selected to achieve good selectivity and correct etching of photoresist and glass. The physical and chemical natures of the etching process make some parameters to be considered. Compatibility between gases and materials determines firstly the process throughput. Also parameters like pressure and radio frequency (RF) power affect process efficiency and must be taken into account in order to achieve good selectivity values.

#### 3.2.1/ SPIN COATING

Here, results regarding spin coating are shown. In particular, approaches to get thick coatings of photoresist. The usual spin process is followed. Deposition of photoresist onto the substrate, previously placed on the spin stage and vacuum fixed. The resist is in liquid state when poured thanks to solvent content. After resist deposition, the spin

chamber is closed and the spin starts according to values of acceleration  $a$  (rpm/s), spin speed  $\omega$  (rpm) and time  $t$  (seconds).

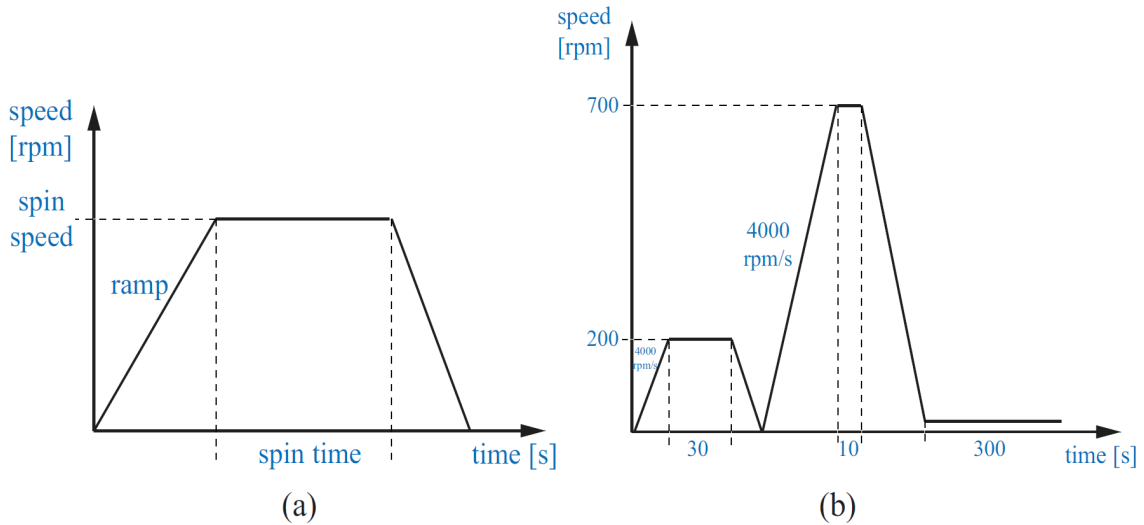


Figure 3.12: (a) Typical coating cycle for spin coating photoresist deposition. (b) Coating cycle for double spin coating of photoresist deposition.

This deposition technique, although widely used, has some limits. Thickness obtained in photoresist films depends mainly on viscosity of the photoresist and speed of the coating cycle. With AZ-4562 photoresist, typical thickness values are between 6 and 15  $\mu\text{m}$  depending on the spin speed. However, special attention must be paid at slow coatings cycle as centrifugal forces toward the edge of the wafer become weaker than frictional forces in the interface between photoresist and substrate which might lead to inhomogeneities in the coated film. Acceleration of the process also is important since during the spinning cycle, the photoresist losses to evaporation most of the solvent in the first few seconds of the coating cycle [Tyona, 2013]. This lost affect directly to the strength of the photoresist and determine its response so subsequent processes like reflow for solvent evaporation previous to exposure.

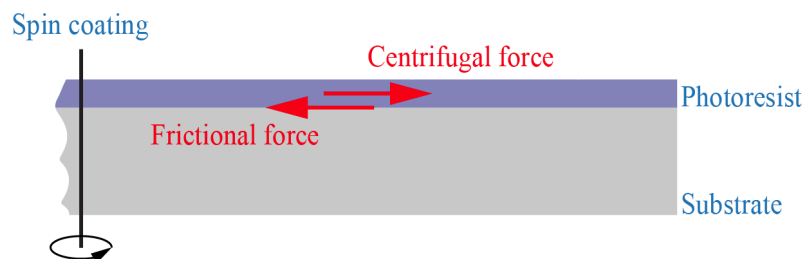


Figure 3.13: Schema of centrifugal and frictional forces during spin coating.

In more details, thickness values obtained through spin coating in this thesis work are shown in figure ???. In the figure, three curves can be differentiated. In the cases represented by the blue and red curves, spins acceleration value is always 3000 rpm/s,

which is a standard value recommended by the engineers in charge of the coating system. The blue one represents the thickness achievable when spinning is done during thirty seconds after resist deposition. Thickness values go from  $5.5 \mu\text{m}$  at 5000 rpm to  $26.25 \mu\text{m}$  at 500 rpm. At slow speeds the complete cover of the substrate becomes complicated as frictional forces are too strong. To achieve higher depths, one solution is reducing the spin time. This is represented by the red curve. Here, coating is made during 7 seconds and thickness values are increased in comparison to the ones obtained during 30 seconds for same speeds. Nevertheless centrifugal forces become less strong as the coating time is shorter, so the limit under which the coatings can be made is lower ( $17,49 \mu\text{m}$  at 1500 rpm). In these two cases, spins acceleration value is always 3000 rpm/s.

In order to increase achievable thickness in photoresist, another approach was developed. The green line represents photoresist thickness when, after deposition, two spins are done in a row (Fig. 3.12 (b)). The idea is that first spin at slow speed extend the photoresist on the wafer and second one, at higher speed, improves the homogeneity of the film. Here, first spin is made at 200 rpm during 30 seconds and just after it has finished, another spin is done at different speed during 10 seconds. In both cases acceleration ramp was of 4000 rpm/s. Acceleration in this case is higher than in previous cases to increase the amount of solvent evaporation. In this way, the photoresist film harden and prevents the surface from suffering thermal shock during the subsequent reflow on the hotplate. After second spin, the substrate was left during 5 minutes in the spin chamber to let solvent evaporate and harden more the photoresist to avoid thermal stress caused by the subsequent reflow.

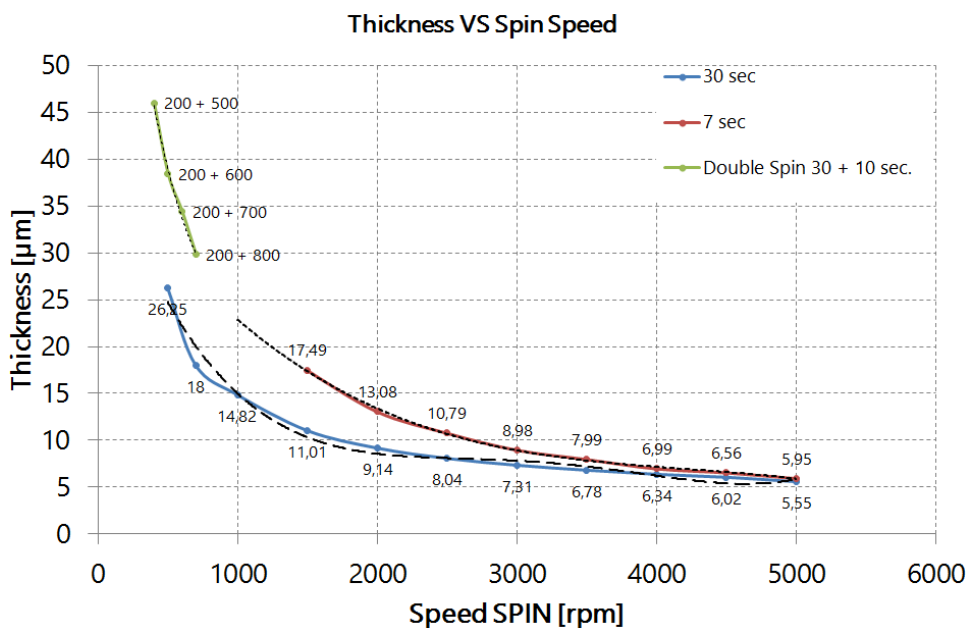


Figure 3.14: Thickness obtained for the photoresist AZ-4562 as a function of the speed spin for two durations. Blue line corresponds to a single spin during 30 seconds, red line corresponds to a single spin during 7 seconds and the green line correspond to thickness obtained through double spins (30 + 10 sec).

Equations 3.1, 3.2 and 3.3 are mathematical expressions (dashed lines in previous figure) obtained through fitting of experimental data for photoresist thickness achievable ( $T$ ) in function of spin speed ( $S$ ) for spin times of 30, 7 seconds and double spin (blue, red and green line in fig. 3.14) respectively. Coefficient of determination ( $R^2$ ) in each case is also shown:

$$T(S) = 4 \cdot 10^{-13} \times S^4 - 5 \cdot 10^{-9} \times S^3 + 2 \cdot 10^{-5} \times S^2 - 0.045 \times S + 42.327 ; \quad R^2 = 0.98 \quad (3.1)$$

$$T(S) = -4 \cdot 10^{-10} \times S^3 + 5 \cdot 10^{-6} \times S^2 - 0.021 \times S + 39.590 ; \quad R^2 = 0.99 \quad (3.2)$$

$$T(S) = 7 \cdot 10^{-5} \times S^2 - 0.133 \times S + 87.485 ; \quad R^2 = 0.99 \quad (3.3)$$

By double spin coating steps, higher thickness is achievable. In case of the highest value ( $46 \mu\text{m}$  at  $200 + 500 \text{ rpm}$ ) homogeneity of photoresist along the substrate was not very good and values differing in  $\pm 4 \mu\text{m}$  were found. In rest of the cases, thickness variations along the coated substrate are shown in tables 3.5 and 3.6. They exhibit maximum variation of thickness along 5 measured points in the substrate (fig. 3.15). In most of cases these variations are smaller than 3 % which means a good homogeneity value for subsequent processes.

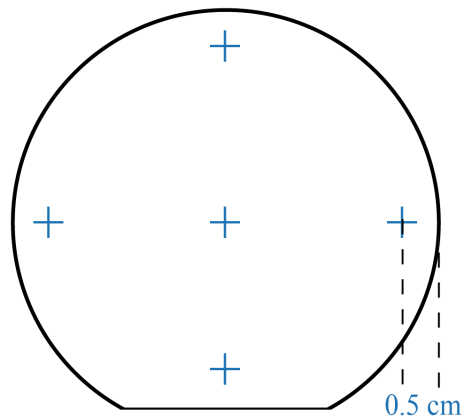


Figure 3.15: Position of measured points to evaluate thickness variations in the coated substrate.

It has to be noticed that for coating speeds under 1000 rpm some of the coated substrates showed a withdraw from edges due to thermal stress when placed on the hot plate for solvent evaporation (Fig. 3.16). In this case, coated wafer was then left longer on the spin stage during 5 minutes after the spin was finished. By doing so, part of the solvent in photoresist evaporates, resist viscosity increases and avoids withdrawal during baking on the hotplate.



### 3.2. CHARACTERIZATION OF PHOTORESIST AZ-4562

Speed [rpm]	Spin 30 s.		Spin 7 s.	
	Thickness [ $\mu\text{m}$ ]	TTV [ $\mu\text{m}$ ]	Thickness [ $\mu\text{m}$ ]	TTV [ $\mu\text{m}$ ]
500	26.26	$\pm 0.4$ (1.5 %)		
700	18	$\pm 0.33$ (1.8 %)		
1000	14.82	$\pm 0.28$ (1.8 %)		
1500	11.01	$\pm 0.3$ (2.7 %)	17.49	$\pm 0.48$ (2.7 %)
2000	9.14	$\pm 0.16$ (1.7 %)	13.08	$\pm 0.16$ (1.2 %)
2500	8.04	$\pm 0.09$ (1.1 %)	10.79	$\pm 0.13$ (1.2 %)
3000	7.31	$\pm 0.19$ (2.5 %)	8.98	$\pm 0.22$ (2.4 %)
3500	6.78	$\pm 0.13$ (1.9 %)	7.99	$\pm 0.29$ (3.6 %)
4000	6.34	$\pm 0.15$ (2.3 %)	6.99	$\pm 0.18$ (2.5 %)
4500	6.02	$\pm 0.09$ (1.4 %)	6.56	$\pm 0.14$ (2.1 %)
5000	5.55	$\pm 0.06$ (1 %)	5.95	$\pm 0.07$ (1.1 %)

Table 3.5: Thickness values and variations obtained for each spin speed.

Speed [rpm]	Thickness [ $\mu\text{m}$ ]	$\Delta$ Thickness [ $\mu\text{m}$ ]
200 + 400	46	$\pm 4$ (8.69%)
200 + 500	38.43	$\pm 2.09$ (5.4%)
200 + 600	34.42	$\pm 1.9$ (5.5%)
200 + 700	29.8	$\pm 0.4$ (1.3%)

Table 3.6: Thickness values and variations obtained for double spins.

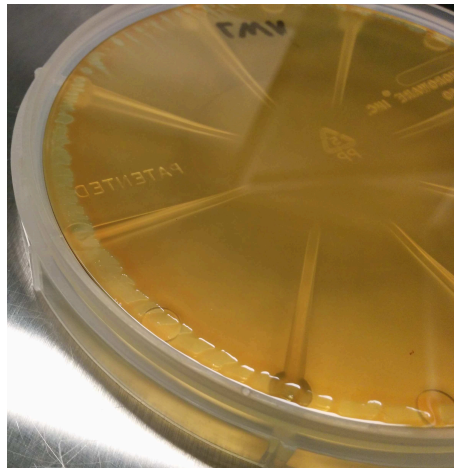


Figure 3.16: Coated substrate with withdraw from edges.

#### 3.2.2/ SOLVENT ELIMINATION AND HYDRATION OF COATED PHOTORESIST

Once the photoresist layer has been deposited onto the substrate, a softbake step is required in order to eliminate remaining solvent and post-hydration (water recovery in the bulk of the photoresist to improve PAC conversion into carboxylic acid during exposure) of photoresist is done. Softbake after photoresist coating (also called post-apply bake or PAB) dries the photoresist (otherwise it would not achieve its solid form [Allresist, 2016]) and fixes residual solvent content [Mueller et al., 1997b, Mueller et al., 1997a]. Indeed, diffusion of resist components during exposure is affected by remaining solvent after soft-



bake which determines the exposure properties and dissolution rate of the photoresist [Mack, 1998]. Problems that an excessive amount of solvent can create in the lithography process, addressed already in section 2.4.1 and 2.4.4 are: change dissolution rate during development [Ouano, 1984, Beauchemin et al., 1994], affects the photoresist optical absorption during the exposure step (Eq. 2.4 and 2.5) deteriorates adhesion to the substrate. Moreover, water concentration in photoresist before exposure also affects the dissolution rate of exposed resist. Films that have not a sufficient time to rehydrate cannot be completely dissolved even at very high doses and/or long development time [Lehar et al., 2001]. Rehydration time is specially important in microlenses fabrication through photoresist reflow [Rocha et al., 2013]. Insufficiently hydrated photoresists show a development rate two or three orders of magnitude slower than well-hydrated ones (Fig. 3.17). Before exposure of photoresist, a certain period of time must be waited to let the photoresist properly hydrate to improve development rate and contrast. For DQN-based photoresist like the one employed in this work, depending on the resist film thickness, a rehydration time of approximated 10 min for 10  $\mu\text{m}$  resist film thickness, one hour for 30-40  $\mu\text{m}$  or even up to 10 hours for resist films up to 100  $\mu\text{m}$  is required [MicroChemicals, 2013d]. This subsection explains the development process regarding these two parameters.

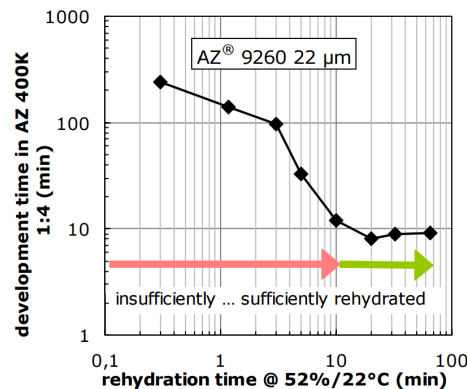


Figure 3.17: Development time (after exposure) as a function of rehydration time (before exposure) for positive photoresist AZ-9260 (similar characteristics to AZ-4562). Source: [MicroChemicals, 2013f]

Concerning solvent evaporation of photoresist, it can be noted that some models are proposed to evaluate theoretically solvent concentration variations in photoresist depending on time and temperature of baking [Chen, 1983, Mack et al., 1994]. Their predictions are based in heat and mass transfer models for solvent diffusion. In this thesis work, the author simply follows the instructions given by the manufacturer (MicroChemicals). They propose the reflow of the coated substrate on a hotplate at 100  $^{\circ}\text{C}$  during 1 minute per  $\mu\text{m}$  resist film thickness [MicroChemicals, 2013e]. By doing this, dark erosion rate during resist development is decreased and possible nitrogen bubbles formation is eliminated.

Nevertheless, when thick photoresist layers have to be accomplished, this temperature becomes too high and substrate edges can also withdraw. In some cases this effect is even worse and the whole photoresist layer collapses (Fig. 3.18). In these cases, in addition to leave the coated substrate during 5 minutes on the spin coater, solvent evaporation was carried through a gradient increase of temperature from 40 to 100  $^{\circ}\text{C}$  in 12 minutes (Fig. 3.19). This solution decreases thermal shock in photoresist and permits

solvent evaporates gradually.

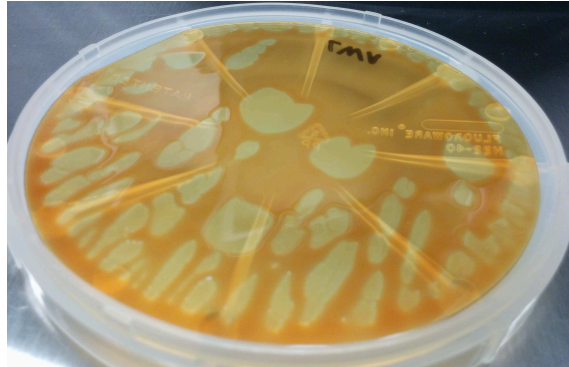


Figure 3.18: Photoresist collapse on substrate because of thermal shock during solvent evaporation.

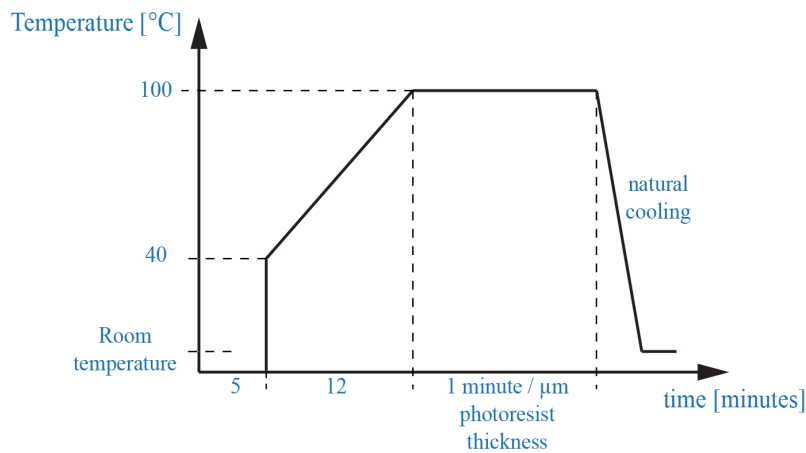


Figure 3.19: Temperature evolution during photoresist solvent evaporation to avoid thermal stress.

After solvent evaporation from photoresist, some time must be left before exposure of photoresist. This period of time corresponds to photoresist rehydration and is necessary to let the photoresist recover from water concentration drop during softbake after coating. To allow a good development rate, a certain water concentration in photoresist is needed. Rehydration occurs through water diffusion from air towards the resist layer. Time necessary to have enough water concentration increases quadratically with film thickness [MicroChemicals, 2010]. Thin films need only a few seconds but when working with thick layers, some hours must be left. In this thesis work, substrates were left from 8 to 10 hours to assure enough time for sufficient water recovery. Air humidity is also important. If the evaporation rate is bigger than the absorption rate (insufficient humidity in the air) rehydration of resist will never be achieved.

### 3.2.3/ PATTERNED COMPONENTS AFTER DEVELOPMENT OF PHOTORESIST

Patterned structure is the result of the combination of energy dose the photoresist receives and development conditions after exposure. The exposed pattern can be modified during the development process due to developer concentration or duration of the step. The goal is to pattern the whole structure without unexposed levels and to always avoid side effects like lifting of photoresist layer or dark erosion of unexposed zones. As the etching process of photoresist in glass shows low selectivity it is preferable to target high thickness of patterned resist. In this thesis work, the effects of double exposure, which consist in two exposition steps of the photoresist without resist development between them, are also investigated. Double exposure in lithography fabrication has been used for the patterning of structures in photosensitive resist in gray-scale mask lithography [Mosher et al., 2009], e-beam fabrication processes [Yoshikawa et al., 1998] or interferometry patterning of photoresist [Kuiper et al., 2001, Xie et al., 2008]. To the author's knowledge, no group has tried yet to achieve higher developed thickness of structured photoresist using double exposure steps in laser based lithography processes.

#### 3.2.3.1/ SINGLE EXPOSURE

First, single exposure is investigated in terms of achievable thickness. First test is an exposed pattern consisting in a series of 100  $\mu\text{m}$  side squares designed from layers 1 (the shallowest) to 63 (the deepest) and exposed at different power values (5 to 100 %). Depth achieved in each case was measured after development and rinsing in deionized water (to stop the development reaction) with a contact profilometer Alpha-Step IQ of KLA Tencor [Tencor, 2010].

Results of pattern exposures are shown in figure 3.20. During development process, basic developer AZ - 400K of Clariant [Clariant, 2002] was used to eliminate the exposed photoresist in an aqueous solution with deionized water in 1:1 concentration (1 part of AZ-400K : 1 parts of deionized water) during 1 minute. The sought result is a ramp with highest rope; going down to. In the figure, it can be seen that for the maximum value of power (100 %, 125 mW) thickness achieved after development is 9.1  $\mu\text{m}$ , being the highest depth achieved after a single exposure. For lower power levels, depth achieved decreases until values from 0.45 to 2.96  $\mu\text{m}$  depth for power values of 5 and 10 %. It can be seen that there exist fluctuations in depth evolution for all exposure powers. The theoretical exposure process follows the rule of deeper the layer, deeper the pattern exposed. These anomalies can be provoked by high developer concentration. At such high concentrations, development becomes very fast and unstable. After 1 minute, the high developer concentration provokes dark erosion effects in unexposed photoresist and some levels of the patterned structure are eliminated.

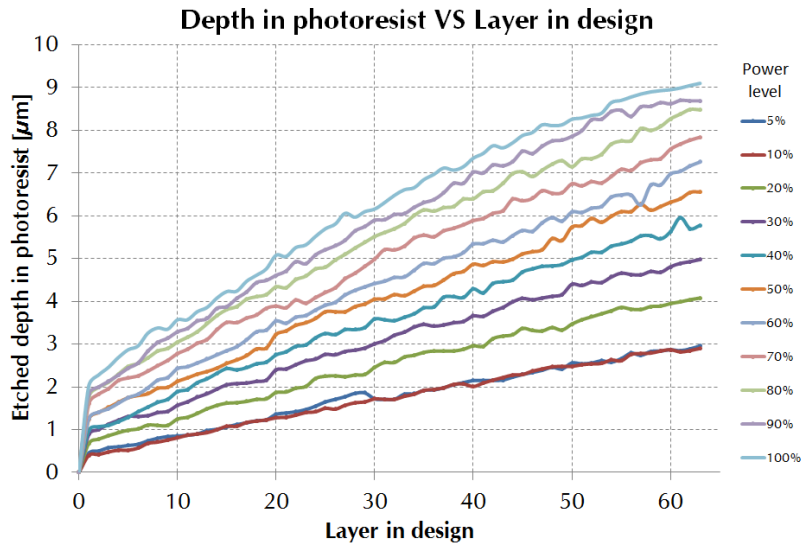


Figure 3.20: Depth achieved in photoresist after single exposure as a function of power exposure and layer in the design.

In order to improve the fluctuations, two solutions can be adopted:

- Reducing developer concentration:** if concentration is reduced (to 1:1.5 or 1:2), dark erosion effects are reduced, specially at borders of unexposed photoresist. Lower concentrations cause longer development processes, making the process more stable and increasing exposed pattern quality. A lower developer concentration was tested (1:2) and it was observed that the shallowest levels remained undeveloped in photoresist no matter how long they were exposed to developer. Moreover, in some cases, resist adhesion to substrate was seriously damaged, causing lifting problems (Fig. 3.21). This effect is observed because during exposure step, energy dose does not reach the photoresist activation energy (Sec. 2.4.1). This is due to a too shallow layer in the design or a too low power value; both effects decrease energy dose the resist receives.

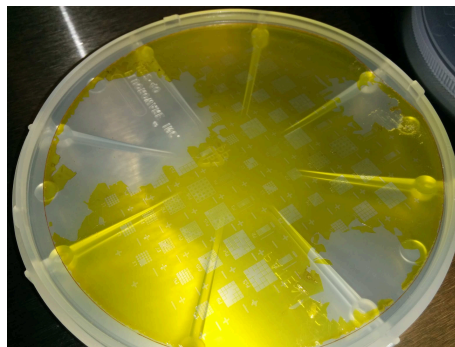


Figure 3.21: Photoresist lifts off the substrate because of a too long development process.

- Increasing number of exposures:** by increasing the number of exposure steps, the amount of energy deposited in each layer increases. Because of the bleaching mechanism in photoresist during exposure due to the carboxylic acid production, a

second exposure step provokes an incrementation in the amount of PAC that converts into carboxylic acid that can be developed. By doing this, depth achieved in photoresist increases, letting user design the structure with more freedom.

In this thesis work, the two options have been conjugated, i.e., a reduction in developer concentration along with a second exposure step in order to increase the range of depth achievable in photoresist and quality of developed structures.

### 3.2.3.2/ DOUBLE EXPOSURE

Second exposure is performed just after the first one is finished. Coated substrate is not moved from stage between the two successive exposures thus alignment accuracy is related to the one of the writing system, i.e. about  $0.1 \mu\text{m}$ . Hence, a 1:2 developer concentration was used to develop the exposed photoresist during 5 minutes. Longer development times, lead to unexposed zones of photoresist suffering dark erosion effects so that some levels of the patterned structures disappear. Obtained results are represented in figure 3.22. In this thesis work the interest of the highest power value is analyzed. As mentioned before, the low selectivity of photoresist during etching process makes this one the most useful level in the patterning step of components, as it is the one that achieves higher depth values. Depth values now range from  $1.4$  to  $16.3 \mu\text{m}$  when pattern is designed from layer 1 to layer 63. As in this case a lower concentration of developer has been employed, previous fluctuations have disappeared, improving quality of the process.

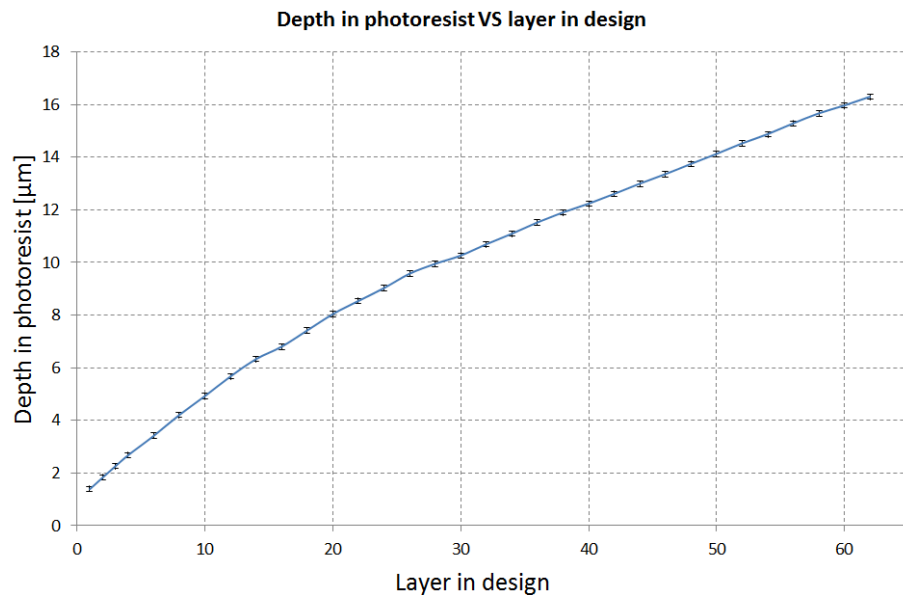


Figure 3.22: Depth achieved in photoresist after double exposure as a function of layer in design.

It can be noticed that depth achieved in photoresist does not follow a linear progression with the energy dose. This is because of the non-linear behavior of intensity within the photoresist bulk (Eq. 2.3). As linear profiles are needed in the designed components,

a linearization of this curve is needed. In equation 3.4, results are fitted to a 3<sup>rd</sup> order polynomial expression representing depth value ( $D$ ) as a function of the layer used ( $L$ ) in the pattern design ( $R^2 = 0.99$ ):

$$D = 4 \cdot 10^{-5} \times L^3 - 0.0061 \times L^2 + 0.4561 \times L + 0.9436 \quad (3.4)$$

Following expression 2.7, the contrast and the contrast curve of the photoresist according to the conditions of this test (double exposure at 125 mW and development with 1:2 developer:deionized water concentration during 5 minutes) can be obtained. Contrast value of the photoresist in this case is  $0.935 < 1$ , which is the value for ideal photoresist with infinite contrast. Figure 3.23 shows the remaining photoresist as a function of the exposure dose ( $D_{63}/D_1$ ) in a logarithmic scale (normalized axes). This figure can be compared to figure 2.11 in section 2.4.1. The obtained slope of the contrast curve corresponds to the response of a low-contrast photoresist which adequate for the exposure at different intensity values.

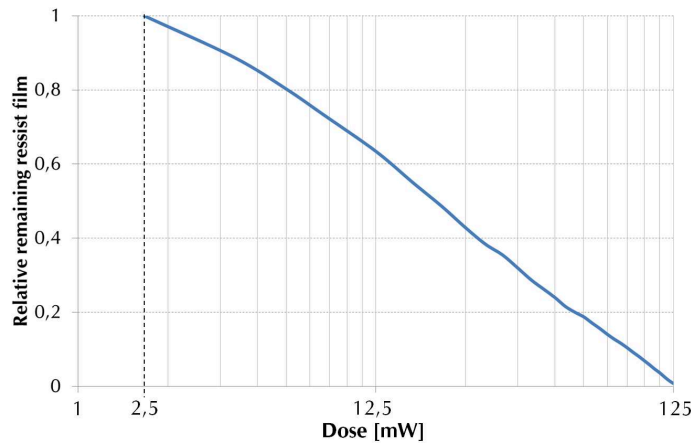


Figure 3.23: Contrast curve of exposed photoresist.

As development process becomes more stable and reactions are not as fast as in case of 1:1 concentration, dark erosion effects are eliminated. Thanks to the second exposure step, levels patterned in shallowest layers can be developed as deposited energy is bigger than in case of a simple exposure. Development time in this case is not long enough to provoke lifting problems in the substrate and exposed photoresist is eliminated in a reasonable time. The double exposure at 125 mW and development with basic developer at 1:2 dilution offers a good contrast curve which makes possible the exposure at different levels and the design of diffractive and refractive components.

### 3.2.4/ BAKING OF DEVELOPED PHOTORESIST

This thesis work focuses on the fabrication of continuous relief profile microoptical components. Hence, to give the stepped developed structures a smooth profile, a baking step after development of discontinuous exposed pattern is added (Fig. 3.24). The technique, also called reflow, has been widely used for the fabrication of refractive components



through resist or polymer melting [Wu et al., 2002, Roy et al., 2009, Badar, 2012]. Most of them consist in the fabrication of microlenses, whose meanly spherical profile minimizes the energy of the component when it melts [Abe et al., 1999]. Nevertheless, a lack of sphericity is sometimes observed as a result of tensions between surface [O'Neill et al., 2002] and resist cross-linking [Audran et al., 2006]. We did not find in the literature an approximation of the reflow technique to give the components a more smooth profile. All of them are referred to the generation of the component by reflow from primitive structures like squares or rectangles of certain volume. In here, the situation is slightly different since the purpose is only to smoothen the steps resulting from the layers based exposure during laser exposure.

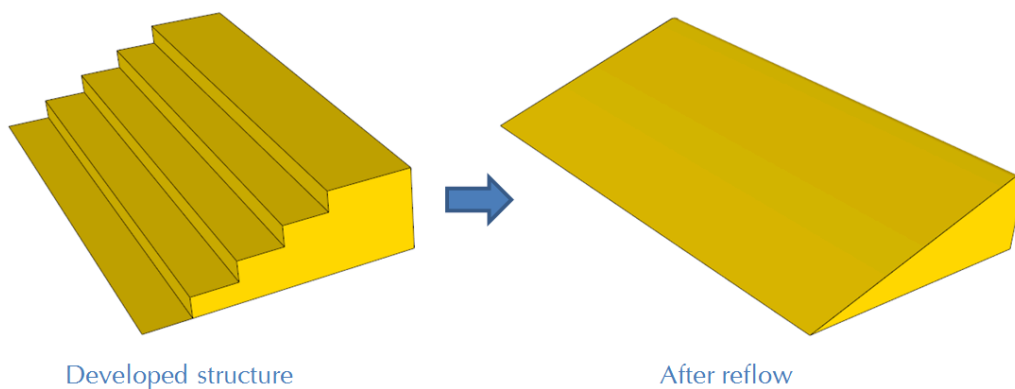


Figure 3.24: Changes in developed structure after baking step.

Baking parameters time and temperature depend on both geometrical and structural factors. Dimensions of patterned structure (height, diameter and number of layers) and melting point of photoresist are taken into account. In case of photoresist AZ-4582, melting point is  $110^{\circ}\text{C}$ . Under this temperature, no observable changes are achieved in the structure. Nevertheless, over the melting point, rapid changes can be observed. In figure 3.25, the profile evolution of 2 different stair-shaped structures (4 and 8 levels) of  $200\ \mu\text{m}$  lateral size and total thickness between  $1.5$  and  $1.8\ \mu\text{m}$  is shown during reflow on a hot plate set at  $120^{\circ}\text{C}$ . Clearly, a tradeoff has to be found between smoothing the stepped zones and letting the main profile (optically interesting) unchanged. For this purpose, it is better to increase the number of levels so that reflow is able to smooth the steps in a reasonable time, without affecting the structure, as it can be seen on the 4 levels structure after 5 minutes reflow (which collapses). With 8 levels, discontinuities in the structure are eliminated after 1 minute reflow, collapse is avoided and profile of the structure is more similar to the original one. So for each fabricated component, a test based in reflow processes at different times is carried and best option is selected.

Obviously, when the structure has higher frequencies, maximum time must be carefully controlled. An example is shown on the figure 3.26. The fabricated pattern corresponds to a diffractive lens of  $500\ \mu\text{m}$  diameter and four levels (a). After development, substrate was placed onto a hotplate during 1 minute as for the previous test. It can be seen that, even if thickness of the component is the same as in previous case, almost the whole pattern has disappeared. Because of the pattern small dimensions ( $3\ \mu\text{m}$  in the outer ring), melted photoresist loses completely its previous shape. In these cases, a much shorter bake process must be applied to avoid losing the initial component profile.

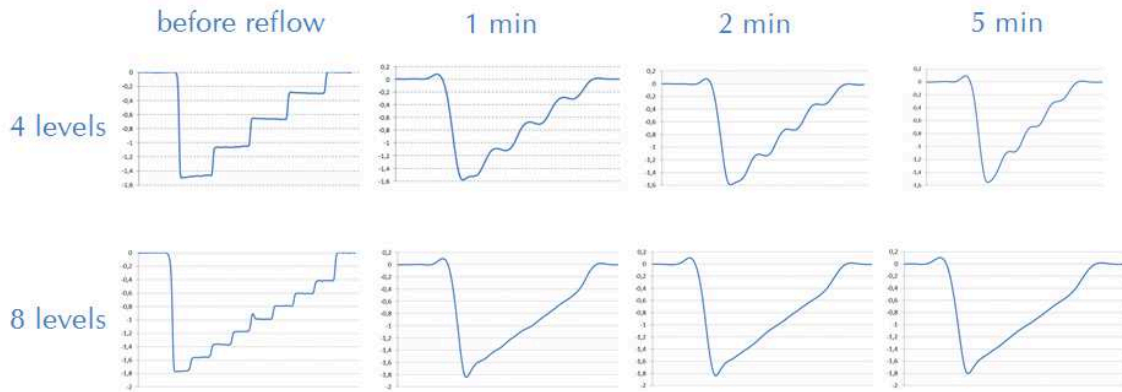


Figure 3.25: Profile evolution of two stair-like structures of 4 and 8 levels during 1, 2 and 5 minutes reflow at  $120^{\circ}\text{C}$ .

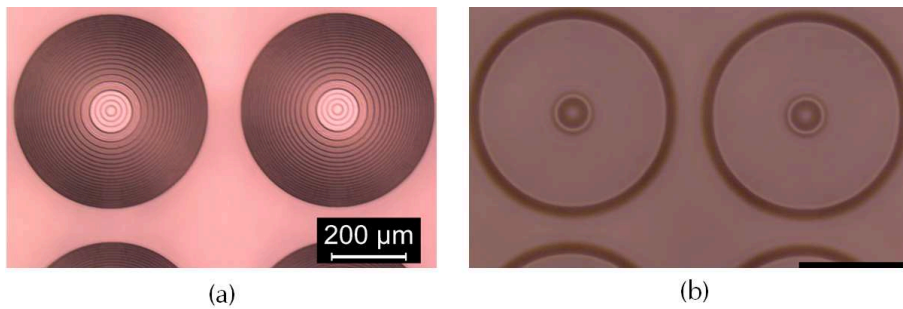


Figure 3.26: (a) Microscope image of a diffractive lens after development process. (b) Microscope image of same lens after 1 minute reflow at  $120^{\circ}\text{C}$ .

### 3.2.5/ PATTERN TRANSFER INTO THE SUBSTRATE

As we are interested in the fabrication of more robust and transparent elements, last step in the fabrication of microoptical components by lithography process concerns the pattern transfer into glass substrate through reactive ion etching (RIE). The technique was introduced in section 2.4.3 and recipes used along with results obtained are presented here.

For the etching process, the RIE-ICP system from Plassys was used [FEMTO-ST, 2015a]. The equipment combines both chemical, based on reactions between free radicals generated in the plasma source and materials to be etched, and physical attacks, through positive ions sputtering, on coated substrate. The substrate is placed into a vacuum chamber on a silica plate (insulate). A radio frequency of 13.56 MHz is applied, creating an electric field and generating the dissociation of gas molecules for the generation of free radicals, ions and electrons. The strong mobility of electrons compared to ions, makes these last move towards the substrate provoking chemical reactions with materials to be etched. As the surface gets negatively charged, positive ions are also attracted to the substrate surface provoking the physical attack of the material and ensuring



the anisotropy of the process. The Plassys system can introduce in the chamber four different gases: Sulfur hexafluoride (SF<sub>6</sub>), Fluoroform (CHF<sub>3</sub>), Hexafluoroethane (C<sub>2</sub>F<sub>6</sub>) and Oxygen (O<sub>2</sub>). Pressure can be down to 10<sup>-5</sup> mbar and the plasma source can be up to 300 W RF. Substrates whose diameter is under 4 inches can be placed in the chamber.

In our case, etched substrate is a borosilicate glass wafer (Borofloat33 from Schott) [Schott, 2016b] of 4 inches and 500 μm thickness (± 25 μm). Its chemical composition is summarized in table 3.7:

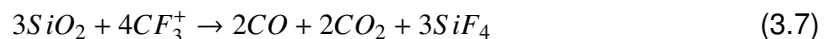
Component	Percentage
Silicon dioxide (SiO <sub>2</sub> )	81%
Boron trioxide (B <sub>2</sub> O <sub>3</sub> )	13%
Sodium oxide / Potassium oxide (Na <sub>2</sub> O/K <sub>2</sub> O)	4%
Aluminium oxide (Al <sub>2</sub> O <sub>3</sub> )	2%

Table 3.7: Composition of Borofloat33 optical glass from Schott.

During etching, plasma oxygen removes photoresist by oxidizing the hydrocarbon material to volatile products (CO, CO<sub>2</sub> and H<sub>2</sub>O) [Madou, 2002]. This gas is usually combined with CF<sub>4</sub>. A balance between pressure and RF power determine plasma anisotropy and possible side effects in photoresist like over etching and non-uniformities [Systems, 2000]. Typical etch rates go from 0.01 to 1 μm/min depending on resist materials, ions energy and reactive gases in the chamber.

For SiO<sub>2</sub> based materials, employed gases are usually fluoride derivatives like SF<sub>6</sub> and C<sub>2</sub>F<sub>6</sub> or CHF<sub>3</sub>. SF<sub>6</sub> reacts with both photoresist and SiO<sub>2</sub> based materials [Jaeger et al., ]. Along with oxygen, this extra-etching force over the photoresist is not convenient here, since it will resulting a too high etching rate of the resist, compared to glass substrate. This gas is, then, not employed in the etching process. Between C<sub>2</sub>F<sub>6</sub> and CHF<sub>3</sub>, the one that shows a strongest fluorine to carbon ratio (F/C), leading to better SiO<sub>2</sub> etching rate, is C<sub>2</sub>F<sub>6</sub> (1:3) [Jansen et al., 1996].

When a mixture of oxygen and C<sub>2</sub>F<sub>6</sub> is employed, both photoresist and glass are etched at a relatively good rate. C<sub>2</sub>F<sub>6</sub> is dissociated in the plasma source to generate CF<sub>3</sub> molecules (React. 3.5), which are ionized in presence of electrons in plasma to CF<sub>3</sub><sup>+</sup> (React. 3.6). This positive ion attacks the substrate surface to react with the SiO<sub>2</sub> molecules of glass and generates CO, CO<sub>2</sub> and SiF<sub>4</sub> (React. 3.7) as byproducts that are evacuated [Campbell et al., 2008]:



Oxygen added to the etching process reacts with CF<sub>x</sub> radicals to enhance free radical F formation, so increasing the F/C rate by removing carbon atoms in the form of CO and CO<sub>2</sub> [Gao et al., 1998]. F radicals also react chemically with SiO<sub>2</sub> on the surface

substrate producing  $\text{SiF}_4$  and oxygen (React. 3.8). Nevertheless, at higher proportions (60 % [Kong et al., 2002]) oxygen, apart from increasing the photoresist etching rate, is diluted and adsorbed on the surface decreasing, then, the etch rate of the process [Mogab et al., 1978]. The ratio  $\text{O}_2/\text{C}_2\text{F}_6$  can be regulated by controlling the volume of gas introduced in the chamber. This ratio along with power and pressure defined in each case determine the selectivity of the etching process.



Selectivity of process is limited primarily by the polymerization point of the gas. Gases like  $\text{CHF}_3$  or  $\text{C}_2\text{F}_6$  create unsaturated compounds in plasma, provoking polymer formation that are deposited on wafer surface and electrodes. This effect, that should be taken into account, adds an extra micro layer onto the substrate that can be hardly eliminated. Limit between polymerization and etching depends on fluorine to carbon ratio. By increasing oxygen level, F/C ratio increases and polymer formation is reduced [McGuire, 1988]. But, increasing oxygen also leads to higher resist etch rate and, subsequently, a lower selectivity in the process. In addition, parameters like low temperature, high hydrogen concentration, low power, high pressure or high monomer concentration increase both polymerization and selectivity [Madou, 2002].

Pressure and power values also play an important role in photoresist and glass etching. Low pressure increases ion directionality and thus physical sputtering etching, increasing both resist and  $\text{SiO}_2$  etching rates [Zhao et al., 1998]. Byproducts are also removed easier at low pressures, making the process less contaminating. A side effect of low pressure is the decrease in ion density, decreasing etch rate and wafer throughput. Higher RF powers favor the production of energetic oxygen, increasing the etching rate of the process [Feng et al., 1996, Lee et al., 2000].

Selectivity of the process has been measured in base of the relation between etching rates of photoresist and glass. For each test, process followed is shown in figure 3.27.

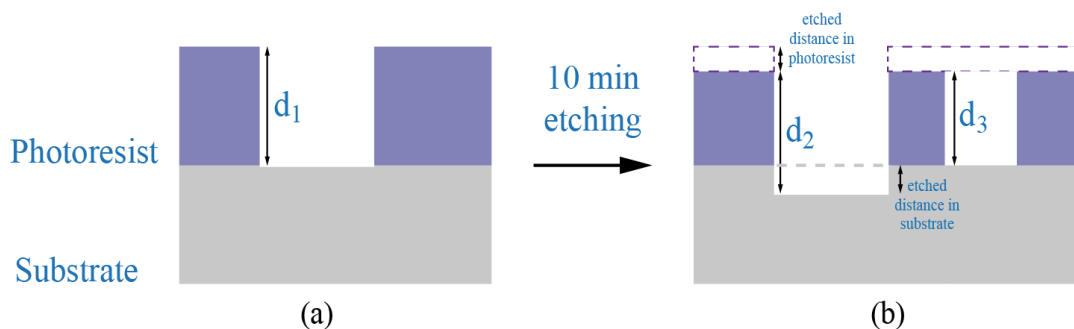


Figure 3.27: Schema of the process followed to measure selectivity.

$d_1$  represents photoresist thickness before etching (fig. 3.27(a)). After 10 minutes etching under each test conditions (concentration of component A and B [sccm], pressure [ $\mu\text{bar}$ ], RF power [W] and time [min]),  $d_2$  and  $d_3$  are obtained (fig. 3.27(b)).  $d_2$  is obtained in the same place where  $d_1$  was measured.  $d_3$  is the photoresist new thickness after carefully scratch the surface and measure with a mechanical profilometer. All distances are

measured in the center of the substrate not far from etched components. Once distances have been measured selectivity of the process can be obtained:

$$\text{Photoresist etching rate (A)} = \frac{(d_1 - d_3) [\mu\text{m}]}{10 [\text{min}]} \quad (3.9)$$

$$\text{Glass etching rate (B)} = \frac{(d_2 - d_3) [\mu\text{m}]}{10 [\text{min}]} \quad (3.10)$$

$$\text{Selectivity of photoresist in glass} = \frac{A}{B} \quad (3.11)$$

In this thesis work several tests have been carried out with  $\text{CHF}_3$ ,  $\text{C}_2\text{F}_6$  and  $\text{O}_2$  gases combined in different way. Concerning selectivity, gases that show better results are  $\text{C}_2\text{F}_6$  combined with  $\text{O}_2$ . For these components, results of best two recipes are summarized in table 3.8.

Recipe	$\text{O}_2$ [sccm]	$\text{C}_2\text{F}_6$ [sccm]	Pressure [ $\mu\text{bar}$ ]	Power [W]	A [ $\mu\text{m}/\text{min}$ ]	B [ $\mu\text{m}/\text{min}$ ]	Selectivity
1	7	20	100	100	0.128	0.053	2.26
2	15	7	100	150	0.247	0.065	3.8

Table 3.8: Tests of photoresist etching in glass.

Selectivity determines vertical dimensions of components to be exposed in photoresist. During the design step, thickness of components in photoresist must be calculated as the product of the final component thickness to be achieved in the substrate and selectivity of photoresist in glass. Regarding this fact, the combination of parameters that offers more freedom in the designing process is recipe 1. In recipe 2, the addition of  $\text{O}_2$  in the mixture along with a decrease of the  $\text{C}_2\text{F}_6$  proportion and the increase of power, provoke an increasing in photoresist etching rate per minute (almost double). Nevertheless, increment in the  $\text{C}_2\text{F}_6$  etching rate is not significant and selectivity of the whole process is much higher than in first case. This can be produced because of the excessive amount of  $\text{O}_2$  in comparison with  $\text{C}_2\text{F}_6$ . As mentioned before, when high proportions of  $\text{O}_2$  are used in the etching process, part of it is diluted and absorbed on the substrate surface. This fact along with the power increment of the process (higher production of  $\text{O}_2$  radicals and polymerization) makes difficult the etching of glass substrate. Recipe 2, however, can be employed when diffractive components are considered. In this case, thicknesses of components in glass are typically between 1 (for single order, or  $2\pi$  steps) and 4  $\mu\text{m}$  (for  $8\pi$ , or multi-order diffractive lens). At these values total thickness in photoresist, according to recipe 2, are between 4 and 15  $\mu\text{m}$ , perfectly attainable according to section 3.2.3. As the etching rate of the photoresist is higher than in recipe 1, the etching process is done faster so quality of surface components in terms of roughness can be improved.

As an example, an exposed pattern consisting in a pyramid of  $d = 1$  mm side and  $h = 1$   $\mu\text{m}$  thickness, divided in 8 levels (size of steps is 0.125  $\mu\text{m}$  height and 62.5  $\mu\text{m}$  width) (Fig. 3.28 (a)) is etched in glass by using recipe number 2. The pattern was exposed at 10% power, so 12.5 mW in the deepest (most energetic) level. The etching process was performed with  $\text{C}_2\text{F}_6$  and  $\text{O}_2$  using parameters of recipe 2 (Table 3.8). Because of the process selectivity, it can clearly be appreciated (Fig. 3.28 (b)) how different dimensions of glass structure are (profile in color red) compared to the resist structure (profile in color

### 3.3. RECIPE FOR FABRICATION OF GLASS-BASED MICROOPTICAL COMPONENTS THROUGH GRAY-SCALE LITHOGRAPHY PROCESS

blue). After etching, patterned structure is 3.8 times smaller than the developed one, as expected from the selectivity value. Nevertheless, stepped profile is maintained and the 8 levels are transferred.

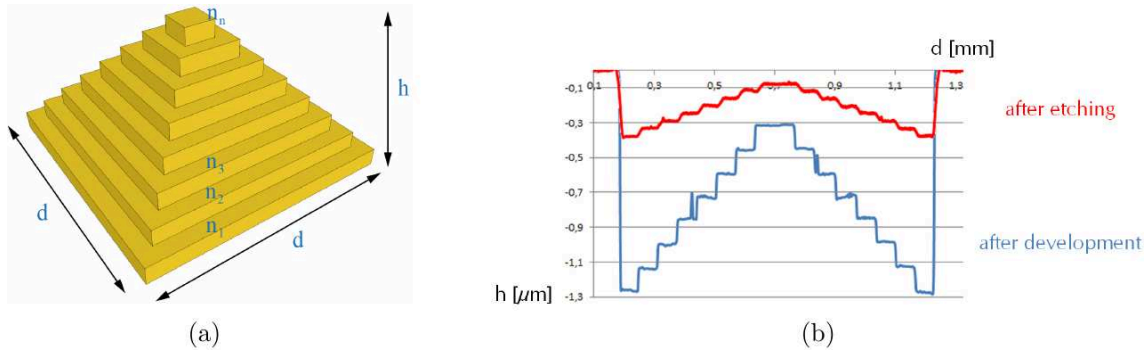


Figure 3.28: (a) Schema of the pyramid structure used in the fabrication process. (b) Profile of developed (blue) and etched (red) pyramid structure of 1 mm side,  $1.3 \mu\text{m}$  thickness and 8 levels.

Characterizations and calibrations of exposure system DWL200 and photoresist AZ-4562, make now possible the fabrication of structures in glass. During the design step, a balance between thickness achievable in photoresist through spin coating, possible depth of components in photoresist through laser exposure and selectivity of the process must be taken into account. These are limiting factors that set the boundary conditions of the process. To achieve a good repeatability from wafer to wafer, whole process should be controlled strictly. Photoresist and developer must be in good condition and used before expiry date. The correct preparation of the photoresist before exposure is mandatory. Alterations in concentration of evaporated solvent, insufficient hydration time or incorrect development of exposed photoresist will lead to unexpected results. This lithography process is quite standard and easily applicable to product manufacturing environment. Next section is a summary of steps to follow for the fabrication of microoptical components by lithography process.

### 3.3/ RECIPE FOR FABRICATION OF GLASS-BASED MICROOPTICAL COMPONENTS THROUGH GRAY-SCALE LITHOGRAPHY PROCESS

Here are exposed a series of steps to follow for the fabrication of microoptical components through gray-scale lithography. This summary of the process development serves as a guide to follow in the fabrication stage. Each step is the result of calibration tasks developed for both DWL200 lithography system and AZ-4562 photoresist:

- **Wafer cleaning.** The substrate is first cleaned by 2 minutes pent in a piranha solution ( $\text{H}_2\text{O}_2:\text{H}_2\text{SO}_4$ , 1:2 concentration) followed by deionized rinsing.

- **Wafer conditioning.** The substrate is then placed onto a hotplate at 120°C during 10 minutes for desorption of surface water. In order to improve resist adhesion, the substrate is coated with a layer of TI-PRIME adhesion promoter by spin coating ( $v=3500$  rpm,  $a=4000$  rpm/s,  $t=20$  s). After coating, 2 minutes onto a hotplate at 120°C, surface is chemically activated forming an hydrophobic layer that improves resist adhesion. Before photoresist deposition onto the wafer (next step), 1 minute must be waited, in order to avoid thermal shock of photoresist when placed onto the hot substrate. In other case, homogeneity of deposition is not assured.
- **Substrate coating.** In function of photoresist desired thickness, number of spins, speed, acceleration and time is selected (Fig. ??). Homogeneity of the process is assured for speeds over 400 rpm in double spin coating.
- **Solvent evaporation and hydration of photoresist.** Prior to exposure step, a correct evaporation of solvent and rehydration have to be achieved in the photoresist (Sec. 3.2.2). Solvent evaporation through baking of the substrate on a hotplate at 100°C during 1 minute per  $\mu\text{m}$  thickness leads to low solvent contents in photoresist which assures a good dissolution rate during development. It also avoids bubbles formation during the exposure step caused by a too low diffusion of produced nitrogen. If high thickness is required, lower temperatures, e.g. 40°C to 100 °C in 12 minutes, should be used to avoid resist withdraw or collapsing problems. After solvent evaporation, coated substrate must recover part of the water lost during baking. In this thesis work, from 8 to 10 hours were waited to assure a correct photoresist rehydration.
- **Photoresist exposure.** According to the pattern designed, exposure of photoresist can be now performed. In this thesis work, the double exposure of photoresist to achieve deeper structures (Sec. 3.2.3.2) has been considered in order to extend range of structures that can be fabricated. Note that the substrate is not moved between exposures so that the alignment system provides 0.1  $\mu\text{m}$  accuracy.
- **Development.** For photoresist development (Sec. 3.2.3), the substrate is soaked in a 1:2 concentration of developer AZ-400K in deionized water during 5 minutes and rinsed. Layers from 1 to 63 are well developed avoiding dark erosion effects. In some cases, when patterns of less than 2  $\mu\text{m}$  thickness have to be exposed, the use of a 1:1 developer concentration with tight time control (less than one minute) can be justified.
- **Baking of coated substrate.** A short baking step is needed (Sec. 3.2.4) can be applied to make the surface relax and remove discontinuities in component profile. 110°C is the AZ-4562 photoresist melting point used in the fabrication process. In this thesis work, this process has been carried on a hot plate at 120°C, ranging from 5 seconds to 4 minutes. Duration will be different as a function of dimension and number of layers in developed pattern.
- **Pattern transfer in glass.** Last step corresponds to the transferring of developed structures into the substrate through reactive ion etching (Sec. 3.2.5). A mixture of  $\text{C}_2\text{F}_6$  (20 sccm) and  $\text{O}_2$  (7 sccm) at 100  $\mu\text{bar}$  and 100 W assures a selectivity value of 2.26 (i.e. the photoresist is etched 2.6 times faster than the borosilicate glass substrate). Prior to

etching, cleaning the chamber with O<sub>2</sub> (15 sccm) plasma at 100  $\mu$ bar and 150 W during 10 minutes can improve repeatability. Measured glass etching rates range between 0.053 and 0.063  $\mu$ m/min so, depending of the thickness objective in the components, etching process can take between 15 minutes (for a 1  $\mu$ m thickness component with recipe 2) and 5 hours (for a 16  $\mu$ m thickness component with recipe 1). As this process might be very long, cleaning the chamber regularly allows to remove possible contaminants caused by reaction byproducts deposited over the walls inside the chamber. The process is, then, improved.

### 3.4/ REALIZATIONS

This last section corresponds to the fabrication of microoptical components and structures following the steps described in previous recipe. Once the response of the photoresist has been adapted to the exposure system, the fabrication of more complex structures can be considered. The depth exposure curve (Eq. 3.4) determines the layer to use in each point of the profile. The system can use two different writing heads to achieve resolutions down to 1  $\mu$ m. This section is devoted, as an example of application of the technology, to the complete fabrication of a microoptical component consisting in a conical microlens for Bessel beam generation. The fabrication process starts with the design of the component adapting double exposure level distribution (Eq. 3.4) to achieve a linear slope for the conical lens. Next steps follow the fabrication recipe described in section 3.3 to achieve the final pattern transfer in glass. After results presentation, analysis and conclusions of the fabrication process are obtained. By considering maximum phase variations and resolutions achievable in this component, the fabrication of this type of lens will set the potential of the considered technique for the fabrication of more complex profiles.

The fabrication of glass-based microaxicons has been considered. First time proposed by McLeod in 1953 [McLeod, 1954], refractive axicons are continuous profile components that produce Bessel beams [McGloin et al., 2005] from an incident collimated beam, which exhibits, rather than a point, a long and narrow focal line along the optical axis. Such non-diffracting unique property makes them useful in applications like alignment and metrology [Häusler et al., 1988, Davis et al., 1996], coherence tomography [Ding et al., 2002], second harmonic generation [Piskarskas et al., 1999] or 2D microfabrication [Li et al., 2009]. Axicons are usually fabricated by diamond turning [Bass et al., 2001] or grinding and polishing [Van LE et al., 2012]. More recently, other fabrication approaches are being used to generate this type of lens and overpass the limitations of classical methods in terms of material restrictions, sizes achievable or quality of optical surface. In the literature we can find very different techniques like in [Philip et al., 2009], where conical-shaped lens were generated at the tip of multimode optical fibers using a selective chemical etching. They observed that fibers immersed in a solution with a particular combination of hydrofluoric acid (HF), buffer (B, an acid-base solution to control the pH value) and deionized water, the etching rate at the core was higher than in the cladding etching, resulting in the formation of negative cones. The process was able to generate microaxicons in the tip of such fibers with cone angles in the range from 14° to 180° although Bessel beam generation is not specified. Other

physical approach is employed in [Cao et al., 2013]. Here, the conical lens consists of a negative photoresist SU8 droplet and a biconcave lens made of BK7 glass of 6 mm diameter. The ensemble is placed into an electric field constructed by two parallel electrodes where the nonuniform electrical pressure deforms the droplet, reaching a new steady shape with a conical profile. When the ensemble is illuminated, the incident wave is first transformed into a spherical wave by the glass lens and then focused into a line by the droplet surface. In their "low-cost" approach, axicons of 6 mm diameter and almost 1 mm height are generated. Because of the nature of the process, the tip of the axicon is rounded and a radius of curvature of almost 1 mm is measured. Bessel beam generation is demonstrated in this case with a focus line of almost 20 mm but hollow beam formation is not specified. Last approach found employs a direct-laser fabrication process. In this case [Huang et al., 2014], a fiber-axicon (an optical fiber with an axicon on its tip) is employed to write on UV-curable optical photoresist to fabricate new axicons and axicon arrays. A 30  $\mu\text{m}$  film of negative photoresist is placed onto a movable stage where horizontal and vertical displacements are controlled with 100 nm step-size precision. A laser diode operating at  $\lambda = 405$  nm exposes the photoresist which undergoes a cross-linking reaction upon UV exposure and polymerizes. Unexposed photoresist is then removed. The development step is investigated as typical wet development methods affect the final shape of exposed photoresist. By the use of compressed air projected onto the substrate, the uncured epoxy is driven out of the substrate. Final roughness of photoresist component was measured below 0.05  $\mu\text{m}$ . The cured photoresist generates the conical shape based on the illumination beam profile so distance between writing lens and photoresist or radius of curvature of writing axicon determine final dimensions of fabricated conical lenses. In the experiments, control of time and power of exposures lead to the fabrication of conical lenses of 25  $\mu\text{m}$  diameter, 30  $\mu\text{m}$  thickness and an apex angle of  $37^\circ$ . Radial Bessel beam formation in the optical is demonstrated.

None of these proposed methods is able to demonstrate hollow beam generation after the non-diffracting beam formation. They do not consider either the transfer of the conical lens in photoresist into more robust material through etching or even the direct fabrication in them. As we have seen glass-based components are more stable than plastic ones in terms of heat tolerance although their fabrication is more challenging. We have not seen these approaches well adapted for mass fabrication as in every case components are generated individually which is, then, very time consuming. In this thesis work we consider all these factors and focus in the direct generation of components in photoresist and subsequent transfer in glass substrate.

#### 3.4.1/ FABRICATION OF GLASS-BASED MICRO AXICONS

For the fabrication of a glass-based micro axicon, the exposed pattern consists in concentric rings placed in different layers to give to the component a conical profile (Fig. 3.29). Once the pattern is exposed and developed, a short reflow on a hot plate at  $120^\circ\text{C}$  results in the continuous conical profile in photoresist. A subsequent etching process with  $\text{C}_2\text{F}_6$  and  $\text{O}_2$  transfers the pattern into glass substrate.

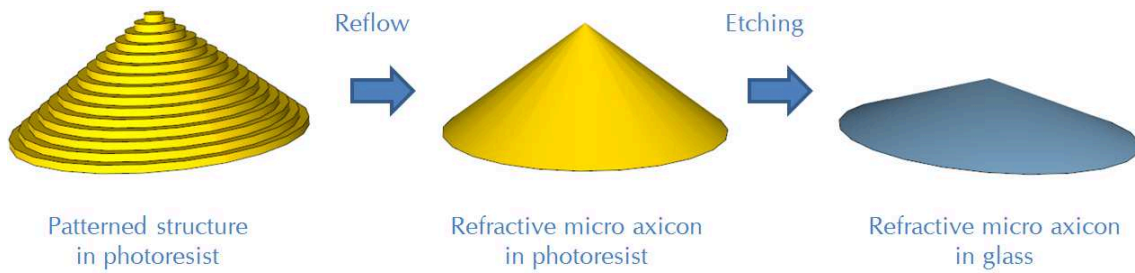


Figure 3.29: Schema of resist stepped structure, refractive profile in photoresist and etched glass micro axicon.

For this refractive component, we aim at achieving the maximum possible thickness within the bulk of the substrate, so this thickness represents the limits of the fabrication process concerning micro component vertical dimensions. For this purpose, double exposure is considered. At maximum power value (100% power in layer 63 of design, i.e. 125 mW) double exposed photoresist depth achieves  $16.3 \mu\text{m}$ . In order to protect unexposed zones of the substrate during etching, it is decided to keep a distance of  $1.5 \mu\text{m}$  over the exposed component. Thus, a total thickness of  $14.8 \mu\text{m}$  is reachable in the developed structure. This thickness will set the etching process duration. Once the whole component is transferred into the substrate, rest of photoresist (protecting layer on the glass substrate) is striped with acetone and piranha.

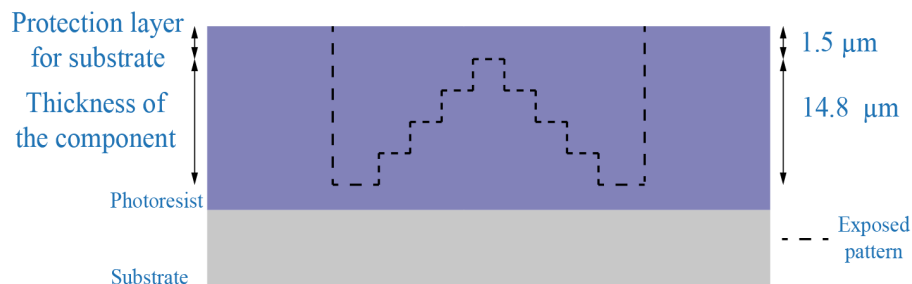


Figure 3.30: Schema of diffractive structure patterned in photoresist with vertical dimensions of design and protection layer.

#### 3.4.1.1/ FABRICATION PROCESS

Fabrication process of considered structure follows three steps:

- Design of pattern to achieve a linear slope in conical lens. A correct distribution of layers is needed in order to achieve a linear profile of the component. The pattern is designed using the whole range of layers available (0 to 63) divided in 32 levels and taking into account a linearization allowing a redistribution of layers according to equation ???. Linearization is made to fabricate a microaxicon of  $900 \mu\text{m}$  diameter and  $14.8 \mu\text{m}$  thickness with an opening angle (angle in the base of the axicon) of  $\alpha=1.85^\circ$ .



After linearization of layer distribution in pattern design, final number of levels is reduced to 27 to avoid several subsequent layers have the same intensity level as a result of the mathematical distribution of the linearization step. Final distribution of layers is shown in table 3.9. Figure 3.31(a) corresponds to profile of the developed component after exposure at 125 mW and focus value -40 where we can appreciate the typical axicon conical surface. Lateral size of steps are  $33.3 \mu\text{m}$  which is largely superior to the minimum feature size reachable by the 10 mm focal length writing lens ( $2.5 \mu\text{m}$ ). Vertical dimensions of exposed levels is  $0.53 \mu\text{m}$ . Figure 3.31(b) is an image of the profile measured with a topography measurement system MSA-500 Micro System Analyzer of Polytec [Polytec, 2000]. In this figure, the sub-pattern division made by the conversion system, dividing the component in 3 sub-pattern lic files can be seen.

Level	Layer assigned	Level	Layer assigned	Level	Layer assigned
1	2	10	15	19	35
2	3	11	17	20	38
3	4	12	19	21	41
4	5	13	21	22	44
5	7	14	23	23	47
6	8	15	25	24	50
7	10	16	28	25	53
8	11	17	30	26	56
9	13	18	33	27	59

Table 3.9: Layers assigned during linearization process.

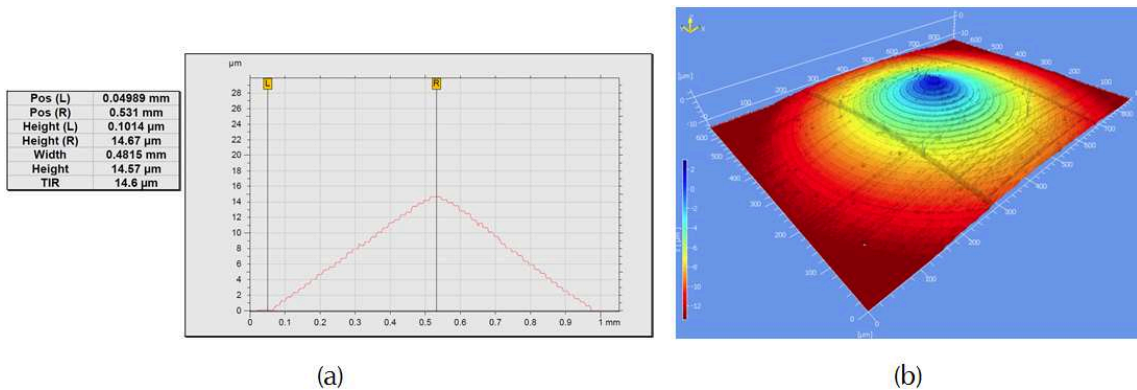


Figure 3.31: (a) Profile of component after development. (b) 3D image of developed component.

- Baking of structure. A baking step was applied to the developed component in a hotplate at  $120^\circ \text{C}$  during 5 seconds (Fig. 3.32). In this case, because of component dimensions and level width ( $16.75 \mu\text{m}$ ), only 5 seconds baking leads to a smooth profile in component surface. An opening angle  $\alpha = 1.8^\circ$  and radius of curvature of 1.5 mm in axicon apex are measured and a reduction in component thickness ( $14 \pm 1 \mu\text{m}$  variations along the substrate) is observed. This side effect of the baking process might be provoked by mechanical relaxation of photoresist and components evaporation at  $120^\circ\text{C}$ . In the baked profile, full lens area roughness values are  $R_a=19.4 \text{ nm}$  and  $R_q=25.86 \text{ nm}$ .

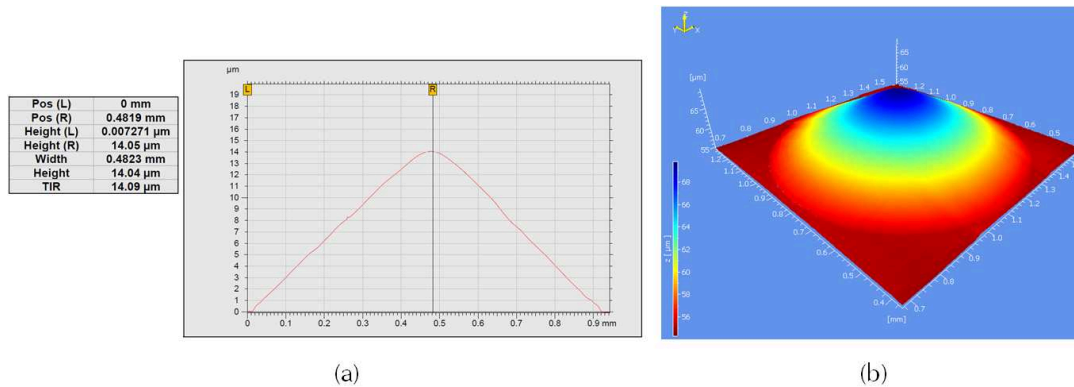


Figure 3.32: (a) Profile of component after baking at  $120^\circ\text{C}$  during 5 seconds. (b) 3D image of baked component.

- Etching of photoresist starts with a 10 minutes step to measure etching rates of photoresist and glass in order to calibrate the process. After this time, etching rates of AZ-4562 and Borofloat 33 are 0.152 and 0.055  $\mu\text{m}/\text{min}$  respectively. As 15,62  $\mu\text{m}$  photoresist have to be etched (14.04 + 1.58  $\mu\text{m}$  layer under the pattern), complete process is 102 minutes long. Nevertheless, after this time, components are not completely transferred into glass substrate. A decrease of etching rates is registered to 0.118 and 0.029  $\mu\text{m}/\text{min}$  in photoresist and glass. Reactive ion etching at low temperature increases the dry etch resistance of organic materials like employed photoresist [Tachi et al., 1988] which is also enhanced by material re-deposited during the process [MicroChemicals, 2013b].

Whole components are finally transferred into the substrate after 150 minutes (Fig. 3.33). The sag is now measured equal to  $3.70 \pm 0.16 \mu\text{m}$ , along with a radius of curvature  $R_c$  of 10,87 mm and an opening angle  $\alpha$  of  $0,47^\circ$ . This long etching process has serious effects on etched components surface, increasing roughness values ( $R_q = 117 \text{ nm}$ ). This effect, bound to process nature, constitutes a limitation in the fabrication of microoptical components by long etching of thick photoresist layer and it has to be taken into account.

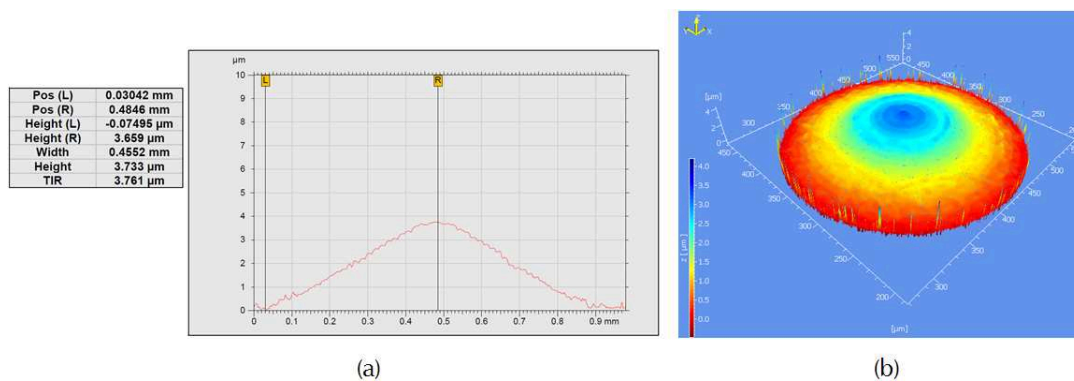


Figure 3.33: (a) Profile of component after etching process. (b) 3D image of etched component.

### 3.4.2/ OPTICAL PERFORMANCE OF GLASS-BASED MICROAXICONS

A schema of the Bessel beam created by an axicon is shown in figure 3.34. When illuminated, the axicon produces a beam for which two zones can be distinguished in the propagation. First one, from A to B, is where all refracted beams coexists. Spatial distribution of the light corresponds to interferences superimposition between all deviated beam and diffraction on the conical vertex (diffraction free beam). Transverse distribution of the resulting field follows a Bessel function [Herman et al., 1991].

In the second zone (beyond B) all deviated beams separate (in geometrical approximation) and a hole appears in the center of the beam (hollow beams). The advantages compared to hollow Laguerre-Gaussian modes are that the phase matches the one of the incident beam, which is zero in case of a collimated beam and that ratio between radius and thickness of the hollow beam can be controlled since both quantities vary differently with  $z$  [Dépret et al., 2002] (hollow beam radius depends on axicon deviation angle ( $\beta$ ) and distance whereas thickness ( $\delta$ ) depends on incident beam radius).

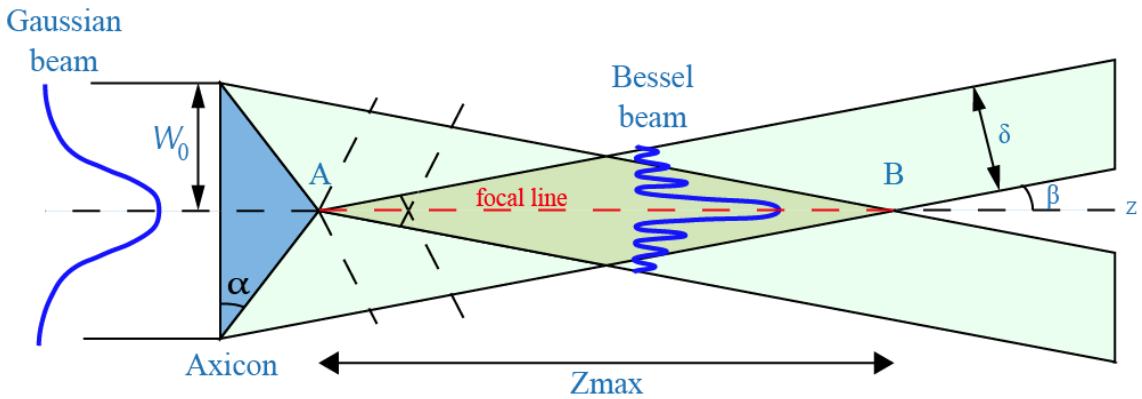


Figure 3.34: Schema of Bessel beam formation behind an axicon.

The incident collimated beam propagating along the  $z$ -axis and centered onto the axicon is deviated with an angle  $\beta$  determined by the opening angle of the cone:

$$\beta = (n - 1)\alpha \quad (3.12)$$

where  $n$  is the axicon material refractive index and  $\alpha$  is the axicon opening angle. Thus,  $Z_{max}$  can be approximated to [McGloin et al., 2005]:

$$Z_{max} \approx \frac{W_0}{\beta} \quad (3.13)$$

Where  $W_0$  is the beam-waist. In our case, with structures of 1 mm diameter and opening angles of  $\alpha \approx 0.5^\circ$ ,  $Z_{max} = 13$  cm, which is not easy to qualify.

In practical realizations, to control waist location and size, a convergent lens is then placed in front of the axicon lens to "compress" the propagation distance. In figure 3.35,

a schema of the propagation of a collimated beam through a convergent lens followed by an axicon, in the geometrical approximation, is shown.

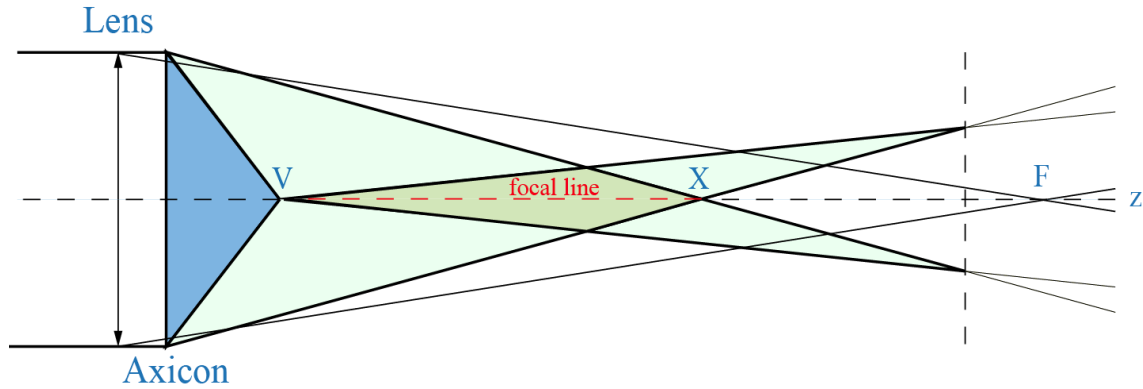


Figure 3.35: Schema of a Bessel beam formation behind an axicon.

Point  $V$  corresponds to the axicon vertex with non-diffracting propagation distance between  $V$  and  $X$ .  $F$  represents the lens focal length.

Intensity distribution of incident collimated beam can be simulated in paraxial conditions after the doublet formed by lens and axicon. Field amplitude distribution after the lens is given by the usual Fresnel approximation to the Kirchhoff integral:

$$I(r, z) = \left| \frac{2\pi}{\lambda z} \int \tau_L(\rho) E_{in}(\rho) \exp\left\{i\pi\rho^2 \left(\frac{1}{\lambda} - \frac{1}{z}\right)\right\} J_0\left(\frac{2\pi}{\lambda z} r\rho\right) \rho d\rho \right|^2 \quad (3.14)$$

where transmittance of the lens is included as:

$$\tau_L(\rho) = \exp\left(-i\frac{k\rho^2}{2f}\right) \quad (3.15)$$

Based on this formula, it is possible to simulate the Gaussian beam propagation if it is only focused by the converging lens ( $\tau(\rho) = 1$  in eq. 3.14). Considering  $W_0=1$  mm,  $\lambda=632.8$  nm and focal length of the lens  $f=20$  mm, the normalized (between transverse planes) Gaussian beam distribution is shown in figure 3.36(a); and the on-axis distribution on figure 3.36(b).

It can be appreciated that beam is indeed converging to  $z=20$  mm, corresponding to the lens focal length since the incident beam is collimated. When a perfect conical lens is added after the lens, transmittance in equation 3.15 becomes:

$$\tau_{ax}(\rho) = \exp(ik(n-1)\rho \tan(\alpha)) \quad (3.16)$$

In this case, the refractive index of Borosilicate glass at  $\lambda=632.8$  nm is  $n=1.4699$ . For an opening angle  $\alpha=0.5^\circ$ , beam propagation is shown in figure 3.37(1). The two previously discussed zones are clearly observable. First one where interferences occur until a distance close to 19 mm, and second one where beams are separated, thus generating

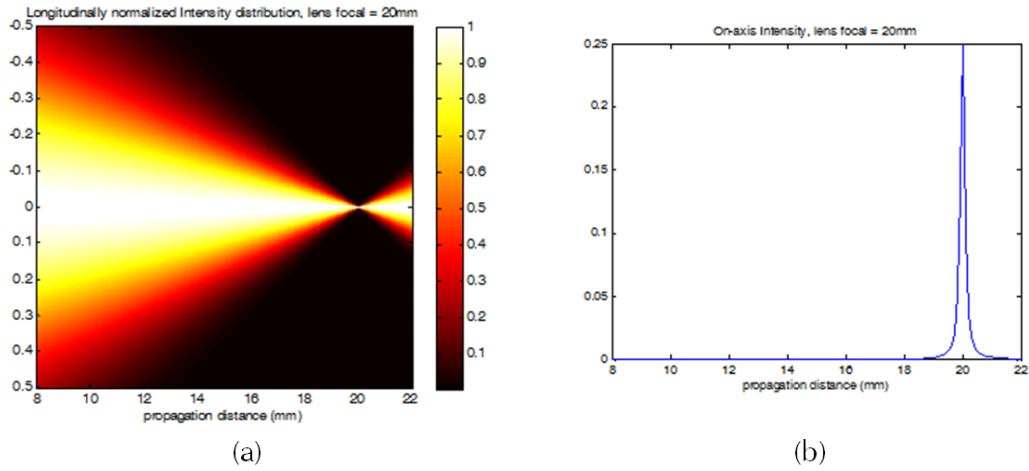


Figure 3.36: (a) Normalized Gaussian beam distribution of 20 mm focal length lens. (b) On-axis intensity.

the hollow beam.

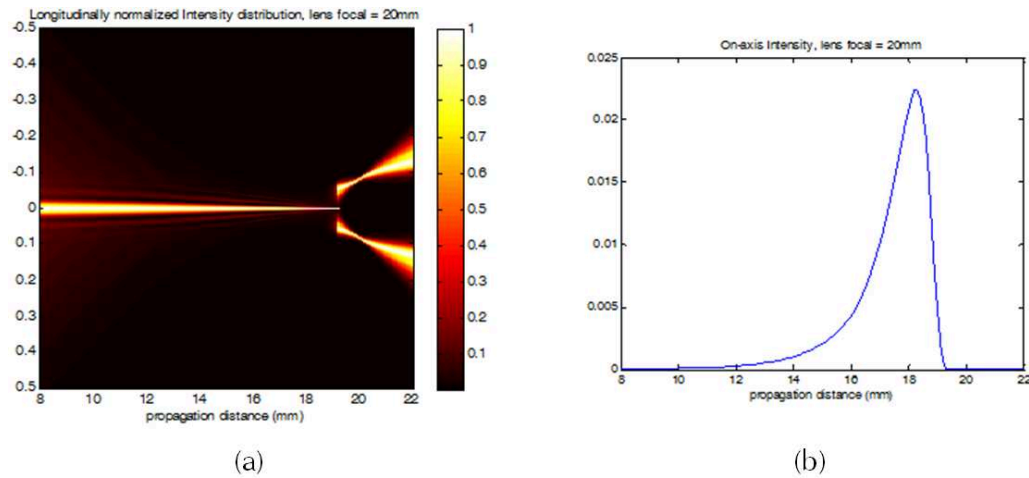


Figure 3.37: (a) Normalized Gaussian beam distribution of same lens with and a perfect axicon of  $\alpha = 0.5^\circ$ . (b) Corresponding on-axis intensity.

It can be noticed that, compared to previous case, maximum on-axis intensity distribution is not placed within the lens focal plane and that the axicon is responsible for a significant longitudinal spread of the on-axis intensity.

In practice, and depending on the fabrication process, the axicon apex is not perfect (sharp) and its bluntness has to be taken into account by introducing an hyperbolic correction to the conical lens shape [Dépret et al., 2002] (Fig. 3.38). Radius of curvature  $R_c$  is introduced so lens thickness  $e_r$  is:

$$e(r) = e_0 - R_c \tan^2(\alpha) \sqrt{1 + \frac{r^2}{R_c^2 \tan^2(\alpha)}} \quad (3.17)$$

where  $e_0$  corresponds to lens thickness for  $R_c=0$  (when vertex is a point).

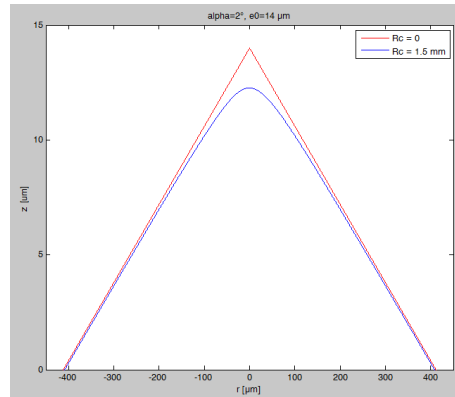


Figure 3.38: Shape of axicons with radius of curvature 0 and 1.5 mm.

In next figure, same beam propagation after an axicon with radius of curvature  $R_c=20$  mm is shown. Two main contributions of vertex bluntness are visible: first, Bessel beam generation is less efficient for short propagation distances and field in the center of the hollow beam does not finally disappear after the focal plane., although this contribution affect mostly zones outside the focal volume.

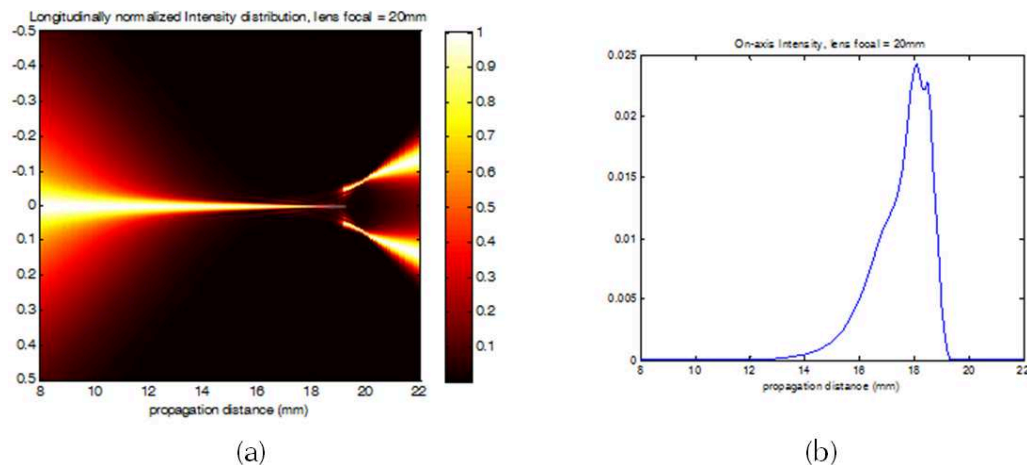


Figure 3.39: (a) Normalized beam distribution with non-perfect axicon ( $\alpha=0.5^\circ$ ,  $R_c=20$ mm). (b) On-axis intensity.

When axicon vertex is deviated from the ideal sharp form in the range of some millimeters, the generated beam does not feature the invariant Bessel beam properties. If the radius of curvature achieves a high value, significant intensity oscillations occur because of the interference between Bessel beams formed by the off-axis part of the conical lens and beams refracted by the bluntness vertex of the axicon [Brzobohatý et al., 2008], behaving as an additional lens.

In order to observe the intensity distribution of fabricated micro axicons, a system (Fig.

3.40) based on the measurement of the 3D intensity point spread function (IPSF) is used [Baranski et al., 2014]. The analyzed transmission is imaged thanks to a microscope objective and a standard camera and reconstructed electronically to observe the whole distribution of the focal volume.

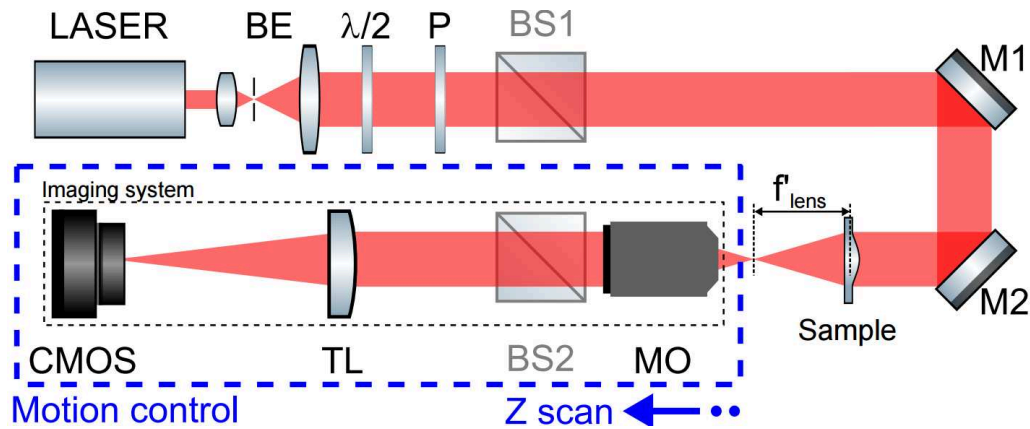


Figure 3.40: Schema of the characterization system. Source: [Baranski et al., 2014]

In the characterization process, a plano-convex lens of focal length = 25.4 mm (Back Focal Plane, BFP = 33.8 mm) has been used to record most of the interesting beam evolution since the motors of the characterization system are limited to 25 mm travel. An aperture stop of 1 mm diameter has also been placed before the lens in order avoid contributions from adjacent fabricated axicons (Fig. 3.41). An He-Ne laser of 632.8 nm has been employed in the characterization tasks which is collimated thanks to the beam expander.

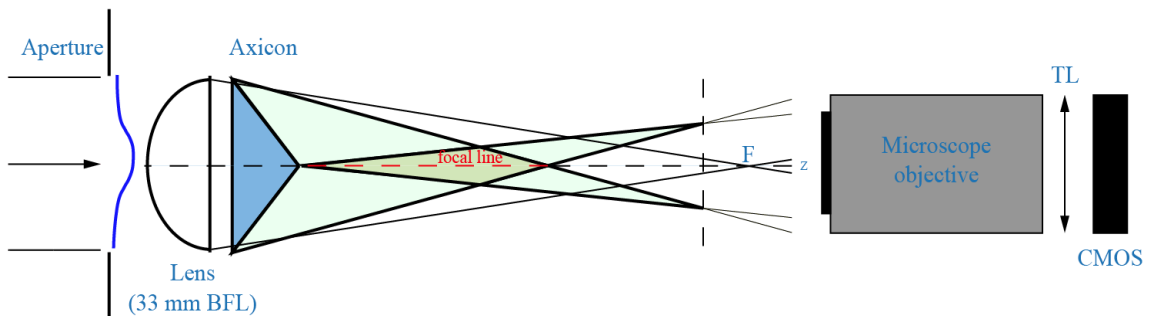


Figure 3.41: Schema of characterization system.

In figures 3.42(a) and 3.42(b) the longitudinally normalized and on-axis intensities of the 25 mm focal length lens are displayed. These figures have been obtained with the characterization system.



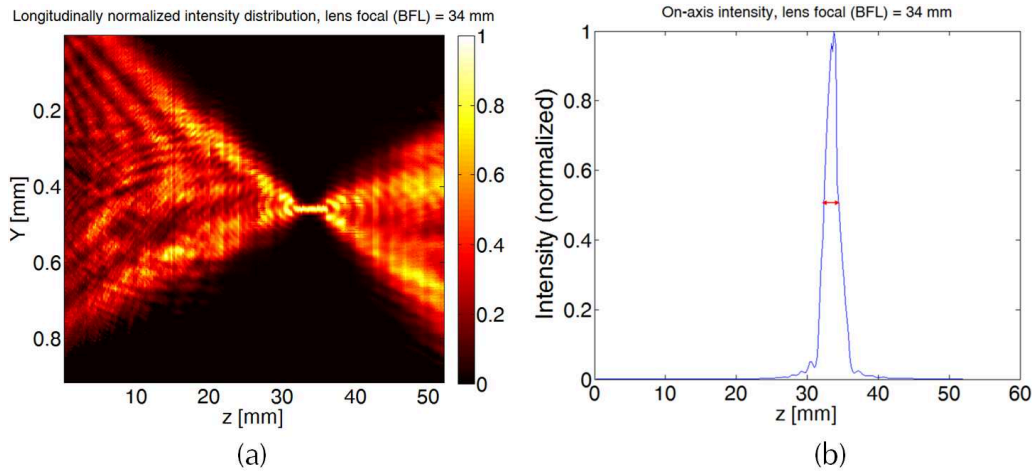


Figure 3.42: (a) Experimental normalized Gaussian beam distribution with a 25.4 mm focal length lens (33.8 mm BFP). (b) On-axis intensity.

It can be noticed that maximum intensity on-axis value corresponds to the back focal plane length of employed lens at a value of 33.8 mm. Hence, when the fabricated axicon is introduced behind the lens, beam distribution evolves according to equations 3.14 and 3.16 (Figs. 3.43(a) and 3.43(b)). Beam shaping can be clearly seen, with an extended on-axis distribution of the energy, agreeing the theory. As theory also predicted, maximum on-axis intensity value does not correspond to lens focal length anymore. In this case, maximum value is placed at 23.6 mm and a certain spread on the maximum intensity is appreciated. This spreading effect is due to the round tip of the fabricated axicons, which modifies the efficiency of the generated Bessel beam at short propagation distances.

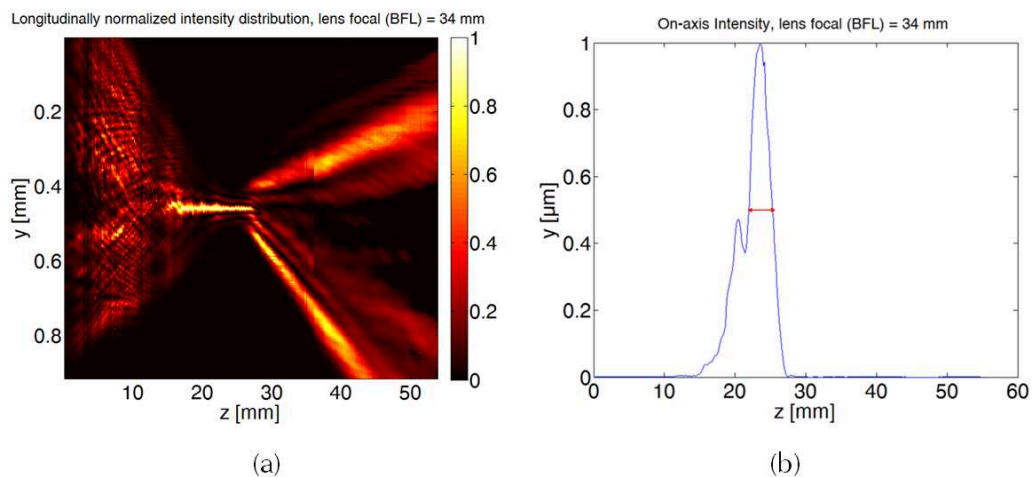


Figure 3.43: (a) Normalized beam distribution with axicon.  $R_c=10.87$  mm,  $e_0=3.77$   $\mu\text{m}$ ,  $\alpha=0.47^\circ$ . (b) On-axis intensity.

According to literature, the intensity profile of generated Bessel beam does not change as the beam propagates along the z-axis [McGloin et al., 2005] until the refracted beams separate (in X or B). However, because of imperfections on the axicon tip, resulting



distribution is influenced by part of the beam propagating close to the optical axis. These waves interfere with the Bessel beam generated behind the axicon. The axial component of the nearly-spherical wave vector resulting from the tip is equal to  $k$  on the optical axis and equal to  $k_z = k \cos \alpha_0$  on the Bessel beam. Thus, these two waves propagate with different wave vector creating a periodic modulation of the axial beam distribution with a period of  $\lambda/(1 - \cos(\alpha_0))$  [Brzobohatý et al., 2008]. Influence of this modulation decreases at axial positions far from the component because of the decreasing influence of the nearly spherical wave.

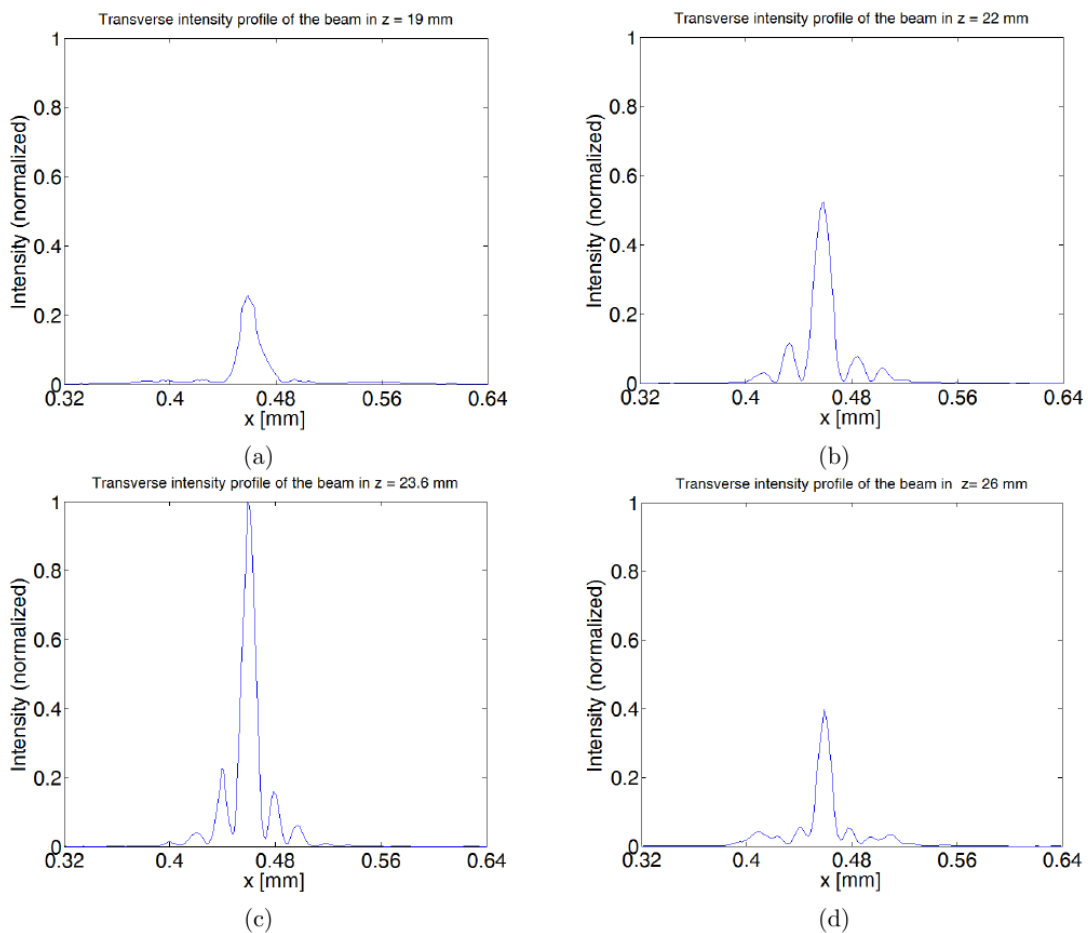


Figure 3.44: Transverse intensity distributions at (a)  $z = 19$  mm., (b)  $z = 22$  mm., (c)  $z = 23.6$  mm. (maximum on-axis intensity) and (d)  $z = 26$  mm.

After intensity reaches its maximum value, formation of hollow beams beyond  $Z_{max}$  is also observed (Fig. 3.45). Dark hollow beams (DHB) are used as optics pipes, optical tweezers and spanners, and become a powerful tool in manipulation and control of microscopic particles (micrometer-sized particles, biological cells) [Berry et al., 2007].

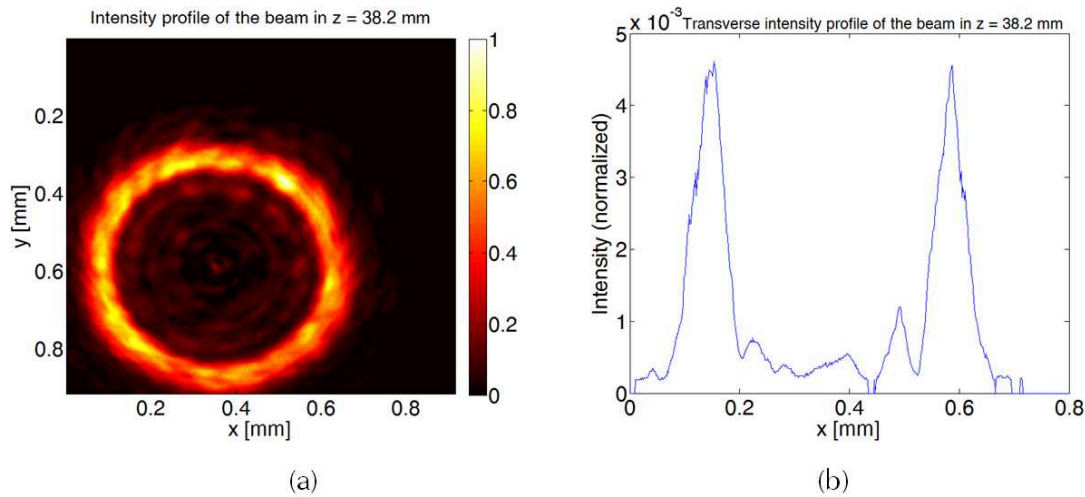


Figure 3.45: (a) Radial intensity distribution of dark hollow beam.  $z=38.2$  mm (b) Transverse intensity distribution.

Consequently, fabricated glass-based axicons following the gray-scale lithography fabrication process fulfill the characteristics of axicons with a certain bluntness onto its tip. Typical focus point of a plano-convex lens is transformed into a focus line followed by hollow beam generation. Beam distribution is affected by the bluntness of axicon tip, as a result of the fabrication process. Optical properties of fabricated lens can be applied in fields where long focus lines are needed as optical tomography or manipulation of nano-meter sized particles with the generated dark hollow beam.

### 3.4.3/ OPTICAL PERFORMANCE OF PHOTORESIST AXICONS

Compared to glass-based optical components, components made directly in resist have clear disadvantages like less resistance in harsh environments, easily subject to physical damage and have a limited useful temperature range. This is the main reason most of them are then etched into glass or semiconductor substrate using dry etching techniques [Zappe, 2013]. But photoresist components are also employed, e.g. as optical waveguides [Shew et al., 2005]. Reflow processes are also widely studied [Popovic et al., 1988, Daly et al., 1990] to generate, e.g. spherical microlenses employed as optical imagers [Badar, 2012] or optical coupling on communication systems [Shyu et al., 2007]. In here, resist based microaxicons are then considered since they provide steeper faces and thus higher opening angles  $\alpha$ . The following characterization shows how a better selectivity between glass and resist could provide steeper axicons.

As in previous case, a plano-convex lens is employed to the beam shaping in the range of the measurement system. In figure 3.46(a), Bessel beam generation can be clearly appreciated. With a rather long focus line (11 mm). Indeed, when the axicon is placed in the system, maximum on-axis intensity is reached at 17.8 mm, after oscillations attributed to the radius of curvature in axicon vertex (Fig. 3.46(b)).

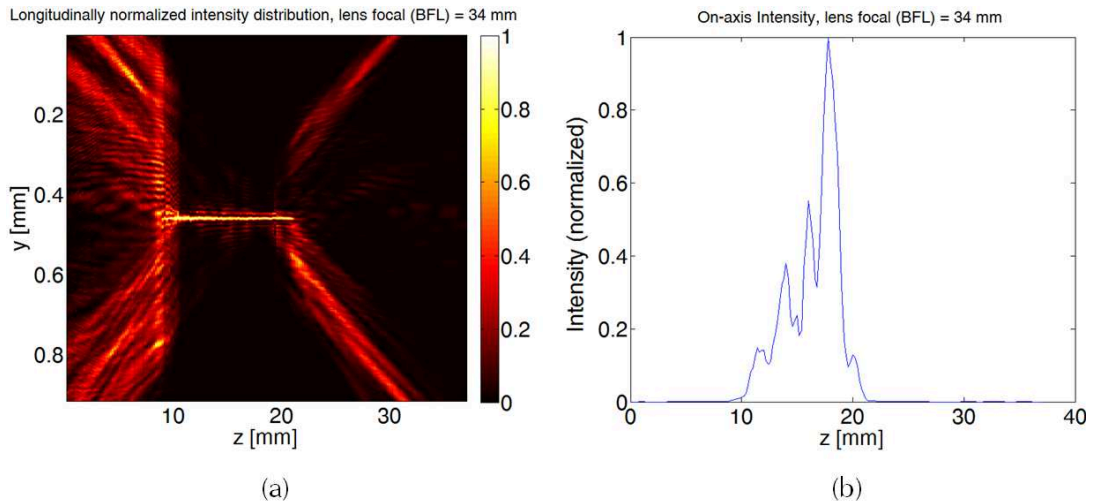


Figure 3.46: (a) Normalized beam distribution with axicon.  $R_c=1.5$  mm,  $e_0=14.04$   $\mu\text{m}$ ,  $\alpha=1.79^\circ$ . (b) On-axis intensity.

After the maximum, hollow beam generation is demonstrated (Fig. 3.47).

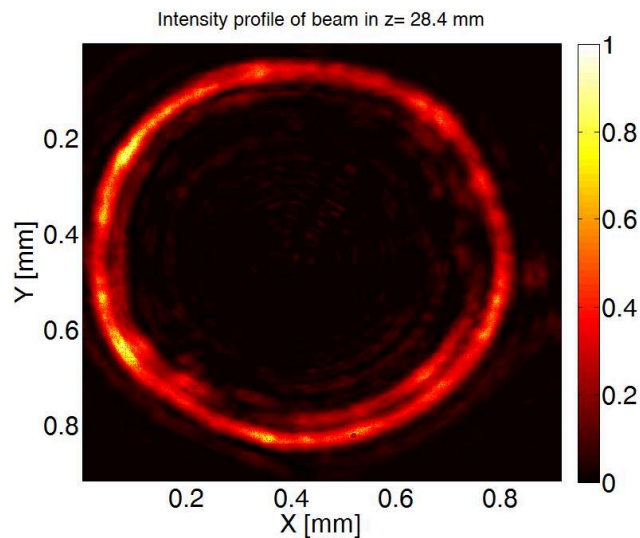


Figure 3.47: Radial intensity distribution of dark hollow beam.  $z=28.4$  mm

### 3.5/ CONCLUSIONS AND PERSPECTIVES OF CHAPTER 3

In this chapter, characterization and fabrication results of glass-based microoptical components by gray-scale lithography process have been presented. Development of the process made with the writing system DWL200 has been extensively presented. In this frame, several issues, such as correction of photoresist layer position have been solved whereas photoresist rest and baking (for solvent evaporation and rehydration), have been optimized. Seek for high thickness photoresist layer and deep exposure led to the development of a double exposure protocols, achieving depths as high as 16  $\mu\text{m}$ .

Development conditions were as well optimized in terms of duration. Finally, structures in resist were transferred into glass with optimized recipes.

In order to probe the efficiency of the system as a flexible tool for microoptical components generation at wafer-level, glass-based microaxicons have been fabricated. This optical component, of great interest in applications like coherence tomography or metrology, generates a long and narrow focal line rather than a point followed by hollow beams generation which are employed like optical tweezers in particles manipulation. Nevertheless, it is challenging to fabricate it at wafer-level e.g. by usual reflow techniques.

In this chapter axicons, first in photoresist, and, after etching, in glass, have been successfully fabricated. In both cases Bessel beam generation is demonstrated. The on-axis intensity profile shows a maximum value displaced from the original position with only a plano-convex lens and a longitudinal spread of the intensity distribution in the optical axis, as theory predict, is observed. Hollow beam generation is also observed. The efficiency of the Bessel beam formation is reduced at short propagation distances because of the radius of curvature in the vertex. With this practical example we confirm the use of gray-scale lithography process as a valuable method for the fabrication of glass-based refractive microoptical components. The considered component, typically fabricated by diamond turning or grinding and polishing, can be then generated by this approach for the direct generation of the refractive profile.

This is just an example of the possibilities of the gray-scale lithography approach for the generation of optical components with profiles out of the standards that are more challenging to be fabricated with other techniques.

Main drawback of the analyzed fabrication process can be the possible variations of etching rates during the pattern transferring into glass substrate if preparation of photoresist or chamber conditions are not well controlled. This could lead to variations in selectivity of the process and, then, unexpected results in vertical dimensions of final components. The scanning nature of the writing technology can also be considered as a disadvantage, overall when the writing lens of 4 mm focal length is employed for which writing times are increased by a factor between 5 and 6 (3 hours for a whole 4 inches wafer) compared to working with the 10 mm focal length one. Time consuming leads to a low efficiency of the considered technique for mass-production. If parallel generation of microoptical components is required, other techniques must be considered.

In this context, the second fabrication approach is studied for the parallel generation of elements with a versatile profile. Like in the case of grey-scale lithography, it can also be considered a direct fabrication technique with the advantage of no fabrication step applied directly on the refractive surface of the components, which reduce the roughness of the generated microlens.

# 4

## FUNDAMENTALS OF GLASS-REFLOW PROCESSES

In pursuit of fabrication technologies able to provide continuous surface relief structures made of glass, laser lithography has proved to be competitive thanks to its versatility. Nevertheless, it remains direct writing whose associated time of process leads more likely to prototyping than larger production (unless it is used for master piece generation able to replicate the structure into glass).

In the following, we aim at the development of a more collective technology dedicated to glass continuous surface structure which is initiated from binary lithography. It subsequently involves glass reflow processes.

Main idea relies on sealing a cavity formed by the assembly of two wafers, one of them structured in silicon and the other one in glass. Annealing at high temperatures produces a variation in glass viscosity so glass surface changes towards or outward the cavity as a function of the pressure of gass trapped in cavities. The control of this deformation allows generating the microcomponent refractive surface. One advantage of this method is the very low surface roughness of components obtained thanks to the contactless nature of the process. In addition, compatibility of employed materials, glass and silicon, with integration processes of MOEMS makes it interesting for numerous applications.

Chapter 4 is then dedicated to the fundamentals of reflow process fabrication techniques. It includes background information that is necessary to understand the results presented in the next chapter. First section is dedicated to the fundamentals of glass reflow processing, regarding properties of glass as an amorphous solid and physical properties of glass materials as a function of their chemical composition. Special focus is made in Borofloat 33 glass substrate, as it is the one employed in this thesis work. Thermal generation of stress in glass materials and annealing process to release them are also considered. Section 4.2 concerns the state of the art of the fabrication of glass-based optical components through glass reflow and blowing processes. During the last 10 years, glass blowing through reflow has been the inner work of several research groups and fabrication of spherical vapor cells, microlenses or spherical shell resonators have been successfully fabricated. In this thesis, the fabrication of refractive glass based microaxicons at wafer-level using glass reflow processes is demonstrated for the first time. This process is based in standard lithography techniques which constitutes a

cheaper and less complex alternative to the traditional axicon fabrication methods like glass polishing and grinding.

#### 4.1/ FUNDAMENTALS OF GLASS PROCESSING AND INDUCED SURFACE DEFORMATIONS IN GLASS BOROFLOAT 33

Glass is a non-crystalline amorphous solid resulting of the fusion of a material cooled from the liquid state to that of a solid form without crystallization. Scientifically, the term *glass* is defined in a broader sense, including every solid with a non crystalline (thus, amorphous) structure at atomic scale and that has a glass transition when heated towards the liquid state. The absence of crystalline structure in glasses means there is a lack in 3D structure symmetry and periodicity (no repeating large scale structures) with same properties in all directions (isotropic) [Brow, 2004].

The formation of glass state can be described as a function of specific volume (volume occupied by unit mass of a material, reciprocal to material density) and temperature according to figure 4.1. The specific volume of a glass material decreases as it is cooled down. The difference between crystal and glass concerns cooling speed. If cooling rate is slow enough, periodic arrangement of glass network occurs, forming periodic structures. At melting point,  $T_M$ , there is a fast decrease of specific volume (crystallization) followed by a contraction of the solid when temperature decreases. In case of glasses, cooling rate is higher than the nucleation rate so the liquid is cooled down to the melting point without molecular arrangement which causes crystallization. There is no abrupt decrease of specific volume as in the case of crystal formation. As cooling process continues, specific volume deviates from the equilibrium line, reaching its final value as a function of the cooling rate.

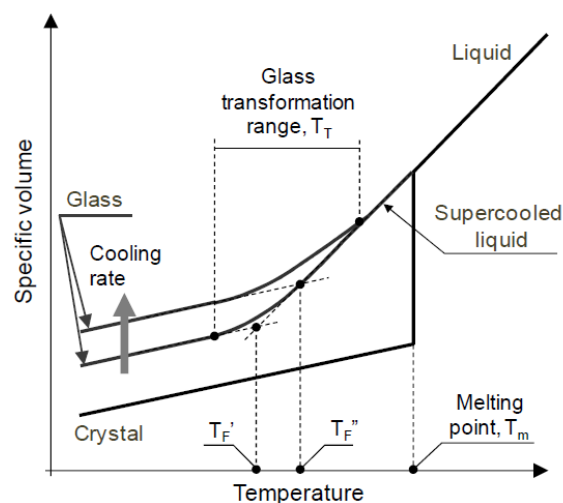


Figure 4.1: Specific volume vs temperature during the state transformation of glass. Source: [Włodarczyk, 2011]

The region of the graphic where specific volume has no linear behavior is called glass transformation range ( $T_T$ ) and is cooling rate dependent. It also represents the transition in amorphous materials from a hard and relatively glassy molten state as the temperature increases [Ehrenstein et al., 2012]. Fictive temperature of glass,  $T_F$  is the point where extrapolated lines of glass and liquid intersect. This temperature depends on the cooling rate and it is higher when glass is cooled faster. It has an influence on physical properties of glass like refractive index or thermal stress resistance. Thus, after heating the glass over the melting point, we can control the cooling rate to fix the fictive temperature and lead the glass to a defined state to adequate its properties according to the fabrication process and desired properties of the optical components.

#### 4.1.1/ CHEMICAL COMPOSITION OF GLASSES

Silica ( $\text{SiO}_2$ ) is the fundamental component of glass. In nature, it is commonly found as quartz sand. Vitrification of quartz occurs when a lightning strikes on sand, forming hollow, branching rootlike structures called fulgurite. Fused quartz is made from chemically pure silica and has the highest melting point ( $1723^\circ\text{C}$ ), smallest thermal expansion and good chemical durability. By adding other components to pure fused silica, it is possible to produce glasses with different optical, thermal and mechanical properties.

As a function of its components, glasses can be classified in four major groups:

- Fused silica, also called vitreous silica glass. Is silica ( $\text{SiO}_2$ ) in vitreous glass form (without crystalline structure). It has a very high melting temperature and high viscosity ( $\eta \sim 10^6 \text{ Pa}\cdot\text{s}$ ) [Bacon et al., 1959] so is difficult to produce by conventional glass-melting processes.
- Soda-lime glass. Its components are mainly silica (72 - 80 %), sodium oxide ( $\text{Na}_2\text{O}$ , 12 - 16 %), lime ( $\text{CaO}$ , 5 - 11 %), magnesia ( $\text{MgO}$ , 2.5 %) and alumina ( $\text{Al}_2\text{O}_3$ , 0.6 %). This kind of glass is most suitable for window or bottles and low temperature incandescent light bulbs. It has a high thermal expansion and transmission in the visible spectrum. However it shows low durability and poor resistance to heat ( $500 - 600^\circ\text{C}$ ). Is also employed for photomasks generation in optical lithography.
- Sodium borosilicate glass. Composed principally by silica (81 %), boron trioxide ( $\text{B}_2\text{O}_3$ , 4.5 %) and aluminum oxide ( $\text{Al}_2\text{O}_3$ , 2 %) and small amounts of alkalis like sodium and potassium oxides. They have low coefficients of thermal expansion ( $3.25 \cdot 10^{-6} \text{ K}^{-1}$ ) [Schott, 2016a] as compared to  $9.1 \cdot 10^{-6} \text{ K}^{-1}$  for typical soda lime glass [Schoot., 2014], making them more dimensionally stable. The low alkali content and coefficient of thermal expansion (CTE) make them have a good chemical durability and thermal shock resistance and particularly compatible for bonding to silicon. In table 3.7, composition of borosilicate glass Borofloat33 of Schott is presented.
- Lead-oxide glass. Main components of this type of glass are pure silica (30 - 60 %), and lead oxide ( $\text{PbO}$ , 20 - 65 %) along with potassium oxide ( $\text{K}_2\text{O}$ , 12 %), soda ( $\text{Na}_2\text{O}$ , 2 %), zinc oxide ( $\text{ZnO}$ , 1.5 %) and alumina (0.4 %). Because of its high density (resulting in a high electron density) they have a high refractive index (more brilliant). They are



used in art, electronics for glass to metal seals and optics for production of lenses and optical fibers. Its ability to absorb gamma frequencies make them suitable for radiation shielding.

#### 4.1.2/ PHYSICAL PROPERTIES OF GLASS

Here, a quick review of some important physical properties concerning glass reflow processes are presented.

##### 4.1.2.1/ THERMAL PROPERTIES

- Thermal conductivity,  $\lambda$ . Represents the ability of a material to transfer heat (Eq. 4.1). Thermal conductivity of glasses is lower compared to crystals because of the irregular arrangement inside the material.

$$\lambda = \frac{1}{A} \cdot \frac{dQ}{dt} \cdot \frac{dT}{dx} \quad (4.1)$$

$dQ/dt$  represents heat flux,  $A$ , area and  $dT/dx$ , temperature gradient over the material. Thermal conductivity of Borofloat 33 can be described using a linear equation from 20 to 160°C:

- Linear coefficient of thermal expansion,  $CTE$ . It represents the response to temperature changes. Solids expand in when they are heated and contract when they are cooled. Thermal expansion originates from atoms vibration, increasing when temperature is increased. Fused silica has a very low thermal expansion coefficient. In the case of glass Borofloat33, its thermal expansion coefficient is comparable to the one of Silicon ( $2.6 \cdot 10^{-6} \text{ K}^{-1}$ ) [joffe., 2016]. This fact is very convenient, since integration processes made at high temperature like anodic bonding [Dziuban, 2007] can be practiced avoiding matching issues and mechanical stress at the interface between them. Thermal expansion coefficient is usually expressed as:

$$\beta = \frac{1}{V} \cdot \left( \frac{dV}{dT} \right)_{P=const} \quad (4.2)$$

As glass is an isotropic material,  $CTE$  coefficient is usually employed (three times smaller than  $\beta$ ). Linear expansion coefficient of glass Borofloat33 follows a linear relation with the temperature from 20 to 500°C (Fig. 4.2(b)).

- Specific heat capacity,  $C_p$ . Represents the amount of heat required ( $Q$ ) to change a unit of mass ( $m$ ) of a substance by a certain temperature interval ( $\Delta T$ ).

$$C_p = \frac{Q}{m \cdot \Delta T} \quad (4.3)$$



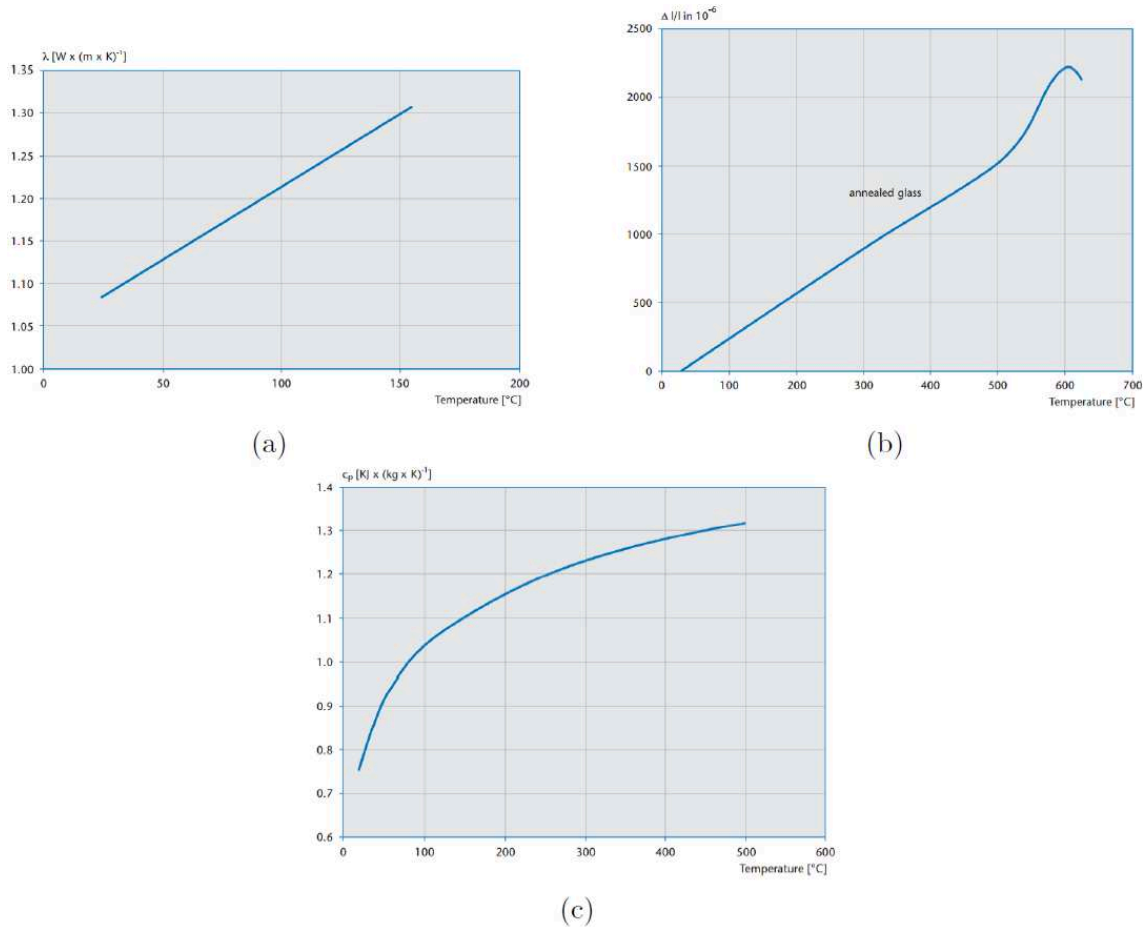


Figure 4.2: Thermal properties of glass Borofloat33 as a function of the temperature. (a) Thermal conductivity,  $\lambda$ . (b) Thermal expansion,  $CTE$ . (c) Specific heat capacity,  $C_p$ . Source: [Schott, 2016a]

In figure 4.2(c), evolution of specific heat capacity of Schott Borfloat33 glass as a function of temperature is shown.

- Internal stress  $\sigma$ . During thermal reflow of glass substrates, stress is generated in the bulk of the substrate. This magnitude can be calculated using equation [Allcock et al., 1995]:

$$\sigma = \frac{E \cdot CTE \cdot \Delta T}{1 - \nu} \quad (4.4)$$

Being  $E$ , the Young's modulus (relation between force and proportional deformation in a material),  $CTE$  the coefficient of thermal expansion,  $\Delta T$  the temperature difference and  $\nu$  the Poisson's ratio (negative ratio of transverse to axial strain). It can be appreciated from the equation that materials with a low  $CTE$  have better response to thermal shock during reflow processes.

#### 4.1.2.2/ OPTICAL PROPERTIES

- Absorption coefficient,  $\alpha$ . Already described in section 2.4.1, the absorption coefficient describes how light propagates through a material following the Lambert-Beer law (Eq. 2.3). In the visible spectrum, most glasses absorb little light, having then a high transmittance in this region. In figure 4.3(a), total optical transmittance and refractive index of glass Borofloat33 are represented as a function of wavelength and thickness of the substrate.

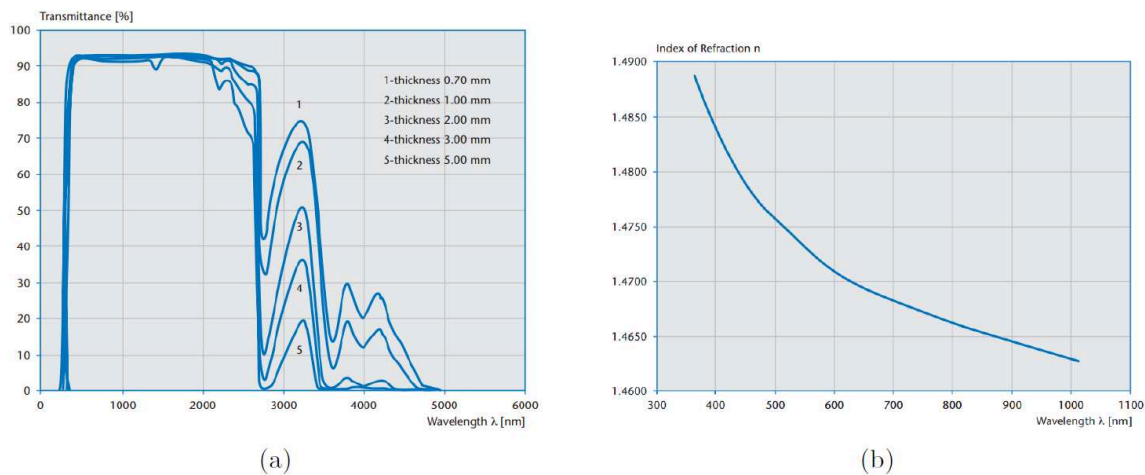


Figure 4.3: (a) Optical transmittance and (b) refractive index,  $n$  of Borofloat33 as a function of the temperature. Source: [Schott, 2016a]

#### 4.1.2.3/ MECHANICAL PROPERTIES

- Concerning reflow processes of optical glasses, viscosity is probably the most important property. Viscosity of a material corresponds to its resistance to deformation when mechanical stress is applied. It determines parameters like melting conditions, annealing or maximum working temperatures. It is a temperature dependent magnitude which can be described by the Arrhenius function  $\eta = \exp(A + B/T)$  [Hrma, 2008] where  $A$  and  $B$  are temperature independent coefficients. In 2007, a viscosity model for predicting the complete viscosity curve of glass was developed [Fluegel, 2007] using global statistical approach and composition-viscosity data for silicate glasses collected from 50 years available in *SciGlass* database [SciGlass, 2016a]. The model is based in the Vogel-Fulcher-Tamman (VTF) Equation  $\log(\eta) = A + B/(T - T_0)$  where  $T$  is temperature in Kelvin and  $A$ ,  $B$  and  $T_0$  are constants [SciGlass, 2016b]. For Borosilicate glass, values are  $A=-2.560$ ,  $B=4852$  and  $T_0=192.5^\circ\text{C}$ .

In figure 4.4 the strong dependence of viscosity and temperature can be appreciated. Values for Borofloat33 are exposed from  $10^{12}$  Pa·s under the strain point to  $10^2$  Pa·s.

In which 5 different viscosity values can be distinguished:

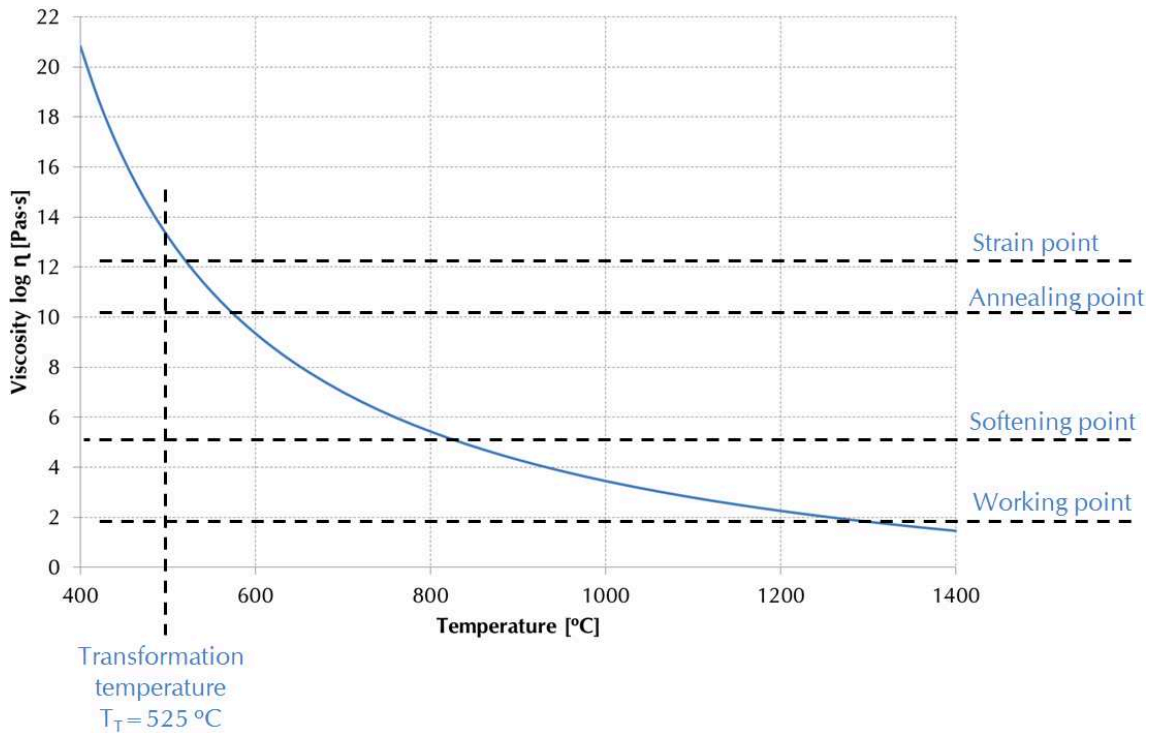


Figure 4.4: Viscosity-temperature relation in Borofloat33 glass.

- Strain point ( $518^{\circ}\text{C}$ ,  $10^{12.34}$  Pa·s). Is the highest temperature at which glass can be cooled down without inducing serious thermal stress.
- Annealing point ( $560^{\circ}\text{C}$ ,  $10^{10.64}$  Pa·s). In this point, any internal stress can be relieved in a few minutes.
- Softening point ( $820^{\circ}\text{C}$ ,  $10^{5.17}$  Pa·s). Over this point, glass is deformed under its own weight.
- Working point ( $1270^{\circ}\text{C}$ ,  $10^{1.94}$  Pa·s). At this viscosity value, glass can be shaped in a glass forming process.
- Transformation temperature ( $525^{\circ}\text{C}$ ,  $10^{1.94}$  Pa·s). Described earlier in details in section 4.1.

#### 4.1.3/ ANNEALING OF GLASS SUBSTRATE

The goal of the annealing process is to relieve the stress created by the cooling below the strain point which occurs during glass reflow processes. During the process (Fig. 4.5), glass is heated to a temperature between the strain and the annealing points (so it does not suffer any other deformation) and kept there until the entire glass bulk reaches

the equilibrium. Temperature value and time depend on the type of glass. Under the strain point temperature, the cooling rate can be increased.

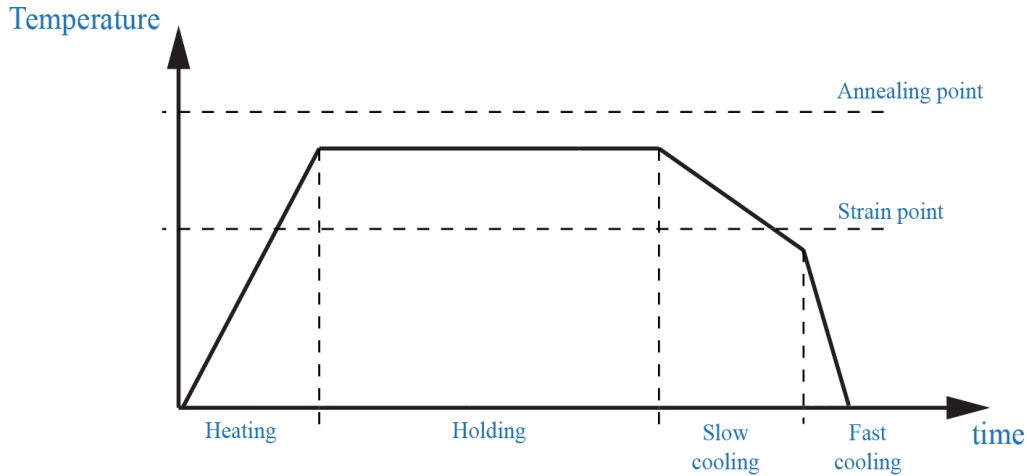


Figure 4.5: Temperature evolution during annealing process.

In table 4.1, some of the mechanical and thermal properties of glass Borofloat33 are summarized.

Density (25° C)	$\rho$	2.2 g/cm <sup>3</sup>
Young's Modulus	E	64 kN/mm <sup>2</sup>
Poisson's Ratio	$\nu$	0.2
Knoop Hardness	HK <sub>0.1/120</sub>	480
Bending strength	$\sigma$	25 MPa
CTE		$3.25 \cdot 10^{-6} \text{K}^{-1}$
Specific Heat Capacity	$C_p$	$0.83 \text{ KJ} \cdot (\text{Kg} \cdot \text{k})^{-1}$
Thermal Conductivity	$\lambda$	$1.2 \text{ W} \cdot (\text{m} \cdot \text{K})^{-1}$
Working point	$10^{1.94} \text{ Pas} \cdot \text{s}$	127° C
Softening point	$10^{5.17} \text{ Pas} \cdot \text{s}$	820° C
Annealing point	$10^{10.64} \text{ Pas} \cdot \text{s}$	560° C
Strain point	$10^{12.34} \text{ Pas} \cdot \text{s}$	518° C
Transformation temperature	$T_T$	525° C

Table 4.1: Mechanical and thermal properties of glass Borofloat33 of Schott.

## 4.2/ STATE OF THE ART OF GLASS REFLOW PROCESSES

The fabrication of microoptical components through glass-blow from silicon cavities has been considered as part of this thesis work. This technique, based on standard MEMS processing, was proposed by P. Merz in 2003 [Merz et al., 2003] under the name of Glass Flow Process (GFP). The method is based on viscous deformation of glass Borofloat33 at a temperature above the glass transition ( $T_g$ , region where materials transitions from a hard to a soft state) to fulfill a pattern structured in a silicon substrate resulting in a replication process [Albero et al., 2008, Albero et al., 2009, Albero et al., 2010] (Fig.

4.6(a)). After anodic bonding of silicon and Borofloat or Pyrex glasses under vacuum pressure, temperature and times are controlled to avoid the complete filling of the etched pattern so the fabrication of spherical microlenses can be accomplished (Fig. 4.6(b)). The contactless forming of the lenses results in a very low surface roughness.

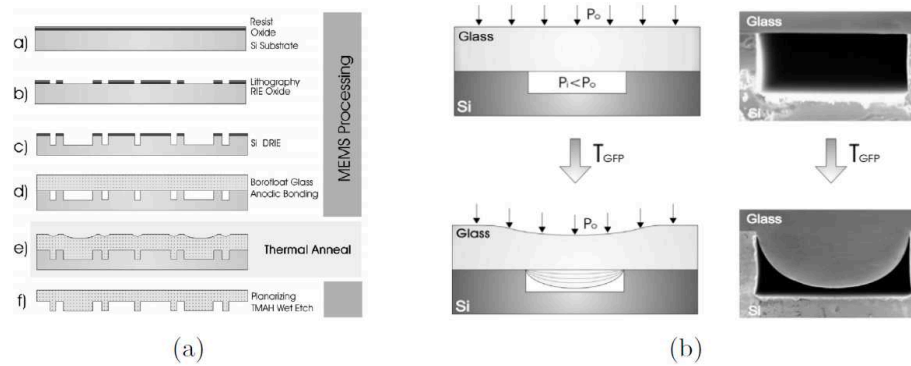


Figure 4.6: (a) MEMS based process sequence of GFP technology. (b) Contactless formation of GFP lens by viscous flow: schematic (left) and SEM cross section of  $50\ \mu\text{m}$  lens (right) before and after thermal anneal at  $720^\circ\text{C}$ . Source: [Merz et al., 2003].

By enclosing cavities at atmospheric pressure, Eklund *et al.* proposed a method for the fabrication of vapor cells by micro glass blowing of Pyrex bonded with etched silicon based on annealing processes at wafer-level [Eklund et al., 2008]. Reduction of glass viscosity during the reflow process along with temperature differences between furnace and enclosed cavities, provoke deformation outward the cavities that can be controlled (Fig. 4.7(a)). They proposed an analytical model to predict the shape of glass shells which matches the experimental data where very thin bubbles have been obtained [Eklund et al., 2007]. Best shapes were obtained for annealing processes of bonded wafers at  $850$  and  $900^\circ\text{C}$  (Fig. 4.7(b)).

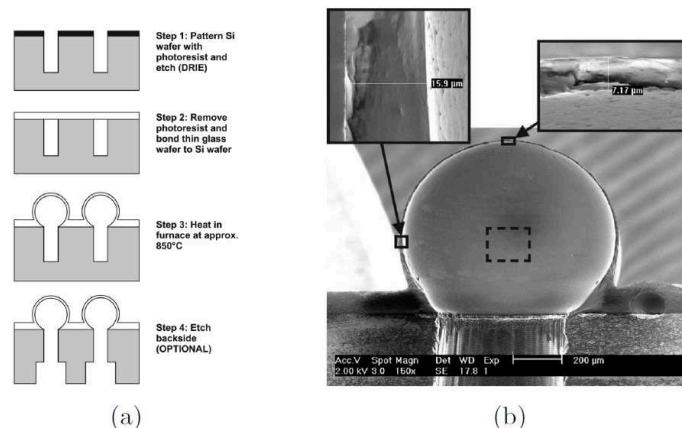


Figure 4.7: (a) Fabrication process for glass blowing on wafer level. (b) Cross section of fabricated hollow glass semisphere. Source: [Eklund et al., 2007].

In 2008, Albero *et al.* fabricated matrices of microlenses with 100% fulfill factor silicon molds double-etched anisotropically in acid solution (Fig. 4.8(a)) and bonded with

Borofloat glass (Fig. 4.8(b)) under vacuum [Albero et al., 2008]. The reflow process in this case is carried at 800°C. The desired shapes and sizes of microlenses is related to the choice of solutions, process conditions along with the quality of silicon substrates. After first etching in KOH, inverted pyramids were obtained with depth dependent on the width of the aperture of the employed mask (third stage of fabrication in figure 4.8(a)). Fabricated microlenses (Fig. 4.8(c)) have focal length from tens of microns up to few millimeters and numerical apertures (NA) from 0.02 to 0.4. One asset is to be intrinsically integrated on silicon mounts that offer high integration possibilities, making this technology very appropriate in MOEMS fabrication field.

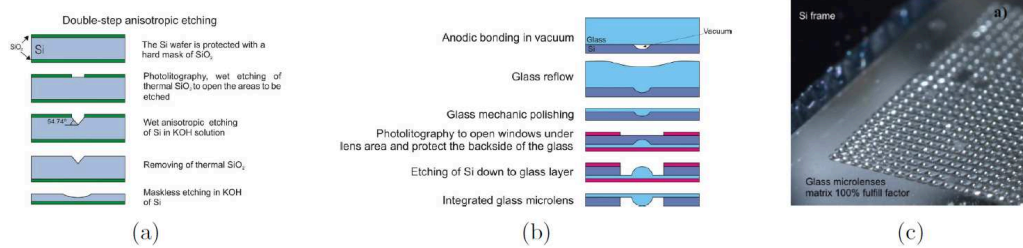


Figure 4.8: (a) Schema of the effect produced by the process of double-step anisotropic etching. (b) Fabrication process of microlenses. (c) Glass microlenses matrix with 100% fulfill factor on a Si frame. Source: [Albero et al., 2008].

P. Igor *et al.* illustrated in 2011 [Prihodko et al., 2011] a new approach for the fabrication of 3D spherical shell MEMS resonator with co-fabricated electromagnetic and electrostatic transduction (Fig. 4.9(a)). The fabrication technique uses the same approach than Eklund *et al.* to create symmetric and high aspect ratio structures in Pyrex glass with millimeter-scale diameter and average thickness of 10 μm (Fig. 4.9(b)) after reflow at 850°C. Note that their concept shows different reservoir sizes leading to different adjacent shells.

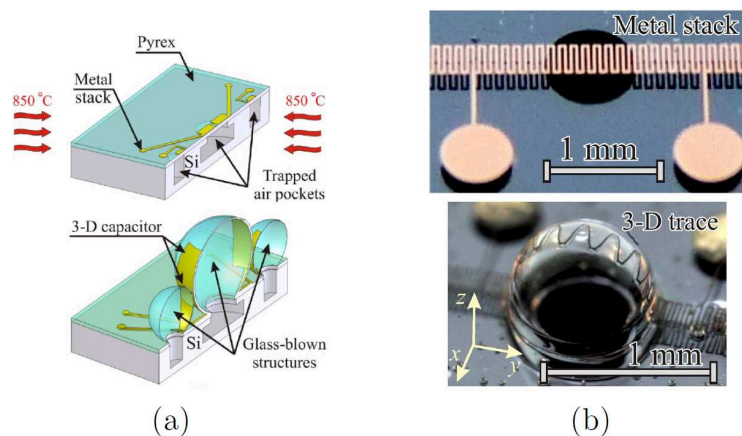


Figure 4.9: (a) Conceptual schematics of a 3D spherical shell resonator fabrication using wafer-scale metal-on-glass stack glassblowing. (b) Photographs of a continuous metal trace fabricated on a glass-blown spherical shell structure. Source: [Prihodko et al., 2011].



In 2012, shape of blown volume of borosilicate was controlled to fabricate glass packages with inclined flat optical windows for MOEMS [Stenchly et al., 2012] for its use as a pico-projector in smartphones. This process is based on a three steps anodic bonding of etched silicon and borosilicate glass (Fig. 4.10(a)). The non-centric arrangement of the silicon islands (enabling flatness of the glass covered zones) leads to an inclination of the silicon-glass stack during the blowing process at a temperature over the softening point of the glass ( $820^{\circ}\text{C}$ ). After silicon removing in KOH solution, the inclined glass substrate is released with a surface roughness of less than 1 nm (Fig. 4.10(b)).

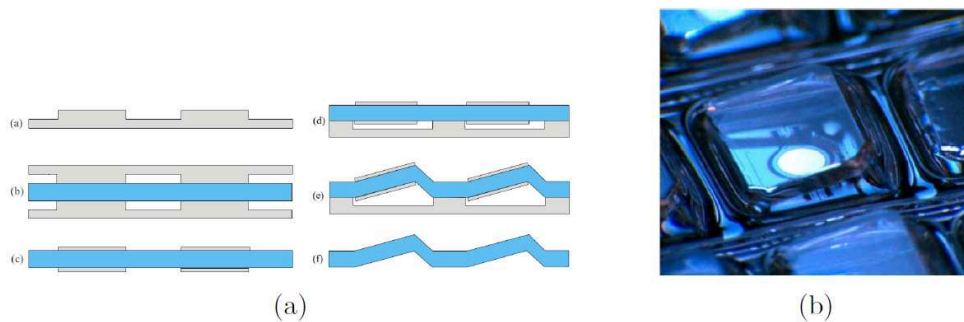


Figure 4.10: (a) Schematic of the process flow for the glass wafer. (b) A detail view of a wafer level vacuum packaged mirror with an inclined window (window size: 3mm x 4mm). Source: [Stenchly et al., 2012].

Fabricated in 2013 [Senkal et al., 2013], and characterized in 2014 [Senkal et al., 2014], D. Senkal *et al.* reported a MEMS process for the fabrication of symmetric 3D wineglass and spherical shell structures using fused quartz and ultra low expansion titania silicate glass (TSG). In this case, ring-shaped cavities (Fig. 4.11(1)) in fused quartz are used during the micro-blowing process at  $1700^{\circ}\text{C}$  with a rapid cooling at  $500^{\circ}\text{C}/\text{min}$ . With this method, TSG MEMS devices with low surface roughness (0.23 nm) and highly symmetry (radial error < 500 ppm) are achieved (Fig. 4.11(b)).

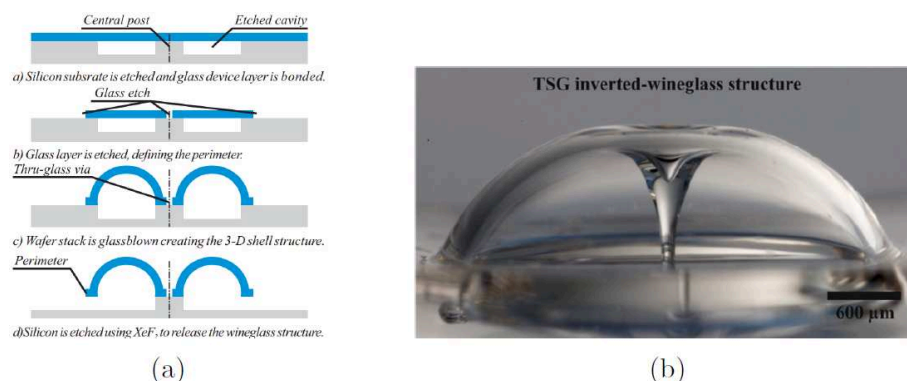


Figure 4.11: (a) Schematic of the process flow for the glass wafer. (b) Optical photograph of glassblown TSG inverted-wineglass structure. Outer diameter is 4200 m. Glassblown at  $1650^{\circ}\text{C}$ . Source: [Senkal et al., 2013].

High fill-factor arrays of millimeter-sized microlenses have been fabricated by glass-reflow

processes in [Albero et al., 2015]. Effects introduced by proximity between lenses and their positioning in a matrix are studied and solutions to main issues are proposed. The characterization is extended in order to estimate the capabilities of the fabricated lenses to provide diffraction-limited optical performance.

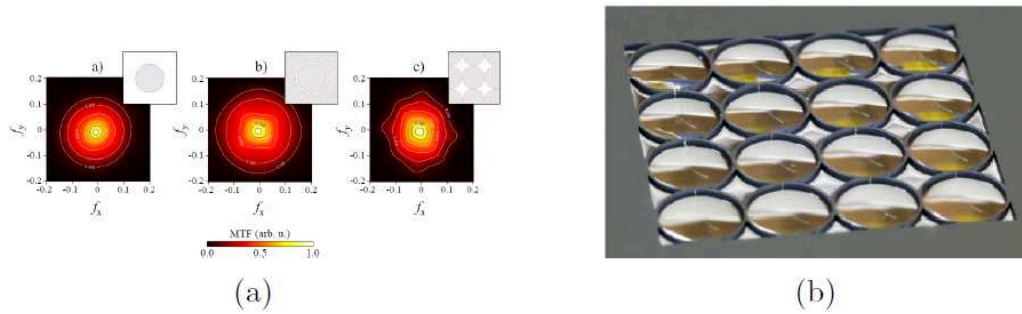


Figure 4.12: (a) Measured 2D Modulated Transfer Function (MTF) of glass millimeter-sized lenses in different situations, *a* single item, *b* square array with applied compensation strategies and *c* square array without compensation. (b) Microfabricated glass lenses. Silicon is selectively eliminated by grinding and polishing for vertical integration purposes. Source: [Albero et al., 2015].

Recently, glass reflow process has been applied in the field of optical sensing. In [Van Toan et al., 2015], Van Toan *et al.* demonstrated the fabrication of borosilicate glass capillarities based on glass reflow into nano-trench for an optical modulator. The micrometer diameter capillarities achieve high transmittance due to refractive index matching when the liquid penetrates into the etched silicon solid. To fulfill the silicon micro-cavities, the glass reflow process is performed in an atmospheric furnace at  $1000^{\circ}\text{C}$  and during 16 hours.

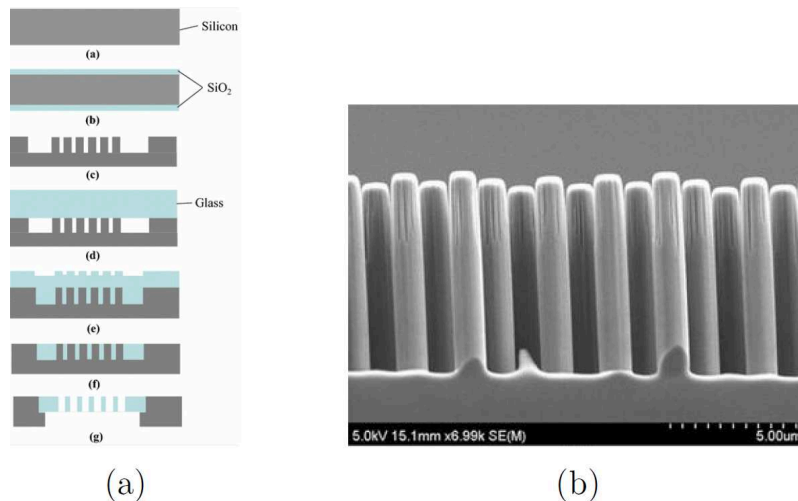


Figure 4.13: (a) Fabrication process. *a* Silicon wafer. *b* Thermal oxidation. *c* Immersion photolithography, RIE and deep RIE. *d* Anodic bonding. *e* Glass reflow process. *f* Lapping and polishing process. *g* Backside photolithography and deep RIE. (b) Cross section view of silicon pillars. Source: [Van Toan et al., 2015].



Next table is provided to summarize some important parameters found in the literature. As we can see, deformed materials in most cases are borosilicate glasses like Pyrex or Borofloat33. Their use is justified because of their compatibility with silicon and integration process of MOEMS. Considering the reflow temperature and parameter controlled in the deformation process, we can see that when deformed volume of reflowed glass must be controlled, lower temperatures are preferred in order to control the time of the reflow step and glass viscosity variations at such temperatures precisely. Control of time is less important when glass must fill the whole mold in the replication process and only pressure inside the cavities is controlled. When blowing of glass is needed, control of time is not important, as it is the equilibrium state between cavities and oven chamber which determines the evolution of the deformed surface.

Ref.	Purpose	Glass type	Reflow temperature [°C]	Control of deformation through
[Merz et al., 2003]	Replication lens (Reflow)	Borofloat33	720	Pressure
[Eklund et al., 2008]	Vapor cells (Blowing)	Pyrex	850-900	Pressure
[Albero et al., 2008]	Replication lens (Reflow)	Borofloat33	800	Pressure
[Prikhodko et al., 2011]	Spherical shell (Blowing)	Pyrex	850	Pressure
[Stenchly et al., 2012]	Packaging (Blowing)	Borosilicate	>820	Pressure
[Senkal et al., 2013]	Spherical shell (Blowing)	Fused quartz/TSG	1700	Pressure
[Albero et al., 2015]	Microlens fabric. (Reflow)	Borofloat33	560-820	Time
[Van Toan et al., 2015]	Glass capillarities (Reflow)	Borosilicate	1000	Pressure

Table 4.2: Summary of some important parameters of glass reflow fabrication.

#### 4.2.1/ CONCLUSIONS OF CHAPTER 4

In this chapter, some of the fundamentals concepts involved in the glass reflow process have been presented where viscosity appears as the most important property, since it determines the melting conditions and working temperatures.

Then, the state of the art of glass reflow process as microcomponents fabrication technique has been reported. This fabrication method is raising in interest because of the compatibility with classic MEMS fabrication techniques and low roughness of fabricated components. Convex microlenses, shell resonators or tilted mirrors are some examples of realizations based on glass reflow at high temperature. The next chapter deals with such approaches to generate continuous surface profile components.



## GLASS REFLOW PROCESSES. CHARACTERIZATIONS AND REALIZATIONS

This chapter focuses on the fabrication of microoptical components using a technique based on glass reflow process. This technique presents several advantages, such as the parallel fabrication capabilities or the high surface quality of the generated component, thanks to the non-contact nature of the process. Indeed, it does not result from a direct contact with a cutting tool (i.e. diamond turning) or a plasma (dry etching). Then, the fabrication through glass blowing constitutes an adapted process to wafer-level fabrication of continuous surface relief profile components. Its conception and vertical integration possibilities are other advantages compared to classical fabrication methods as it only involves standard MEMS fabrication equipments.

As an example of its application, once again, axicons have been attempted. The fabrication of microaxicons by glass blowing process involves the generation of concentric ring-shaped cavities etched in silicon and sealed with a glass substrate at atmospheric pressure (Fig. 5.1). The reflow process at high temperature leads to a rise in pressure within the cavities combined with a decrease of glass viscosity. This combination will create a blowing effect that modifies the upper part of the glass substrate. This effect, along with size, position and number of cavities determine the final form of the glass substrate. A complete characterization of all parameters must be done to obtain the correct lens profile that generates the desired Bessel beam.

This optical component, that generates a focus line rather than a point, is of great interest in applications like alignment and metrology or optical tomography. The generation of hollow beams carried by axicons after the interference zone where diffraction-free beams are generated is used, between others, as optical tweezers in molecular manipulation.

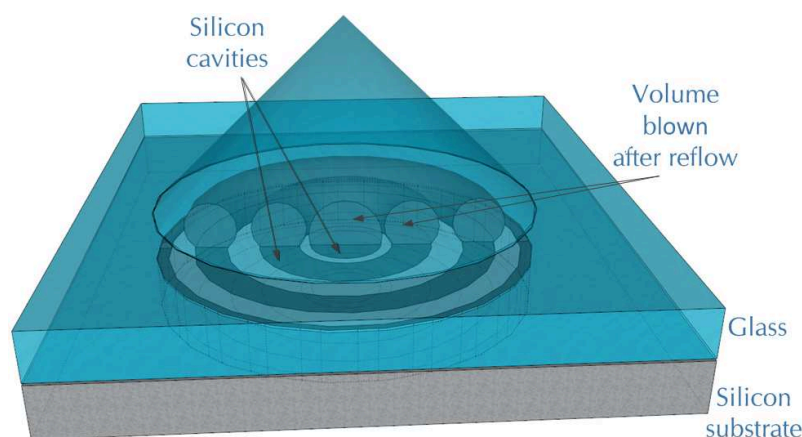


Figure 5.1: Schema of an axicon fabricated by the proposed technique.

Chapter 5 is organized as follows. Section 5.1 concerns the principle of the glass blowing process and technologies involved in the generation of optical components. Second section is devoted to the fabrication process. A description of how components are generated when cavities are sealed at vacuum and atmospheric process is detailed. In this thesis work, cavities sealed at atmospheric pressure have been employed to generate, as an example of refractive component with a versatile profile, glass-based microaxicons. In section 5.3, the characterization process to control the generated deformations in glass is shown. For this purpose, cavities with different sizes and shapes are placed at variable distances to study glass evolution during deformations. Once the process is fully characterized, the fabrication of microaxicons is then considered. In section 5.4, a complete fabrication recipe is described. Last section (5.5) is dedicated to the analysis of the optical performance of fabricated axicons. Conical lenses of 1 and 2 mm diameter, 4.5 and 40  $\mu\text{m}$  thickness and angles between  $0.5^\circ$  and  $2.5^\circ$ , respectively have been successfully fabricated.

### 5.1/ PRINCIPLE AND TECHNOLOGIES INVOLVED IN THE FABRICATION

The principle of the fabrication technique is to enclose a defined pressure into a silicon cavity sealed with glass. By increasing the temperature of the sealed cavity, changes in glass viscosity lead to modifications of the surface profile over the cavity. When cavities have been created and sealed, temperature is raised over the annealing point of the glass ( $560^\circ\text{C}$  in case of glass Borofloat33). The increase of temperature provokes, besides a change of glass viscosity, a variation in the pressure level within the hermetic cavity. This combination creates the deformation of glass surface until ultimately a state of equilibrium between pressures inside and outside the cavities. In function of pressure at which wafers are bonded, and so pressure inside the cavities, volume decreases or increases (Fig. 5.2). In the first case, glass is deformed towards the silicon cavity (sealed at vacuum pressure) and with a precise control of time, convex profiles can be created [Albero et al., 2015]. In the second case, the increase of pressure during the annealing process, provokes gas expansion in the cavity similar to a piston that pushes

and modifies the upper glass wafer surface.

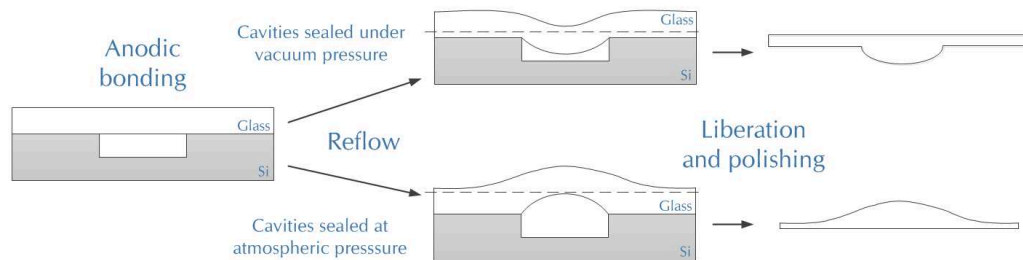


Figure 5.2: Simplified schema of glass blowing fabrication process.

In the fabrication process, several technologies are involved. Cavities are generated in a silicon substrate by dry etching. This technology was already described in section 2.4.3. After cavities generation, they are sealed by anodic bonding with a glass substrate. Here, an electric field (100-1000 V) at high temperature (200°C-400°C) is applied between substrates in contact, which provokes the mobility of positive sodium ions in the glass towards the negative electrode. The potential drop between glass and the anode (silicon) creates the covalent bonds between the two surfaces. Cleanliness and very low roughness of surfaces is essential [Takagi et al., 1997]. Once cavities have been sealed, the reflow process takes part in an oven, technique already described in this manuscript. Final components are obtained after silicon liberation through grinding and optical quality in glass surface is obtained through surface polishing. First one uses a rotating tool, also called grinding wheel, to remove material. The surface grinder is composed by an abrasive material (usually silicon carbide, or SiC) that reduces grinded material and leads to a flat surface. Second one uses an abrasive and corrosive chemical colloid in combination with a polishing pad rotated with different axes of rotation (i.e. non concentric) to remove material and even any irregular topography with resolutions down to Angstrom levels.

Our fabrication process is inspired in the work developed by Merz where the process was limited to microlenses generation [Merz et al., 2003]. He also described the blowing process for generation of convex microlens surfaces by enclosing the cavities not under vacuum but under "normal pressure conditions" so gas in cavities expands when heated [Quenzer et al., 2010]. This fabrication approach has several advantages considered in this thesis work as contactless (and direct) generation of glass-based components or parallel fabrication at wafer-level. Other advantage of the blowing process is that changes in viscosity or time are not main parameters as they are hard to control precisely. In our case, we focus on the development of a general technique to create more complex profiles.

## 5.2/ GLASS BLOWING AS A FABRICATION PROCESS

First step concerns the generation of cavities in a four inches silicon substrate. First, photolithography is performed with SPR220 photoresist [Koukharenko et al., 2005] coated onto the substrate at 2500 rpm during 30 seconds to get a 3  $\mu\text{m}$  thickness layer

(Fig. 5.3 a)). This photoresist is specially recommended for DRIE etching process with a selectivity value of 100:1. Pattern in photoresist is generated by standard UV-exposition of photoresist in a EVG620 Automated Mask Alignment System [EVGroup, 2016b]. After pattern generation, exposed photoresist is eliminated in a solution of MF26A basic developer [Bae et al., 2010] and deionized water during 70 seconds (Fig. 5.3 b)).

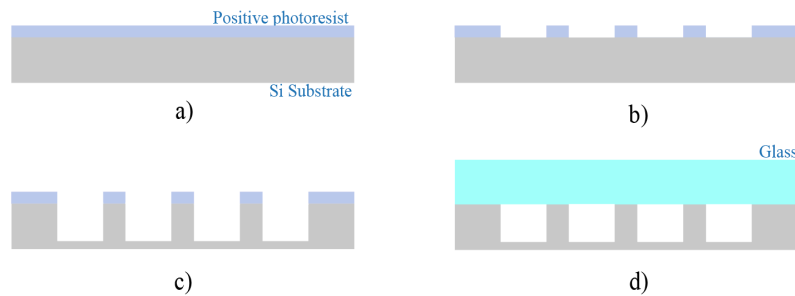


Figure 5.3: First part of the fabrication process until anodic bonding between the wafers.

Silicon is then etched anisotropically by DRIE (Fig. 5.3 c)) in a SPTS Rapier System [FEMTO-ST, 2016a] at 2700 W and 70 mTorr pressure. After photoresist removing, anodic bonding between silicon and glass wafer is performed at a defined pressure. In this thesis work,  $500 \pm 25 \mu\text{m}$  thickness Borofloat33 glass from Schott has been used. In order to get good results, preparation of wafers is mandatory, as anodic bonding defects are then translated into profile anomalies during the reflow step. After the etching process, some photoresist can get adhered to the substrate. A first rinsing in acetone is done to eliminate as much photoresist as possible and avoid its redeposition on the surface (grass marks). Then the silicon wafer is immersed in acetone and kept 4 minutes in an ultrasound bath. This process is repeated two times. After second bath, silicon is rinsed in deionized water and immersed in a piranha solution for two minutes. After a new rinsing in deionized water, both wafers (silicon and Borofloat) are cleaned in boiling  $\text{H}_2\text{O}_2$  during 20 minutes. This step eliminates eventual traces of organic rest on the substrates and properly prepares the surface for the anodic bonding. After, wafers are rinsed and immersed in deionized water in a beaker to be cleaned in a CL200 Cleaner System [FEMTO-ST, 2016b]. Once wafers are completely free of particles, the bonding process can be done.

The union of Si-Glass by anodic bonding is performed with an EVG501 Wafer Bonder System [EVGroup, 2016a], which is capable of creating a defined pressure inside the chamber while performing the bonding process. Before the bonding step, the machine should be cleaned with ethanol and a dust-cloth to avoid vacuum leaks on joints and cover. It also fasten the process. Once the chamber is clean, the substrates can be introduced. The bonding process, realized in 3 steps at 500, 700 and 100 V, assures a perfect anodic union between silicon and glass. After bonding, wafers are introduced in a boiling bath of  $\text{H}_2\text{O}_2$  during ten minutes and rinsed in deionized water.

When bonded wafers are clean, they are introduced in a furnace at a temperature higher than the annealing point of the glass. The process is then governed by the ideal gas law,  $PV=nRT$ . Increasing temperature causes, in addition to the increase of glass viscosity,

a variation of pressure inside the cavities. This combination leads to the deformation of the glass surface to reach the equilibrium. Depending on pressure inside cavities during the bonding process, volume inside the cavities decreases or increases. In subsections 5.2.1 and 5.2.2 both options are analyzed.

### 5.2.1/ CAVITIES SEALED UNDER VACUUM PRESSURE

In this case, the difference between cavities and furnace chamber pressure is big enough to avoid the equilibrium situation, i.e. if wafers are left a long time in the furnace, glass will almost completely fill the cavities. However, time can be controlled to stop the process before the convex profile of the lens touches the bottom part of the silicon cavity (Fig. 5.4 a)). This control of time instead of low pressure is convenient, since the last would require a precise control of pressure level within the silicon cavities, which is difficult in the corresponding pressure range. Thickness of fabricated lens is defined by the time spent inside the furnace at a temperature ( $650^{\circ}\text{C}$ ) over the annealing point of the glass. When final thickness value is achieved, melting rate must be reduced by a relatively abrupt decrease of furnace temperature, otherwise, natural cooling lets the deformation process continue for undetermined time and rate. If thermal shock is too high, stress at the silicon-glass interface will be generated and a wafer bowing effect is detected. This situation would lead to variations in components thickness during the liberation of lenses through grinding and polishing. To avoid this undesirable effect, an annealing step at  $600^{\circ}\text{C}$  for several hours after reflow lets the interface stress be minimized.

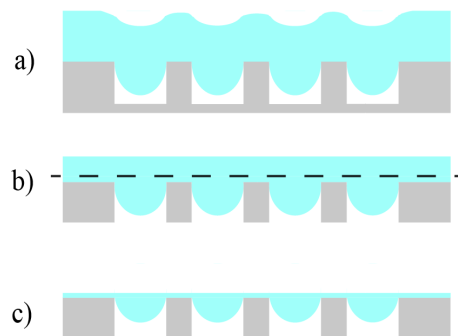


Figure 5.4: Fabrication process for cavities enclosed under vacuum pressure.

After reflow, lenses are liberated by grinding the back side of the glass substrate and polishing to obtain optical quality surface (Fig. 5.4 c)). Silicon can be grinded or etched isotropically by wet etching in KOH or TMAH (Tetramethylammonium hydroxide) solution. In the first case, strict control of the process is required in order to avoid serious damage to the glass deformed surface. DRIE is another option to eliminate the silicon, but it would degrade the surface quality of the lenses, as cavities depth is expected to vary along the whole substrate.

This technique has been successfully developed in our group in order to generate matrices of glass lenses [Albero et al., 2015] and also dense matrices of glass lens doublets [Albero et al., 2016] thanks to the vertical integration capability. Nevertheless,

the profiles being limited to nearly spherical ones, the second approach was attempted.

### 5.2.2/ CAVITIES SEALED UNDER ATMOSPHERIC PRESSURE

The second approach relies on blowing. Here, the bonding process between the silicon and glass substrates is performed at a pressure equal to the atmospheric one (1000 - 1045 mBar). When bonded wafers are introduced into the furnace and temperature is increased over the annealing point of the glass, differences between volume in cavities and furnace chamber make the pressure inside the cavities push the upper surface of the cavities to reach the equilibrium state (Fig. 5.5(a)). This force is similar to a piston effect that makes the surface of glass wafer deform outwards the cavities. This surface is then intended to be used as the refractive surface of the optical component. This blowing effect is proportional to the size of the etched cavity. Deformation occurs isotropically and spherically through the reflowed glass when single circular cavities are etched, similarly to Eklund work for the generation of vapor cells [Eklund et al., 2008]. When the equilibrium state is achieved and pressure inside cavities and furnace chamber is similar, deformation stops and temperature in the furnace can be decreased. An annealing step at 560°C for several hours minimizes thermal stress in the interface between silicon and glass, in order to avoid wafer-bowing when bonded wafers are cooled down. When the reflow process is finished, glass liberation can be performed (Fig. 5.5(b)). In this case, grinding and polishing of silicon substrate and inner part of blown glass is applied (Fig. 5.5(c)).

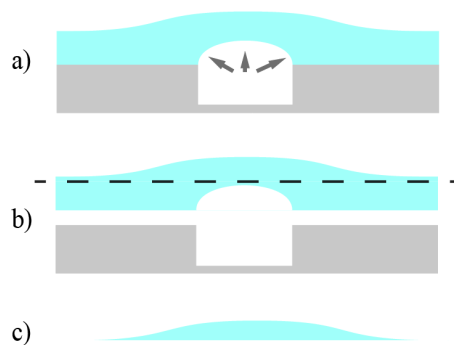


Figure 5.5: Fabrication process for cavities enclosed under atmospheric pressure.

All tests have been practiced in standard 4 inches silicon wafers, p-type dopant of  $525 \pm 25 \mu\text{m}$  thickness and 4 inches glass wafers Borofloat33 of Schott of  $500 \pm 25 \mu\text{m}$  thickness. Process at high temperature has been done in an oxidation furnace of AET Technologies [FEMTO-ST, 2016c]. Furnace chamber is 1 meter long and its circular section is 17 centimeters diameter. Maximum temperature achievable is  $1200^\circ\text{C}$  with a maximum slope of  $100^\circ\text{C}/\text{min}$ . During reflow process, the substrate is placed onto a quartz support placed in the center of the tube (Fig. 5.6).



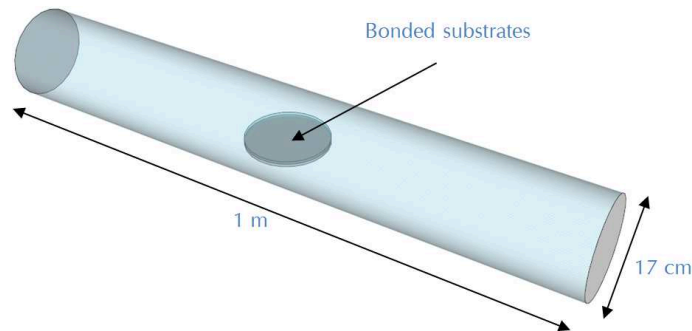


Figure 5.6: Schema of AET oxidation furnace employed in the fabrication process.

### 5.3/ CHARACTERIZATION OF THE PROCESS

#### 5.3.1/ VOLUME EVOLUTION IN RECTANGULAR CAVITIES

First test is practiced to check the evolution of volume blown in sealed cavities etched in silicon and measure deformations provoked in upper glass surface. This first analysis is intended to give an idea of the dimensions of cavities that can be employed and their effect in glass surface according to distance between them. For this purpose, rectangular cavities have been etched in a silicon substrate (Fig. 5.7(a)) with depth ( $d$ ) and length ( $l$ ) of  $300\ \mu\text{m}$  and variable width ( $w$ ) (Fig. 5.7(b)) from  $5$  to  $200\ \mu\text{m}$  in series ( $5, 10, 20, 30, 40, 50, \dots, 190, 200$ ). Separation ( $s$ ) from one cavity to the next one is proportional to cavity width ( $w$ ).

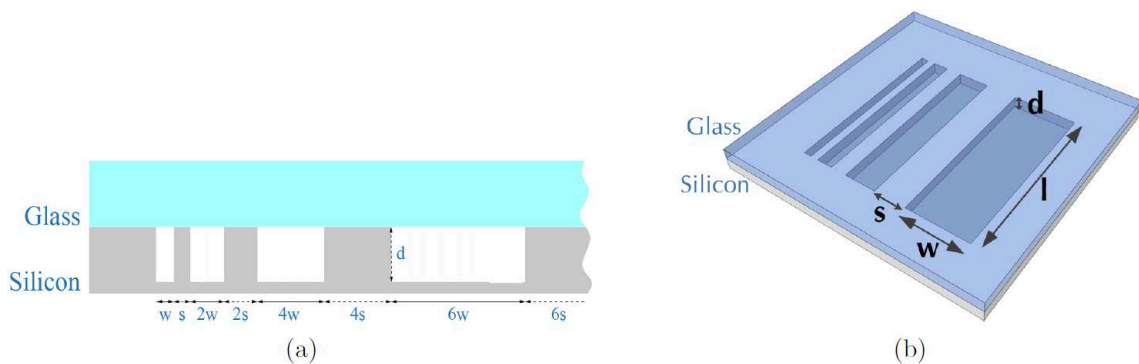


Figure 5.7: Test 1. (a) Schema of rectangular cavities etched in silicon and sealed with glass substrate. (b) 3D image of same schema.

After cavities etching in silicon substrate and anodic bonding between glass and silicon wafers, the reflow process is done. In this first case, temperature is raised until the softening point of Borofloat33 glass ( $820^\circ\text{C}$ ) at  $30.4^\circ\text{C}/\text{min}$ . After reaching maximum temperature, wafers are cooled down in the furnace at natural speed in a non-oxidizing atmosphere (azote gas). Temperature evolution and time are exposed in figure 5.8.

### 5.3. CHARACTERIZATION OF THE PROCESS

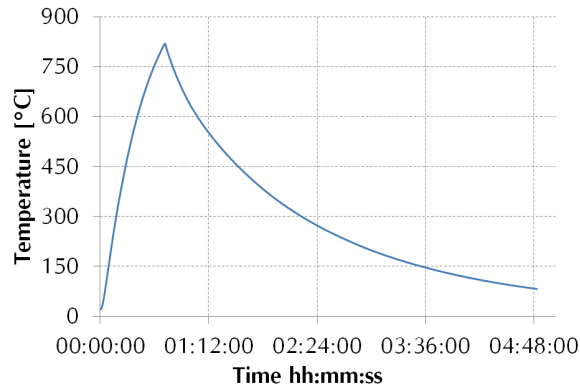


Figure 5.8: Temperature evolution during the reflow process at softening point glass.

Reflow process takes in total approximately 5 hours to be completed (mostly due to cooling) and bonded wafers are taken out from the furnace when temperature is under 80°C. As glass has reached its softening point, it has been deformed according to changes in pressure within silicon cavities consecutive to the rise of temperature. Because of this pressure difference between cavities and furnace at high temperature and thanks to low viscosity of glass, volume in cavities has expanded and acted as a piston effect which modifies the upper surface of glass substrate. In figure 5.9, the obtained by saw dicing cross section of bonded wafers after reflow process is shown. As it can be appreciated in the Scanning Electronic Microscope (SEM) image, upper surface of glass substrate is no longer flat and variations on the surface according to the blowing effect can be noticed.

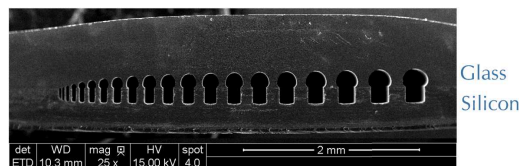


Figure 5.9: SEM image of a group of blown cavities of different sizes after reflow process.

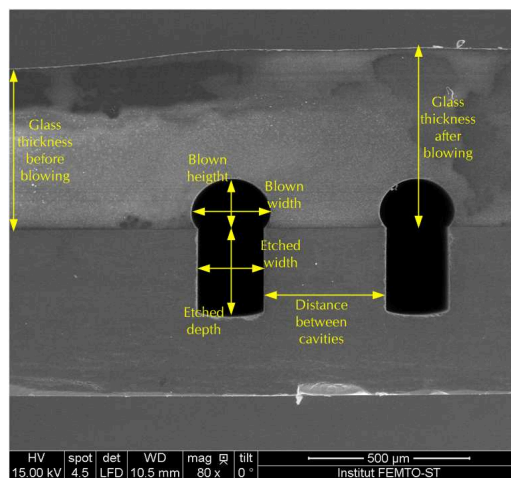


Figure 5.10: Cross section SEM image of two cavities and parameters measured in characterization process.

Induced deformations in glass surface are different depending on size of cavities and distances between them. Since the glass substrate is  $500\ \mu\text{m}$  thick, smaller cavities does not create a noticeable effect on the upper surface. On the contrary, volume enclosed in biggest cavities increases exceeding in some cases the volume etched in silicon during the DRIE step. Next figure shows three isolated cavities of  $20$ ,  $130$  and  $200\ \mu\text{m}$  width. It can first be noticed that depth value is not the same in all cavities. Depth achievable in cavities during the etching process of silicon is cavity width dependent and under a certain level (typically  $20\ \mu\text{m}$  wide), depth homogeneity is not assured. Here, the difference between deformations induced on glass surface during the blowing process is clearly visible. In the first case (Fig. 5.11(a)) pressure generated in the cavity during the reflow process is not strong enough to even generate a glass cavity. However, bigger cavities (Fig. 5.11(c)) creates a spherical glass cavity responsible for noticeable deformations on glass surface. This deformation constitutes the refractive profile of the eventual microoptical component.

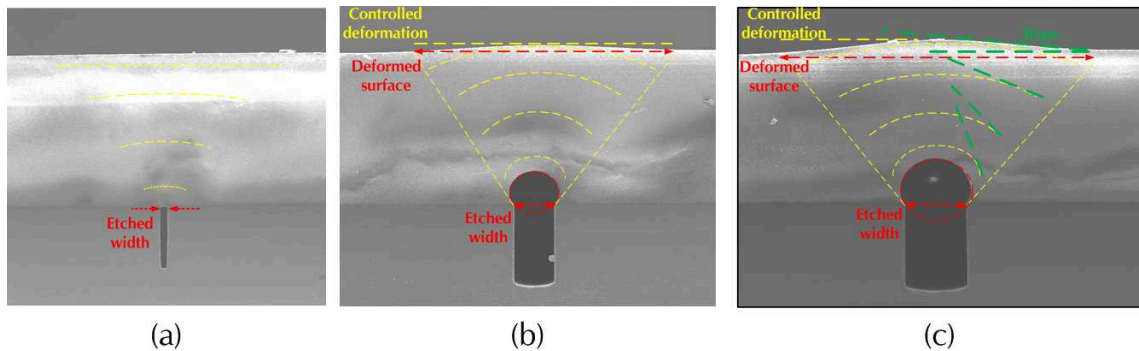


Figure 5.11: Cross section SEM image of a silicon cavity bonded with glass substrate of (a)  $20$ , (b)  $130$  and (c)  $200\ \mu\text{m}$  width.

In next figure, some parameters concerning the evolution of created cavities and upper surface of glass substrate as a function of the width of the etched cavities are shown. In figure 5.12(a), the evolution of the dimensions of the created cavities is presented. Blue and red lines represent the height and width measured in the cavities created after the reflow step and the green line represents the lateral size of the deformed upper glass surface. Considering the shape of the cavities we can see that the evolution of the height created inside the cavity is not linear to the etched width as it could have been expected. This is attributed to local variations in glass viscosity in zones close to the silicon surface. In these regions, glass should be less viscous and, then, volume created can evolve easier in the horizontal direction than push the glass vertically. As effects on upper surface of glass are difficult to measure for small cavities, the deformed surface (green line) data is not available for every etched width values. However, we find a relation of magnification of  $6.00 \pm 0.15$  between the etched width of silicon cavities and the deformed surface of glass. This means that for the smallest deformation measurable ( $102\ \mu\text{m}$  etched width), the size of the deformed surface is  $0.625\ \text{mm}$ . As changes during reflow within the bulk of the substrate are nearly isotropic, this relation is proportional to the thickness of the glass substrate ( $500\ \mu\text{m}$ ) and for smaller values of thickness, proportional values of magnification can be found.

In figure 5.12(b), we can see that even if the height of the cavities is not linear with the etched width of cavities, glass thickness pushed in the surface (blue line) follows an almost linear evolution. Non linearities observed in the evolution of height blown in cavities are softened (but not completely corrected) by glass substrate thickness and, then, deviations in glass thickness pushed are smaller. In this figure, the slopes measured (green dashed line in figure 5.11(c)) in the glass deformation range from  $1.28^\circ$  to  $4.18^\circ$ . As in the case of the deformed surface data, changes provoked by smaller cavities are not noticeable in the glass surface and, then, difficult to measure. For  $500\ \mu\text{m}$  thickness glass substrate we find a proportion of  $0.018 \pm 0.001$  between the width of etched cavities and the slope of the deformation generated at this temperature.

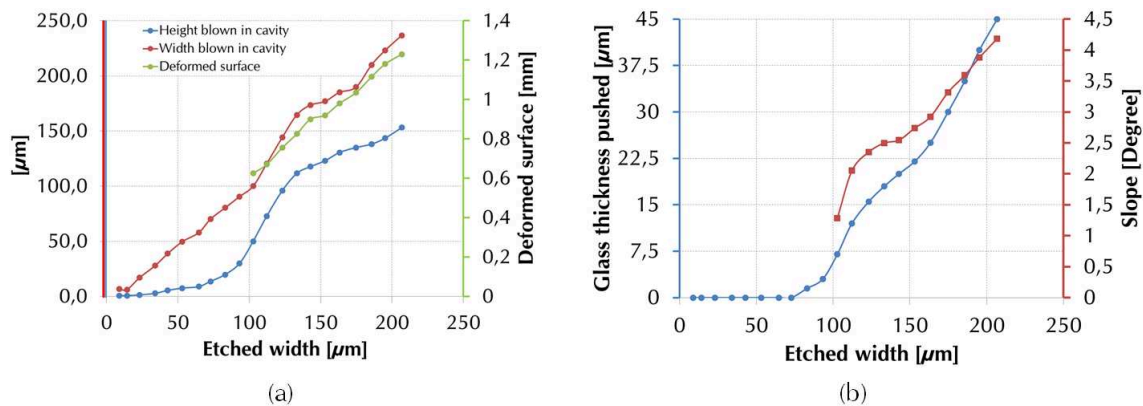


Figure 5.12: Evolution of cavities and glass surface after reflow at  $820^\circ\text{C}$ . (a) Height (blue) and width (red) measured in blown cavities and deformed surface on glass (green). (b) Thickness pushed (blue) and slope (red) measured in glass surface.

So by varying the etched width of cavities we can generate a range of continuous components within the values presented. In this case, changes in glass surface have been studied for a  $500\ \mu\text{m}$  thickness wafer. If thickness of substrate is reduced, changes provoked during the reflow step should be proportional to the ones presented due to the isotropy of the reflow process.

In order to compare the effects caused by separation between cavities, two series where the separation is either equivalent to the cavity width ( $s = w \times 1$ ) or to 5 times the cavity ( $s = w \times 5$ ) have been reflowed.

Figures 5.13(a) and 5.13(b) show the evolution of height and width measured in the blown volume inside cavities as a function of etched width of cavities for two different separations between them. Each point represents one cavity from the smallest tested one ( $5\ \mu\text{m}$  width) to the biggest one ( $200\ \mu\text{m}$  width). As it can be appreciated, larger the cavity, more spherical the profile is. Separation between cavities affects the shape of blown volume only when cavities bigger than  $100\ \mu\text{m}$  width are etched. In these cases, when separation is smaller (X1) blown volume reaches higher height values and then bigger deformations are provoked in the upper glass surface.

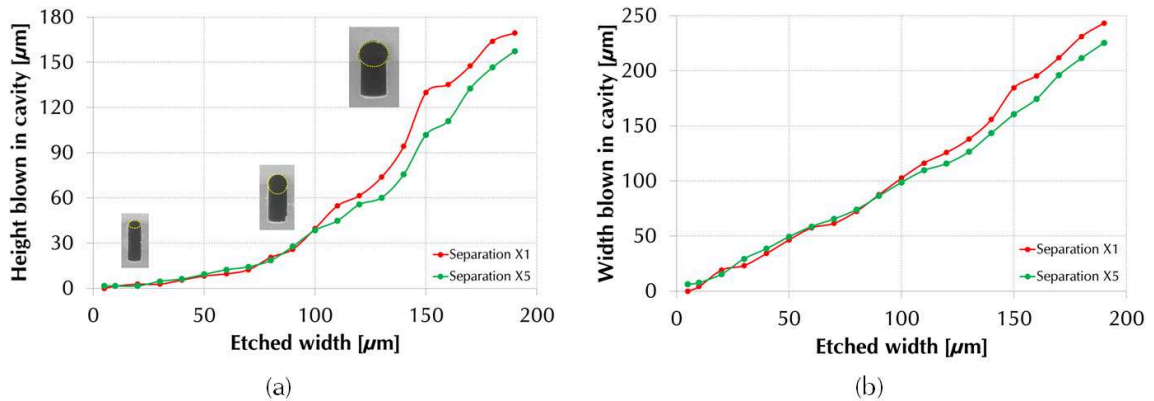


Figure 5.13: (a) Height and (b) width evolution of blown volume in cavities as a function of etched width.

Now, when looking at the corresponding deformation produced in the upper glass surface as a function of width of the etched cavity (Fig. 5.14), it can be appreciated that deformation generated in glass surface tend to increase according to the area of the etched cavity. Concerning separation between cavities, we observed that for smaller separations (X1), deformations measured in glass surface are bigger in almost every case, i.e. contributions from adjacent cavities add up. Hence, separation between cavities can be employed to extend the height of the generated upper deformation. However, for cavities less spaced, this tendency holds after a certain value. For cavities of  $180 \mu\text{m}$  width and bigger, glass surface has been deformed almost  $80 \mu\text{m}$  outwards the cavity which is considered the maximum deformation achievable at softening point when substrate of  $500 \mu\text{m}$  is considered. This saturation state might be due to changes in shape of generated volume inside glass substrate. As it was mentioned before, viscosity near silicon substrate might be lower than in the bulk of the glass. This is traduced into an expansion of volume inside the cavities in the horizontal direction stronger than in the vertical orientation and, then, deformation induced in the upper glass substrate are lower.

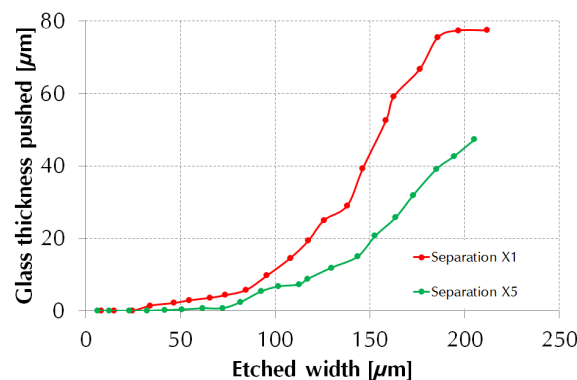


Figure 5.14: Influence of separation between cavities onto pushed glass thickness.

Several conclusions can be already done. Concerning cavity size, glass surface changes start for width values larger than  $20 \mu\text{m}$  when the Si cavity depth is  $300 \mu\text{m}$ . In next subsections, cavities with a width smaller than  $25 \mu\text{m}$  are not employed, as they do

not deform glass sufficiently during the reflow process. Regarding separation between cavities, it has been demonstrated that it contributes significantly to the height of glass surface when the separation is in the range of the width. We have seen that, for example, two cavities separated by  $30\ \mu\text{m}$  generate the same deformation ( $1.5\ \mu\text{m}$ ) than one cavity of  $80\ \mu\text{m}$  width. In this range of width values, resolution is relatively low but can be convenient for the generation of continuous refractive profiles.

### 5.3.2/ RING-SHAPED CONCENTRIC CAVITIES

When the substrate is so thick, several tens of microns height can be obtained but at the price of a lower resolution. Then, considering microoptical components fabrication, refractive profiles are more adapted for this process and among them, aspheric or conical components are the ones showing more difficulties to be made by the usual reflow approach. So, as an example of optical component that can be generated by the presented technology, glass-based microaxicons fabrication has been, once again, considered.

Here, etching of ring-shaped concentric cavities that should lead to controlled profiles having a cylindrical symmetry have been studied. In order to analyze induced variations in glass surface, cavities of different sizes and separations have been tested. In designs, a central circular cavity has been etched and surrounding rings placed at a defined separation determine final profile of the optical component. The purpose is to straighten up the profile generated by the central cavity with the concentric ring in order to tend to a conical profile. Cavities are in all cases  $300\ \mu\text{m}$  depth and total diameter of components have been fixed to 1 and 2 mm. As it can be appreciated in figures 5.15(a) and 5.15(b), one central cavity ( $w_c$ ) is surrounded by a certain number of rings of width  $w_1, w_2, \dots, w_n$  placed each one at a separation  $s_1, s_2, \dots, s_n$  of the previous ring. Variations in separation and width lead to different profiles on the upper glass substrate. Substrates are, as in previous subsection,  $500 \pm 25\ \mu\text{m}$  thick.

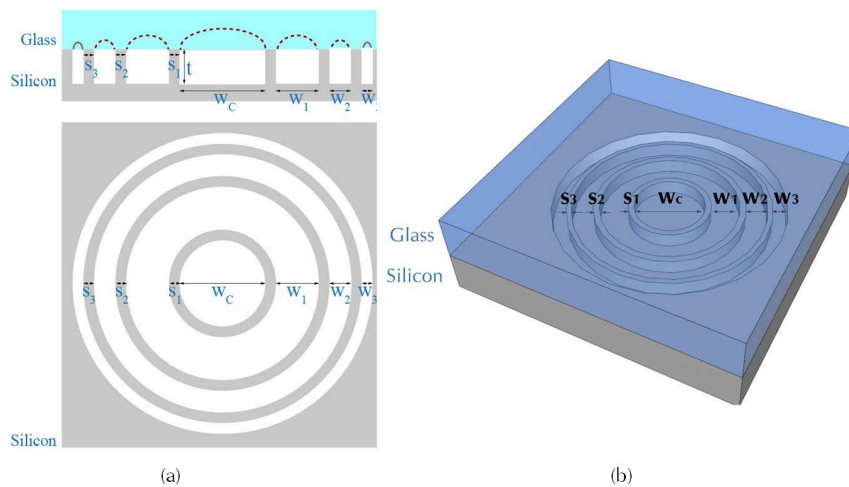


Figure 5.15: (a) Schema of ring-shaped concentric cavities etched in silicon and sealed with glass substrate. (b) 3D image of same schema.



Figure 5.16 is a microscope image of one group of cavities after etching before bonding with glass substrate Borofloat33 tested during the experiments. It consists in one central cavity of diameter  $w_c$  surrounded by three concentric rings of size  $w_1, w_2, w_3$ . In this case, separation  $s_1, s_2, s_3$  is constant. Bottom part of the image shows the measured profile at the center of the structure proving the homogeneity of the etching step.

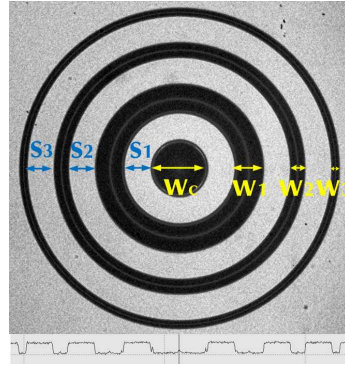


Figure 5.16: Microscope image and profile measured of cavities etched in silicon.

Cavities are spaced by constant separation distances, whereas cavities widths are changed according to the previous subsection results. Concerning number, size and separation between cavities, numerous combinations have been tested. In this manuscript, six of the most significant ones are presented. Components of 1 and 2 mm diameter composed by one central cavity ( $w_c$ ) and three rings ( $w_1 - w_3$ ) placed at different separations have been analyzed. Table 5.1 summarizes dimensions of components in each case. It can be appreciated that separation between cavities is decreased in each combination while width values are adapted to maintain total diameter of the component.

Diameter [mm]	Combination	Separation [ $\mu\text{m}$ ]	$w_c$ [ $\mu\text{m}$ ]	$w_1$ [ $\mu\text{m}$ ]	$w_2$ [ $\mu\text{m}$ ]	$w_3$ [ $\mu\text{m}$ ]
1	1	75	200	100	50	25
	2	50	200	125	75	50
	3	25	200	150	100	75
2	1	158	500	175	75	25
	2	133	500	200	100	50
	3	108	500	225	125	75

Table 5.1: Geometrical values of etched cavities.

Here, reflow process have been performed at two different temperatures,  $800^\circ\text{C}$  (Fig. 5.17(a)) and  $850^\circ\text{C}$  (Fig. 5.17(b)). Different temperatures lead to different viscosity and pressure values and, then, different deformation in glass surface. These differences are appreciated in terms of radius of curvature ( $R_c$ ) and sag of the fabricated component.

### 5.3. CHARACTERIZATION OF THE PROCESS

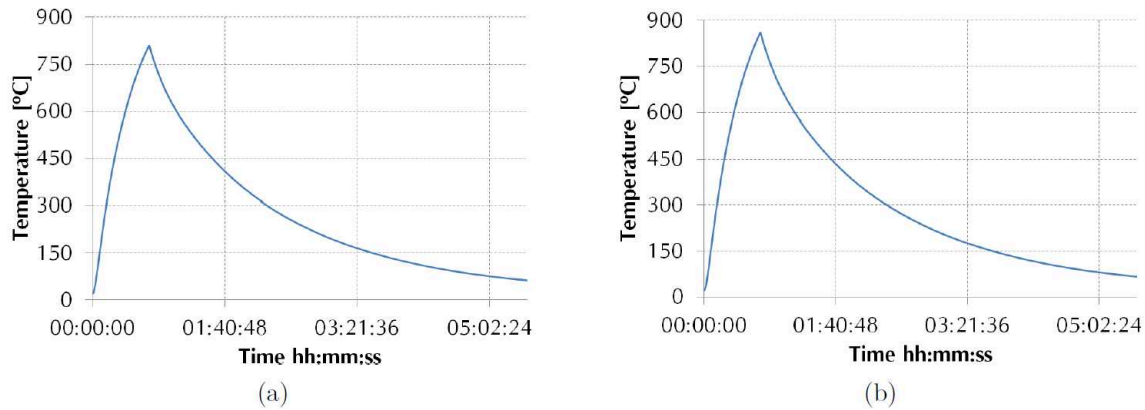


Figure 5.17: Temperature evolution during the reflow process at (a) 800°C and (b) 850°C.

After reflow processes at 800 and 850°C, profiles of components are measured with the MSA-500 MEMS analyzer of Polytec. In this case, deformations measured in glass surface show a spherical tendency. In order to characterize the profile of deformed glass surface, the general aspheric equation has been employed:

$$h(r) = \frac{1}{R_c} \frac{r^2}{1 + \sqrt{1 - (K + 1)r^2/R_c^2}} \quad (5.1)$$

Where  $h$  corresponds to the lens sag,  $r$  is the distance to optical axis,  $R_c$  is the radius of curvature and  $K$  is the conic constant of the lens. With this expression, any conical surface can be generated depending on the value of the conic constant  $K$  [Mahajan, 1998].

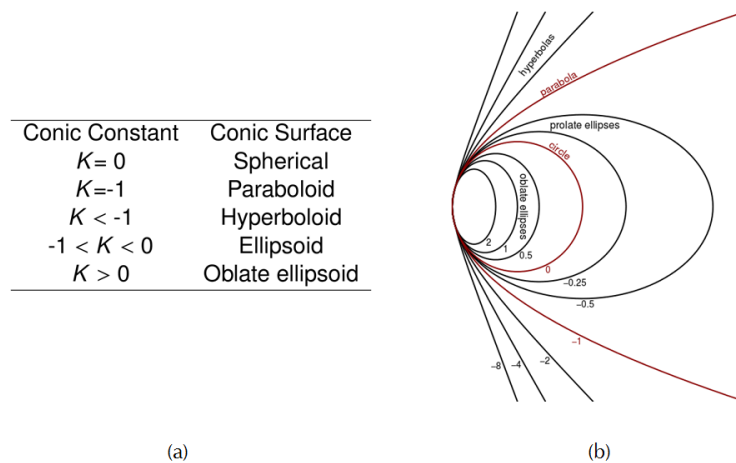


Figure 5.18: (a) Conic surface generated depending on magnitude and sign of the conic constant,  $K$ . (b) Graphic representation of shapes generated for different  $K$  values at constant radius of curvature  $R_c$ . Source: [Wikipedia, 2015].

In order to characterize the changes provoked in glass surface as a function of sizes and separation of cavities etched in silicon, a fitting between radius of curvature and conic constant has been implemented in each case. Results are summarized in table 5.2.



Diam.[mm]	Reflow [ $^{\circ}$ C]	Sep. [ $\mu$ m]	Sag [ $\mu$ m]	$K$	$R_c$ [ $\mu$ m]	NA	Opening angle
1	800	75	8.81	-1147	8000	0.029	$1^{\circ}$
		50	14.89	-510.5	4410	0.053	$1.7^{\circ}$
		25	21.62	-210.5	3496	0.067	$2.47^{\circ}$
	850	75	62.75	-12	1645	0.141	$7.15^{\circ}$
		50	64.63	-12.4	1623	0.143	$7.36^{\circ}$
		25	83.94	-5.9	1323	0.175	$9.52^{\circ}$
2	800	158	94.86	-80.5	1500	0.299	$5.41^{\circ}$
		133	111.41	-47	1570	0.286	$6.35^{\circ}$
		108	117.21	-22.6	3000	0.154	$6.68^{\circ}$
	850	158	119	-38	2000	0.299	$6.78^{\circ}$
		133	123.17	-32	2150	0.214	$7.02^{\circ}$
		108	124.85	-17.9	3034	0.153	$7.11^{\circ}$

Table 5.2: Fitted values for cavities etched with different sizes and separations.

According to the results analyzed, several conclusions can be obtained:

- As distance between cavities is reduced, along with an increment in size, thickness (sag) of components increases. This effect is generated because of the increased volume blown in the cavities (bigger size) in a smaller area (reduced separation). These cumulative effects lead to bigger deformations in the upper surface of glass substrate.
- Components have larger sag with increasing temperature. It can be appreciated that for same combinations of cavities size and separation, components have much larger sag values at  $850^{\circ}$ C. As expected, following the ideal gas law, higher temperatures provoke an increment in the volume inside the cavity. This effect is combined to the lower viscosity of glass at higher temperatures. Then, bigger deformations can be induced in the bulk of glass substrate.
- Fabricated components show conical profiles with a very negative conic constant whose amplitude decreases with the increased sag of components, along with a reduction of the radius of curvature. Both effects lead to more flat profiles in components which is convenient for the generation of the considered lens. This relation responds to equation 5.1 behavior only in case of lenses of 1 millimeter. In the case of 2 mm lenses, the effect is reversed and an increment on the radius of curvature is observed when cavities become closer. This is then interesting since we might be able to control the two parameters separately. In next figures, this effect is appreciated clearly.

In next figures, an example of how size and separation of cavities influence shape of generated component is presented. Size and position of etched cavities are represented in grey color at the bottom of each figure. Influence between volume generated by adjacent cavities leads to components with a more linear profile when separation between cavities increases and their size is reduced (Fig. 5.19(c)). It was observed that flattest profiles were obtained when size of a ring is half of the previous one at constant separation. This is actually what is needed for the fabrication of axicons. In next subsection, components with such relations have been fabricated and demonstrated to behave like axicons.

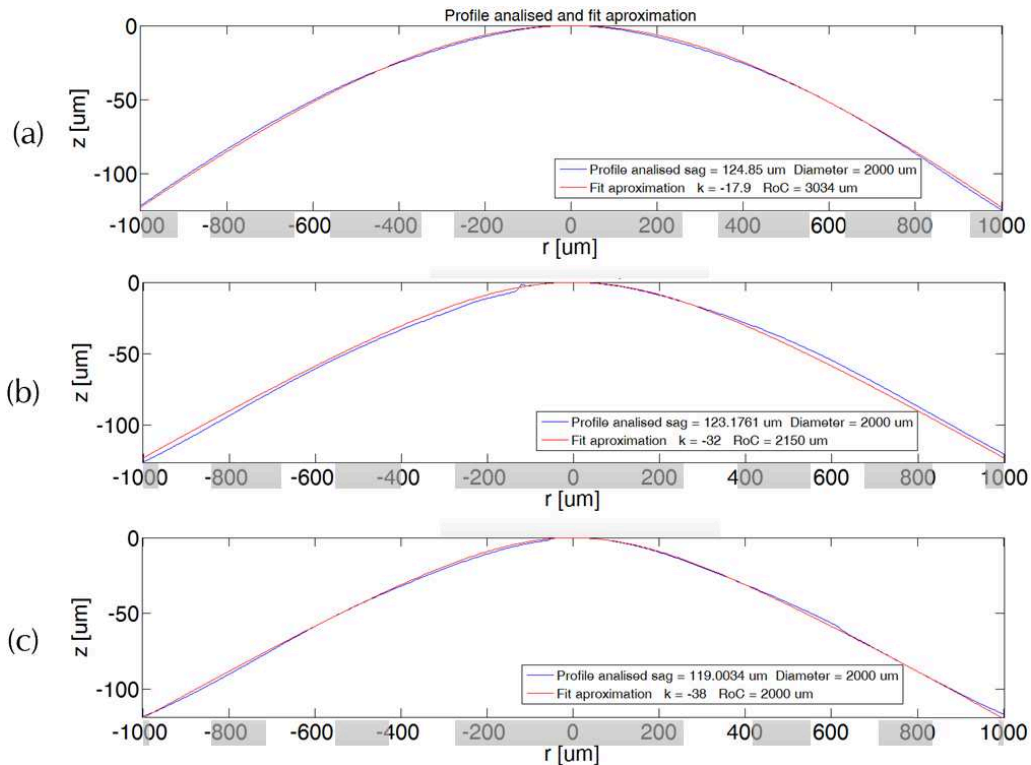


Figure 5.19: Measured and fitted profile for component of 2 mm diameter heated at 850°C. Separation between cavities is (a) 108  $\mu\text{m}$ , (b) 133  $\mu\text{m}$ , (c) 158  $\mu\text{m}$ .

However, an important drawback was first experienced when reflow process is performed at wafer level. At temperatures over 800°C, different dilatations of wafers tend to bend the wafers stack and TTV in substrates can reach values over 300  $\mu\text{m}$ . This effect, provoked by internal stress generated at high temperatures, leads to important uniformities in substrate thickness after grinding of silicon, making glass wafer very fragile. Manipulation becomes then very complicated. Consequently, an annealing step at 560°C (annealing point of glass Borofloat33) for several hours is applied in next runs to release internal stress generated during the reflow process. With this solution, we expect to reduce the bowing effect and improve homogeneity in glass thickness after silicon removal.

### 5.3.3/ CONICAL LENS GENERATION

As previous tests show, best relation in size and separation between cavities is observed when the size of a cavity is about 0.5 times smaller than the previous one. With this relation, flat lateral profiles can be obtained in order to accomplish a component with an axicon profile.

So, based on this relation, several combinations have been tested. In particular, silicon patterns made of two (Fig. 5.20(a) and fig. 5.21(a)) and four (Fig. 5.20(b) and fig. 5.21(b)) rings have been reflowed. Relation between cavity size (300  $\mu\text{m}$  depth) and separation is shown in table 5.3.

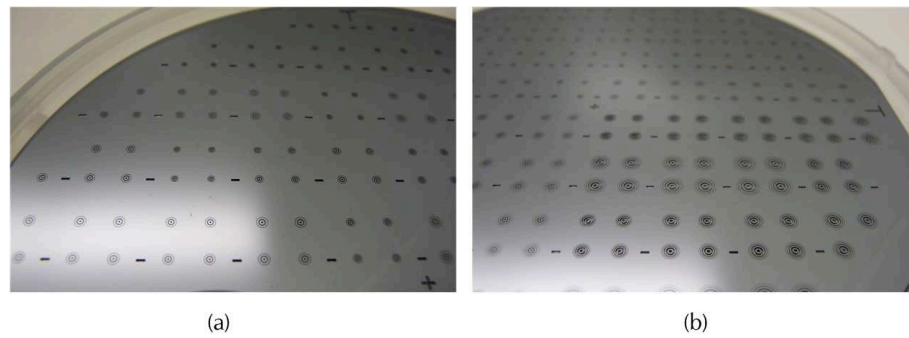


Figure 5.20: Photography of silicon wafer with cavities etched with (a) two and (b) four rings before anodic bonding onto a glass wafer.

Diameter [mm]	Separation [ $\mu\text{m}$ ]	$w_c$ [ $\mu\text{m}$ ]	$w_1$ [ $\mu\text{m}$ ]	$w_2$ [ $\mu\text{m}$ ]	$w_3$ [ $\mu\text{m}$ ]	$w_4$ [ $\mu\text{m}$ ]
0.9	100	200	100	50		
1.95	100	400	200	100	50	25

Table 5.3: Geometrical values of etched cavities of components fabricated with two and four rings.

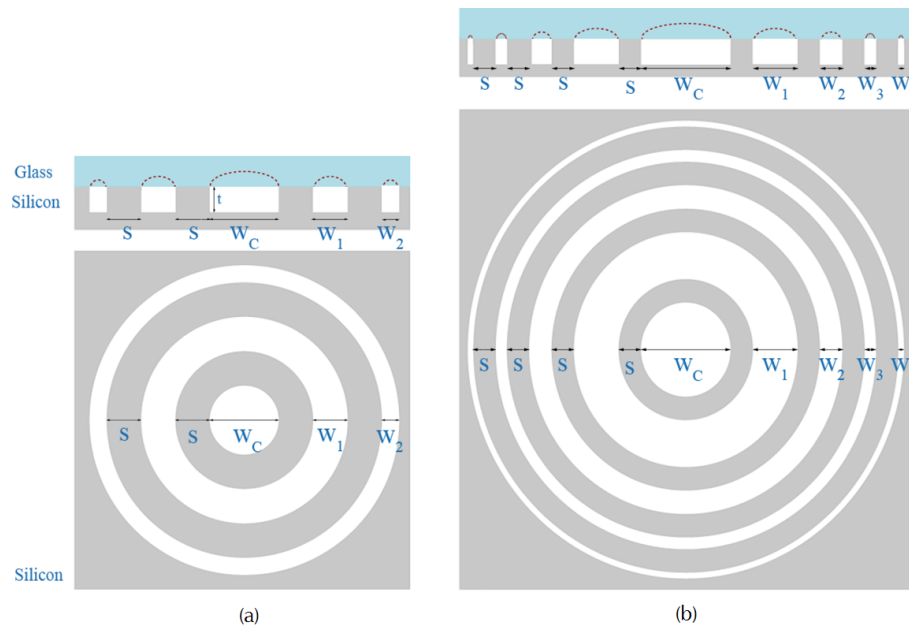


Figure 5.21: Schema of ring-shaped concentric cavities etched in silicon and sealed with glass substrate. (a) 0.9 mm and (b) 1.95 mm diameter lens.

To avoid wafer bowing observed earlier, a first attempt was to add an annealing step at  $560^\circ\text{C}$  for 3h30 to the reflow step. Figure 5.22 shows evolution of temperature during the reflow step. In this case, a raise of  $30^\circ\text{C}/\text{min}$  is applied to reach the high temperature of  $850^\circ\text{C}$ . After reaching the maximum, wafers are cooled down to the annealing point of glass Borofloat33 ( $560^\circ\text{C}$ ) and are kept at this temperature for 3.5 hours in order to release generated stress. Wafers are then cooled down to room temperature. The whole reflow process is more than 7 hours long because of the incorporation of the annealing

step.

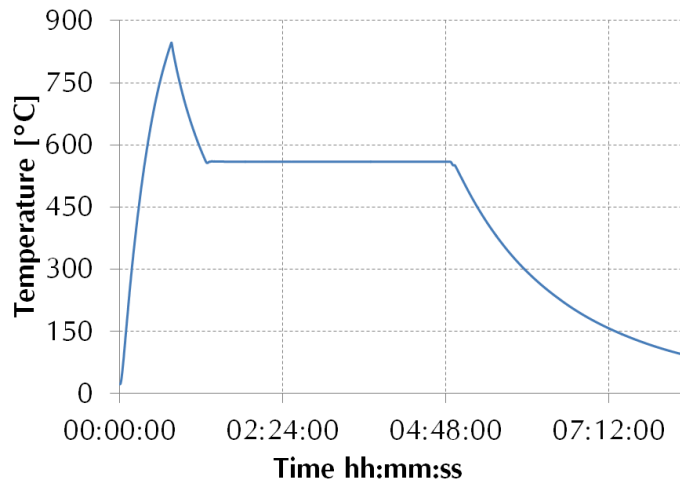


Figure 5.22: Temperature evolution during the reflow process at 850°C and annealing process at 560°C during 3h30m.

Such annealing allowed to reduce the bowing effects by almost three, from TTV of 300  $\mu\text{m}$  to 119  $\mu\text{m}$ . To completely eliminate silicon and liberate the components a total thickness of more than 890  $\mu\text{m}$  was grinded. As total thickness of bonded wafers (silicon + glass) is a bit more than 100  $\mu\text{m}$ , liberated glass is still very fragile for manipulation.

Consequently, to further decrease wafer bowing, a change in the reflow process was applied. It was decided to heat bonded wafers in a furnace at 700°C for 4 hours to eliminate possible generated stress during the reflow. Figure 5.23 shows temperature evolution in this case.

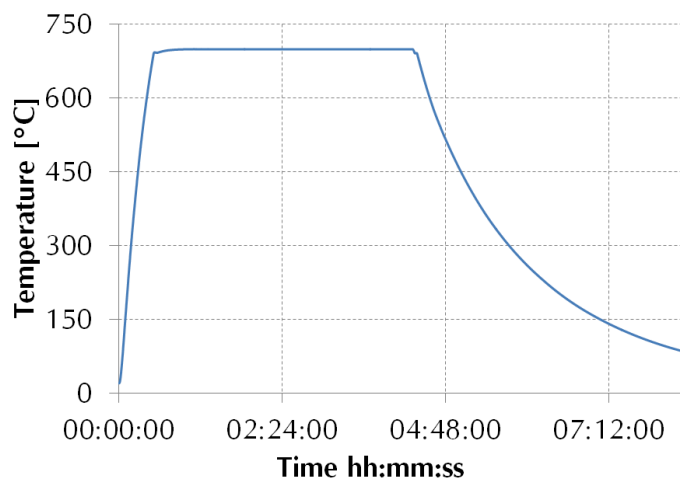


Figure 5.23: Temperature evolution during the reflow process at 700°C during 4h.

By doing so, bowing is clearly reduced and bonded wafers have a TTV of 20  $\mu\text{m}$ , almost six times smaller than in previous case. Thanks to this improvement in the reflow step, glass substrate is liberated after only 700  $\mu\text{m}$  thickness of silicon (500  $\mu\text{m}$ ) grinding and

glass ( $200\ \mu\text{m}$ ) polishing. Total thickness of glass substrate is more than  $300\ \mu\text{m}$  and manipulation becomes much easier.

In figure 5.24 a SEM image of the cross section of the component fabricated with four rings after reflow is shown. It can be appreciated the central cavity ( $w_c$ ) as well as the cross section of four rings ( $w_1, w_2, w_3, w_4$ ) and separation ( $s$ ) between them. It can also be noticed the controlled deformation provoked by blowing effect which represents the profile of the fabricated optical component. After grinding of silicon and polishing of glass surface, the optical component is liberated.

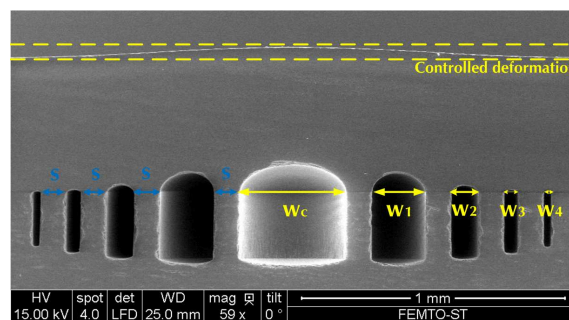


Figure 5.24: Cross section SEM image of etched silicon bonded with glass substrate after reflow process at  $700^\circ\text{C}$ .

Next figures correspond to the measured profile of fabricated components after reflow and glass liberation. Figure 5.25(a) corresponds to a component designed with a central cavity and two surrounding rings and figure 5.25(b) represents a component designed with four rings. As it can be seen, side of components is almost completely flat in the component designed with two rings. However, a certain radius of curvature remains on the lenses vertex. This effect, attached to the nature of the fabrication process, has a negative effect on the Bessel beam generation, as it was explained in section 3.4.2.

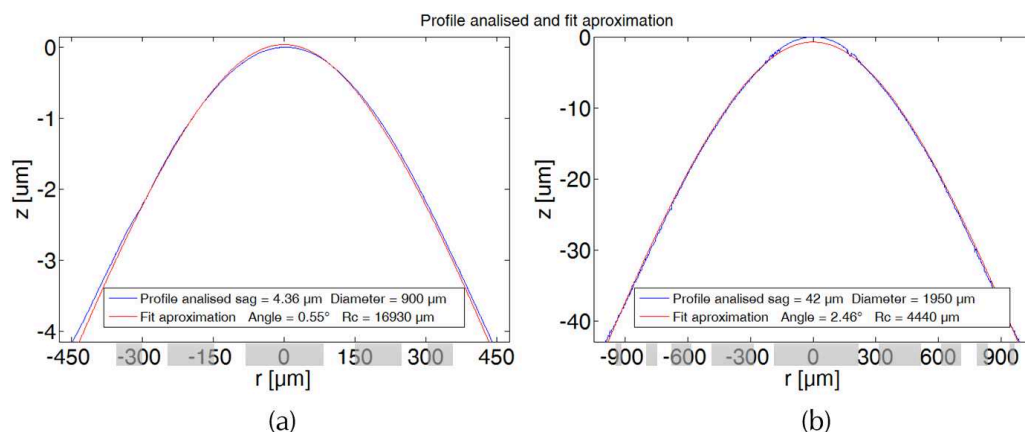


Figure 5.25: Measured and fitted profile of fabricated components after glass liberation. Components fabricated with (a) two and (b) four rings. Position of cavities is represented in grey color at the bottom of each profile

#### 5.4. RECIPE FOR PARALLEL FABRICATION OF GLASS-BASED AXICONS THROUGH GLASS REFLOW PROCESS

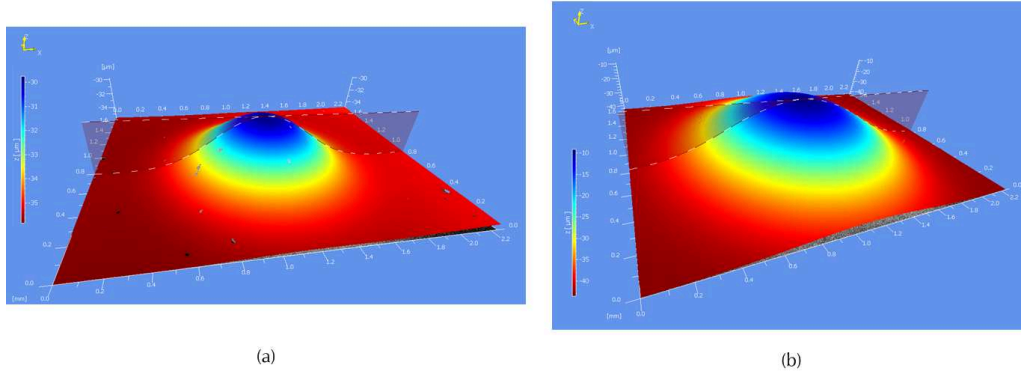


Figure 5.26: 3D optical surface topography of components fabricated with (a) two and (b) four rings.

As these profiles are close to a conical lens profile, a fitting using equation 3.38 was applied to find values of radius of curvature ( $R_c$ ), sag ( $e_0$ ) and opening angle ( $\alpha$ ). Results are represented in figure 5.25 and exposed in table 5.4. Deviation angle  $\theta$  (Eq. 3.12) and numerical aperture ( $NA = n \cdot \sin(\alpha)$ ) values are also calculated.

Diameter [mm]	Sag [ $\mu\text{m}$ ]	$R_c$ [ $\mu\text{m}$ ]	$\alpha$	$\theta$	NA
0.9	4.36	16930	$0.55^\circ$	$0.258^\circ$	0.00663
1.95	42	4440	$2.46^\circ$	$1.155^\circ$	0.02965

Table 5.4: Fitting results for fabricated lenses.

Generated components, depending on the ring number, have quite different features. 0.9 mm diameter lens fabricated with two etched rings has a sag of  $4.36 \mu\text{m}$  ( $\pm 0.09 \mu\text{m}$  variations along the wafer), with an opening angle of  $0.5^\circ$ . As reflow was applied at  $700^\circ\text{C}$  sag values are different to the ones obtained when the reflow step is done at  $800^\circ\text{C}$  ( $\approx 8.81 \mu\text{m}$ ,  $\alpha = 1^\circ$ ) or  $850^\circ\text{C}$  ( $\approx 62 \mu\text{m}$ ,  $\alpha = 7^\circ$ ). In the case of lens fabricated with four etched rings, thickness of the component is  $42 \mu\text{m}$  ( $\pm 0.18 \mu\text{m}$  variations along the wafer) which, compared to the smaller lens means a smaller radius of curvature and bigger opening angle in the base of the axicon according to the fitting equation employed. In next section a recipe for the fabrication of glass-based axicons through glass reflow process is provided.

#### 5.4/ RECIPE FOR PARALLEL FABRICATION OF GLASS-BASED AXICONS THROUGH GLASS REFLOW PROCESS

In this section, steps followed for the parallel fabrication of glass-based axicons at wafer-level through glass reflow at high temperature are summarized. The process consists in the assembling of two wafers at atmospheric pressure, one of them etched with concentric ring cavities. Variations in glass viscosity along with changes in pressure inside cavities provokes deformations in glass upper surface. Size and separation between cavities determine the profile of the optical component after glass liberation. In this thesis work, silicon and glass substrates are both  $500 \pm 25 \mu\text{m}$  thick.

- **Pattern design** for cavity generation on silicon substrate. Among all combinations tested in experiments, deformations generated during the blowing process that are closer to conical axicon profile were found when size of the cavity (at constant depth) is half the size of previous one at constant separation. Following this rule fabricated conical lenses show the typical transmission of a non-diffracted Bessel beam generated by an axicon. Note that conical profile is observed for different reflow temperatures allowing the control of the sag and the opening angle of the generated component.
- First step concerns **substrate and mask cleaning** before photoresist deposition. A piranha bath (two parts of  $\text{H}_2\text{SO}_4$  by one of  $\text{H}_2\text{O}_2$ ) during two minutes and rinsing in deionized water is enough to eliminate possible organic residues.
- **Wafer conditioning**. Prior to resist deposition, silicon wafer is placed onto a hotplate at  $120^\circ\text{C}$  during 10 minutes for water desorption from surface. To improve photoresist adhesion, a layer of TI-PRIME is deposited by spin coating on silicon substrate ( $v=3500$  rpm,  $a=4000$  rpm/s,  $t=20$  s). After TI-PRIME deposition, 2 minutes at  $120^\circ\text{C}$  on a hotplate assures chemical activation of the surface and increases photoresist adhesion. To avoid thermal shock during photoresist deposition, silicon wafer must be at room temperature so 1 minute waited after surface activation.
- **Substrate coating**. Spin coating of silicon is performed with photoresist SPR220 at 2500 rpm and 3000 rpm/s during 30 seconds to obtain a  $3\ \mu\text{m}$  thickness layer. 90 seconds at  $115^\circ\text{C}$  after coating assures solvent evaporation of photoresist. High selectivity compared to silicon (100:1) makes it specially recommended for deep cavities generation.
- **Exposure of photoresist**. EVG620 Automated Mask Alignment System is employed for pattern generation in photoresist. Exposed zones of substrate are eliminated after 70 seconds in MF26A basic developer bath and rinsing in deionized water.
- **Cavities generation in silicon substrate**. Deep Reactive Ion Etching is performed at 2700 W and 70 mTorr pressure. *Bosch* process is applied with  $\text{SF}_6$  and  $\text{C}_4\text{F}_8$  gases to create cavities in silicon of  $300\ \mu\text{m}$  depth. Rests of photoresist on substrate are eliminated after an acetone bath in ultrasounds during 4 minutes. This process is repeated twice, followed by a piranha bath and rinsing in deionized water.
- Before **wafer bonding**, complete cleaning of silicon and glass substrates is mandatory. A hot bath in  $\text{H}_2\text{O}_2$  for 20 minutes and post rinsing in deionized water eliminates any organic rest on wafers. After cleaning, anodic bonding between silicon and glass substrates is generated at  $300^\circ\text{C}$  and atmospheric pressure in a EVG501 Wafer Bonder System.
- Once bonded wafers have been cleaned, the **reflow process** can be performed. Prior to reflow step, bonded wafers are cleaned in a  $\text{H}_2\text{O}_2$  boiling bath during 10 minutes and rinsed in deionized water to eliminate any possible organic particle on the surface. Substrates are then introduced in a furnace at temperature above the annealing point



of glass (560°C in Borofloat33). In this thesis work, reflow processes have been carried at temperatures between 700°C and 850°C. At softening point of Borofloat (820°C), isolated cavities of different width generate components ranging from 1.3° to 4.2° and 1.5 μm to 45 μm thickness. Then several groups of cavities have been placed at different distances and reflowed at 800°C and 850°C. In these cases, sag values ranged from 8.81 μm to 124.85 μm and slope angles from 1° to 9.52°. Considering bowing effects of bonded substrates after reflow, best results have been obtained after reflow process at 700°C during 4 hours. This temperature along with a positive gradient of 30°C/min and natural cooling down after annealing process assures the absence of bowing effects observed at temperatures above 800°C.

• **Glass substrate liberation.** Final step consists in lenses liberation by grinding and polishing of silicon substrate. In this work we applied CMP (Lapping and Chemical-mechanical planarization) performed with the Logitech PMS and Alpsitec E460 systems to obtain low resulting roughness in the back side of the fabricated lens (< 3 nm RMS). In some cases, blown volume can be in the order of hundreds of μm thickness. That means liberated glass substrate is, in some cases, 200 to 300 μm thick. In order to avoid substrate damage when liberated, a 1 mm thickness Borofloat33 glass wafer is glued to the glass substrate (Fig. 5.27). For this, NBA-107 UV Curing Adhesive of Norland Products is employed [Norland, 2016]. This type of adhesive is used for temporary bonding of glass surfaces that need to be easily separated in the future [Sarvar et al., 2002]. The adhesive cures in minutes at room temperature under UV light exposure (350 - 380 nm). Once silicon and blown glass are grinded and polished, the glass substrate can be liberated from the glued wafer after a ten hours bath in acetone. Then the glass substrate is rinsed in deionized water and cleaned in piranha solution to eliminate any rest of adhesive or other compounds.

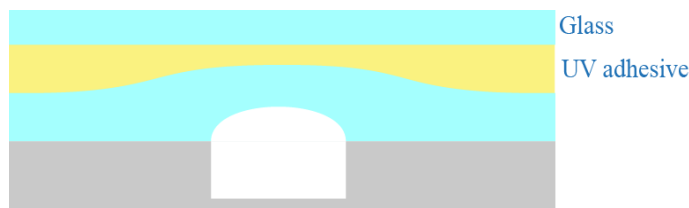


Figure 5.27: Schema of bonded wafers after reflow glued to glass substrate with UV adhesive ready for backside polishing.

## 5.5/ OPTICAL PERFORMANCE OF MICROAXICONS FABRICATED BY GLASS BLOWING PROCESS

Similarly as for axicons fabricated by gray-scale lithography in chapter 3, optical performance of microoptical components fabricated by micro glass blowing is analyzed in this section. Dimensions of components were given in table 5.4. Quality of lenses concerns the formation of Bessel beams when illuminated by a Gaussian beam through its optical axis. To control waist location and size, a convergent lens of focal length 25.4 mm (33.8 mm BFP) is placed between laser source and axicons. Set-up employed to obtain intensity distribution after axicons is the same as employed in section 3.4.1.



Figure 5.28 is a picture of the set-up used in tests to obtain transmission distributions of fabricated components. Some important elements concerning the imaging system have been highlighted.

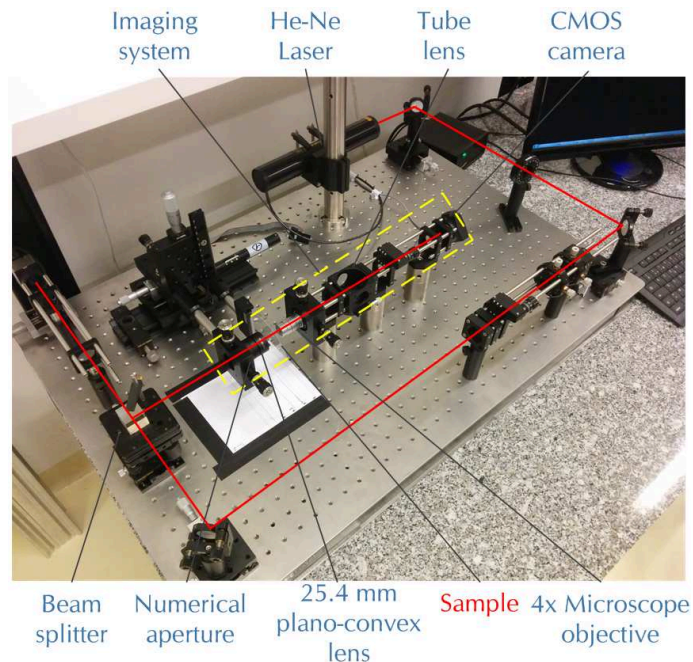


Figure 5.28: Set-up image to observe transmissive components when illuminated by a Gaussian beam.

As mentioned earlier, Bessel beams formation through axicons includes the generation of a long narrow focal line along the optical axis (Fig. 3.34).

### 5.5.1/ OPTICAL PERFORMANCE OF TWO RINGS BASED MICROAXICON

Axicons fabricated from two rings surrounding a central cavity have a 0.9 mm diameter, 4.36  $\mu\text{m}$  sag, radius of curvature 16930  $\mu\text{m}$  and opening angle  $\alpha = 0.55^\circ$ . An aperture stop is employed in the set-up to illuminate the component under test only and avoid contributions from neighboring components, its diameter is 1 mm. When illuminated by the laser beam, normalized (from transverse plane to plane) intensity follows a distribution shown in figure 5.29(a). Comparing to beam generated by plano-convex lens (Fig. 3.42(a)) it can be observed a longitudinal spread of on-axis intensity distribution. From figure 5.29(b),  $z_{max}$  is measured 16 mm long. Oscillations after maximum at  $z=26.4$  mm (FWHM is measured 15  $\mu\text{m}$ ) are caused by the systematically created vertex bluntness, attached to the nature of the fabrication process. This side effect of the fabrication technique also reduces efficiency of Bessel beam formation, specially concerning the first 20 mm where nearly spherical beams generated close to the optical axis have major influence on the intensity distribution. This effect decreases with distance from axicon vertex where beams refracted far from optical axis interfere and generate the desired Bessel distribution.

## 5.5. OPTICAL PERFORMANCE OF MICROAXICONS FABRICATED BY GLASS BLOWING PROCESS

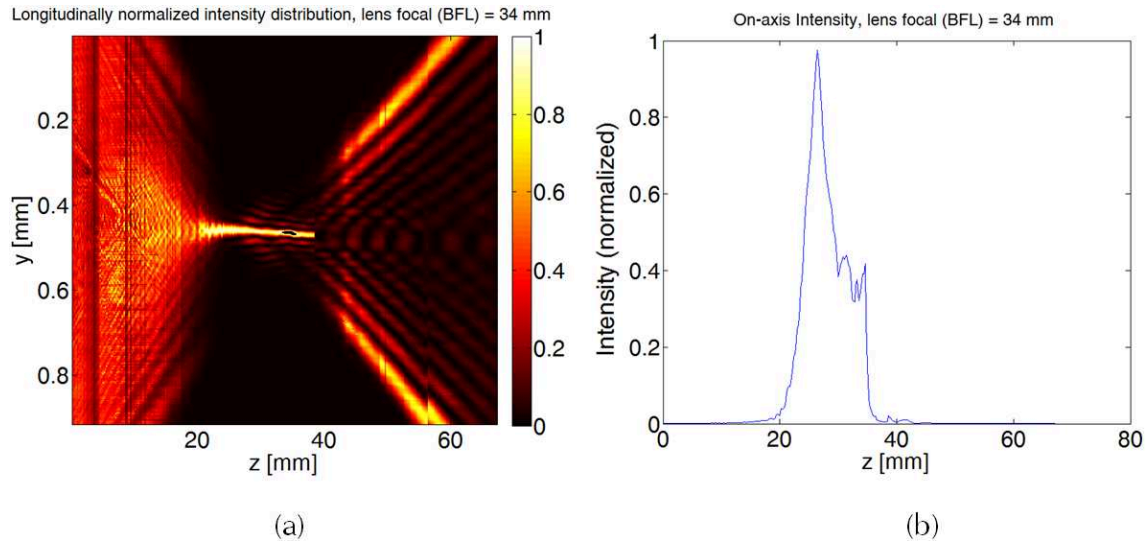


Figure 5.29: (a) Longitudinal normalized intensity distribution of two rings fabricated axicon. (b) On-axis intensity.

Round shape of axicon tip generates converging nearly spherical waves that interfere with Bessel beams generated behind the axicon modulating the field distribution along propagation in z-axis (Figs. 5.30(a) to 5.30(b)). As it was observed in axicons fabricated by gray-scale lithography influence of this modulation decreases at axial positions far from the axicon because decreasing influence of nearly spherical waves.

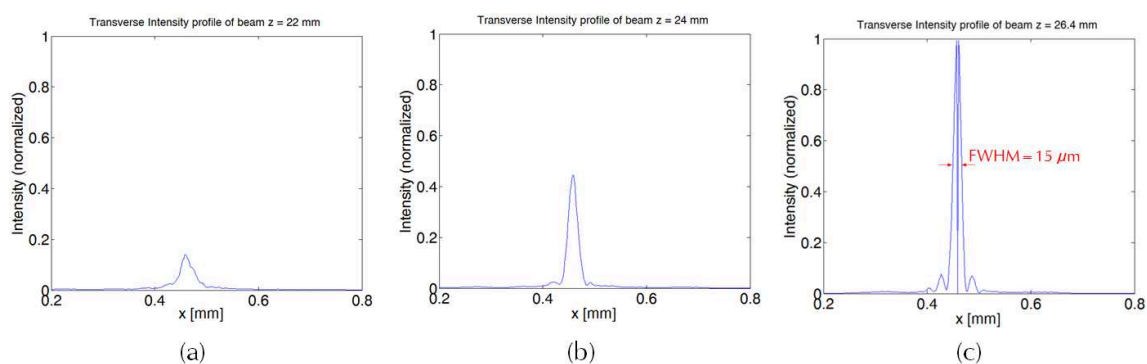


Figure 5.30: Intensity distribution with analyzed axicon at (a)  $z = 22$  mm., (b)  $z = 24$  mm. and (c)  $z = 26.4$  mm. (maximum on-axis intensity).

Hollow beam formation is observed after  $z_{max}$  (Fig. 5.31(a)). In figure 5.31(b) smaller intensity peaks can be appreciated. These oscillations are attributed to diffraction of the Gaussian beam onto the aperture stop. Nevertheless, hollow beams are created.

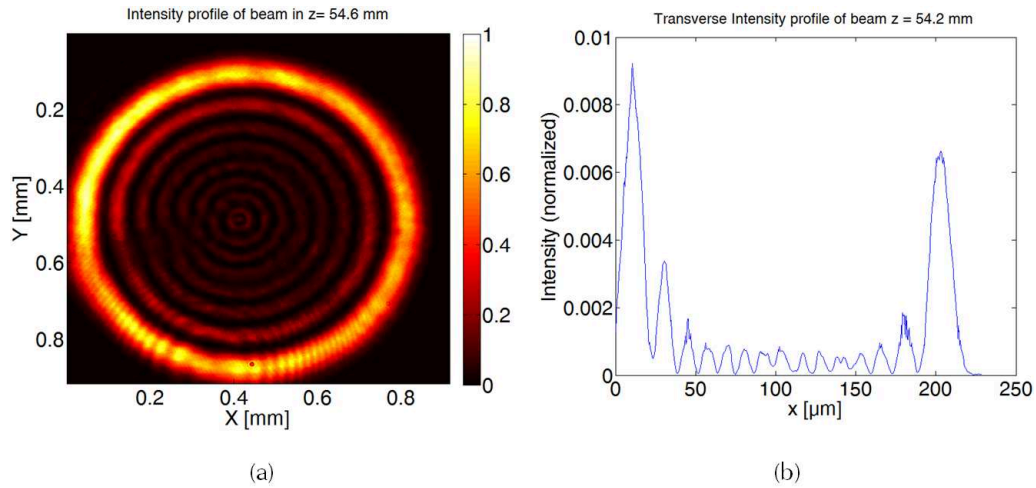


Figure 5.31: (a) Radial intensity distribution of dark hollow beam.  $z=54.6$  mm (b) On-axis intensity.

### 5.5.2/ OPTICAL PERFORMANCE OF FOURS RINGS BASED AXICON

In this case, axicons fabricated with four rings show a 1.95 mm diameter,  $42 \mu\text{m}$  sag, radius of curvature  $R_c = 4440 \mu\text{m}$  and opening angle  $\alpha = 2.46^\circ$ . Aperture employed in measurements has a 2 mm diameter. Bessel beam generation is also observed here (Fig. 5.32(a)). Maximum on-axis intensity value is localized at  $z=17.6$  mm (Fig. 5.32(b)), which is more than 16 mm before focal plane of the plano-convex lens (33.8 mm) employed and measured propagation distance  $z_{max}$  is 11 mm long. Non-diffracting beam is detected at 14.4 mm from axicon vertex due to radius of curvature in fabricated lens. Longitudinal spread of on-axis intensity is also observed.

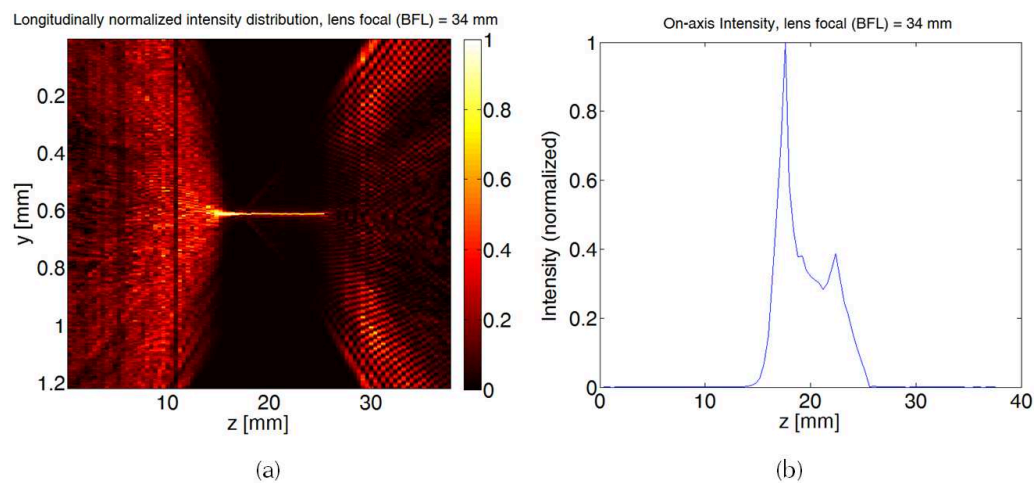


Figure 5.32: (a) Longitudinal normalized intensity distribution of two rings fabricated axicon. (b) On-axis intensity.

Experimental results are cross-checked with simulated ones. The calculation is based once again on Fresnel approximation to the Kirchhoff integral described in section 3.4.2.

## 5.5. OPTICAL PERFORMANCE OF MICROAXICONS FABRICATED BY GLASS BLOWING PROCESS

The experimental conditions remain slightly different since in the simulation, the three optical components responsible for beam shaping are considered thin and located in the same plane. This last feature can explain the longitudinal shift of few millimeters of the experimental Bessel generation. Nevertheless, general behavior is in reasonable agreement. The figure 5.33 displays the normalized intensity distributions for a perfect axicon (no bluntness, (a), (b)) and fabricated axicon ( $R_c=4.44\text{mm}$ , (c), (d)). (a) and (c) differs from (b) and (d) in the aperture diameter.

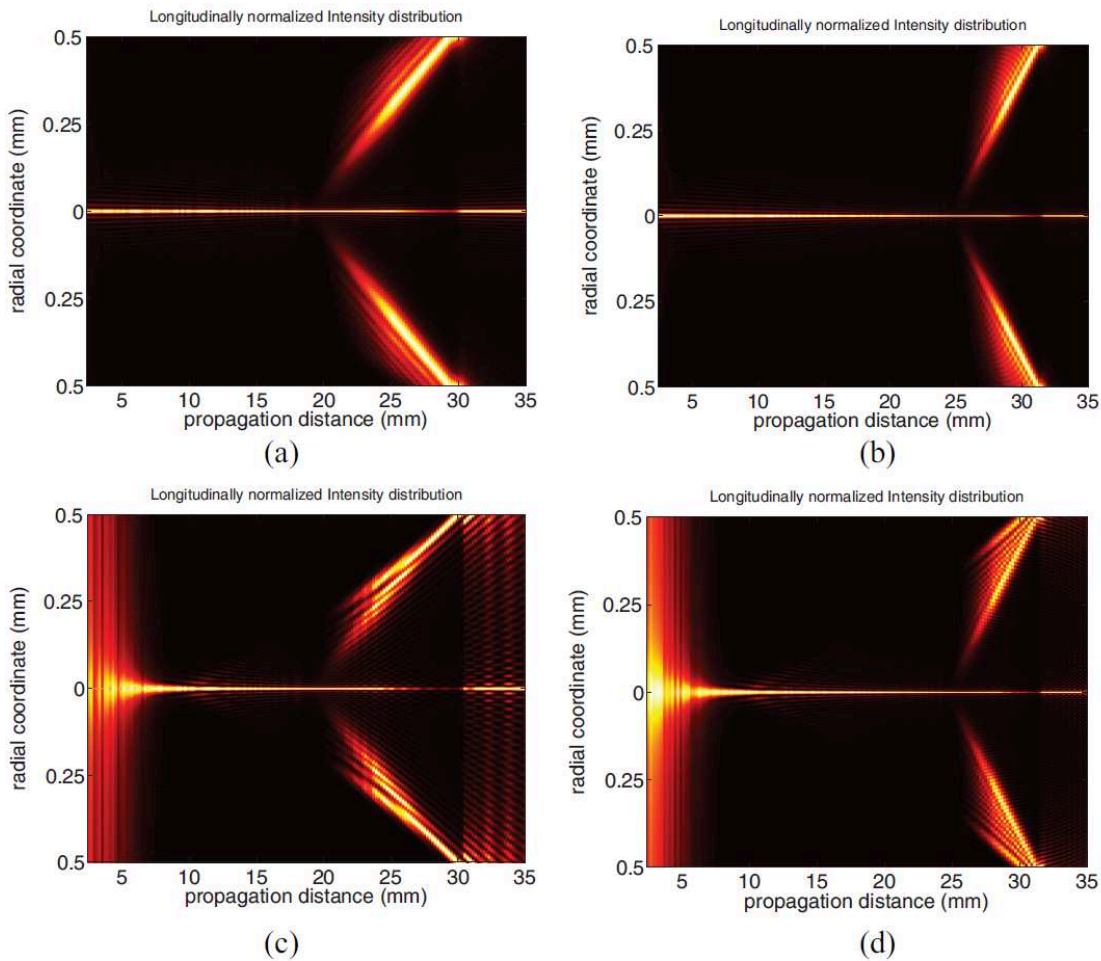


Figure 5.33: Calculated intensity distributions (Normalized by the maximum value in each longitudinal plane) along the propagation axis for 4 rings-based axicons ( $\alpha=2.46^\circ$ , incident collimated Gaussian beam,  $W_o=5\text{ mm}$ ). Axicon parameters and experimental conditions are changed to see the influence onto Bessel beam generation. (a) Ideal axicon (no bluntness,  $R_c = 0$ ) – Aperture radius  $\phi= 0.96\text{ mm}$ . (b) Ideal axicon (no bluntness,  $R_c = 0$ ) – Aperture radius  $\phi= 1.96\text{ mm}$ . (c) Fabricated axicon ( $R_c = 4.44\text{ mm}$ ) – Aperture radius  $\phi= 0.96\text{ mm}$ . (d) Fabricated axicon ( $R_c = 4.44\text{ mm}$ ) – Aperture radius  $\phi= 1.96\text{ mm}$ .

It is clear that bluntness affects the non-propagating beam by the contribution of a spherical wavefront whose weight is especially noticeable for the short propagation distances. Interferences between rounded and flat parts of the axicon profile are also responsible for more oscillating side lobes of the hollow part. Depending on the radius



of curvature of the vertex, the hollow beam is not as contrasted. The aperture is also responsible for shaping variations, on the first hand by modifying the numerical aperture of the lens (clearly visible on the angle of hollow beam between (a) and (b)) and by adding diffraction effects (smaller diameter in (c) compared to (d)).

Finally, the experimental figure 5.32(a) can be compared to the figure 5.33(c) where contributions of the rounded vertex and from aperture can be clearly identified.

To better visualize the longitudinal extension of the non-diffracting field, the same calculated curves are displayed in figure 5.34 where the intensity is no longer normalized plane to plane but instead, is raised to the power of 0.3. It can be better noted that aperture size directly affects this extension, and that rounded vertex “delays” the non-diffracting beam generation. As shown in figure 5.34(c), the latter is nearly 10 mm long as it is measured experimentally.

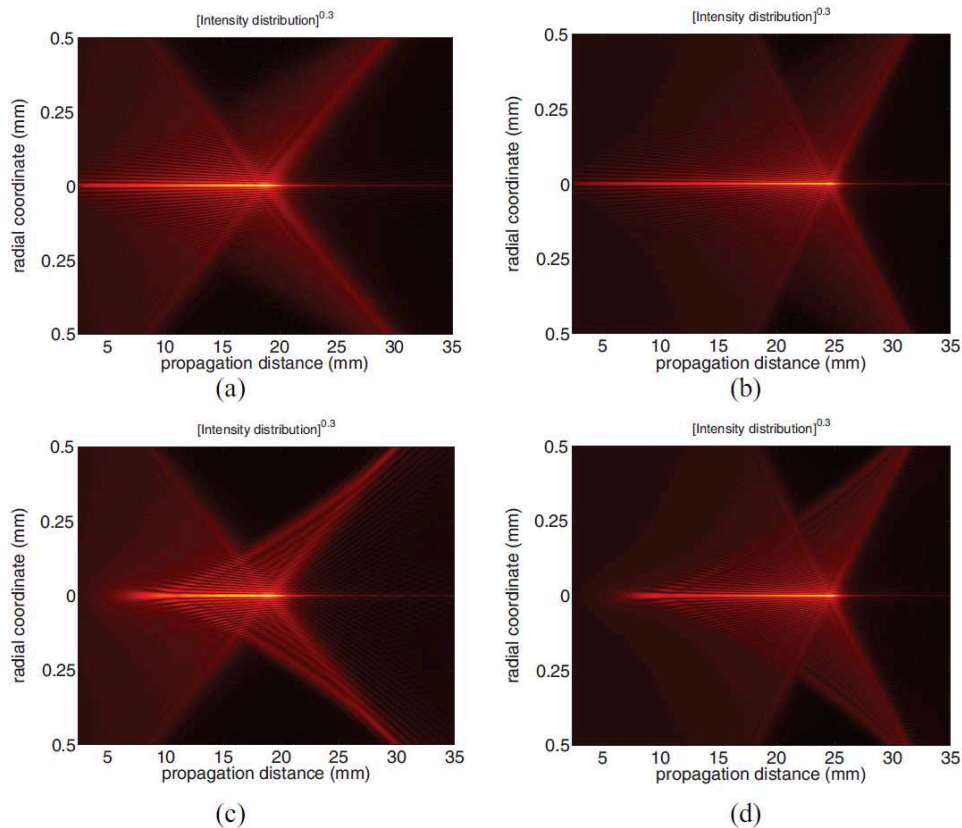


Figure 5.34: Calculated intensity distributions (with exponent 0.3 for better visualization) along the propagation axis for 4 rings-based axicons ( $\alpha=2.46^\circ$ , incident collimated Gaussian beam,  $W_0=5$  mm). Axicon parameters and experimental conditions are changed to see the influence onto Bessel beam generation. (a) Ideal axicon (no bluntness,  $R_c = 0$ ), aperture radius  $\phi= 0.96$  mm. (b) Ideal axicon (no bluntness,  $R_c = 0$ ), aperture radius  $\phi= 1.96$  mm. (c) Fabricated axicon ( $R_c = 4.44$  mm), aperture radius  $\phi= 0.96$  mm. (d) Fabricated axicon ( $R_c = 4.44$  mm), aperture radius  $\phi= 1.96$  mm.

Figures 5.35(a) to 5.35(c) show the evolution of transverse intensity profile of beam in

## 5.5. OPTICAL PERFORMANCE OF MICROAXICONS FABRICATED BY GLASS BLOWING PROCESS

the propagation distance  $z_{max}$ . Maximum here is registered at  $z=17.6$  mm. Compared to two rings based axicon, maximum is localized almost 10 mm before under same measurement conditions. This is caused by the increased opening angle which in this case is  $2.46^\circ$ . According to equation 3.12, larger opening angles cause deviated beams with a larger angle  $\beta$  and, then, shorter propagation distance  $z_{max}$  (Eq. 3.13). Evolution of the transverse intensity profile for three different positions of the non-diffracting zone has also been simulated and exposed in figure 5.36 where similarities with the experimental results are found regarding amplitude and frequency of oscillations.

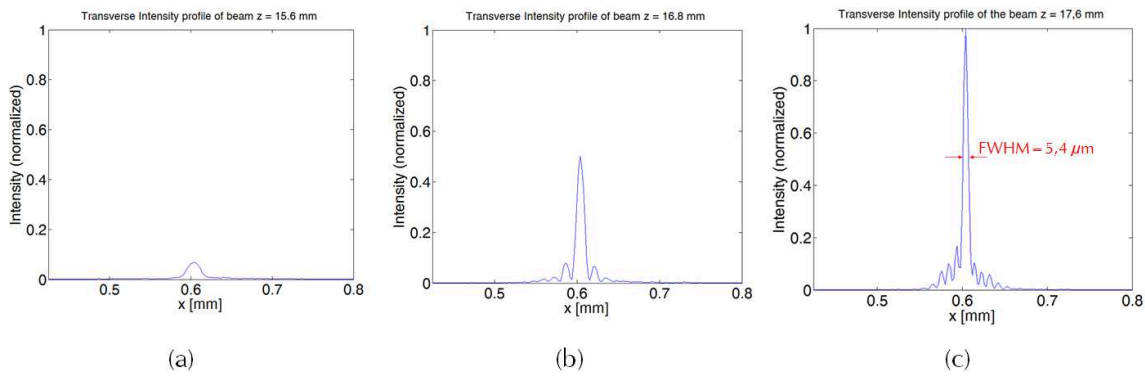


Figure 5.35: Intensity distribution with analyzed axicon at (a)  $z= 15.6$  mm., (b)  $z= 16.8$  mm. and (c)  $z= 17.6$  mm. (maximum on-axis intensity).

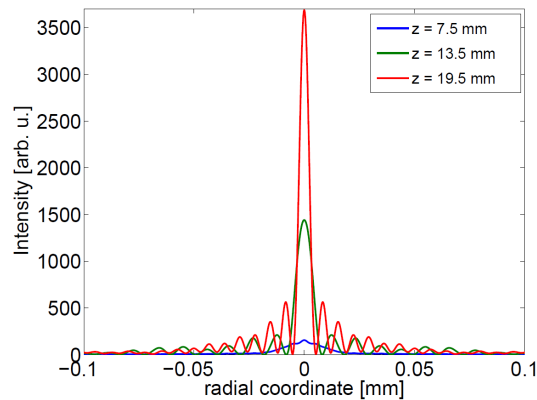


Figure 5.36: Calculated transverse intensity profile of the beam generated by the 4 rings-based axicons ( $\alpha=2.46^\circ$ ,  $R_c = 4.44$  mm, incident collimated Gaussian beam  $W_o=5$  mm, aperture radius  $\phi= 0.96$  mm) for 3 distinct longitudinal positions (non-diffracting zone).

Hollow beam generation is barely observed in this type of fabricated axicon, due to strong diffraction effects along with larger angle, as it can be appreciated in figure 5.37(a). Transverse intensity profile (Fig. 5.37(b)) at this point shows maximum values at the exterior part of the beam but distribution is very influenced by diffraction onto the 2 mm aperture stop along with the bluntness generated because of the round tip in the fabricated axicon. Transverse intensity profile has been simulated (Fig. 5.38) in two different position of the hollow beam zone. Here we can appreciate that position

of maximum is similar to experiments in  $z=35$  mm (red line) but diffraction and larger opening angle also provoke larger intensity values in inner zones of the hollow beam.

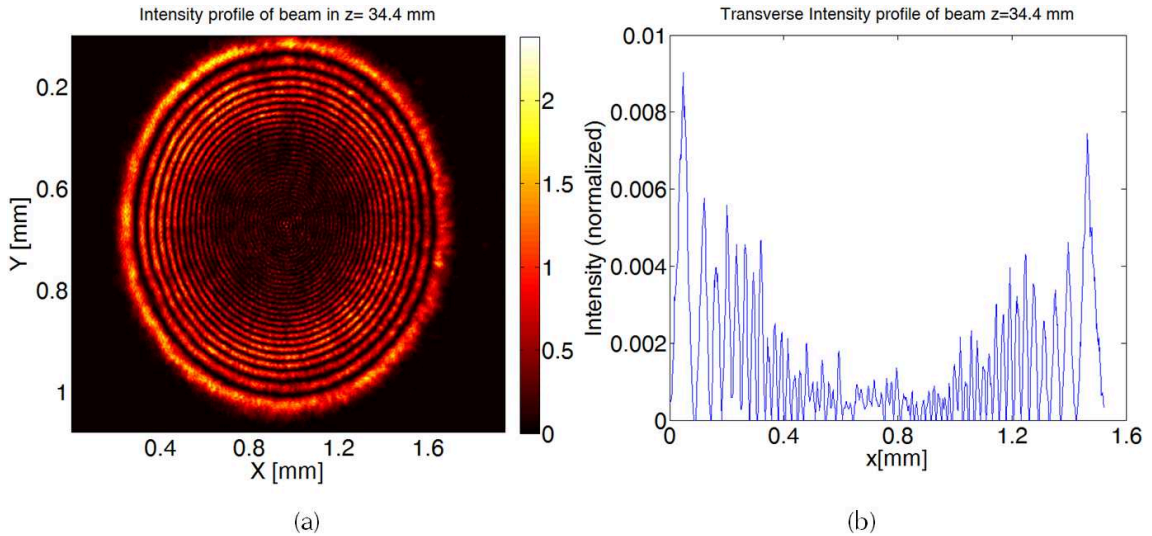


Figure 5.37: (a) Radial intensity distribution of dark hollow beam.  $z=34.4$  mm (b) On-axis intensity.

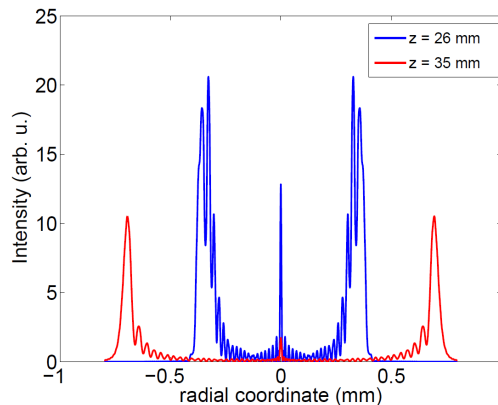


Figure 5.38: Calculated transverse intensity profile of the beam generated by the 4 rings-based axicons ( $\alpha=2.46^\circ$ ,  $R_c = 4.44$  mm, incident collimated Gaussian beam  $W_o=5$  mm, aperture radius  $\phi= 0.96$  mm) for 2 distinct longitudinal positions in the hollow zone.

In next table, position of maximum intensity and non-diffracting propagation distance of the two fabricated type of axicons are summarized. We can conclude that the higher radius of curvature in the 0.9 mm axicon delays, on one hand, the formation of the Bessel beam and, on the other hand, the apparition of the hollow beam after the non-diffracting zone, which is traduced in a larger non-diffracting zone. The smaller aperture employed in the 0.9 mm axicon has two effects. Firstly, it provokes the apparition of larger side lobes in the hollow beam zone that we do not observe in the 1.95 mm axicon. Secondly, as numerical aperture of the lens is reduced, the angle of the hollow beam in the 1.95

mm axicon is slightly larger ( $52.17^\circ$ ) than in the 0.9 mm axicon ( $48^\circ$ ). Both effects agree with simulations and experimental observations.

Diameter [mm]	$R_c$ [ $\mu\text{m}$ ]	$\alpha$	Position of max. [mm]	Non-diffracting zone[mm]	$Z_{max}$ [mm]
0.9	16930	$0.55^\circ$	26.4	20-36	16
1.95	4440	$2.46^\circ$	17.6	14-25	11

Table 5.5: Fitting results for fabricated lenses.

## 5.6/ ROUGHNESS AND REPEATABILITY OF BLOWING PROCESS

Low roughness of surface components is one advantage of this fabrication technique. As refractive surface of components is obtained with a contactless process, high quality surface, comparable to that of the bulk glass substrate, is assured. Before glass reflow, roughness values below 4.5 nm are obtained ( $R_q$ ). After annealing process at  $700^\circ\text{C}$  during 4 hours roughness increases up to 5 nm RMS in the two rings-based axicon and 25 nm RMS in the four rings-based axicon due to surface exposition in surrounding nitrogen gas flow and particles inside the furnace in course of the reflow step. To achieve optical quality in back side of lenses surface is polished with colloidal silica of 30 nm diameter, leading to roughness lower than 3 nm RMS. These values concerning surface quality are smaller than axicons obtained by computer numerical control (CNC) [Thorlabs, 2016] and comparable to ones obtained by grinding and polishing in freeform manufacturing [Infrared, 2009].

Regarding repeatability of reflow process, maximum sag variation from wafer to wafer are  $0.7 \mu\text{m}$  in case of four rings axicons out of  $42 \mu\text{m}$ , i.e. 1.7% variations and  $0.2\mu\text{m}$  out of  $4.36 \mu\text{m}$ , i.e.  $< 5 \%$  when two ring axicons are fabricated. Although this should not be critical for axicons applications, these alterations might be due to variations in cavities depth as a result of variations introduced by previous fabrication steps. We have to remind that, during silicon etching, reduction in the width value of cavities leads to variations in cavities depth. Cleanliness of substrates prior to anodic bonding is also very important, as minimum organic particles deposited onto the surface might lead to larger changes in the bulk of the glass wafer during the reflow step. TTV of glass substrate before reflow must also be considered as it represents alterations in the distance between etched cavities in silicon and upper surface of glass which affects glass thickness pushed in the surface and, then, sag of fabricated lens.

## 5.7/ CONCLUSIONS OF CHAPTER 5

In this chapter, technology of parallel glass blowing for microoptical components generation has been developed. First tests made in rectangular cavities were done to observe volume evolution of blown cavities inside glass and dimensions of glass deformations in upper surface of  $500 \mu\text{m}$  glass thickness substrate. Through these tests, conclusions



concerning cavity sizes and separations were obtained. It was observed that cavities smaller than  $15\ \mu\text{m}$  side do not introduce any change in glass surface so they are not employed in the reflow process. Concentric ring-shaped cavities were tested at  $800^\circ\text{C}$  and  $850^\circ\text{C}$  with different sizes and separations. Through these tests, it was observed that glass profiles are closer to conical axicon profile when size of the cavity (at constant depth) is half the size of previous one at constant separation. It was also observed that reflow process applied on glass-silicon stack at more than  $800^\circ\text{C}$  generates strong bowing. This drawback generates important inhomogeneities in glass thickness when silicon is grinded and polished. To avoid this effect reflow temperature was reduced down to  $700^\circ\text{C}$  and an annealing step of 3.5 hours was applied. With this solution, TTV is reduced to  $20\ \mu\text{m}$  and component profiles with flat conical surfaces can be generated.

In this thesis work axicons of 0.9 and 1.95 mm diameters have been successfully fabricated. Sag values of 4.36 and  $42\ \mu\text{m}$  and opening angles of  $0.55^\circ$  and  $2.46^\circ$  were measured. Optical performance of fabricated components have been tested and Bessel beam generation demonstrated. To the author's knowledge, this is the first generation of glass-based micro axicons fabricated through glass reflow process. This fabrication technique constitutes an alternative, less complex and cheaper than usual fabrication techniques like casting or surface grinding and polishing.

Practical use of axicons with sizes like the ones we generated can be found in the literature. Axicons with small opening angle ( $< 0.5^\circ$ ) are extensively employed in surface nanopatterning applications because of the extended depth of field of generated Bessel beams [Duocastella et al., 2012]. These components are preferred to spatial light modulators (SLM) as, even if they provide the widest range of intensity profiles, they tend to have relatively low damage thresholds limiting their field of use in material processing to low average power processes [Milne et al., 2008]. Examples of patterning applications can be found in fields like microdrilling where long depth of field (non-diffracting distance) increase the tolerance of the focal plane during processing, generating holes with same characteristics over long distances in materials like silicon [Kohno et al., 2004] or chromium [Amako et al., 2005]. Axicons with opening angles of  $1^\circ$  are also employed as optical tweezers for controlled rotation of microscopic particles [McGloin et al., 2003] or particle guiding along the Bessel beam axis over a distance of 1 mm [Arlt et al., 2001]. In [Anguiano-Morales et al., 2008], a combination of an amplitude mask and an axicon with an opening angle of  $0.5^\circ$  and 2.5 cm diameter (size achievable by both technologies proposed in this thesis work) are studied to generate field distributions that differ from the typical Bessel one and its possible applications in photonic structures or multiple-beam optical tweezers. These are just some examples to justify the practical interest of the proposed component in the field of microoptics.

Before comparing the two technologies we employed in the fabrication of the considered component, one remark about the evolution of the volume generated in etched cavities during the reflow step must be done. Since in the ideal gas law,  $PV = nRT$ ,  $n$  and  $R$  are both constants, the law can also be written as  $P_1V_1/T_1 = P_2V_2/T_2$  where subindex 1 and 2 correspond to the initial and final state of the gas inside the cavities.  $P_1$  corresponds to the pressure at which cavities were sealed (atmospheric pressure). The reflow is carried at atmospheric pressure inside the furnace and at the end of the heating process, the equilibrium state between gas inside the cavities and gas in the furnace is reached and

pressure inside cavities is equal to the atmospheric one again ( $P_2 = P_1$ ). So we can simplify the previous expression and calculate the volume generated inside the cavities as  $V_2 = (T_2/T_1)V_1$ , where  $T_2$  is the temperature at which the reflow step is performed,  $T_1$  is the temperature at which cavities were bonded ( $350^\circ\text{C}$ ) and  $V_1$  corresponds to the volume enclosed by the cavity.  $V_2$  can be then represented as a linear function with  $V_1$  where the slope of such function corresponds to the relation between temperature  $T_2/T_1$ .

In figure 5.39, the evolution of the area generated during reflow inside the glass is exposed as a function of the area of the cavity etched in silicon for two reflow temperatures,  $700^\circ\text{C}$  (blue line, temperature evolution during reflow represented in figure 5.23) and  $834^\circ\text{C}$  (green line, temperature with similar evolution as in figure 5.8). In the first case, we remind here that after reaching the temperature objective, we leave the stack during four hours at  $700^\circ\text{C}$  to release the stress caused in the process. Here, theoretical factor  $T_2/T_1 = 1.56$  which is larger than the slope of the experimental function (1.09). We believe that this inequality between theoretical and experimental observations is due to the fact that we still do not reach the equilibrium state between cavities and oven chamber due to high viscosity of glass at  $700^\circ\text{C}$  ( $10^7$  Pa-s) that does not allow volume to completely expand inside the cavities. This, nevertheless, does not prevent us from controlling the generated deformations and fabricate components with the desired conical shape. In the second case, temperature evolution of reflow is different and after reaching the maximum ( $834^\circ\text{C}$ ), the stack is cooled down.  $T_2/T_1 = 1.77$  and slope of experimental evolution closer (1.65). This might mean that gas inside cavities has still not reached the equilibrium state ( $P_2 = P_1$ ) or that temperature in cavities is not the same as in the oven chamber. One possible solution could be extend the reflow process some minutes at the objective temperature so volume inside cavities can reach the equilibrium state.

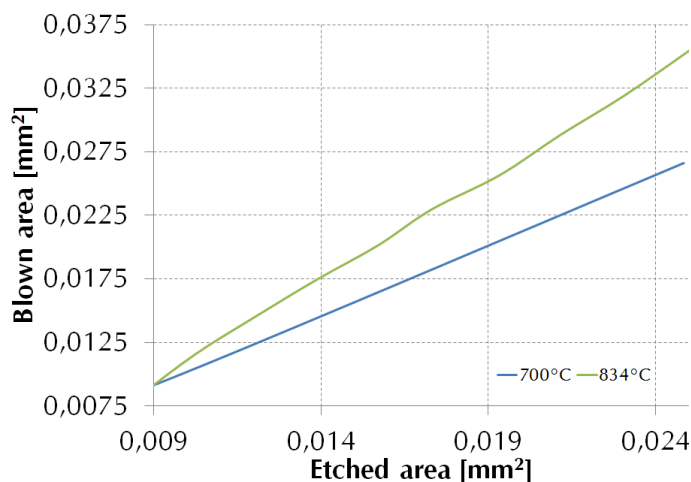


Figure 5.39: Evolution of blown area inside etched cavities as a function of the etched area.

Next, and last, chapter concerns the conclusions and perspectives of the work developed in this thesis work where available and achievable geometries of both technologies are studied for the generation of other components with complex profiles.

## GENERAL CONCLUSIONS AND PERSPECTIVES OF WORK

In this thesis work, two approaches have been studied and adapted for the parallel generation of optical components made of glass. One of them, well known and employed in several other laboratories, is variable dose laser beam lithography. Its capability to generate variable surface profiles in photoresist with subsequent etching in more robust substrates like glass or silicon has been one source of optical components fabrication for the last thirty years. In this work, exposure capabilities of Heidelberg DWL200 lithography system have been demonstrated and adapted to optical response of positive photoresist AZ-4562 of MicroChemicals for the generation of glass-based microaxicons. Microaxicons have been successfully fabricated. Nevertheless, as etching process of glass is characterized by low selectivity when it is transferred from such resist, total height of components in glass is limited to few micrometers. Moreover, long etching performed on photoresist provokes re-deposition of organic compounds and high roughness in glass surface was measured.

Then, the second technological approach based on glass microblowing was introduced. Induced deformations in glass substrate heated at annealing temperature have been controlled to generate the refractive surface of components. Glass-based microaxicons have been generated with this technique and demonstrated the ability for continuous surface relief components generation.

After characterization and calibration of both technologies employed in the fabrication of glass-based microaxicons, we can compare them in base of some important parameters of fabricated components like flatness, bluntness and roughness of generated optical surfaces. These analyses will serve to know the possibilities of these technologies for the direct fabrication of other type of components with more complex profiles.

- Considering **flatness** of generated profile, both technologies offer good results. In laser lithography, the controlled exposure of photoresist at different energy levels leads to the final shape of the components. Size and number of levels employed in the design will determine, along with the baking step, the flatness of the generated profiles. Vertical dimensions of components can be divided in a shorter or larger number of levels, always respecting the minimum feature size achievable by the writing lenses (0.9 and 2.5  $\mu\text{m}$  for the 4 and 10 mm focal length writing lens). If flat continuous profiles are desired,

---

designing the structures with large lateral size levels (between 50 and some hundreds of micrometers) could lead to long baking steps. In these cases, a certain change in the dimensions of the exposed profile is observed so short baking steps are then preferred to better control the generated surface. In this thesis work, microaxicons of 900  $\mu\text{m}$  diameter and 14.8  $\mu\text{m}$  thickness, divided in 27 levels, with an opening angle of  $\alpha=1.85^\circ$  have been demonstrated. Lateral size of steps is 33.3  $\mu\text{m}$  and 0.53  $\mu\text{m}$  height. In this case, a baking step at 120°C during only 5 seconds is enough to eliminate discontinuities between levels and achieve a flat and low roughness (25.86 nm RMS) in photoresist components. After etching, a degradation of the surface quality was observed due the long etching process to transfer the pattern into the glass surface. This effect has to be considered when component with sag values larger than 3  $\mu\text{m}$  are considered. In the second technology employed (glass reflow), flatness of profiles is defined by size and distance between cavities. For the fabrication of the considered component (or others where flat profiles are desired) several combinations placing cavities of different size and distance between them have been tested. Best results were observed when size of a ring is half of the previous one at constant separation. With this combination, flat profiles have been observed at 700°C and 850°C. Sag of deformed glass and opening angle of generated axicons is 42 and 119  $\mu\text{m}$  and 2.46° and 6.78°, respectively.

- Other parameter, very important in the considered component, is the **bluntness** generated on the tip of the axicon. We have seen how this bluntness reduces the efficiency of the non-diffracting beam formation, specially in short propagation distances. The bigger the radius of curvature generated, the more distance is needed to generate the Bessel beam as we observed in simulations and experiments. Both technologies are very flexible in the design of components so different radius of curvature can be generated. Concerning laser lithography, axicons generated in photoresist have a radius of curvature of 1.5 mm when level steps are 33.3  $\mu\text{m}$  wide and 0.53  $\mu\text{m}$  height. Bluntness on the tip is increased after the etching step to transfer the component into glass substrate. We remind that in this thesis work we have looked for the maximum thickness achievable in glass for fabricated components through double exposure of photoresist and long DRIE in glass. This last step provokes an increment of the radius of curvature until 10.87 mm, which provokes that Bessel beam formation is delayed to 15 mm distance in the optical axis from the axicon. These values can be reduced if smaller step levels are designed (limited by the minimum feature size of the writing lenses) with increased vertical dimensions or if thinner layers of photoresist are employed (so the etching of photoresist is shorter and re-deposition of organic materials does not modify the selectivity of the process). In the case of components fabricated by glass reflow, bluntness generated in the deformed surface of the substrate is defined by the size of the central cavity and thickness of the substrate. Radius of curvature of 0.44 mm and 16.9 mm have been measured in the 1.95 and 0.9 mm sag axicons. Here, formation of non-diffracting beams is observed at 14 and 20 mm distance from the axicon tip respectively. If thickness of substrate is reduced, isotropic deformations generated by the volume created inside the cavities have to propagate over a shorter distance to the upper surface and, then, larger deformations are induced in the glass surface. If thickness of glass substrate is reduced to some hundreds of micrometers, shape of deformed surface would be similar to the shape of the volume created inside the cavities, which, in the case of isolated cavities, would be mainly spherical with a radius of curvature proportional to the width of the etched cavity.

• Concerning **roughness** of profile of fabricated components, glass reflow offers clearly advantages compared to laser lithography, as profile is generated without any process performed directly onto the glass surface. Here, roughness values of generated components were 5 nm RMS in the axicons with 0.9 mm diameter and 25 nm RMS in the axicons fabricated with 1.95 mm diameter. These values are (respectively) 23 and 5 times lower than the one obtained in the surface generated after etching the photoresist components into glass (117 nm RMS). This is very convenient considering that the total amount of light scattered by a surface (TIS, Total Integrated Scatter) is related to the surface roughness according to the next equation [Bennett et al., 1961]:

$$TIS_{BP}(R_q) = R_0 \left[ 1 - e^{-\left(\frac{4\pi R_q \cos\theta_i}{\lambda}\right)^2} \right] \quad (6.1)$$

where  $R_0$  is the theoretical reflectance of the surface,  $R_q$  is the RMS roughness of the surface,  $\theta_i$  is the angle of incidence on the surface and  $\lambda$  is the wavelength of the incident radiation. The above definition of TIS and its paraxial smooth surface approximation (for normal incidence) is [Harvey et al., 2012]:

$$TIS \approx (4\pi R_q / \lambda)^2 \quad (6.2)$$

According to this expression, fabricated axicons have a TIS of 24% in the case of the axicon with 1.95 mm diameter and only 0.98% in the case of 0.9 mm diameter axicons which is comparable to values obtained in plastic surfaces generated by single point diamond turning [Eckhardt, 2016].

Short-term perspectives of work concern encountered problems like reducing the high roughness (up to 117 nm RMS) measured in components fabricated by laser lithography. CO<sub>2</sub> short laser pulses directly applied on glass surfaces have been demonstrated as a useful method to reduce roughness of components profile. Strong absorption of glass materials at  $\lambda = 10.5 \mu\text{m}$  provokes that only a very thin layer of material arrives to the softening point that flows because of the surface tension so small discontinuities are eliminated [Laguarta et al., 1994]. This solution has been applied to the polishing of microfluidic channels where the bottom part of the channel is irradiated with a pulsed CO<sub>2</sub> laser, decreasing the roughness value by more than three times [Serhatlioglu et al., 2016]. The quality of generated channels is studied to be applied in optical imaging. In [Vega et al., 1998], large spherical lenses of 80 mm diameter were previously heated over the transformation point of employed glass to avoid induced thermal stress. After high-power CO<sub>2</sub> laser irradiation, initial roughness measured in component was over 500 nm. After polishing process, RMS roughness values were around 1 nm. In this thesis work, rough values observed in components fabricated by laser lithography can be reduced with a similar treatment and some tests are planned to improve the surface quality of generated microaxicons.

Other problem found during this work was the observed bowing when bonded wafers were heated in the furnace at temperatures over 800°C. This is attributed to wafers different dilatations tend to bend the wafer stack. When temperature is over 850°C, TTV reached values over 300 μm. A first attempt to solve this problem was to apply an annealing step at 560°C during 3.5 hours after reflow in order to release generated

---

stress. In this way, TTV was reduced to  $119\mu\text{m}$ , which is still a high value. In addition, it can be noticed that because of bowing, liberated glass wafer after reflow was only 100 or  $200\mu\text{m}$  thickness, what made glass substrate very fragile and complicates its possible integration in other systems. Minimum TTV was measured when reflow was performed at lower temperature ( $700^\circ\text{C}$ ) during 4 hours. During silicon grinding, a glass substrate was employed as a support glued to the reflowed glass wafer to protect the fabricated components. Although this is a valid approach, blowing efficiency is limited as well as thickness of components generated in glass surface, since at this temperature, the latter is two or three times lower than for components generated at  $800^\circ\text{C}$  or  $850^\circ\text{C}$  (Table 5.2). In order to increase the range of achievable geometries in components generated by glass reflow through the use of larger reflow temperatures ranges, a solution could consist in sandwiching the glass wafer to be reflowed (Fig. 6.1) between 2 similar silicon wafers. The upper one being opened (through etching) on top of optical components to be blown. In addition to bowing limitation, this would also give a silicon frame able to support quite thin glass components.

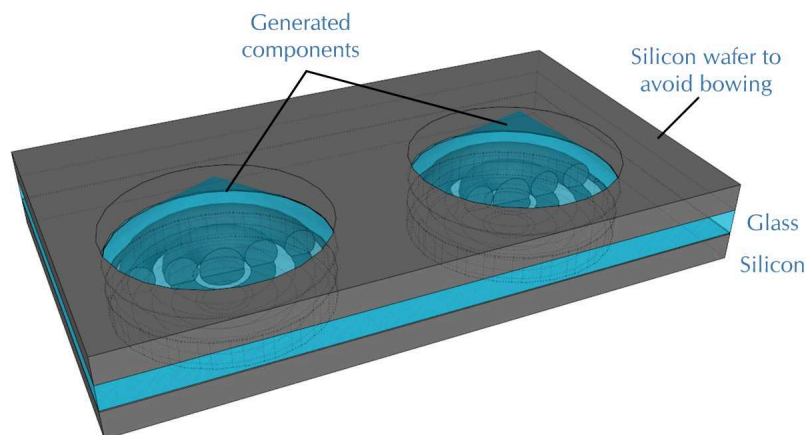


Figure 6.1: 3D schema of two silicon wafers bonded to a glass wafer to avoid wafer bowing during reflow.

Next figure represents a cross section schema. Here, a second silicon wafer is etched with holes large enough to allow the blowing process evolving (Fig. 6.2(a)). This wafer is then bonded to the previously bonded glass and silicon wafers, aligned above the cavities. During reflow, dilatations of silicon wafers (same CTE) should be compensated and, then, bowing effects canceled. By employing a second silicon wafer we should be able to reflow glass at higher temperature and generate components with larger sag values.

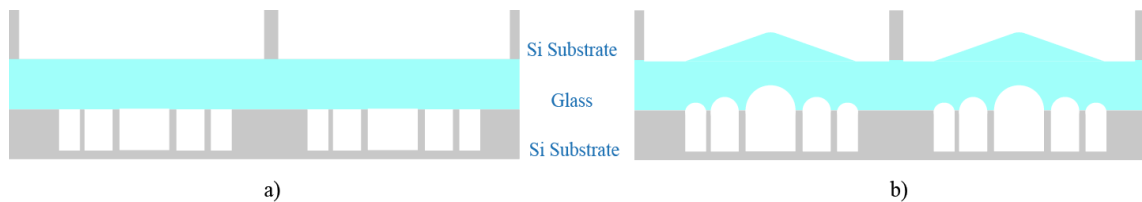


Figure 6.2: Cross section schema of two silicon wafers bonded to a glass wafer to avoid wafer bowing during reflow at temperatures over  $800^{\circ}\text{C}$ . (a) Before reflow. (b) After reflow

The two technologies are intended to be more generic and according to the 1<sup>st</sup> tests performed to generate microaxicons, we can try to analyze the achievable geometries we could generate with these two technologies.

In the case of laser lithography, vertical resolution achievable in photoresist observed during the calibration of resist and writing system was  $0.02\ \mu\text{m}$  for a single exposure at  $6.25\ \text{mW}$ . Lateral resolution is limited by the minimum feature size the system can achieve which is  $0.9$  and  $2.5\ \mu\text{m}$  for the  $4$  and  $10\ \text{mm}$  focal length writing lens respectively. In our experiments, levels with minimum step size were  $0.53\ \mu\text{m}$  height and  $3.5\ \mu\text{m}$  width. Maximum feature size is limited vertically to  $16.3\ \mu\text{m}$  reached with double exposure at maximum power, i.e.  $125\ \text{mW}$ . Components with horizontal dimensions ranging from few micrometers to some millimeters can be easily generated. If followed, the proposed recipes can lead to the fabrication of any component within the given dimensional limits. Redistribution of layers following the linearization expression can be employed to easily assign an energy dose in each point of the component surface opening this techniques to the fabrication of non-symmetrical free-forms.

In the case of components generated by glass reflow, isolated cavities have been reflowed at softening point of Borofloat to generate deformations in  $500\ \mu\text{m}$  thickness glass substrate with angles ranging from  $1.3^{\circ}$  to  $4.2^{\circ}$  and  $1.5\ \mu\text{m}$  to  $45\ \mu\text{m}$  sag. Shape of these deformations is mainly spherical but more versatile profiles can be generated by placing cavities of different sizes at defined positions. By doing this, glass-based components have been directly generated in glass surface at temperatures between  $700^{\circ}\text{C}$  and  $850^{\circ}\text{C}$  to obtain components with sag values from  $8.81\ \mu\text{m}$  to almost  $125\ \mu\text{m}$  and slope angles from  $1^{\circ}$  to  $9.5^{\circ}$ . Thickness of glass substrate is very important as all geometrical values measured in deformed glass are proportional to the distance between silicon and glass upper surface. Perspectives of work with this technology concern the fabrication of components based on thinner glass substrates. This would be possible if a silicon substrate is added as a support on the upper part of the glass wafer. We believe that if thickness of glass wafer is reduced (by purchasing thinner wafers or by polishing it) size of deformed surface can be reduced and, then, components with smaller feature size can be considered. This would be particularly interesting in the case of continuous diffractive components where the depth does not exceed few microns (phase shift  $< 2\pi$ ). From the analysis of isolated cavities heated at softening point (Fig. 5.12(a)), deformed surface is found linearly proportional to the width of the etched cavity. Using trigonometry relations (Fig. 6.3), we calculate that deformations propagate from silicon surface to glass upper surface with angles between  $27^{\circ}$  ( $100\ \mu\text{m}$  etched width) and  $45^{\circ}$  ( $200\ \mu\text{m}$  etched width) to the normal direction to silicon surface. Hence, we can

---

approximate the value of the deformed substrate if thickness of the glass wafer is reduced.

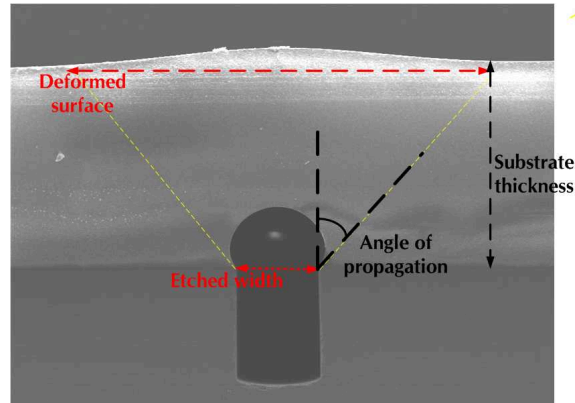


Figure 6.3: SEM image of cross section of reflowed cavity and measured parameters to obtain the propagation angle of deformations.

It is clear that final geometry of generated components is a function of several parameters like size and position of etched cavities, glass thickness substrate and reflow temperature. In this thesis work, we have characterized these parameters for glass substrates of  $500 \mu\text{m}$  thickness bonded to silicon wafers with  $300 \mu\text{m}$  deep cavities etched with different sizes. In order to obtain a complete calibration of the fabrication process, some experiments must still be done. Components with higher slope values could be considered if a reduction of the glass substrate before reflow is performed. At fixed temperature, angle of generated slopes in glass surface is increased by a factor proportional to the thickness of the substrate. A reduction of the glass substrate would also lead to noticeable changes in glass surface when small cavities are employed but these changes are difficult to predict with the available results. Nevertheless, this fabrication approach could be very versatile with a high degree of freedom in the design of components.

In the first chapter of this manuscript we talked about diffractive optical components (DOEs) and we saw that quantization of refractive profiles leads to maximum thickness reduced to  $t_{max} = \lambda/(n - 1)$ . This means that for applications in the visible spectrum, total thickness of single-order components can range between 1 and  $2 \mu\text{m}$ . In the case of laser beam lithography, we have probed the fabrication of  $3.7 \mu\text{m}$  thickness glass-based components. This thickness corresponds to a phase shift of  $5.5\pi$  at  $\lambda = 633\text{nm}$ , which means that the fabrication of multi-order diffractive components can be considered. In case of single-order diffractive lens fabrication, thickness values are easily achievable. If in the etching step we employ proposed recipe 2 (table 3.8), which would lead to a shorter etching process and, then, less rough surface, components in photoresist must have thickness values that range from 4 and  $7.5 \mu\text{m}$ . Spin coating of photoresist between 3000 and 5000 rpm leads to the desired layer thickness. Double exposure can be performed at 125 mW with 10 different levels within the requested range. If circular symmetrical components are considered, the achievable period of outermost zones is limited horizontally by the minimum feature size of the writing lens ( $2.5 \mu\text{m}$  in the case of the 10 mm focal length lens). Depending on diameter of considered component, if this period is too small to be generated by the proposed technology, the profile quantization can be made by multiples of  $2\pi$  (multi-order DOEs) since no changes are induced on



the monochromatic wave. Thickness of outer zones are, then, increased and their slope is decreased, being possible its fabrication. During the calibration of the lithography system, multi-order diffractive Fresnel lens of NA=0.1, 500  $\mu\text{m}$  diameter and 6.5  $\mu\text{m}$  thickness ( $\phi = 12\pi$ ) divided in 4 levels were generated in photoresist with 40 zones (Fig. 6.4).

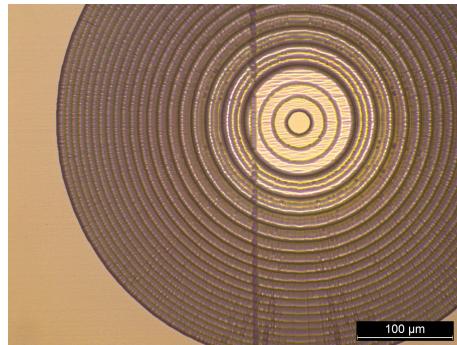


Figure 6.4: SEM image of cross section of reflowed cavity and measured parameters to obtain the propagation angle of deformations.

Generation of diffractive components by glass reflow is more challenging. First, a reduction of glass thickness should be performed because, as we have seen when working with 500  $\mu\text{m}$  thickness glass substrate, smallest deformed surface is 0.6 mm wide when employing isolated cavities. This fact implies that the diameter of the considered diffractive component would be some centimeters wide which would be impossible to integrate in most of optical systems. As we can not completely predict the geometry of deformed glass if substrate thickness is reduced, some experiments should be done with thinner glass substrates.

Different geometrical requirements of optical components lead us to employ one fabrication technique or another. In the case of diffractive lenses, as components are few microns deep, high resolutions are needed in order to generate local slopes with sharp phase jumps to obtain high efficiency. Here, laser lithography is the correct selection. Optical free-forms with small features could also be generated with this technique, as local variations of energy dose would lead to the variable profile necessary in the component. If pure refractive optical components are considered, sag values required in components are nearly impossible to be generated with this technology. The photoresist etching would lead to components too thin to change the characteristics of the incident wave front. This type of components, where aspheric lenses or axicons can be included, are more easily fabricated by glass reflow. Size of such components can be easily achieved with this fabrication approach, where reflow at different temperatures lead to sag values between few microns and more than 100  $\mu\text{m}$ . The characteristics of the fabrication technique lead to purely continuous profiles, necessary in this type of components.



# BIBLIOGRAPHY

- [Abe et al., 1999] Abe, S., et Sheridan, J. T. (1999). **Curvature correction model of droplet profiles**. *Physics Letters A*, 253(5):317–321.
- [Aebersold et al., 2010] Aebersold, J., Walsh, K., et Beggans, M. (2010). **Utilization of direct write lithography to develop ultra high aspect ratio (> 100: 1) drie silicon pillars**. In *2010 18th Biennial University/Government/Industry Micro/Nano Symposium*, pages 1–5. IEEE.
- [Albero et al., 2010] Albero, J., Gorecki, C., Nieradko, L., Päivänranta, B., Gomez, V., Thienpont, H., et Passilly, N. (2010). **Matrixes of unconventional micro-optical components molded with etched silicon**. *Journal of the European Optical Society-Rapid publications*, 5.
- [Albero et al., 2008] Albero, J., Nieradko, L., Gorecki, C., Ottevaere, H., Gomez, V., et Pietarinen, J. (2008). **Si moulds for glass and polymer microlenses replication**. In *Photonics Europe*, pages 69920A–69920A. International Society for Optics and Photonics.
- [Albero et al., 2009] Albero, J., Nieradko, L., Gorecki, C., Ottevaere, H., Gomez, V., Thienpont, H., Pietarinen, J., Päivänranta, B., et Passilly, N. (2009). **Fabrication of spherical microlenses by a combination of isotropic wet etching of silicon and molding techniques**. *Optics express*, 17(8):6283–6292.
- [Albero et al., 2014] Albero, J., Perrin, S., Bargiel, S., Baranski, M., Passilly, N., Gauthier-Manuel, L., et Gorecki, C. (2014). **Arrays of millimeter-sized glass lenses for miniature inspection systems**. In *SPIE Photonics Europe*, pages 91300U–91300U. International Society for Optics and Photonics.
- [Albero et al., 2015] Albero, J., Perrin, S., Bargiel, S., Passilly, N., Baranski, M., Gauthier-Manuel, L., Bernard, F., Lullin, J., Froehly, L., Krauter, J., et others (2015). **Dense arrays of millimeter-sized glass lenses fabricated at wafer-level**. *Optics express*, 23(9):11702–11712.
- [Albero et al., 2016] Albero, J., Perrin, S., Passilly, N., Krauter, J., Gauthier-Manuel, L., Froehly, L., Lullin, J., Bargiel, S., Osten, W., et Gorecki, C. (2016). **Wafer-level fabrication of multi-element glass lenses: lens doublet with improved optical performances**. *Optics letters*, 41(1):96–99.
- [Allcock et al., 1995] Allcock, G., Dyer, P., Elliner, G., et Snelling, H. (1995). **Experimental observations and analysis of co2 laser-induced microcracking of glass**. *Journal of applied physics*, 78(12):7295–7303.
- [Allresist, 2016] Allresist (2016). **Faqs concerning photoresists from allresist**.

- [Amako et al., 2005] Amako, J., Yoshimura, K., Sawaki, D., et Shimoda, T. (2005). **Laser-based microprocesses using diffraction-free beams generated by diffractive axicons**. In *Lasers and Applications in Science and Engineering*, pages 497–507. International Society for Optics and Photonics.
- [Amarie et al., 2005] Amarie, D., Rawlinson, N. D., Schaich, W. L., Dragnea, B., et Jacobson, S. C. (2005). **Three-dimensional mapping of the light intensity transmitted through nanoapertures**. *Nano letters*, 5(7):1227–1230.
- [Ams et al., 2009] Ams, M., Marshall, G. D., Dekker, P., Piper, J. A., et Withford, M. J. (2009). **Ultrafast laser written active devices**. *Laser & Photonics Reviews*, 3(6):535–544.
- [Anguiano-Morales et al., 2008] Anguiano-Morales, M., Martínez, A., Iturbe-Castillo, M. D., et Chávez-Cerda, S. (2008). **Different field distributions obtained with an axicon and an amplitude mask**. *Optics Communications*, 281(3):401–407.
- [Anner, 1990] Anner, G. (1990). **Planar processing primer van nostrand reinhold**. *New York*, p413.
- [Aristizabal et al., 2013] Aristizabal, S. L., Cirino, G. A., Montagnoli, A. N., Sobrinho, A. A., Rubert, J. B., Mansano, R. D., et others (2013). **Microlens array fabricated by a low-cost grayscale lithography maskless system**. *Optical Engineering*, 52(12):125101–125101.
- [Arlt et al., 2001] Arlt, J., Garces-Chavez, V., Sibbett, W., et Dholakia, K. (2001). **Optical micromanipulation using a bessel light beam**. *Optics Communications*, 197(4):239–245.
- [Audran et al., 2006] Audran, S., Faure, B., Mortini, B., Regolini, J., Schlatter, G., et Hadziioannou, G. (2006). **Study of mechanisms involved in photoresist microlens formation**. *Microelectronic engineering*, 83(4):1087–1090.
- [Bacon et al., 1959] Bacon, J. F., et Hasapis, A. A. (1959). **Viscosity of molten silica**. *Journal of Applied Physics*, 30(9):1470–1471.
- [Badar, 2012] Badar, F. (2012). **Fabrication of microlens in polymers with thermal reflow**.
- [Bae et al., 2010] Bae, Y. C., Liu, Y., Cardolaccia, T., et Trefonas III, P. (2010). **Compositions and methods for multiple exposure photolithography**. US Patent App. 12/781,486.
- [Baranski et al., 2014] Baranski, M., Perrin, S., Passilly, N., Froehly, L., Albero, J., Bargiel, S., et Gorecki, C. (2014). **A simple method for quality evaluation of micro-optical components based on 3d ipsf measurement**. *Optics express*, 22(11):13202–13212.
- [Bass et al., 2001] Bass, M., Van Stryland, E. W., Williams, D. R., et Wolfe, W. L. (2001). **Handbook of optics**, volume 2. McGraw-Hill New York.
- [Beauchemin et al., 1994] Beauchemin, B., Ebersole, C., et Daraktchiev, I. (1994). **The influence of absorbed solvent on novolak and resist film dissolution and thermal behavior**.

- [Beich, 2005] Beich, W. S. (2005). **Injection molded polymer optics in the 21st century**. In *Optics & Photonics 2005*, pages 58650J–58650J. International Society for Optics and Photonics.
- [Bennett et al., 1961] Bennett, H., et Porteus, J. (1961). **Relation between surface roughness and specular reflectance at normal incidence**. *JOSA*, 51(2):123–129.
- [Bernacki et al., 1995] Bernacki, B. E., Miller Jr, A. C., Maxey, L. C., Cunningham, J. P., Moreshead, W. V., et Noguès, J.-L. R. (1995). **Hybrid optics for the visible produced by bulk casting of sol-gel glass using diamond-turned molds**. In *SPIE's 1995 International Symposium on Optical Science, Engineering, and Instrumentation*, pages 463–474. International Society for Optics and Photonics.
- [Berry et al., 2007] Berry, M., Bloembergen, N., Erez, N., Greenberger, D., et Wolf, E. (2007). **Progress in Optics**, volume 50. Elsevier.
- [Bertsch et al., 1999] Bertsch, A., Lorenz, H., et Renaud, P. (1999). **3d microfabrication by combining microstereolithography and thick resist uv lithography**. *Sensors and Actuators A: Physical*, 73(1):14–23.
- [Biesenbach et al., 1994] Biesenbach, J., Loosen, P., Treusch, H.-G., Krause, V., Koesters, A., Zamel, S., et Hilgers, W. (1994). **Fabrication of aspheric cylindrical microlenses with the diamond turning technology**. In *Proceedings of the SPIE*, volume 2263, pages 152–163.
- [Bodas et al., 2007] Bodas, D., et Khan-Malek, C. (2007). **Direct patterning of quantum dots on structured pdms surface**. *Sensors and Actuators B: Chemical*, 128(1):168–172.
- [Bogdanov et al., 2000] Bogdanov, A., et Peredkov, S. (2000). **Use of su-8 photoresist for very high aspect ratio x-ray lithography**. *Microelectronic Engineering*, 53(1):493–496.
- [Bogdanov, ] Bogdanov, A. L. **Use of su-8 negative photoresist for optical mask manufacturing max-lab, university of lund, se-221 00, lund sweden.[online] pp. 1-11.**
- [Bogdanov, 2000] Bogdanov, A. L. (2000). **Su-8 negative photoresist for optical mask manufacturing**. In *Microlithography 2000*, pages 1215–1225. International Society for Optics and Photonics.
- [Borrelli et al., 1985] Borrelli, N. F., Morse, D. L., Bellman, R. H., et Morgan, W. L. (1985). **Photolytic technique for producing microlenses in photosensitive glass**. *Applied optics*, 24(16):2520–2525.
- [Bowen et al., 1994] Bowen, J., Blough, C., et Wong, V. (1994). **Otud5 fabrication of optical surfaces by laser pattern generation**. *TECHNICAL DIGEST SERIES-OPTICAL SOCIETY OF AMERICA*, 13:153–153.
- [Brinksmeier et al., 2012] Brinksmeier, E., Riemer, O., et Gläbe, R. M. (2012). **Fabrication of complex optical components: from mold design to product**. Springer Science & Business Media.
- [Brow, 2004] Brow, R. (2004). **Introduction to glass science**. *Cer103*.

- [Brugger et al., 1997] Brugger, J., Beljakovic, G., Despont, M., De Rooij, N., et Vettiger, P. (1997). **Silicon micro/nanomechanical device fabrication based on focused ion beam surface modification and koh etching.** *Microelectron Engineering*, 35(LMIS1-ARTICLE-2005-015):401–404.
- [Brunet et al., 2002] Brunet, M., O'Donnell, T., O'Brien, J., McCloskey, P., et Mathuna, S. C. O. (2002). **Thick photoresist development for the fabrication of high aspect ratio magnetic coils.** *Journal of Micromechanics and Microengineering*, 12(4):444.
- [Brzobohatý et al., 2008] Brzobohatý, O., Cižmár, T., et Zemánek, P. (2008). **Quasi-bessel beam generated by oblate-tip axicon.** In *16th Polish-Slovak-Czech Optical Conference on Wave and Quantum Aspects of Contemporary Optics*, pages 714126–714126. International Society for Optics and Photonics.
- [Campbell et al., 2008] Campbell, S. A., Campbell, S. A., et Stephen, A. C. (2008). **Fabrication engineering at the micro-and nanoscale.** Number Sirsi) i9780195320176.
- [Cao et al., 1998] Cao, L., Li, B., et Zhao, J. H. (1998). **Etching of sic using inductively coupled plasma.** *Journal of the Electrochemical Society*, 145(10):3609–3612.
- [Cao et al., 2013] Cao, Z., Wang, K., Wu, S., et Wu, Q. (2013). **Fabrication of refractive axicons utilizing electrostatic force.** *Optik-International Journal for Light and Electron Optics*, 124(18):3761–3763.
- [Chen, 1983] Chen, B. (1983). **Investigation of the solvent-evaporation effect on spin coating of thin films.** *Polymer Engineering & Science*, 23(7):399–403.
- [Chen et al., 2010] Chen, F., Liu, H., Yang, Q., Wang, X., Hou, C., Bian, H., Liang, W., Si, J., et Hou, X. (2010). **Maskless fabrication of concave microlens arrays on silica glasses by a femtosecond-laser-enhanced local wet etching method.** *Optics express*, 18(19):20334–20343.
- [Cheng et al., 2002] Cheng, Y., Huang, T.-y., et Chieng, C.-C. (2002). **Thick-film lithography using laser write.** *Microsystem Technologies*, 9(1-2):17–22.
- [Chopra, 2015] Chopra, J. (2015). **Analysis of lithography based approaches in development of semi conductors.** *arXiv preprint arXiv:1502.05887*.
- [Chou et al., 1995] Chou, S. Y., Krauss, P. R., et Renstrom, P. J. (1995). **Imprint of sub-25 nm vias and trenches in polymers.** *Applied physics letters*, 67(21):3114–3116.
- [Clariant, 2002] Clariant (2002). **Az developer, 400k, and 421k inorganic developers.**
- [Clariant, 2013] Clariant (2013). **Az 4500 series thick film photoresists. product data sheet.**
- [Cowie, 1994] Cowie, J. (1994). **Wet development of polymer resists: A guide to solvent selection.** *Advanced Materials for Optics and Electronics*, 4(2):155–163.
- [Czajkowski, ] Czajkowski, A. **Specifying an aspheric surface.**
- [Daly et al., 1990] Daly, D., Stevens, R., Hutley, M., et Davies, N. (1990). **The manufacture of microlenses by melting photoresist.** *Measurement Science and Technology*, 1(8):759.



- [Daniel et al., 1999] Daniel, J., et Moore, D. (1999). **A microaccelerometer structure fabricated in silicon-on-insulator using a focused ion beam process.** *Sensors and Actuators A: Physical*, 73(3):201–209.
- [Davis et al., 1996] Davis, J. A., Carcole, E., et Cottrell, D. M. (1996). **Range-finding by triangulation with nondiffracting beams.** *Applied optics*, 35(13):2159–2161.
- [Dépret et al., 2002] Dépret, B., Verkerk, P., et Hennequin, D. (2002). **Characterization and modelling of the hollow beam produced by a real conical lens.** *Optics communications*, 211(1):31–38.
- [Dill et al., 1975] Dill, F. H., Hornberger, W. P., Hauge, P. S., et Shaw, J. M. (1975). **Characterization of positive photoresist.** *IEEE Transactions on electron devices*, 22(7):445–452.
- [Ding et al., 2002] Ding, Z., Ren, H., Zhao, Y., Nelson, J. S., et Chen, Z. (2002). **High-resolution optical coherence tomography over a large depth range with an axicon lens.** *Optics Letters*, 27(4):243–245.
- [Dudley et al., 2003] Dudley, D., Duncan, W. M., et Slaughter, J. (2003). **Emerging digital micromirror device (dmd) applications.** In *Micromachining and Microfabrication*, pages 14–25. International Society for Optics and Photonics.
- [Dunkel et al., 2012] Dunkel, J., Wippermann, F., Brückner, A., Bräuer, A., et Tünnermann, A. (2012). **Laser lithographic approach to micro-optical freeform elements with extremely large sag heights.** *Optics express*, 20(4):4763–4775.
- [Duocastella et al., 2012] Duocastella, M., et Arnold, C. B. (2012). **Bessel and annular beams for materials processing.** *Laser & Photonics Reviews*, 6(5):607–621.
- [Dziuban, 2007] Dziuban, J. A. (2007). **Bonding in microsystem technology**, volume 24. Springer Science & Business Media.
- [Eckhardt, 2016] Eckhardt (2016). **Optical scattering and surface roughness.**
- [Ehbets et al., 1992] Ehbets, P., Gale, M., Herzig, H., et Prongué, D. (1992). **High-efficiency continuous surface-relief gratings for two-dimensional array generation.** *Optics letters*, 17(13):908–910.
- [Ehrenstein et al., 2012] Ehrenstein, G. W., Riedel, G., et Trawiel, P. (2012). **Thermal analysis of plastics: theory and practice.** Carl Hanser Verlag GmbH Co KG.
- [Eisner et al., 1996] Eisner, M., et Schwider, J. (1996). **Transferring resist microlenses into silicon by reactive ion etching.** *Optical Engineering*, 35(10):2979–2982.
- [Ekhorutomwen et al., 1996] Ekhorutomwen, S., et Sawan, S. P. (1996). **Critical review on photoresists.** In *Polymers in Optics: Physics, Chemistry, and Applications*, pages 214–238.
- [Eklund et al., 2007] Eklund, E. J., et Shkel, A. M. (2007). **Glass blowing on a wafer level.** *Journal of microelectromechanical systems*, 16(2):232–239.
- [Eklund et al., 2008] Eklund, E. J., Shkel, A. M., Knappe, S., Donley, E., et Kitching, J. (2008). **Glass-blown spherical microcells for chip-scale atomic devices.** *Sensors and Actuators A: Physical*, 143(1):175–180.

- [El-Kareh, ] El-Kareh, B. **Fundamentals of semiconductor processing technologies.** 1995. Norwell, Massachusetts: Kluwer Academic Publisher.
- [EVGroup, 2016a] EVGroup (2016a). **Evg 501 wafer bonding system.**
- [EVGroup, 2016b] EVGroup (2016b). **Evg 620 automated mask alignment system.**
- [Faklis et al., 1995] Faklis, D., et Morris, G. M. (1995). **Spectral properties of multiorder diffractive lenses.** *Applied Optics*, 34(14):2462–2468.
- [Fang et al., 2013] Fang, F., Zhang, X., Weckenmann, A., Zhang, G., et Evans, C. (2013). **Manufacturing and measurement of freeform optics.** *CIRP Annals-Manufacturing Technology*, 62(2):823–846.
- [FEMTO-ST, 2015a] FEMTO-ST (2015a). **Bati de gravure rie-ccp (plassys).**
- [FEMTO-ST, 2015b] FEMTO-ST (2015b). **Masqueur lithographie optique heidelberg dwl 200.**
- [FEMTO-ST, 2016a] FEMTO-ST (2016a). **Bâti de gravure drie-icp silicium (rapier spts).**
- [FEMTO-ST, 2016b] FEMTO-ST (2016b). **CI200 cleaner bonder. ir200 inspection module.**
- [FEMTO-ST, 2016c] FEMTO-ST (2016c). **Four triple tube pour oxydation et traitements thermiques.**
- [Feng et al., 1996] Feng, M., Guo, J., Lu, Y., et Chang, E. (1996). **Reactive ion etching of gan with bcl 3/sf 6 plasmas.** *Materials chemistry and physics*, 45(1):80–83.
- [Ferrer et al., 2007] Ferrer, A., Diez-Blanco, V., Ruiz, A., Siegel, J., et Solis, J. (2007). **Deep subsurface optical waveguides produced by direct writing with femtosecond laser pulses in fused silica and phosphate glass.** *Applied Surface Science*, 254(4):1121–1125.
- [Fischer et al., 2000] Fischer, R. E., Tadic-Galeb, B., Yoder, P. R., et Galeb, R. (2000). **Optical system design.** Citeseer.
- [Fluegel, 2007] Fluegel, A. (2007). **Glass viscosity calculation based on a global statistical modelling approach.** *Glass Technology-European Journal of Glass Science and Technology Part A*, 48(1):13–30.
- [Fujita et al., 1982] Fujita, T., Nishihara, H., et Koyama, J. (1982). **Blazed gratings and fresnel lenses fabricated by electron-beam lithography.** *Optics letters*, 7(12):578–580.
- [Gale, 1997a] Gale, M. (1997a). **Direct writing of continuous-relief micro-optics.** Taylor & Francis, London.
- [Gale et al., 1994a] Gale, M., Rossi, M., Kunz, R., et Bona, G. (1994a). **Laser writing and replication of continuous-relief fresnel microlenses.** *TECHNICAL DIGEST SERIES-OPTICAL SOCIETY OF AMERICA*, 11:306–306.
- [Gale, 1997b] Gale, M. T. (1997b). **Replication techniques for diffractive optical elements.** *Microelectronic Engineering*, 34(3):321–339.



- [Gale et al., 1983] Gale, M. T., et Knop, K. (1983). **The fabrication of fine lens arrays by laser beam writing**. In *1983 International Technical Conference/Europe*, pages 347–353. International Society for Optics and Photonics.
- [Gale et al., 1992] Gale, M. T., Lang, G., Raynor, J., Schütz, H., et Prongué, D. (1992). **Fabrication of kinoform structures for optical computing**. *Applied optics*, 31(26):5712–5715.
- [Gale et al., 1991] Gale, M. T., Lang, G. K., Raynor, J. M., et Schuetz, H. (1991). **Fabrication of micro-optical components by laser beam writing in photoresist**. In *ECO4 (The Hague'91)*, pages 65–70. International Society for Optics and Photonics.
- [Gale et al., 1994b] Gale, M. T., Rossi, M., Pedersen, J., et Schuetz, H. (1994b). **Fabrication of continuous-relief micro-optical elements by direct laser writing in photoresists**. *Optical Engineering*, 33(11):3556–3566.
- [Gary E. Flores, 2016] Gary E. Flores, Warren W. Flack, E. T. (2016). **An investigation of the properties of thick photoresist film**.
- [Gattass et al., 2008] Gattass, R. R., et Mazur, E. (2008). **Femtosecond laser micromachining in transparent materials**. *Nature photonics*, 2(4):219–225.
- [Genkin et al., 1994] Genkin, V. N., et Myl'nikov, M. (1994). **Correlation between the sensitivity and the contrast of polymer resists for developing in good and bad solvents**. In *SPIE's 1994 Symposium on Microlithography*, pages 752–754. International Society for Optics and Photonics.
- [GmbH, 2016] GmbH, M. P. M. (2016). **Az 4500 series. general information**.
- [Gower, 2000] Gower, M. C. (2000). **Industrial applications of laser micromachining**. *Optics Express*, 7(2):56–67.
- [Grigorescu et al., 2009] Grigorescu, A., et Hagen, C. (2009). **Resists for sub-20-nm electron beam lithography with a focus on hsq: state of the art**. *Nanotechnology*, 20(29):292001.
- [Guerin et al., 1997] Guerin, L., Bossel, M., Demierre, M., Calmes, S., et Renaud, P. (1997). **Simple and low cost fabrication of embedded micro-channels by using a new thick-film photoplastic**. In *Transducers*, volume 97, pages 1419–1422.
- [Hanak et al., 1973] Hanak, J., et Russell, J. (1973). **Sputter-etching technique for recording holograms or other fine-detail relief patterns in hard durable materials**. US Patent 3,733,258.
- [Harriott et al., 1986] Harriott, L., Scotti, R., Cummings, K., et Ambrose, A. (1986). **Micromachining of integrated optical structures**. *Applied physics letters*, 48(25):1704–1706.
- [Haruna et al., 1990] Haruna, M., Takahashi, M., Wakahayashi, K., et Nishihara, H. (1990). **Laser beam lithographed micro-fresnel lenses**. *Applied optics*, 29(34):5120–5126.
- [Harvey et al., 2012] Harvey, J. E., Schröder, S., Choi, N., et Duparré, A. (2012). **Total integrated scatter from surfaces with arbitrary roughness, correlation widths, and incident angles**. *Optical Engineering*, 51(1):013402–1.

- [Harvey, 1997] Harvey, T. G. (1997). **Replication techniques for micro-optics**. In *Lasers and Optics in Manufacturing III*, pages 76–82. International Society for Optics and Photonics.
- [Hatakoshi et al., 1990] Hatakoshi, G., Amano, A., Ueda, K., Kawachi, M., Terashima, K., et Uematsu, Y. (1990). **Grating axicon for collimating čerenkov radiation waves**. *Optics letters*, 15(23):1336–1338.
- [Häusler et al., 1988] Häusler, G., et Heckel, W. (1988). **Light sectioning with large depth and high resolution**. *Applied Optics*, 27(24):5165–5169.
- [He et al., 2015] He, C., Zong, W., Cao, Z., et Sun, T. (2015). **Theoretical and empirical coupled modeling on the surface roughness in diamond turning**. *Materials & Design*, 82:216–222.
- [Heckele et al., 2003] Heckele, M., et Schomburg, W. (2003). **Review on micro molding of thermoplastic polymers**. *Journal of Micromechanics and Microengineering*, 14(3):R1.
- [Herman et al., 1991] Herman, R., et Wiggins, T. (1991). **Production and uses of diffractionless beams**. *JOSA A*, 8(6):932–942.
- [Herzig, 1997] Herzig, H. P. (1997). **Micro-optics: elements, systems and applications**. CRC Press.
- [Herzig et al., 2001] Herzig, H. P., Schilling, A., Stauffer, L., Vokinger, U., et Rossi, M. (2001). **Efficient beamshaping of high-power diode lasers using micro-optics**. In *International Symposium on Optical Science and Technology*, pages 134–141. International Society for Optics and Photonics.
- [Hocheng et al., 2004] Hocheng, H., et Hsieh, M. (2004). **Signal analysis of surface roughness in diamond turning of lens molds**. *International Journal of Machine Tools and Manufacture*, 44(15):1607–1618.
- [Hoerni, 1959] Hoerni, J. (1959). **Patent no. 3025589**.
- [Hrma, 2008] Hrma, P. (2008). **Glass viscosity as a function of temperature and composition: A model based on adam–gibbs equation**. *Journal of Non-Crystalline Solids*, 354(29):3389–3399.
- [Huang et al., 2014] Huang, H., Chen, S., Zou, H., Li, Q., Fu, J., Lin, F., et Wu, X. (2014). **Fabrication of micro-axicons using direct-laser writing**. *Optics express*, 22(9):11035–11042.
- [Infrared, 2009] Infrared, I.-V. (2009). **Diamond turning capabilities**.
- [ioffe., 2016] ioffe. (2016). **Si-silicon**.
- [Ivanov, 1992] Ivanov, V. S. (1992). **Radiation chemistry of polymers**, volume 5. Vsp.
- [Jaeger et al., ] Jaeger, R. C., Neudeck, G. W., et Pierret, R. F. **Introduction to micro-electronic fabrication, 2002**.
- [Jahns et al., 1992] Jahns, J., Brenner, K., Däschner, W., Doubrava, C., et Merklein, T. (1992). **Replication of diffractive microoptical elements using a pmma molding technique**. *Optik*, 89(3):98–100.

- [Jansen et al., 1996] Jansen, H., Gardeniers, H., de Boer, M., Elwenspoek, M., et Fluitman, J. (1996). **A survey on the reactive ion etching of silicon in microtechnology**. *Journal of micromechanics and microengineering*, 6(1):14.
- [Jiao et al., 2006] Jiao, X., Wang, P., Zhang, D., Tang, L., Xie, J., et Ming, H. (2006). **Numerical simulation of nanolithography with the subwavelength metallic grating waveguide structure**. *Optics express*, 14(11):4850–4860.
- [Juodkazis et al., 2009] Juodkazis, S., Mizeikis, V., et Misawa, H. (2009). **Three-dimensional microfabrication of materials by femtosecond lasers for photonics applications**. *Journal of Applied Physics*, 106(5):051101.
- [Kalus et al., 1998] Kalus, M., Frey, M., Buchmann, L.-M., Reimer, K., et Wagner, B. (1998). **Free 3d shaping with grey-tone lithography and multidose e-beam writing**. *Microelectronic engineering*, 41:461–464.
- [Kaste et al., 2014] Kaste, N., Filbert, A., Mescheder, U., Rang, T., et Rang, G. (2014). **Process development for 3d laser lithography**. *WIT Transactions on The Built Environment*, 137:139–150.
- [Kemme, 2009] Kemme, S. (2009). **Microoptics and nanooptics fabrication**. CRC Press.
- [Kim et al., 2013] Kim, J. M., Dutta, P. S., Brown, E., Borrego, J. M., et Greiff, P. (2013). **Wafer-scale processing technology for monolithically integrated gasb thermophotovoltaic device array on semi-insulating gaas substrate**. *Semiconductor Science and Technology*, 28(6):065002.
- [Kley, 1997] Kley, E.-B. (1997). **Continuous profile writing by electron and optical lithography**. *Microelectronic Engineering*, 34(3):261–298.
- [Kohno et al., 2004] Kohno, M., et Matsuoka, Y. (2004). **Microfabrication and drilling using diffraction-free pulsed laser beam generated with axicon lens**. *JSME International Journal Series B Fluids and Thermal Engineering*, 47(3):497–500.
- [Kong et al., 2002] Kong, S.-M., Choi, H.-J., Lee, B.-T., Han, S.-Y., et Lee, J. (2002). **Reactive ion etching of sic using c2f6/o2 inductively coupled plasma**. *Journal of electronic materials*, 31(3):209–213.
- [Koukharenko et al., 2005] Koukharenko, E., Kraft, M., Ensell, G., et Hollinshead, N. (2005). **A comparative study of different thick photoresists for mems applications**. *Journal of Materials Science: Materials in Electronics*, 16(11-12):741–747.
- [Kruse et al., 2016] Kruse, K., Burrell, D., et Middlebrook, C. (2016). **Three-dimensional patterning in polymer optical waveguides using focused ion beam milling**. *Journal of Micro/Nanolithography, MEMS, and MOEMS*, 15(3):034505–034505.
- [Kufner et al., 1993] Kufner, M., Kufner, S., Frank, M., Moisel, J., et Testorf, M. (1993). **Microlenses in pmma with high relative aperture: a parameter study**. *Pure and Applied Optics: Journal of the European Optical Society Part A*, 2(1):9.
- [Kuiper et al., 2001] Kuiper, S., van Wolferen, H., van Rijn, C., Nijdam, W., Krijnen, G., et Elwenspoek, M. (2001). **Fabrication of microsieves with sub-micron pore size by laser interference lithography**. *Journal of Micromechanics and Microengineering*, 11(1):33.

- [Kweon et al., 2007] Kweon, G., et Kim, C. (2007). **Aspherical lens design by using a numerical analysis**. *JOURNAL-KOREAN PHYSICAL SOCIETY*, 51(1):93.
- [Kyser et al., 1974] Kyser, D., et Murata, K. (1974). **Quantitative electron microprobe analysis of thin films on substrates**. *IBM Journal of Research and Development*, 18(4):352–363.
- [LAAS/CNRS, 2016a] LAAS/CNRS (2016a). **Lithographie laser : Dwl 200**.
- [LAAS/CNRS, 2016b] LAAS/CNRS (2016b). **Manufacturing of chromium masks and reticles**.
- [Laermer et al., 1996] Laermer, F., et Schilp, A. (1996). **Method of anisotropically etching silicon**. US Patent 5,501,893.
- [Laguarta et al., 1994] Laguarta, F., Lupon, N., et Armengol, J. (1994). **Optical glass polishing by controlled laser surface-heat treatment**. *Applied optics*, 33(27):6508–6513.
- [LeCompte et al., 2001] LeCompte, M., Gao, X., et Prather, D. W. (2001). **Photoresist characterization and linearization procedure for the gray-scale fabrication of diffractive optical elements**. *Applied Optics*, 40(32):5921–5927.
- [Lee et al., 2008] Lee, E., et Hahn, J. W. (2008). **The effect of photoresist contrast on the exposure profiles obtained with evanescent fields of nanoapertures**. *Journal of Applied Physics*, 103(8):083550.
- [Lee et al., 2000] Lee, J.-M., Chang, K.-M., Kim, S.-W., Huh, C., Lee, I.-H., et Park, S.-J. (2000). **Dry etch damage in n-type gan and its recovery by treatment with an  $n \sim 2$  plasma**. *Journal of Applied Physics*, 87(11):7667–7670.
- [Lehar et al., 2001] Lehar, O. P., Spak, M. A., Meyer, S., Dammel, R. R., Brodsky, C. J., et Willson, C. G. (2001). **Resist rehydration during thick film processing**. In *26th Annual International Symposium on Microlithography*, pages 463–474. International Society for Optics and Photonics.
- [Li et al., 2009] Li, X.-F., Winfield, R., O'Brien, S., et Crean, G. (2009). **Application of bessel beams to 2d microfabrication**. *Applied Surface Science*, 255(10):5146–5149.
- [Lorenz et al., 1998] Lorenz, H., Despont, M., Fahrni, N., Brugger, J., Vettiger, P., et Renaud, P. (1998). **High-aspect-ratio, ultrathick, negative-tone near-uv photoresist and its applications for mems**. *Sensors and Actuators A: Physical*, 64(1):33–39.
- [Lu et al., 2006] Lu, Y., Mapili, G., Suhali, G., Chen, S., et Roy, K. (2006). **A digital micro-mirror device-based system for the microfabrication of complex, spatially patterned tissue engineering scaffolds**. *Journal of Biomedical Materials Research Part A*, 77(2):396–405.
- [Lullin et al., 2015] Lullin, J., Bargiel, S., Lemoal, P., Perrin, S., Albero, J., Passilly, N., Froehly, L., Lardet-Vieudrin, F., et Gorecki, C. (2015). **An electrostatic vertical microscanner for phase modulating array-type mirau microinterferometry**. *Journal of Micromechanics and Microengineering*, 25(11):115013.
- [Luxorion, 2016] Luxorion (2016). **Astigmatism (iii)**.

- [Mack, 1994] Mack, C. (1994). **The lithography tutor**. *Microlithography World*, Winter.
- [Mack, 2008] Mack, C. (2008). **Fundamental principles of optical lithography: the science of microfabrication**. John Wiley & Sons.
- [Mack, 1988] Mack, C. A. (1988). **Absorption and exposure in positive photoresist**. *Applied Optics*, 27(23):4913–4919.
- [Mack, 1998] Mack, C. A. (1998). **Modeling solvent effects in optical lithography**. University of Texas at Austin.
- [Mack et al., 1994] Mack, C. A., DeWitt, D. P., Tsai, B. K., et Yetter, G. (1994). **Modeling of solvent evaporation effects for hot plate baking of photoresist**. In *SPIE's 1994 Symposium on Microlithography*, pages 584–595. International Society for Optics and Photonics.
- [Madou, 2002] Madou, M. J. (2002). **Fundamentals of microfabrication: the science of miniaturization**. CRC press.
- [Mahajan, 1998] Mahajan, V. N. (1998). **OPTICAL IMAGING AND ABERRATIONS: PART I: RAY GEOMETRICAL OPTICS**. Bellingham: SPIE-The International Society for Optical Engineering.
- [McClure, 1991] McClure, E. (1991). **Manufacturers turn precision optics with diamond**. *Laser Focus World*, 27(2):95–105.
- [McGloin et al., 2005] McGloin, D., et Dholakia, K. (2005). **Bessel beams: diffraction in a new light**. *Contemporary Physics*, 46(1):15–28.
- [McGloin et al., 2003] McGloin, D., Garcés-Chávez, V., et Dholakia, K. (2003). **Interfering bessel beams for optical micromanipulation**. *Optics letters*, 28(8):657–659.
- [McGuire, 1988] McGuire, G. E. (1988). **Semiconductor materials and process technology handbook**. William Andrew.
- [McKenna et al., 2010] McKenna, C., Walsh, K., Crain, M., et Lake, J. (2010). **Maskless direct write grayscale lithography for mems applications**. In *2010 18th Biennial University/Government/Industry Micro/Nano Symposium*, pages 1–4. IEEE.
- [McLeod, 1954] McLeod, J. H. (1954). **The axicon: a new type of optical element**. *JOSA*, 44(8):592–597.
- [Merz et al., 2003] Merz, P., Quenzer, H., Bernt, H., Wanger, B., et Zoberbier, M. (2003). **A novel micromachining technology for structuring borosilicate glass substrates**. In *TRANSDUCERS, Solid-State Sensors, Actuators and Microsystems, 12th International Conference on, 2003*, volume 1, pages 258–261. IEEE.
- [MicroChemicals, 2007a] MicroChemicals (2007a). **Exposure of photoresists**.
- [MicroChemicals, 2007b] MicroChemicals (2007b). **General properties of az®/ti photoresist**.
- [MicroChemicals, 2010] MicroChemicals (2010). **High-resolution photoresist processing**.



- [MicroChemicals, 2013a] MicroChemicals (2013a). **Development of photoresist.**
- [MicroChemicals, 2013b] MicroChemicals (2013b). **Dry etching with photoresist masks.**
- [MicroChemicals, 2013c] MicroChemicals (2013c). **Optical parameters of photoresists.**
- [MicroChemicals, 2013d] MicroChemicals (2013d). **Rehydration of photoresist.**
- [MicroChemicals, 2013e] MicroChemicals (2013e). **Softbake of photoresist films.**
- [MicroChemicals, 2013f] MicroChemicals (2013f). **Thick resist processing.**
- [MicroChemicals, 2013g] MicroChemicals (2013g). **Thick resist processing.**
- [MicroChemicals, 2016] MicroChemicals (2016). <http://www.microchemicals.com/>.
- [MicroTec, 2016] MicroTec, S. (2016). **Suss microtec website.**
- [Milne et al., 2008] Milne, G., Jeffries, G. D., et Chiu, D. T. (2008). **Tunable generation of bessel beams with a fluidic axicon.** *Applied physics letters*, 92(26):261101.
- [Mogab et al., 1978] Mogab, C., Adams, A., et Flamm, D. L. (1978). **Plasma etching of si and sio<sub>2</sub>—the effect of oxygen additions to cf<sub>4</sub> plasmas.** *Journal of applied physics*, 49(7):3796–3803.
- [Mosher et al., 2009] Mosher, L., Waits, C. M., Morgan, B., et Ghodssi, R. (2009). **Double-exposure grayscale photolithography.** *Journal of Microelectromechanical Systems*, 18(2):308–315.
- [Mueller et al., 1997a] Mueller, K. E., Koros, W. J., Mack, C. A., et Willson, C. G. (1997a). **Diffusivity measurements in polymers: Iv. acid diffusion in chemically amplified resists.** In *Microlithography'97*, pages 706–711. International Society for Optics and Photonics.
- [Mueller et al., 1997b] Mueller, K. E., Koros, W. J., Wang, Y. Y., et Willson, C. G. (1997b). **Diffusivity measurements in polymers: Iii. quartz crystal microbalance techniques.** In *Microlithography'97*, pages 871–878. International Society for Optics and Photonics.
- [Nakasuji et al., 1990] Nakasuji, T., Kodera, S., Hara, S., Matsunaga, H., Ikawa, N., et Shimada, S. (1990). **Diamond turning of brittle materials for optical components.** *CIRP Annals-Manufacturing Technology*, 39(1):89–92.
- [Nejadmalayeri et al., 2005] Nejadmalayeri, A. H., Herman, P. R., Burghoff, J., Will, M., Nolte, S., et Tünnermann, A. (2005). **Inscription of optical waveguides in crystalline silicon by mid-infrared femtosecond laser pulses.** *Optics letters*, 30(9):964–966.
- [Nock et al., 2008] Nock, V., et Blaikie, R. J. (2008). **Fabrication of optical grayscale masks for tapered microfluidic devices.** *Microelectronic Engineering*, 85(5):1077–1082.
- [Norland, 2016] Norland (2016). **Norland blocking adhesive 107.**

- [Nussbaum et al., 1997] Nussbaum, P., Voelkel, R., Herzig, H. P., Eisner, M., et Haselbeck, S. (1997). **Design, fabrication and testing of microlens arrays for sensors and microsystems**. *Pure and applied optics: Journal of the European optical society part A*, 6(6):617.
- [of Technology, 2008] of Technology, R. I. (2008). **Resist sensitivity & contrast**.
- [Oikawa et al., 1981] Oikawa, M., Iga, K., Sanada, T., Yamamoto, N., et Nishizawa, K. (1981). **Array of distributed-index planar micro-lenses prepared from ion exchange technique**. *Japanese journal of applied physics*, 20(4):L296.
- [Olympus, 2012] Olympus (2012). **Cutoff frequency and airy disk size**.
- [O'Neill et al., 2002] O'Neill, F. T., et Sheridan, J. T. (2002). **Photoresist reflow method of microlens production part i: Background and experiments**. *Optik-International Journal for Light and Electron Optics*, 113(9):391–404.
- [Oppliger et al., 1994] Oppliger, Y., Sixt, P., Stauffer, J., Mayor, J., Regnault, P., et Voirin, G. (1994). **One-step 3d shaping using a gray-tone mask for optical and micro-electronic applications**. *Microelectronic Engineering*, 23(1-4):449–454.
- [Orloff et al., 1996] Orloff, J., Swanson, L., et Utlaut, M. (1996). **Fundamental limits to imaging resolution for focused ion beams**. *Journal of Vacuum Science & Technology B*, 14(6):3759–3763.
- [Osellame et al., 2012] Osellame, R., Cerullo, G., et Ramponi, R. (2012). **Femtosecond Laser Micromachining: Photonic and Microfluidic Devices in Transparent Materials**, volume 123. Springer Science & Business Media.
- [O'shea et al., 1995] O'shea, D. C., et Rockward, W. S. (1995). **Gray-scale masks for diffractive-optics fabrication: li. spatially filtered halftone screens**. *Applied optics*, 34(32):7518–7526.
- [Ouano, 1984] Ouano, A. (1984). **Dependence of dissolution rate on processing and molecular parameters of resists**.
- [Paniez et al., 1992] Paniez, P. J., Festes, G., et Chollet, J.-P. E. (1992). **Physical description of lithographic processes: correlation between bake conditions and photoresist contrast**. In *Micro-DL Tentative*, pages 623–637. International Society for Optics and Photonics.
- [Park et al., 2005] Park, J., Lee, N.-E., Lee, J., Park, J., et Park, H. (2005). **Deep dry etching of borosilicate glass using sf 6 and sf 6/ar inductively coupled plasmas**. *Microelectronic engineering*, 82(2):119–128.
- [Paulus et al., 1999] Paulus, M., Michel, B., et Martin, O. J. (1999). **Near-field distribution in light-coupling masks for contact lithography**. *Journal of Vacuum Science & Technology B*, 17(6):3314–3317.
- [Pease, 1981] Pease, R. (1981). **Electron beam lithography**. *Contemporary Physics*, 22(3):265–290.
- [Philip et al., 2009] Philip, G. M., et Viswanathan, N. K. (2009). **Fabrication of negative micro axicons in optical fibers via chemical etching**. *Oral presentation in ICOP*.

- [Piskarskas et al., 1999] Piskarskas, A., Smilgevičius, V., Stabinis, A., Jarutis, V., Pašiškevičius, V., Wang, S., Tellefsen, J., et Laurell, F. (1999). **Noncollinear second-harmonic generation in periodically poled ktiopo 4 excited by the bessel beam.** *Optics letters*, 24(15):1053–1055.
- [poliFAB, 2016] poliFAB (2016). **Karl süss spin coater rc8.**
- [Polytec, 2000] Polytec (2000). **Msa-500 micro system analyzer.**
- [Popovic et al., 1988] Popovic, Z. D., Sprague, R. A., et Connell, G. N. (1988). **Technique for monolithic fabrication of microlens arrays.** *Applied optics*, 27(7):1281–1284.
- [Prikhodko et al., 2011] Prikhodko, I. P., Zotov, S. A., Trusov, A. A., et Shkel, A. M. (2011). **Microscale glass-blown three-dimensional spherical shell resonators.** *Journal of Microelectromechanical Systems*, 20(3):691–701.
- [Puthankovilakam et al., 2014] Puthankovilakam, K., Scharf, T., Tan, Q., Herzig, H. P., Nguyen, D., Vogler, U., Bramati, A., et Voelkel, R. (2014). **Shaping intensity behind amplitude masks for proximity correction lithography: design, measurement, and realization.** In *SPIE Optical Engineering+ Applications*, pages 92031B–92031B. International Society for Optics and Photonics.
- [Quenzer et al., 2010] Quenzer, H. J., Merz, P., et Bott, U. (2010). **Method for producing single microlenses or an array of microlenses.** US Patent 7,716,950.
- [Queste, 2008] Queste, S. (2008). **La gravure sèche profonde.** In *Annales françaises des microtechniques et de chronométrie*, volume 78, pages 43–53. Société française des microtechniques et de chronométrie.
- [Radtke et al., 2007a] Radtke, D., Duparré, J., Zeitner, U. D., et Tünnermann, A. (2007a). **Laser lithographic fabrication and characterization of a spherical artificial compound eye.** *Optics express*, 15(6):3067–3077.
- [Radtke et al., 2007b] Radtke, D., et Zeitner, U. D. (2007b). **Laser-lithography on non-planar surfaces.** *Optics Express*, 15(3):1167–1174.
- [Rammohan et al., 2011] Rammohan, A., Dwivedi, P. K., Martinez-Duarte, R., Katepalli, H., Madou, M. J., et Sharma, A. (2011). **One-step maskless grayscale lithography for the fabrication of 3-dimensional structures in su-8.** *Sensors and Actuators B: Chemical*, 153(1):125–134.
- [Reimer et al., 1997] Reimer, K., Hofmann, U., Jürss, M., Pilz, W., Quenzer, H. J., et Wagner, B. (1997). **Fabrication of microrelief surfaces using a one-step lithography process.** In *Micromachining and Microfabrication*, pages 2–10. International Society for Optics and Photonics.
- [Reyntjens et al., 2001] Reyntjens, S., et Puers, R. (2001). **A review of focused ion beam applications in microsystem technology.** *Journal of Micromechanics and Microengineering*, 11(4):287.
- [Rocha et al., 2013] Rocha, R., Maciel, M., Carmo, J., et Correia, J. (2013). **High-quality surface microlenses based on rehydration.**
- [Rossi et al., 1995] Rossi, M., Kunz, R., et Herzig, H.-P. (1995). **Refractive and diffractive properties of planar micro-optical elements.** *Applied optics*, 34(26):5996–6007.



- [Roy et al., 2003] Roy, D., Basu, P., Raghunathan, P., et Eswaran, S. (2003). **Novolak resins: structure elucidation by multidimensional nmr techniques and correlation with lithographic performance.** *Polymer international*, 52(5):757–767.
- [Roy et al., 2009] Roy, E., Voisin, B., Gravel, J.-F., Peytavi, R., Boudreau, D., et Veres, T. (2009). **Microlens array fabrication by enhanced thermal reflow process: Towards efficient collection of fluorescence light from microarrays.** *Microelectronic Engineering*, 86(11):2255–2261.
- [Rubin, 1972] Rubin, I. (1972). **Injection moulding.** John Wiley & Sons, New York.
- [Rudmann et al., 2004] Rudmann, H., et Rossi, M. (2004). **Design and fabrication technologies for ultraviolet replicated micro-optics.** *Optical Engineering*, 43(11):2575–2582.
- [Ryoo et al., 2011] Ryoo, H., Kang, D. W., et Hahn, J. W. (2011). **Analysis of the line pattern width and exposure efficiency in maskless lithography using a digital micromirror device.** *Microelectronic Engineering*, 88(10):3145–3149.
- [Samad et al., 2014] Samad, R. E., MACHADO, L. M., JUNIOR, V., NILSON, D., et ROSSI, W. d. (2014). **Ultrashort laser pulses machining.**
- [Sampsel, 1994] Sampsel, J. B. (1994). **Digital micromirror device and its application to projection displays.** *Journal of Vacuum Science & Technology B*, 12(6):3242–3246.
- [Sarvar et al., 2002] Sarvar, F., Hutt, D. A., et Whalley, D. C. (2002). **Application of adhesives in mems and moems assembly: a review.** In *Polymers and Adhesives in Microelectronics and Photonics, 2002. POLYTRONIC 2002. 2nd International IEEE Conference on*, pages 22–28. IEEE.
- [Schnabel, 2004] Schnabel, B. (2004). **Microlithographic pattern generation for optics.** In *Microoptics*, pages 29–41. Springer.
- [Schoot., 2014] Schoot. (2014). **Ar-glas.**
- [Schott, 2016a] Schott (2016a). **Schott borofloat 33.**
- [Schott, 2016b] Schott (2016b). **Schott borofloat 33.**
- [SciGlass, 2016a] SciGlass (2016a). **Sciglass information system.**
- [SciGlass, 2016b] SciGlass (2016b). **Vogel-fulcher-tamman equation.**
- [Seidel et al., 1990] Seidel, H., Csepregi, L., Heuberger, A., et Baumgärtel, H. (1990). **Anisotropic etching of crystalline silicon in alkaline solutions i. orientation dependence and behavior of passivation layers.** *Journal of the electrochemical society*, 137(11):3612–3626.
- [Senkal et al., 2013] Senkal, D., Ahamed, M., Trusov, A., et Shkel, A. (2013). **High temperature micro-glassblowing process demonstrated on fused quartz and ule tsg.** *Sensors and Actuators A: Physical*, 201:525–531.
- [Senkal et al., 2014] Senkal, D., Ahamed, M., Trusov, A., et Shkel, A. (2014). **Electrostatic and mechanical characterization of 3-d micro-wineglass resonators.** *Sensors and Actuators A: Physical*, 215:150–154.

- [Serhatlioglu et al., 2016] Serhatlioglu, M., Ortaç, B., Elbuken, C., Biyikli, N., et Solmaz, M. E. (2016). **Co2 laser polishing of microfluidic channels fabricated by femtosecond laser assisted carving**. *Journal of Micromechanics and Microengineering*, 26(11):115011.
- [Shaw et al., 1977] Shaw, J., Frisch, M., et Dill, F. (1977). **Thermal analysis of positive photoresist films by mass spectrometry**. *IBM Journal of Research and Development*, 21(3):219–226.
- [Shew et al., 2005] Shew, B., Kuo, C., Huang, Y., et Tsai, Y. (2005). **Uv-liga interferometer biosensor based on the su-8 optical waveguide**. *Sensors and Actuators A: Physical*, 120(2):383–389.
- [Shyu et al., 2007] Shyu, R. F., Yang, H., Tsai, W.-R., et Tsai, J.-C. (2007). **Micro-ball lens array fabrication in photoresist using ptfe hydrophobic effect**. *Microsystem Technologies*, 13(11-12):1601–1606.
- [Singh et al., 2009] Singh, A., Shirolkar, M., Lalla, N. P., Malek, C. K., et Kulkarni, S. (2009). **Room temperature, water-based, microreactor synthesis of gold and silver nanoparticles**. *International Journal of Nanotechnology*, 6(5-6):541–551.
- [Sinzinger et al., 2006] Sinzinger, S., et Jahns, J. (2006). **Microoptics**. John Wiley & Sons.
- [Stenchly et al., 2012] Stenchly, V., Quenzer, H.-J., Hofmann, U., Eisermann, C., et Bencke, W. (2012). **Viscous hot glass forming for optical wafer level packaging of micro mirrors**. *Procedia Engineering*, 47:64–67.
- [Stern et al., 1994] Stern, M. B., et Jay, T. R. (1994). **Dry etching for coherent refractive microlens arrays**. *Optical Engineering*, 33(11):3547–3551.
- [Swanson, 1989] Swanson, G. J. (1989). **Binary optics technology: the theory and design of multi-level diffractive optical elements**. Technical Report, DTIC Document.
- [Swanson et al., 1989] Swanson, G. J., et Veldkamp, W. B. (1989). **Diffractive optical elements for use in infrared systems**. *Optical Engineering*, 28(6):286605–286605.
- [Sweatt et al., 2008] Sweatt, W., Gill, D., Ada, D., Vasile, M., et Claudet, A. (2008). **Diamond milling of micro-optics**. *IEEE Aerospace and Electronic Systems Magazine*, 23(1):13–17.
- [Systems, 2000] Systems, M. P. (2000). **Controlled chemical plasma etching for advanced technology applications. application note**.
- [Tachi et al., 1988] Tachi, S., Tsujimoto, K., et Okudaira, S. (1988). **Low-temperature reactive ion etching and microwave plasma etching of silicon**. *Applied physics letters*, 52(8):616–618.
- [Takagi et al., 1997] Takagi, H., Maeda, R., Chung, T. R., et Suga, T. (1997). **Low temperature direct bonding of silicon and silicon dioxide by the surface activation method**. In *Solid State Sensors and Actuators, 1997. TRANSDUCERS'97 Chicago, 1997 International Conference on*, volume 1, pages 657–660. IEEE.

- [Tam et al., 2014] Tam, L.-h., et Lau, D. (2014). **A molecular dynamics investigation on the cross-linking and physical properties of epoxy-based materials.** *RSC Advances*, 4(62):33074–33081.
- [Teague et al., 1981] Teague, E. C., Vorburger, T. V., Maystre, D., et Young, R. (1981). **Light scattering from manufactured surfaces.** *CIRP Annals-Manufacturing Technology*, 30(2):563–569.
- [Tencor, 2010] Tencor, K. (2010). **Alpha-step iq.**
- [Thiénot et al., 2006] Thiénot, E., Domingo, F., Cambril, E., et Gosse, C. (2006). **Reactive ion etching of glass for biochip applications: Composition effects and surface damages.** *Microelectronic engineering*, 83(4):1155–1158.
- [Thorlabs, 2016] Thorlabs, I. (2016). **Axicons.**
- [Tseng et al., 2003] Tseng, A. A., Chen, K., Chen, C. D., et Ma, K. J. (2003). **Electron beam lithography in nanoscale fabrication: recent development.** *IEEE Transactions on electronics packaging manufacturing*, 26(2):141–149.
- [Tyona, 2013] Tyona, M. (2013). **A theoretical study on spin coating technique.** *Advances in materials Research*, 2(4):195–208.
- [Van LE et al., 2012] Van LE, A., et Richardi, N. J. (2012). **Axicons and methods of making the same.** US Patent App. 13/448,289.
- [Van Toan et al., 2015] Van Toan, N., Sangu, S., Inomata, N., et Ono, T. (2015). **Glass capillaries based on a glass reflow into nano-trench for controlling light transmission.** *Microsystem Technologies*, pages 1–6.
- [Vega et al., 1998] Vega, F., Laguarda, F., et others (1998). **Laser application for optical glass polishing.** *Optical Engineering*, 37(1):272–279.
- [Voelkel, 2012] Voelkel, R. (2012). **Wafer-scale micro-optics fabrication.** *Advanced Optical Technologies*, 1(3):135–150.
- [Voelkel et al., 2011] Voelkel, R., Weible, K. J., et Eisner, M. (2011). **Wafer-level micro-optics: trends in manufacturing, testing, and packaging.** In *SPIE Optical Systems Design*, pages 81690C–81690C. International Society for Optics and Photonics.
- [Waits et al., 2005] Waits, C., Morgan, B., Kastantin, M., et Ghodssi, R. (2005). **Micro-fabrication of 3d silicon mems structures using gray-scale lithography and deep reactive ion etching.** *Sensors and Actuators A: Physical*, 119(1):245–253.
- [Waits et al., 2002] Waits, C. M., Modafe, A., et Ghodssi, R. (2002). **Investigation of gray-scale technology for large area 3d silicon mems structures.** *Journal of Micromechanics and Microengineering*, 13(2):170.
- [Waldo III, 1990] Waldo III, W. G. (1990). **Method of optimizing photoresist contrast.** US Patent 4,891,094.
- [Wang et al., 2006] Wang, L., Jin, E. X., Uppuluri, S. M., et Xu, X. (2006). **Contact optical nanolithography using nanoscale c-shaped apertures.** *Optics express*, 14(21):9902–9908.

- [Wang et al., 2015] Wang, W.-S., Lullin, J., Froemel, J., Wiemer, M., Bargiel, S., Passilly, N., Gorecki, C., et Gessner, T. (2015). **Multi-wafer bonding technology for the integration of a micromachined mirau interferometer**. In *SPIE OPTO*, pages 93750P–93750P. International Society for Optics and Photonics.
- [Whelan, 2012] Whelan, A. (2012). **Polymer technology dictionary**. Springer Science & Business Media.
- [Wikipedia, 2015] Wikipedia (2015). **Conic constant**.
- [Wikipedia, 2016] Wikipedia (2016). **Electron-beam lithography**.
- [Wlodarczyk, 2011] Wlodarczyk, K. L. (2011). **Surface deformation mechanisms in laser smoothing and micromachining of optical glasses**. PhD thesis, Heriot-Watt University.
- [Wu et al., 2015] Wu, C.-E., Wei, D., Zhang, C., et Song, H. (2015). **Low-contrast photoresist development model for opc application at 10nm node**. In *SPIE Advanced Lithography*, pages 94260N–94260N. International Society for Optics and Photonics.
- [Wu et al., 2002] Wu, M.-H., et Whitesides, G. M. (2002). **Fabrication of two-dimensional arrays of microlenses and their applications in photolithography**. *Journal of micromechanics and microengineering*, 12(6):747.
- [Xie et al., 2008] Xie, Q., Hong, M., Tan, H., Chen, G., Shi, L., et Chong, T. (2008). **Fabrication of nanostructures with laser interference lithography**. *Journal of alloys and compounds*, 449(1):261–264.
- [Yan et al., 2010] Yan, J., Zhang, Z., et Kuriyagawa, T. (2010). **Tool wear control in diamond turning of high-strength mold materials by means of tool swinging**. *CIRP Annals-Manufacturing Technology*, 59(1):109–112.
- [Yao et al., 2000] Yao, J., Su, J., Du, J., Zhang, Y., Gao, F., Gao, F., Guo, Y., et Cui, Z. (2000). **Coding gray-tone mask for refractive microlens fabrication**. *Microelectronic Engineering*, 53(1):531–534.
- [Yoshikawa et al., 1998] Yoshikawa, N., Itoh, M., et Yatagai, T. (1998). **Binary computer-generated holograms for security applications from a synthetic double-exposure method by electron-beam lithography**. *Optics letters*, 23(18):1483–1485.
- [Zappe, 2013] Zappe, H. (2013). **Laser diode microsystems**. Springer Science & Business Media.
- [Zhang et al., 2010] Zhang, Y.-L., Chen, Q.-D., Xia, H., et Sun, H.-B. (2010). **Designable 3d nanofabrication by femtosecond laser direct writing**. *Nano Today*, 5(5):435–448.
- [Zhao et al., 1998] Zhao, Q., et Kohl, P. A. (1998). **Reactive ion etching of silicon containing polynorbornenes**. *Journal of The Electrochemical Society*, 145(4):1257–1262.
- [Zhu et al., 2013] Zhu, H., Isikman, S. O., Mudanyali, O., Greenbaum, A., et Ozcan, A. (2013). **Optical imaging techniques for point-of-care diagnostics**. *Lab on a Chip*, 13(1):51–67.





## Abstract:

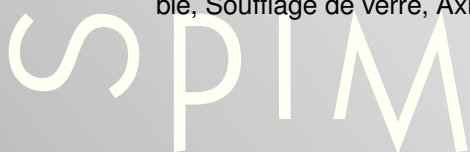
Miniaturization of imaging systems shows nowadays a strong potential for many applications, in particular, e. g., for novel biomedical devices. Related imaging specifications require a substantial effort onto the development of high quality microoptical components. Better control of light propagation and features in such systems is also of particular interest. Components should then e.g. contain optical aberrations in order to reach high resolutions. In purpose of searching higher diffraction efficiencies or resolutions, optical components with well-controlled continuous phase profiles are sought. In addition, they also should be made of robust materials to handle their further assembly into miniaturized devices. Consequently, the manuscript focuses on the design and the parallel fabrication of such microoptical components made of glass. To that end, two technologies have been studied and optimized, namely gray-scale lithography and glass-blowing processes. As an example, glass-based microaxicons have been fabricated and Bessel beams generation has been demonstrated. This type of beam exhibits a long non-diffractive propagation distance along the optical axis followed by a dark hollow shape which makes them useful in many different applications. This work has been supported by the SMYLE (Smart Systems for a Better Life) European project and the Franche-Comté Regional Council.

**Keywords:** Microoptical components, MOEMS, Microfabrication, Laser beam lithography, Photoresist, Glass-reflow, Glass-blowing, Axicon, Bessel beams.

## Résumé :

La miniaturisation des systèmes d'imagerie présente aujourd'hui un fort potentiel dans plusieurs domaines, dont le développement de nouveaux dispositifs biomédicaux. Les exigences associées concernant l'imagerie demandent un effort substantiel dans le développement de composants optiques de haute qualité. Un meilleur contrôle de la propagation de la lumière ou de ses caractéristiques dans de tels systèmes est également important. Les composants doivent donc, par exemple, contenir les aberrations optiques pouvant affecter la résolution des systèmes. Dans l'objectif d'améliorer l'efficacité de diffraction des composants ou la résolution, la mise en oeuvre de composants optiques dont le profil de phase continu est bien contrôlé est une voie intéressante. Ces composants devraient, de plus, être réalisés à partir de matériaux robustes en vue de leur assemblage au sein de dispositifs miniatures. Ce manuscrit de thèse de doctorat porte donc sur la conception et la fabrication parallèle de tels micro-composants optiques réfractifs réalisés en verre. Dans ce but, deux technologies ont été étudiées et optimisées, la lithographie à niveaux de gris et un procédé de soufflage de verre. En exemple, des microaxicons en verre ont été fabriqués et la génération de faisceaux de Bessel démontrée. Ce type de faisceau est caractérisé par une longue distance de propagation non-diffractive le long de l'axe optique, suivie d'une forme de faisceaux creux, qui les rend très utiles dans de nombreux domaines. Ces travaux de thèse ont été soutenus par le projet SMYLE (Small Systems for a Better Life) et le Conseil Régional de Franche-Comté.

**Mots-clés :** Microcomposants optiques, MOEMS, Microfabrication, Lithographie laser, Résine photosensible, Soufflage de verre, Axicon, Faisceaux de Bessel.

The logo for the SPIM (École doctorale SPIM) features the letters 'S', 'P', 'I', and 'M' in a large, white, sans-serif font. The 'S' is stylized with a thick, white, curved underline that extends to the left and then curves back under the 'P'. The 'P', 'I', and 'M' are stacked vertically to the right of the 'S'.